Part I: Broadband Modeling of Aftershocks from the Joshua Tree, Landers, and Big Bear Sequences, Southern California

Part II: Characteristics of the June 28, 1992, Big Bear Mainshock from TERRAscope Data: Evidence for a Multiple-Event Source

Thesis by
Laura Ellen Jones

In Partial Fulfillment of the Requirements
for the Degree of
Doctor of Philosophy

California Institute of Technology
Pasadena, California

1995

(Submitted January 17, 1995)

Copyright © 1995

Laura Ellen Jones

All rights reserved

Acknowledgments

When true simplicity is gained,
to bow and to bend
We shan't be ashamed.
To turn, turn will be our delight,
'Till by turning, turning
We come round right.

Shaker Hymm

This portion of my thesis has been the most difficult to write, since I have so many people to thank and so little space in which to express my appreciation properly. My time at Caltech has been occasionally trying, but always a period of growth and discovery for me. When I briefly entertained the notion of leaving graduate school, I realized that (unhappy as I might be at that particular moment), I was doing what I really wanted to do. Nothing else would suffice.

Many people have taught, encouraged, and guided me during my tenure here. My advisor, Don Helmberger, gave me his appreciation for waveform data, and helped to form me into the observational scientist I am now becoming. I thank him for his constancy, his good humor, and his compassion. Joann Stock has been a mentor and a friend for many years, and is a wonderful role model as well. Susan Hough showed me how rewarding and exciting a collaboration can be. I thank her for her interest in me, in my career, and especially for her input and efforts on Big Bear. I thank Hiroo

Kanamori for his continuing efforts to maintain and expand the TERRAscope array, and also for his patient and careful answers to my numerous questions.

Bob Sharp has been a good friend and a diligent correspondant. I thank him for his affection, for Pahoehoe, and for the letters which I hope will continue to fly between us.

One of the benefits of being part of an organism like the Seismological Laboratory is access to the people who form it. I consider myself lucky to have been part of a large and enthusiastic research group. Ed Garnero, Craig Scrivner, Xiao–dong Song, Xi Song, Dave Wald, and Lianshe Zhao have all contributed to my understanding of seismology, and have helped in many small (and some large) ways with this thesis. I thank Blair Zajac for his assistance with encapsulated post-script, and for his friendship. Shawn Larsen wrote the plotting code which generated many of the figures in this thesis.

I've been very lucky with officemates as well. I'll miss each of my officemates (Guang-quing Chen, Monica Kohler, Kuo–Fong Ma and Igor Sidorin) sorely, and only hope that I end up with a group of similarly congenial and well–adjusted people in my new position.

Ann Freeman, Cheryl Contopulous, and all of the other good women who keep the Seismo–lab office running smoothly have my gratitude and admiration. The two Anns (Freeman and Hutton) deserve special thanks for mothering me when I most needed it.

Laurie Patterson, my chemistry and physics teacher at La Canada High School, deserves my thanks for encouraging me to pursue a career in the physical sciences.

The faculty at Pasadena City College are to be commended for their fine Earth Sciences program. I am proud to have my roots at PCC, and hope for their continued success in a time of budgetary cutbacks.

I also thank the faculty at University of California, Riverside, especially Professors Peter Sadler and Stephen Park, with whom I wrote my first research paper.

Friendships outside of the division have also helped to sustain me through the many years I spent in school. I thank: Achim Ditzen (for his matter-of-fact missives from abroad), Suzanne Elsasser (for creature and kitchen comforts), Gretchen Hamm (for

loyalty, affection and excellent letters), Mark O'Dell (for grace under pressure), Michal Peri (for her encouragement, breakfasts, and for producing both a thesis and a daughter simultaneously), Priscilla Piano (fellow wine-snob and gutter-groveler), Helen Qian (fellow shutter-bug and restless spirit), Robert Spero (for encouraging me to become a scientist), Craig Steele (for admiration on the good days, scolding and concern on the worst days, and contemplative presence all the days in between), and lastly, Jon (for his interest and many years of patient listening).

Finally, I thank Jeff Hammond for his love and companionship, and give special thanks to my father, who convinced me I could do anything I wanted to do.

Remembering Cynthia Gale Arvesen,

with love and peace.

Abstract

Laura Ellen Jones, Ph.D.

California Institute of Technology, 1995

The Joshua Tree, Landers and Big Bear earthquake sequences recorded on the broadband TERRAscope array in Southern California provide an unusually large data set of high–quality three–component broadband waveforms from small to moderately sized earthquakes. This data set offers the opportunity of detailed large–scale studies of these smaller but nonetheless potentially damaging earthquakes. What follows is a detailed study of over sixty $M > 3.8$ aftershocks in three regions: north and south of the Pinto Mountain fault in the Mojave desert (associated with the Joshua Tree and Landers sequences), and within the San Bernardino mountains block (associated with the Big Bear sequence). Source parameters, including depths, moments, and durations, for sixty $M_w > 3.8$ earthquakes from the Joshua Tree, Landers, and Big Bear sequences are presented here. These events occurred between April of 1992 and November of 1994; the list of events comprises nearly every aftershock above $M3.8$ for which we could obtain coherent TERRAscope data and accurate timing and location information.

Choice of velocity model affects the accuracy of the source estimations and the error associated with estimations of moment, though it appears that for Landers events recorded at stations within or near the Mojave region, a simple one–dimensional velocity

model is adequate. To minimize model–associated error, however, a velocity model for the Mojave region is developed and presented. This model is used in the computation of the synthetic Green's functions used in estimates of source parameters for many of the earthquakes presented here.

The existence of such a large data set from events in the same region (the Mojave desert) also allows systematic investigation of station effects for the five TERRAscope stations used in this study: Goldstone (GSC), Isabella (ISA), Pasadena (PAS), Pinyon Flats (PFO), and Seven Oaks Dam (SVD). For each event, moments and durations are computed for each station, and these examined for systematic variations of moment with azimuth and with source–receiver distance.

Moments and durations are computed for each aftershock we study, and stress–drops inferred from these appear to vary with location, with respect to previous seismic activity, and proximity to previous (i.e., Landers) rupture. A strong correlation of increased stress–drop with depth is noted for the Big Bear region; the same is not observed for Mojave aftershocks.

The June 28, 1992, Big Bear earthquake is commonly considered to be an aftershock of the earlier $M_w = 7.3$ Landers mainshock, and as such has been perhaps overlooked. However, it is a significant and enigmatic event in its own right. Its rupture history was obscured by controversy over epicentral location, lack of observed surface rupture, and the complexity of source suggested by the mainshock waveforms themselves. From overall patterns of seismicity and long–period focal studies, rupture is generally assumed to have propagated northeast. However, mainshock locations from both strong–motion and TERRAscope data are consistent and do not lie on this assumed fault plane. Further, directivity analysis suggests significant energy propagating northwest along the presumed antithetic fault–plane. A combination of directivity analysis, point–source empirical Green's function analysis, and line–source directivity analysis together indicate that a two–fault event is necessary to produce the waveforms observed during the

Big Bear mainshock. These results suggest that the Big Bear earthquake comprised at least two substantial subevents, with the initial subevent rupturing towards the northwest on the presumed antithetic fault plane. Several seconds later, rupture initiated on the northeast striking plane.

Contents

List of Figures

List of Tables

Chapter 1

Introduction

> And the rocks themselves shall be moved. They heave to their own necessities, to stirrings and prickings from within and without...
> The mountains are no more fixed than the stars. When granite forms under the earth's crust, great chunks of it bob up, I read somewhere, like dumplings. The continents themselves are beautiful pea-green boats...
>
> Annie Dillard, *Teaching a Stone to Talk*, 1982.

1.1 Broadband Modeling

The field of broadband modeling is young; we are still learning about the complexities of modeling such data, and occasionally make observations and obtain results we can't yet fully explain. It is possible that after reviewing this thesis, one might ask oneself: "Why bother modeling data broadband?" After all, filtered data certainly give visually neater waveform fits, lower errors in the estimation of moment, and often more consistent results in the estimation of source–parameters. Inherent trade–offs between source complexity and structural heterogeneity complicate efforts to accurately and efficiently model either source or structure. This is a problem faced by anyone who attempts to model local or regional waveforms, but it becomes much stickier when the modeling is done broadband. Idiosyncrasies of individual stations and related site effects represent

an additional, certainly interesting level of complexity which we document, and which we must somehow address during the course of modeling these sources.

However, bearing in mind that much of the error can be assigned to some combination of inadequate strunctural models, lack of detailed information about the idiosyncracies of each station, and in the limit, insufficient computing resources or disk storage space, the results we do obtain with simple source–time functions and one– or two–dimensional models are often surprisingly good. Unmodeled variation in amplitude or duration from station to station increases the error in the moment estimations, yet these same variations contain useful information about source, path, or station effects. Broadband data also contain a wealth of previously unexploited information about source complexity, though this complexity may complicate efforts to fit waveforms with a point–source solution.

1.2 Outline of Thesis

The body of the thesis that follows consists of two long chapters and two appendices. Each of the two chapters is self–contained, with its own abstract, introduction, and conclusion or discussion sections. This results in some redundacy of material between chapters. The appendices comprise a library of waveform modeling for Landers aftershocks north and south of the Pinto Mountain fault.

1.2.1 Overview of Chapter 2

Chapter 2 details the results of large-scale study of aftershocks from three recent California earthquakes: the Joshua Tree precursor to the Landers quake, the Landers quake, and the Big Bear aftershock to the Landers quake. All three earthquakes possessed substantial fore– and aftershock sequences of their own. The modeling in this study was done using data from a sparse broadband array; data from three to at most five stations

from the broadband TERRAscope array was used to find high-quality source parameters for approximately 60 small–to–moderately sized events occurring in Southern California between April, 1992 and November, 1994.

The methods we developed and employed and some of the mysteries and pitfalls we encountered while modeling a large and surprisingly diverse data set are outlined in the first half of Chapter 2. A new velocity model for the Mojave region is introduced, and used in further source estimations. As error associated with moment estimation is a well–known problem, we examine variations in the moment estimation between stations, and with increasing source–station distance. The second portion of Chapter 2 discusses the results from the application of the methods outlined earlier. The analysis is organized regionally, and to some extent chronologically. The Joshua Tree sequence is discussed first, followed by subsequent (post–Landers) seismic activity south of the Pinto Mountain fault. Activity along and off the trace of the Landers rupture (north of the Pinto Mountain fault) is then discussed, followed by off–fault activity on the Garlock fault and in the Big Bear region.

1.2.2 Overview of Chapter 3

In Chapter 3, we present results from the broad-band study of the complex Big Bear mainshock. The Big Bear mainshock was largely overlooked in the aftermath of the larger Landers quake, though it is an interesting and puzzling event, and caused enough damage in Big Bear City to be deserving of study in its own right. The conclusions drawn in this study are based on a number of very different methods of analysis, all of which yielded consistent results. Though the Big Bear mainshock was assumed to have ruptured along a north–east trending plane, an assumption based largely on long–term aftershock distribution, the location of the Big Bear mainshock northwest of the northeast–trending swath of seismicity associated with the assumed fault–plane makes this problematic. This chapter presents results of a broadband study of the Big Bear

mainshock based on event directivity, point–source theoretical and empirical Green's function modeling, and line–source modeling.

Chapter 2

Broadband Modeling of Aftershocks From the Landers, Joshua Tree and Big Bear Sequences

When two plates scrape along each other
like a mother and a daughter
it is called a fault.

Sharon Olds, 1980. *Quake Theory*

2.1 Abstract

The Joshua Tree, Landers and Big Bear sequences began on April 23, 1992 at 02:25 GMT with a M_w4.3 foreshock which preceded the M_w6.1 Joshua Tree mainshock by approximately 2 hours and 25 minutes. The Landers earthquake comprised rupture on six separate faults, if rupture south of the Pinto Mountain fault (on the Eureka Peak fault) is included, and its aftershock sequence included earthquakes in many regions unassociated with rupture, including the aftershocks South of the Pinto Mountain fault,

in the Big Bear region, and including an energetic cluster of aftershocks north of the city of Barstow. In this paper, we present source parameters, including depths and durations, for sixty $M_w > 3.8$ earthquakes from the Joshua Tree, Landers, and Big Bear sequences. These events occurred between April of 1992 and November of 1994; the list of events presented includes nearly every aftershock above $M3.8$ for which we could obtain coherent TERRAscope data and accurate timing and location information. It includes a related, high stress-drop $M5.3$ earthquake which occurred along the Garlock fault on July 11, 1992.

As error associated with moment estimation results from both model misfit and site effects: we develop and present a new one–dimensional velocity model for the Mojave structure, and use this model in further source estimations. For a given event, we compute moment for each station, and examine the results for systematic variations of moment with azimuth. We find that stations Goldstone (GSC) and Seven Oaks Dam (SVD) generally yield higher than average moments, while stations Pinon Flats (PFO) and Isabella (ISA) yield moment estimations lower than average. For stations SVD and PFO, this behavior itself varies with source–receiver distance. Moments are averaged over between three and five stations (whatever is available) to give an average moment estimation for the event.

Stress drops for these earthquakes appear to vary systematically with location, with respect to previous seismic activity, proximity to previous rupture (i.e., with respect to the Landers rupture), and with tectonic province. In general, for areas north of the Pinto Mountain fault, stress-drops of aftershocks located off the faults involved with the Landers rupture are higher stress-drop than those located on the fault, with the exception of aftershocks on the newly recognized Kickapoo (Landers) fault. South of the Pinto Mountain fault, where there is a history of seismic swarms, but no single through-going fault, in general stress-drops are not unusually high. For the Big Bear region, stress drops appear to correlate with depth, with the deepest events yielding

the highest stress-drops. Further, events in this region overall yield higher stress-drops than in the Mojave region, associated with the Landers and Joshua Tree sequences.

2.2 Introduction

The M_w7.3 Landers earthquake of 11:58 GMT, June 28, 1992, was preceded by the M_w6.1 Joshua Tree mainshock, now considered a precursory event [Stein et al., 1994] which has its own substantial fore– and aftershock sequence. Aftershocks from the Joshua Tree mainshock were distributed north of the Pinto Mountain fault into regions ruptured by the Landers sequence. The Landers event was followed by tens of thousands of aftershocks [Kanamori et al., 1992; Hauksson et al., 1993; Sieh et al., 1993], many in areas with no surface rupture. The largest of these was the Big Bear earthquake that occurred three hours later and was associated with significant damage in Big Bear City.

Larger fore– and aftershocks from the Joshua Tree, Landers and Big Bear sequences were recorded on scale by six broadband TERRAsope stations (GSC, ISA, PAS, PFO, SVD and SBC). In this study we use records from the first five stations, as records from station SBC are noisy, distant and contaminated by propagation through basin structure. For TERRAscope stations Goldstone (GSC) and Pinyon Flats (PFO), due north and nearly south of the Landers rupture, we construct profiles of aftershocks from the Landers earthquake. These include earthquakes in areas associated with surface rupture (north of the Pinto Mountain fault), south of the Pinto Mountain fault, and associated with the Barstow swarm. The aftershocks form rough profiles following the general trend of the Landers rupture. Records at these distances are dominated by crustal arrivals and Moho–reflected arrivals, which suggest a crust thinner (depth to the Moho is 28 km) and slower than the standard Southern California Model [Hadley and Kanamori, 1978; Dreger and Helmberger, 1991] and lacking the gradient at the base of the crust (Conrad) which characterizes the widely used Standard Model. We

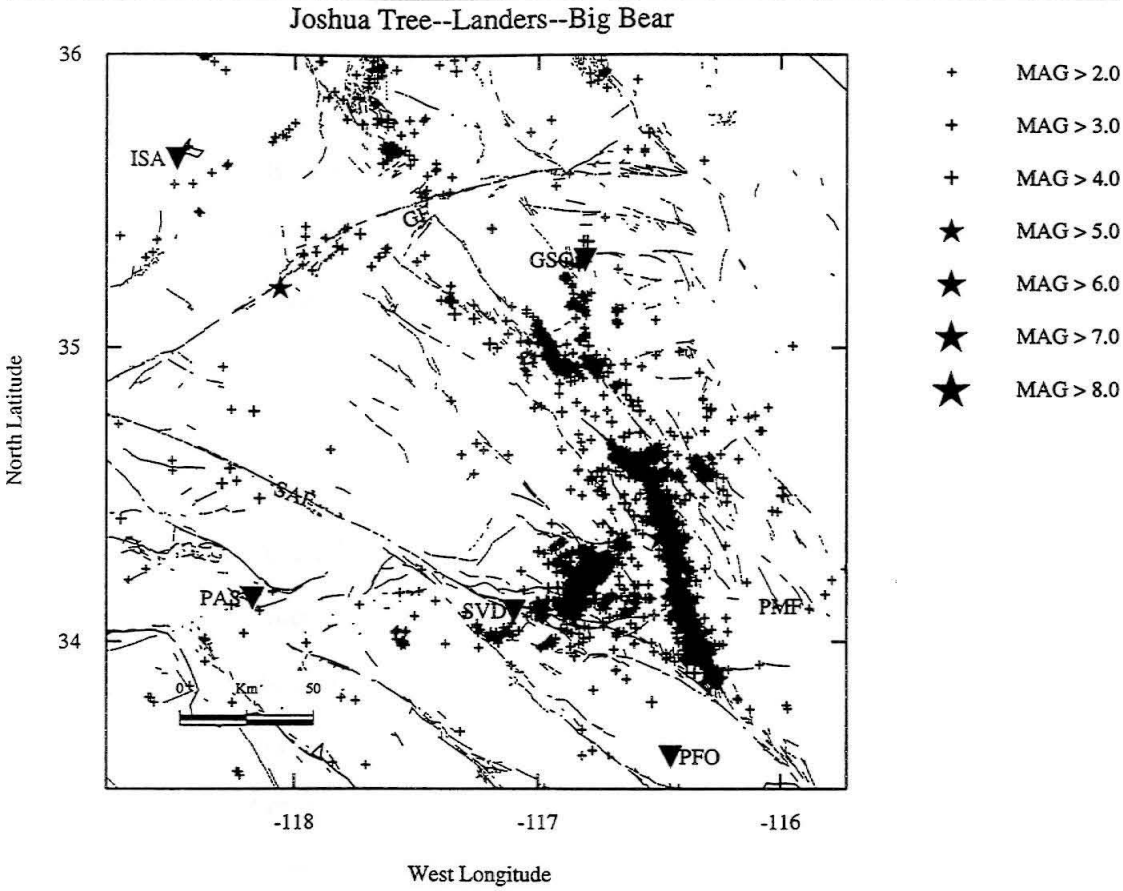

Figure 2.1: Location map showing main events and aftershocks from the Joshua Tree, Landers and Big Bear sequences. Map covers seismicity from April 23, 1992, to December 31, 1992. Faults are indicated as follows: SAF (San Andreas fault), GF (Garlock fault), PMF (Pinto Mountain fault).

present a new velocity model for the Mojave region which features a thin, slow crust. Using this model, we obtain source mechanisms, moments and source durations for each of the aftershocks in the profiles, and in addition, any significant ($M > 3.7$) Joshua Tree–Landers aftershock between April, 1992 and October, 1994 for which coherent TERRAscope data were available. We determine source parameters and stress-drops for 56 significant ($M_w > 4$) earthquakes associated with the Joshua Tree, Landers and Big Bear sequences, plus the Big Bear mainshock, using a grid–search algorithm developed by Zhao and Helmberger [1994]. The data were fit to theoretical Green's functions broadband and after convolution with a long–period instrument response. The selection of earthquakes examined includes every event above magnitude 3.9 for which coherent, high signal–to–noise TERRAscope data are available (Figure 2.1, Tables 2.3, 2.4, 2.5, 2.6).

Along with the plentiful aftershocks local to the Landers rupture, the months and weeks following the Landers mainshock saw an increase in regional seismicity, arguably triggered by changes in regional stresses due to the Landers event [Hill et al., 1993]. Significant ($M_w > 3.8$) and more distant aftershocks and "triggered" events associated with the Landers earthquake, such as a very high stress-drop $M_w5.3$ event occurring on July 11, 1992 on the Garlock fault, and the complex $M_w6.5$ Big Bear earthquake and related events are also examined.

The Big Bear earthquake is associated with its own fore– and aftershock sequences, including several earthquakes in the $M4-5$ range. We determine high–quality fault–plane solutions for 15 significant ($M > 3.9$) aftershocks, including the more recent April 4, 1994 19:04 GMT $M_w4.6$ Lake Arrowhead aftershock, and a $M_w4.2$ Banning Pass event which occurred on May 31, 1993 at 08:55 GMT. We obtain information about source directivity for events as small as $M = 4$ by examining azimuthal variations in source duration for selected events.

Finally, results from the Mojave region (Joshua Tree, Landers, Barstow sequences,

Garlock earthquakes) and the eastern Transverse ranges (Big Bear, Arrowhead, Banning) are compared. While we observe systematic variation in stress-drop with tectonic environment and source depth, we see no evidence that stress-drops for earthquakes in the regions studied increase with increasing moment.

2.3 Data

The earthquakes examined in this study were recorded on the broadband instruments of the TERRAscope array, which was and continues to be undergoing expansion. Thus, events recorded in 1992 were recorded at the six stations GSC, ISA, PAS, PFO, SVD, and SBC (of which we use records from the former five), while more recent events may include records from stations Needles (NEE), Barrett (BAR), and Victorville (VTV). Before modeling, instrument gain was removed from the raw velocity records; they were detrended and integrated once. A butterworth bandpass filter with corners at 0.04 and 7 Hz was applied twice. Filtering was minimal so that the broadband nature of the records might be preserved. In cases where the event was fairly large and close to a particular station, low–gain records (accelerograms) from TERRAscope were used. They were processed similarly: gain removed, detrended, twice integrated, and bandpass filtered.

2.4 Structural Modeling: the Mojave Model

Studies to date on several moderately–sized Southern California earthquakes suggest that a relatively simple plane–layered velocity model often explains much of the observed waveforms. Waveforms from the June 28, 1991 Sierra Madre earthquake, centered within the TERRAscope array, were well–modeled at several azimuths from the event by the Standard Southern California model [Dreger and Helmberger, 1991]. Studies of several other events also suggest that this standard model is appropriate for use in the Southern California region. However, it quickly became apparent that the standard model did

not work well for Landers aftershocks recorded at stations in the Mojave Desert. The copious high–quality aftershock data recorded at local to regional distances give us the opportunity to develop a path–specific model for the Mojave region.

Aftershocks from the Landers sequence recorded at TERRAScope stations Goldstone (GSC) and Pinon Flats (PFO) provide high quality profiles of broadband data from events located and recorded in the Mojave block, as such possessing source–receiver paths which are contained entirely within this region. We initially considered station Seven Oaks Dam (SVD) for a third profile, but records from this station are complex and unusually noisy due to site effects and the only semi-permanent nature of the installation [L. Astiz, personal comm., 1994].

We model a profile of aftershocks trending south–to–north at station GSC; the reverse profile is modeled at station PFO. Source–receiver paths for these profiles, and station locations, are shown on Figure 2.2. Figures 2.3, 2.4, 2.5 and 2.6, 2.7, 2.8 show three-component profiles to stations GSC and PFO, respectively. The model used is the Mojave model presented in this paper (Table 2.1), and the events modeled have source depths between 8 and 11 km, roughly average for this sequence. The source mechanisms used in the modeling shown in Figures 2.3– 2.8 are computed using the methods discussed in Section 2.5. In order to construct the Mojave model, we first make an estimate of the source mechanisms for the events we use for the profiles, assuming the standard Southern California model [Table 2.2] [Hadley and Kanamori, 1977]. After the Mojave model was derived, we refined the original source and moment estimations for the profile events, using the new model.

This model has a thinner crust (28 km versus 35 km) than the standard California model, and slower P and S wave crustal velocities. It is also missing the gradient at the base of the crust (the so–called "Conrad" discontinuity) which characterizes the standard model.

The choice of stations GSC and PFO for this modeling task was natural and for-

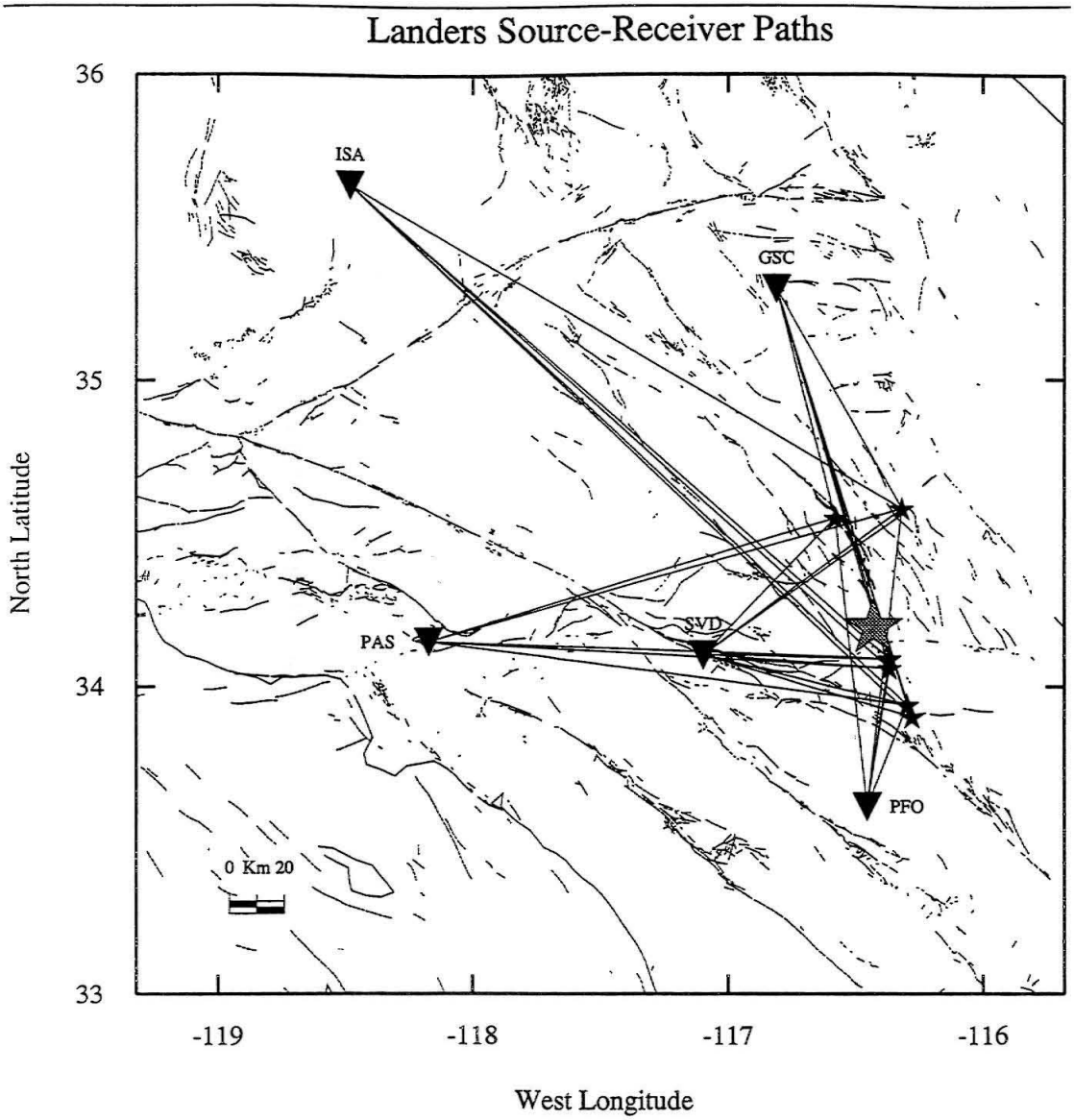

Figure 2.2: Source–receiver paths for the profiles used in source modeling, and in the construction and testing of the Mojave Model. Stations GSC, PFO and SVD were used primarily in the estimation of source mechanisms for Landers and Joshua Tree events. Stations ISA and PAS were included as needed, to create a robust solution in cases where the solution appeared unstable. Source–event paths for stations GSC and PFO were used in the development of the Mojave model (Table 2.1).

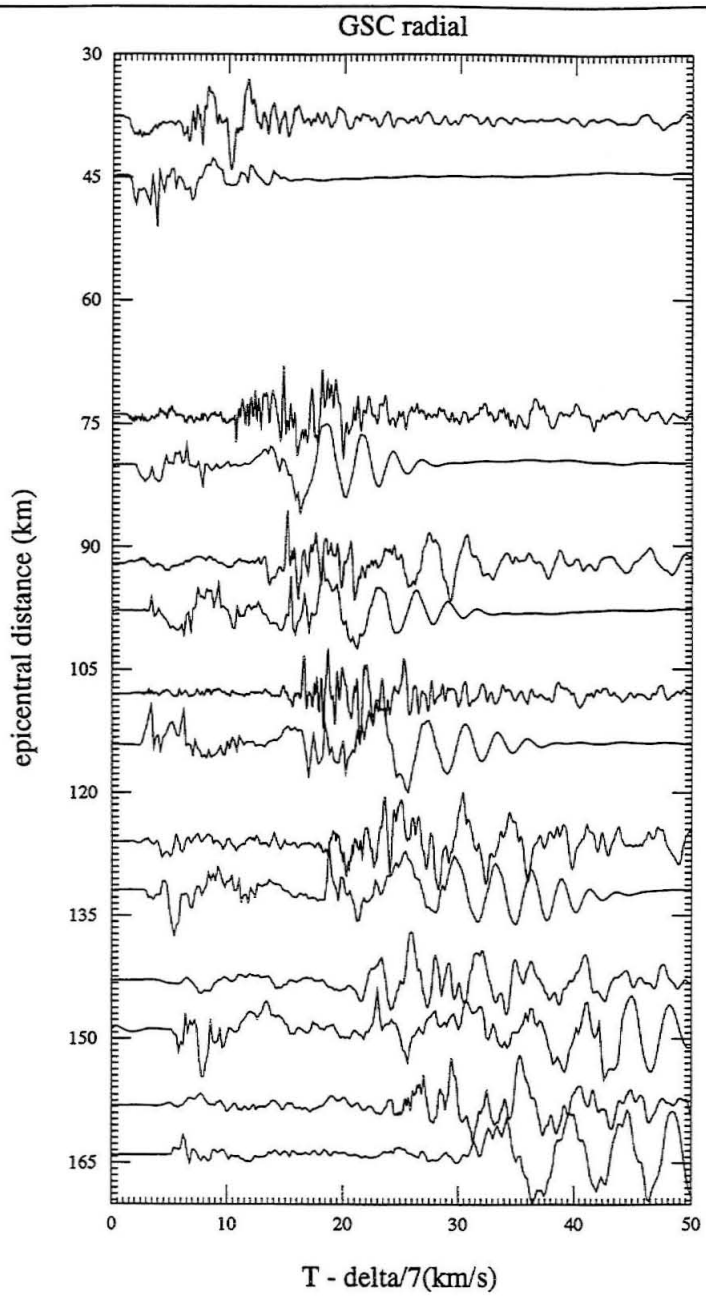

Figure 2.3: Profile of Landers data and modeling for the radial component of displacement, as recorded at station GSC. This profile ranges north to south, with source–receiver distances from about 40 to 160 km. Instrument gain is removed from the raw velocity records, which are integrated once and minimally filtered to retain broadbanded character. Records are modeled and shown broadband; here the observed displacement records are shown in bold line above synthetics. Synthetics are generated using the Mojave model and the frequency–wavenumber method.

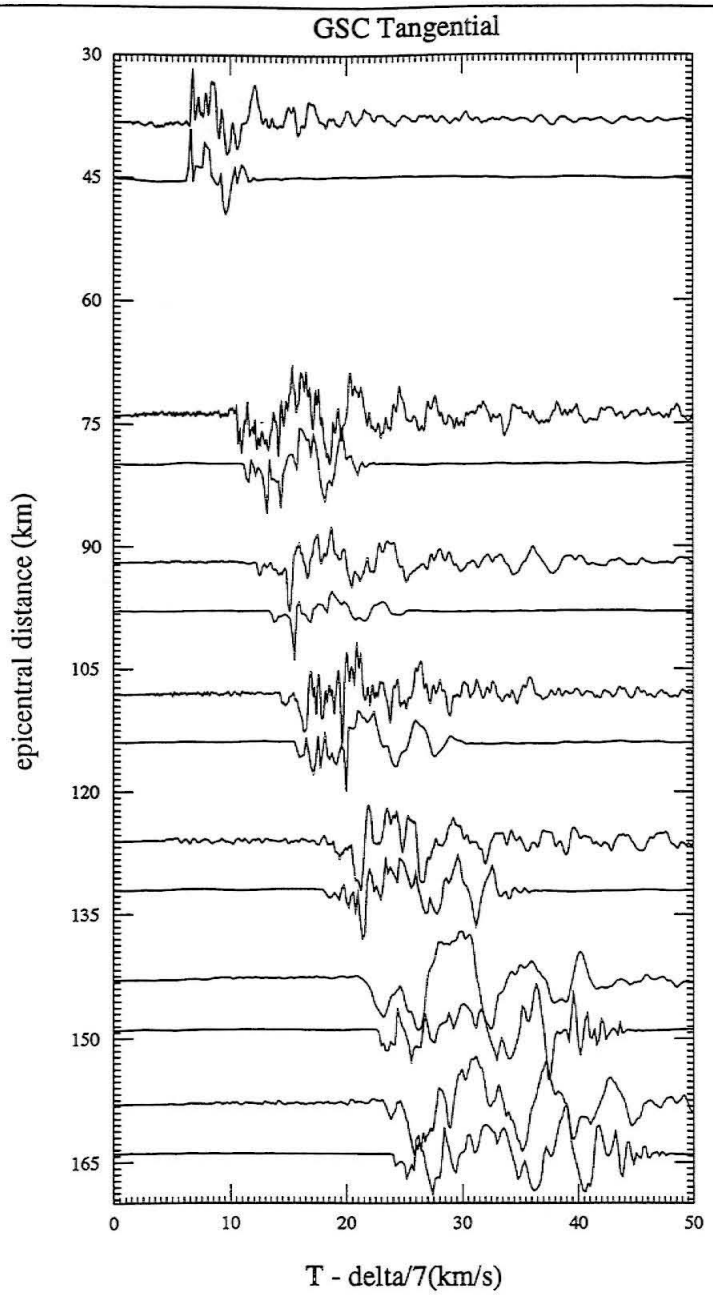

Figure 2.4: Profile of Landers data and modeling for the tangential component of displacement at GSC.

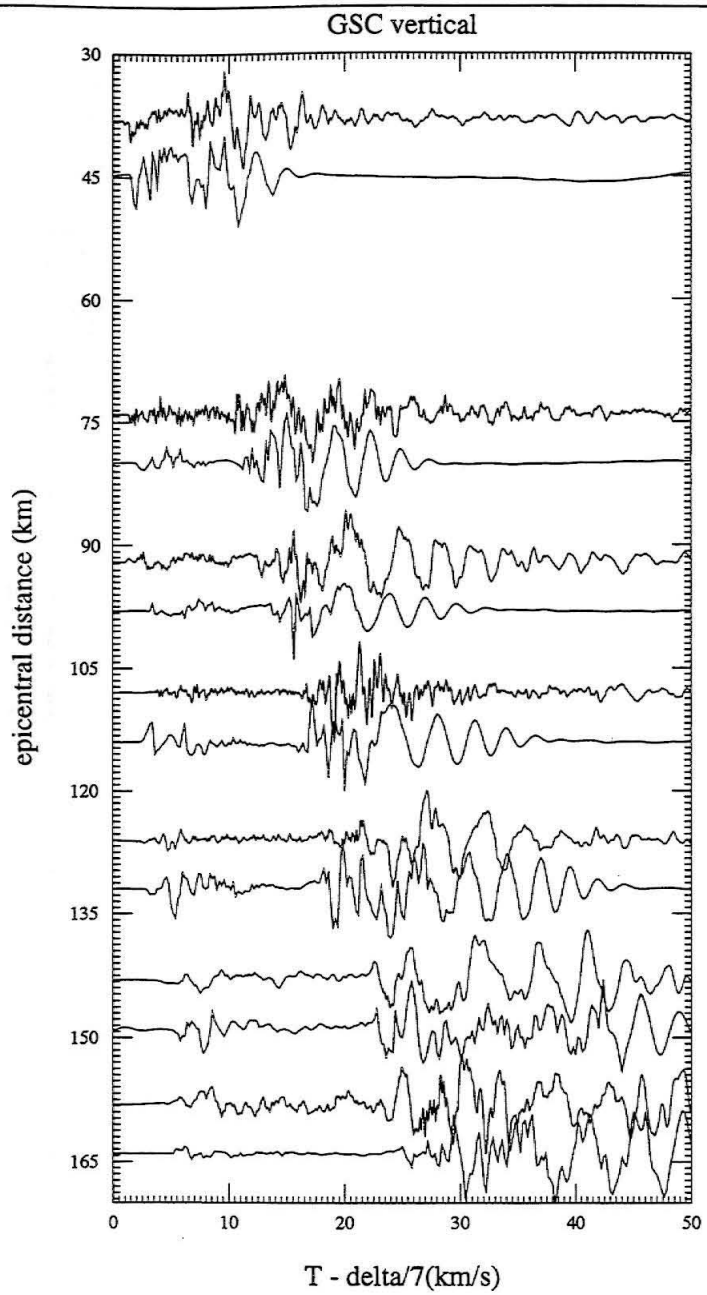

Figure 2.5: Profile of Landers data and modeling for the vertical component of displacement at GSC.

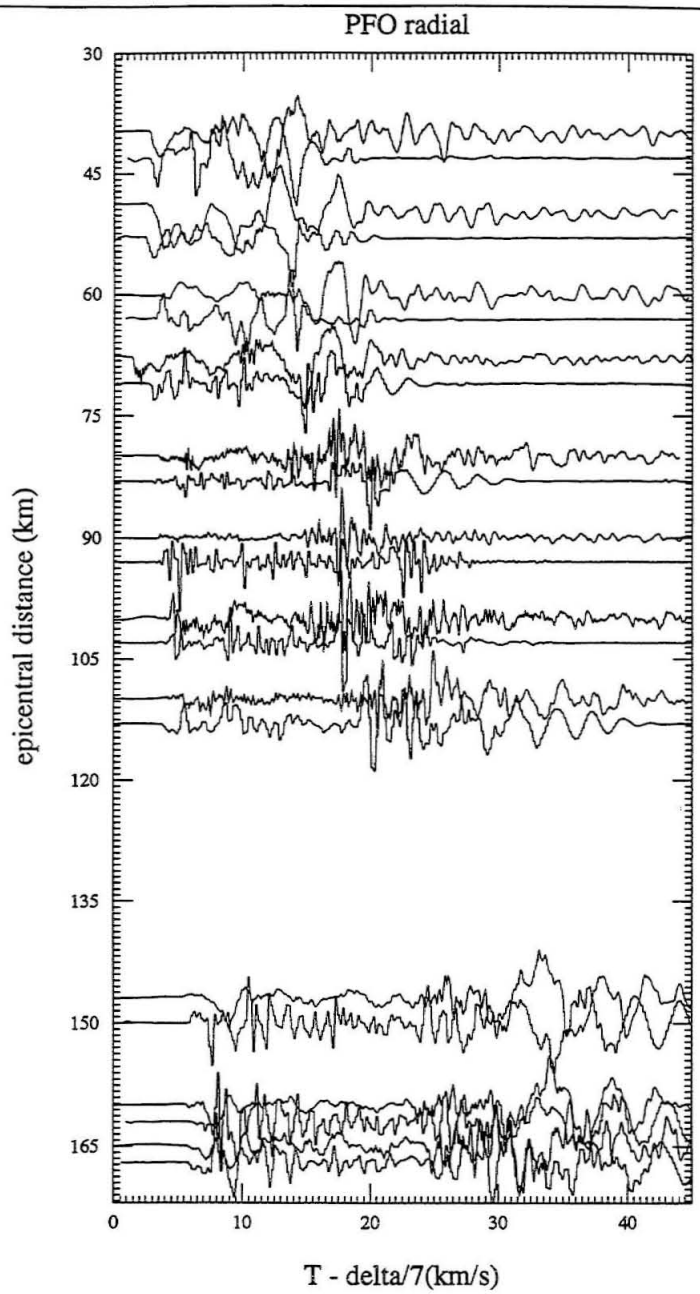

Figure 2.6: Profile of Landers data and modeling for the radial component of displacement, as recorded at station PFO. This profile ranges south to north, with source–receiver distances from about 40 to 160 km. Records are modeled and shown broadband; here the observed displacement records are shown in bold line above synthetics. Synthetics are generated using the Mojave model and the frequency–wavenumber method.

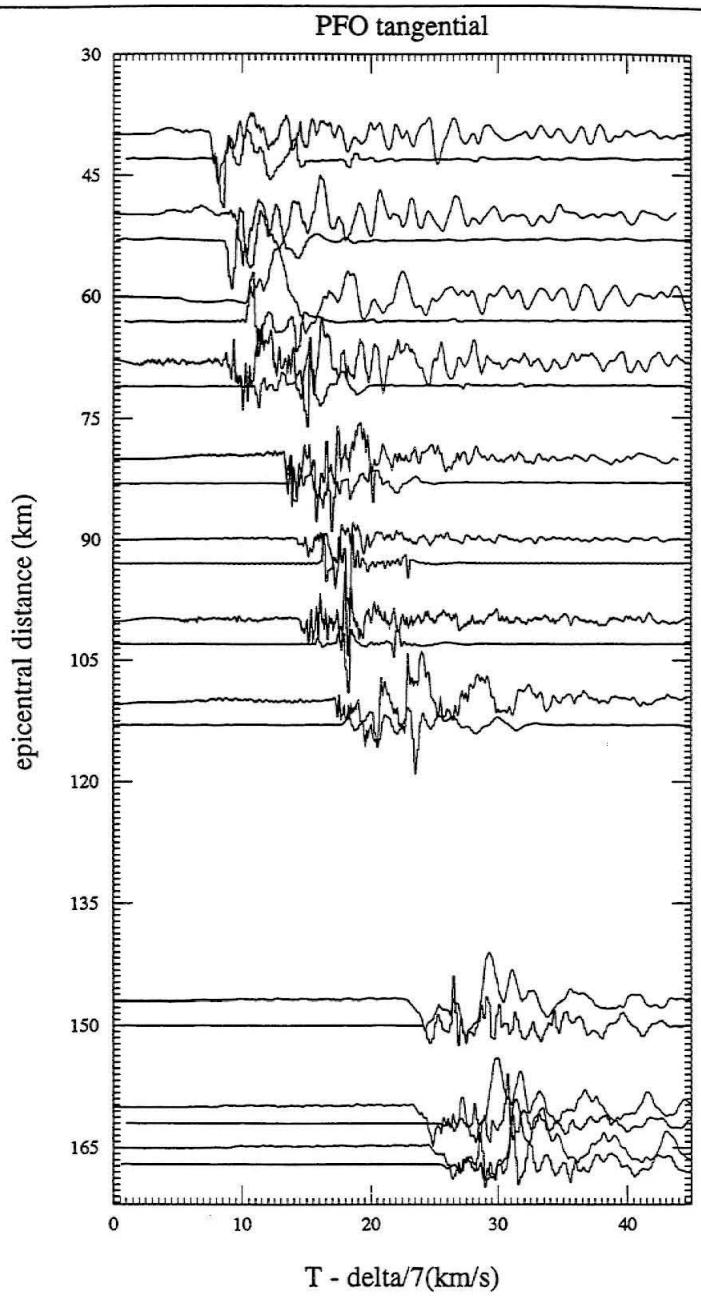

Figure 2.7: Profile of Landers data and modeling for the tangential component of displacement, PFO.

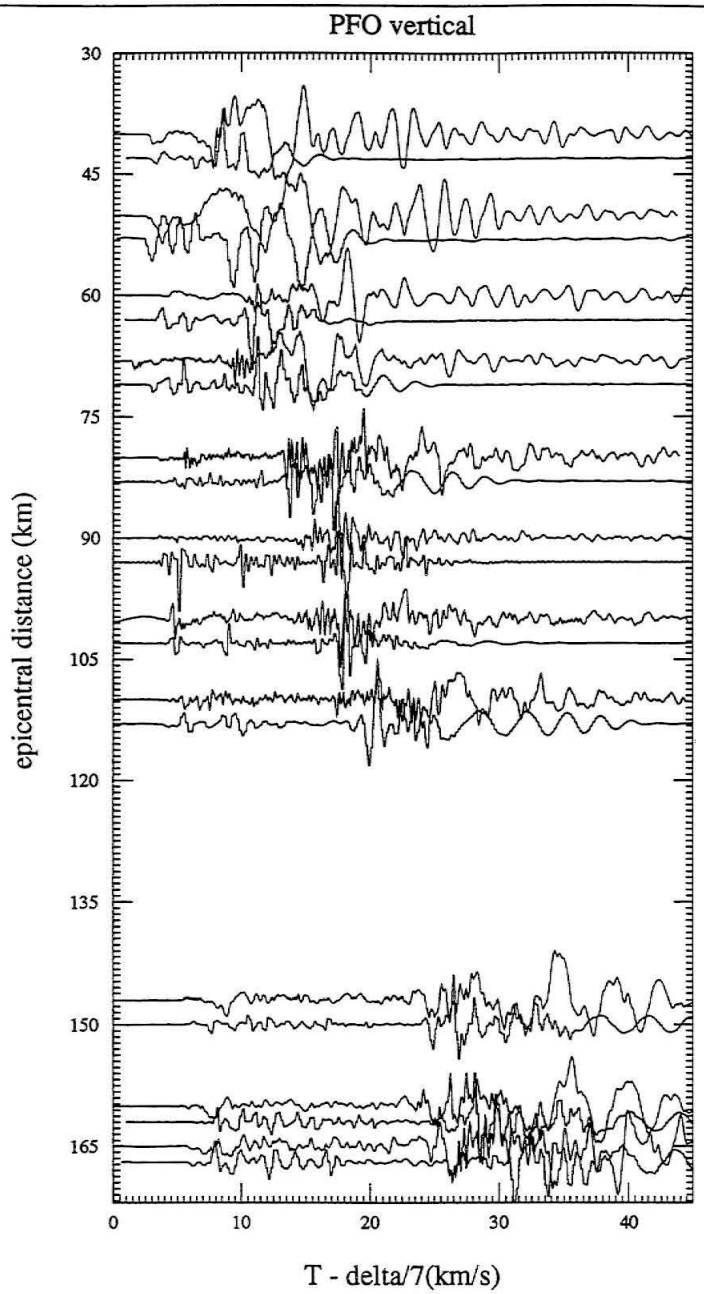

Figure 2.8: Profile of Landers data and modeling for the vertical component of displacement, PFO.

Table 2.1: Mojave Model

V_p (km/s)	V_s (km/s)	ρ (g/cm^3)	depth km
5.00	2.60	2.40	2.5
5.50	3.45	2.40	5.5
6.30	3.60	2.67	28.0
7.85	4.40	3.42	half space

tunate, since Landers events recorded at these two stations form natural north–south profiles. However, the locations of stations GSC and PFO nearly due north and south (respectively) of the aftershocks practically insures that many of them will be P–wave nodal at both stations, since many of these events have northerly strikes (parallel to the Landers rupture). Thus P_{nl} to surface wave amplitude ratios for the vertical and radial components are difficult to match, and the P_{nl} amplitudes shown in Figures 2.3 and 2.5, for example, are often too large. (Note that the P_{nl} waveform is the first few seconds or tens of seconds of the record, between the first P arrival and the arrival of S or S_n.) Conversely, the tangential component is at or near maximum, so it is much easier to model, as seen in Figure 2.4.

2.5 Overview of Theory and Method

Average source parameters for the aftershocks considered in this study are estimated using a grid–search algorithm developed by Zhao and Helmberger [1994]. This algorithm selects the source mechanism which minimizes the L1 and L2 norms between the data and the synthetics, using P_{nl} waveforms and whole waveforms for all three components to produce a stable solution from a relatively sparse data set and an imperfect structural model. For a given depth, the solution space (strike, dip, and rake)

Table 2.2: Southern California Model

V_p (km/s)	V_s (km/s)	ρ (g/cm^3)	depth km
5.50	3.18	2.40	5.5
6.30	3.64	2.67	16.0
6.70	3.87	2.80	32.0
7.85	4.50	3.42	half space

[Hadley and Kanamori, 1978; Dreger and Helmberger, 1991]

is gridded and searched at 10° intervals. Once a minimum error solution is found, the resulting parameter space is gridded at 1° intervals and searched once again. The procedure desensitizes the misfit in timing between principal crustal arrivals in the data and synthetic by fitting portions of the waveforms independently. Given the development of Green's functions specific to paths within the Mojave block, we use a sparse array (usually three stations) and the data both broadband and after convolution with a long–period Press-Ewing (LP3090) instrument response. Modeling results (broad band and long–period waveform fits) for a selection of the Landers aftershocks studied are shown in Appendices I and II.

2.5.1 M_b versus M_{lp} (M_o)

For each event studied, we compute both a broadband solution and a long–period solution. This is done for several reasons. The Mojave model is fairly reliable for the source–receiver paths in question, which is critical since the array (usually three stations) we use is sparse. However, for many of the smaller events we study, the raw Frequency–Wavenumber Green's functions (prior to convolution with a preferred source–time function) do not match the very high frequency content of the data we are attempting to

model. Thus applying a long–period filter might help to produce a more stable solution. However, often the smaller events are fairly noisy, and applying the LP3090 instrument response can amplify ambient noise prior to the first P arrival, and also within the P_{nl} portion of the record. In this case, the broadband solution (source parameters) might be more reliable. Broadband records are also more useful in the estimation of source duration. Unfortunately, broadband records are sensitive to high–frequency site amplification, path effects, and the possible effects of source directivity, all of which would affect the apparent event "duration" at each station, and could contribute to richer high-frequency content in the waveforms, making them more difficult to model.

Thus, we use broadband records to estimate source durations for each station individually, and obtain an effective (average) duration for the event. We also obtain source parameters and estimate event depth using broadband waveforms. An LP3090 instrument response is then applied to the broadband records, and we again estimate source parameters, including depth and moment, using these long–period records. The resulting solutions (which include an average of the moment computed at each station) should be less affected by high–frequency path and site effects at any given station.

2.5.2 Apparent Site Effects From Broadband Data

In the process of modeling the aftershocks shown in this study, it quickly became apparent that there was some systematic variation or bias in the broadband moments as computed at each station. As discussed earlier, moments are computed at each station and for each component, and these values are averaged to give an overall moment estimation for the event. For some stations, the elevated moments seem to correlate with distance from station to event. Other stations produce moments which are higher than average irrespective of source–receiver distance. Since aftershocks along or near the Landers rupture have roughly the same azimuths to stations GSC and PFO (though they span an arc of roughly 60 degrees for station SVD), we show normalized moments for

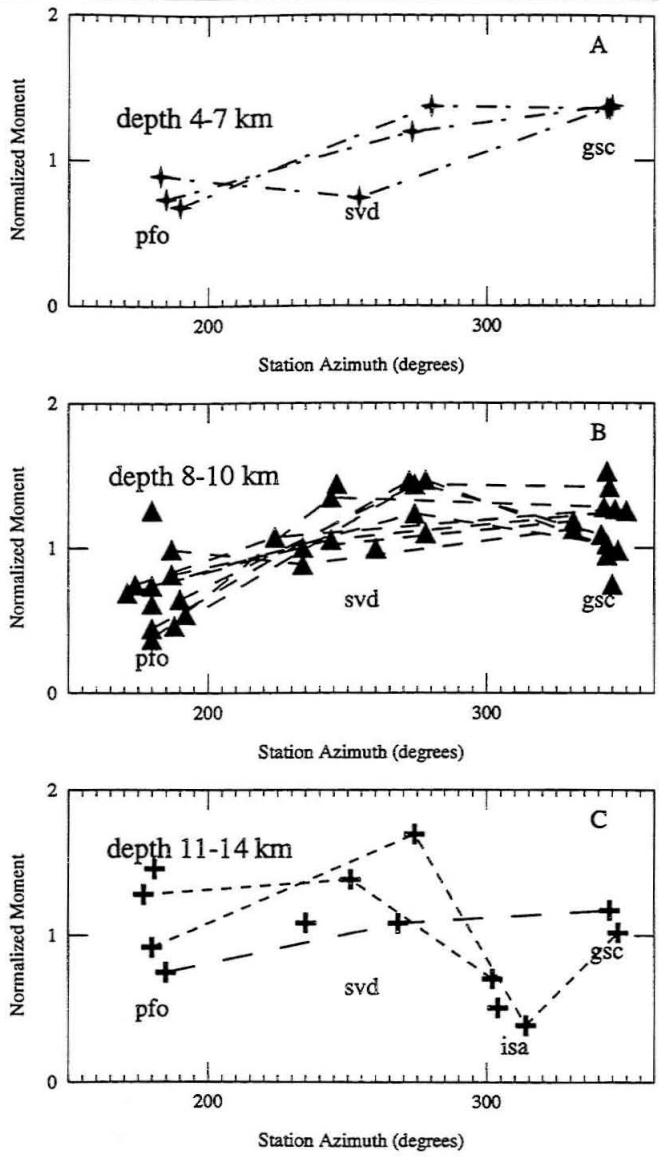

Figure 2.9: Normalized moments shown by event and station for Landers aftershocks. Moments shown are for the Tangential component of motion, and are normalized by division by the average moment from the tangential component for all three stations. The tangential component was selected as it was perceived to be less sensitive to path heterogeneity, and generally had less high–frequency energy content than the other components. Panel *a* shows results for shallow events (5-7 km); panel *b* shows results for moderate events (8-10 km), while panel *c* shows results for deeper events (11-14 km).

each station and event, plotted against station azimuth (Figure 2.9). Moments specific to each event are connected by dashed lines, and the average station azimuth for these events is indicated in each panel (PFO at around 190 degrees, SVD at 250-270 degrees, and GSC at about 345 degrees). Results for each depth range are shown separately. Panel 2.9b shows most clearly that across all events, station PFO generally produces lower than average moments, while stations SVD and GSC produce higher than average moments. The other depths exhibit similar behavior between stations. Panel 2.9c includes some moments at station ISA (around 300 to 310 degrees azimuth) and it is apparent here that this station also produces comparatively low moment estimations.

We also investigated the behavior of these normalized station–specific moments with increasing epicentral distance (Figure 2.10), to see if high moments correlate with comparatively short source–receiver distances. It is immediately clear that station SVD shows distance–related bias in moment estimations, with the generally higher than average values for all distances, but with this effect most pronounced at near-in distances. Station PFO shows nearly the opposite, with low values overall, but lowest values close to the station. Both of these patterns could be direct evidence of site effects most prominent at close–in distances, for which energy arrives at the station at fairly low angles to the horizontal, and thus is more affected by structural complexity around the site. Station GSC shows elevated moment values overall, while station ISA shows generally lower than average values. The latter may be due to this station's much larger than average source–receiver distances (it is roughly twice as distant from most events as other stations), or to overall path effects from an inadequate structural model. Station PAS shows more of the behavior we might expect from a station exhibiting little site effects: the normalized moment values hover around 1. For stations exhibiting primarily site effects, we would expect to see the normalized moment values approach 1 as distance increases, as seen at station PFO (Figure 2.10).

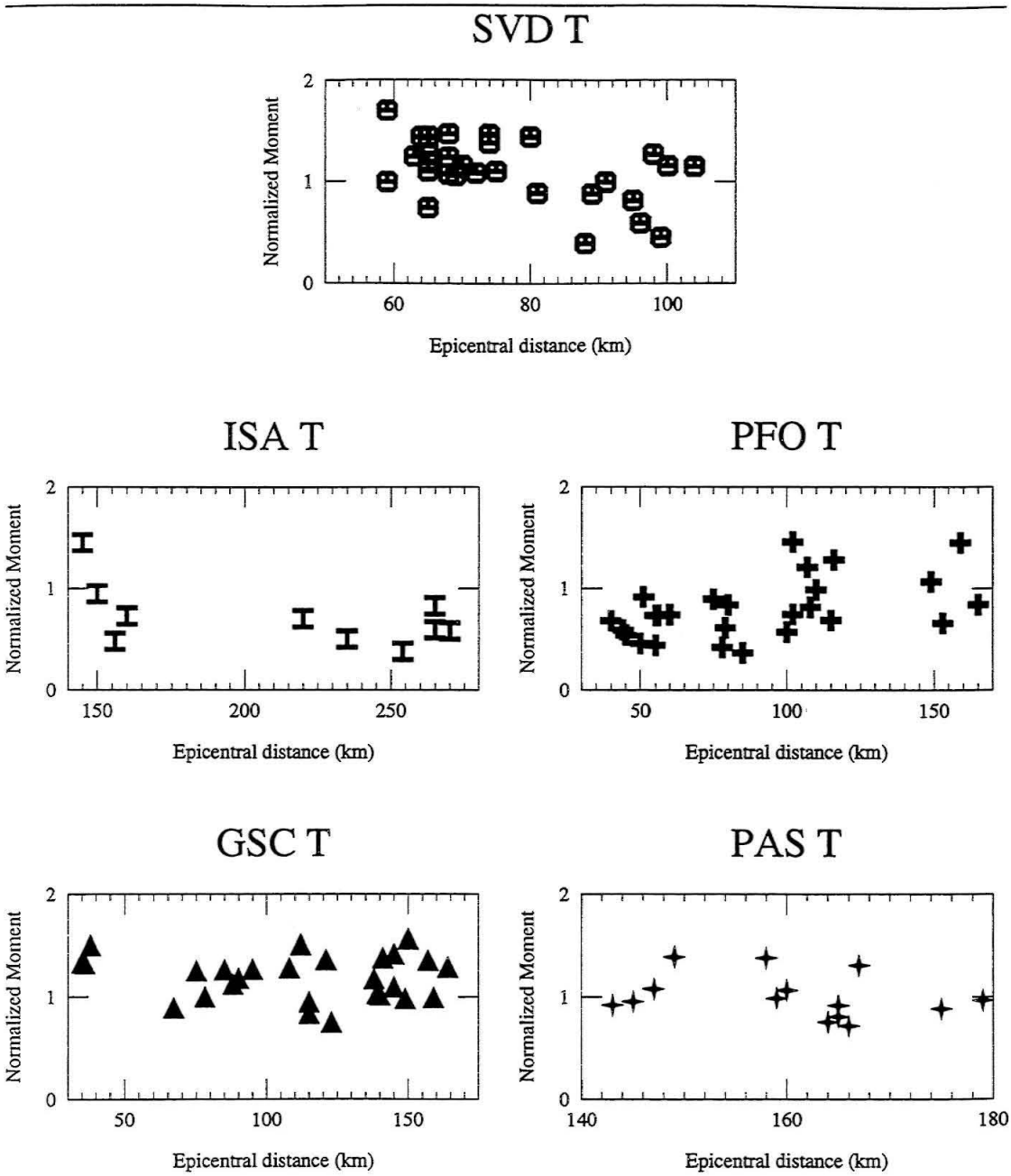

Figure 2.10: Normalized moments for each station, plotted against source–receiver distance. Note that the minimum and maximum distance bounds differ between stations. Station identification is shown at the top of each plot, and epicentral distance across the bottom.

2.5.3 Moments and Error

Estimation of seismic moment is usually associated with a fair degree of error. Upwards of 50% error associated with the estimation of moment has been deemed acceptable, even satisfactory, and even higher error is common. For our purposes and given our choice of methods, this error can be assigned to several causes, among them model misfit, noise in the data, and mislocation of the source. We attempt to minimize error in our estimations by making them both broadband and after convolution with a long period filter (LP3090 response), and by eliminating noisier waveforms from the solution unless they are absolutely necessary for adequate azimuthal coverage. Amplitude mismatch between data and synthetic can be an important factor in generating high errors in the moment estimation. The Raleigh wave is especially sensitive to path heterogeneity [Song et al., 1994], and the resulting waveform complexity is difficult to model theoretically, especially assuming a one–dimensional structure. Synthetics from two–dimensional models begin to show some of this behavior, however [Stead, 1990]. To adjust to the limits imposed on us by the use of our one–dimensional model, we downweight the radial component by half (relative to the vertical and tangential components) in our solutions, or remove it altogether if it is exceptionally noisy or otherwise anomalous. Since the P_{nl} portion of the radial component is not affected by path complexity as the surface wave (the Rayleigh wave) is, we use and do not downweight the P_{nl} portion of the radial waveform. P_{nl} waveforms (radial and vertical) might be omitted only at nodal stations for events which are especially small and therefore unusually noisy.

Source Depths

Source depths are determined directly from the surface reflected phases S_mS or sS_mS, or estimated by cycling through depth–dependent Green's functions (2, 5, 8, 11, 14, and 17 km) to obtain an average depth for the event (Figures 2.11, 2.12(. We employ a catalog of Green's functions appropriate to the Mojave model, which are computed

at 5 km distance intervals from 35 km to 400 km, and assuming source depths listed above. For the Garlock and Big Bear earthquakes, we use a similar catalog of Green's functions from the standard Southern California model. In general, the mechanisms and depths obtained in this study are consistent with those obtained by other workers (e.g., see Table 2.5). In some cases, however, the depths we obtain are not as shallow as those obtained by others. One such event follows below.

An Example Event

As an example, we model the August 5, 1992, 22:22 GMT Landers aftershock (Figure 2.11, 2.12). Fits for all three components (including the radial) are shown. Error space for the depth determination is shown in Figure 2.13. Our estimation scheme suggests a depth of between 5 and 8 km for this event, though others have located it at a depth of less than 2 km. Figure 2.11 shows modeling results assuming a depth of 5 km, while Figure 2.12 shows results for an assumed source-depth of 8 km. P_{nl} to surface–wave amplitude ratios on the vertical and radial components of motion suggest a depth of about 5 km, while ratios of body wave to Love wave amplitudes suggest a depth of 8 km or greater. Indeed, separation between $S_m S$ and $sS_m S$ phases on the tangential components at stations PFO (epicentral distance 155 km), ISA (160 km) and PAS suggest a depth arguably deeper than 8 km.

Figure 2.11: Broadband modeling for the August 5, 1992 22:22 (Barstow) aftershock. Source depth was estimated at between 5 and 8 km by cycling through synthetics appropriate to source depths from 2 to 17 km, and finding a minimum error solution. Event duration was similarly estimated. Synthetics are generated using the F-K method and the Mojave model. This plot shows waveform fits assuming a depth of 5 km; the next plot shows the depth of 8 km.

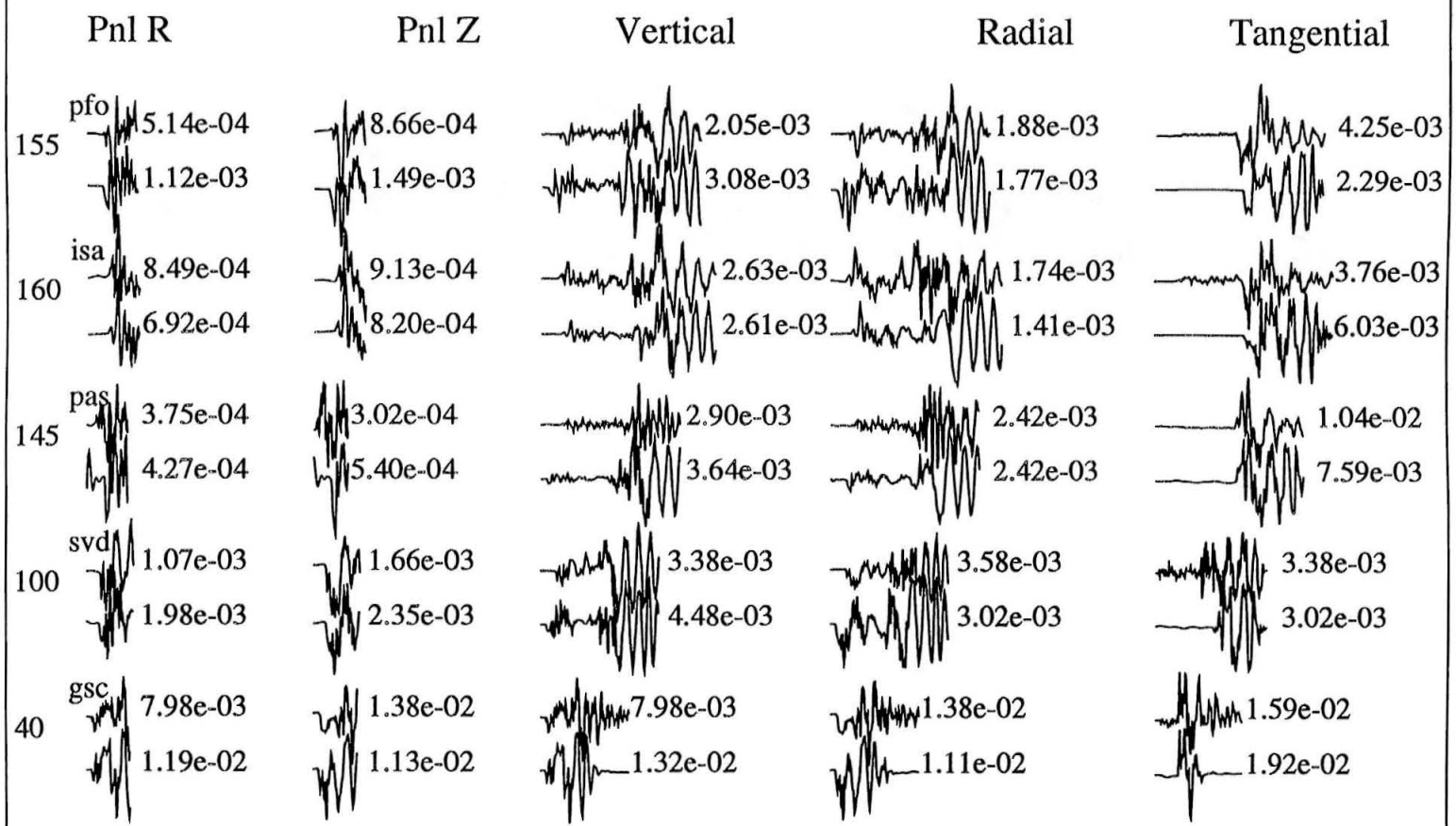

Broad Band 6.593e22 dyn-cm

Event 14, Table 4. Barstow h=5

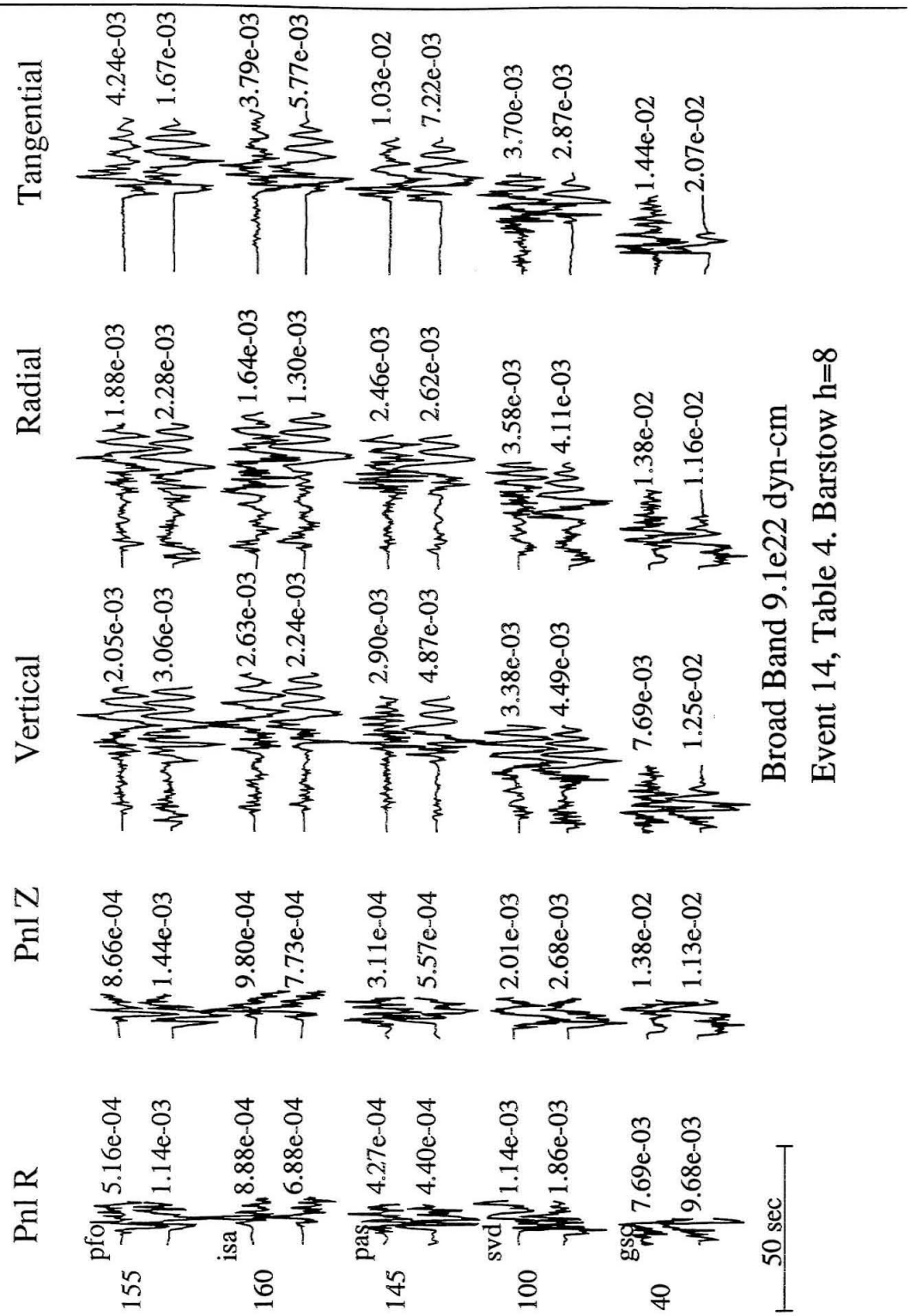

Figure 2.12: Broadband modeling for the August 5, 1992, 22:22 (Barstow) event. Source depth is 8 km.

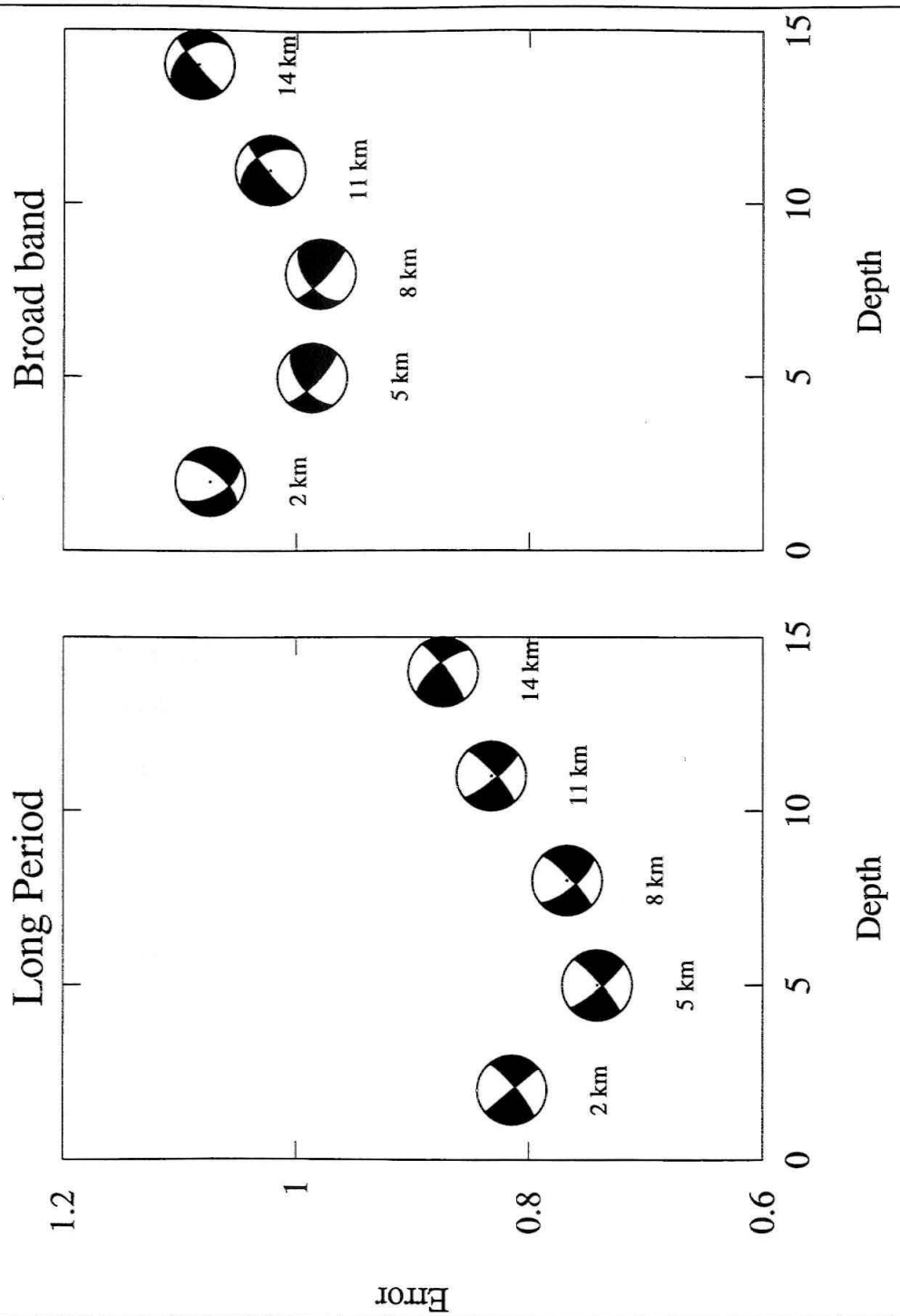

Figure 2.13: Error space for the August 5, 1992, 22:22 (Barstow) event. Source depths are indicated across the bottom of the plot, and error on the vertical axis. The left–hand panel shows error from the Long–period solution, and the right–hand panel shows error from the broadband solution. Focal spheres appropriate to each depth indicate data points; note that long–period focal spheres show more consistency.

2.5.4 Source–time Functions and Stress–drops

Effective source–time functions are determined for each event both by direct grid–search; that is, by seeking a best–fit source–duration while estimating the source–parameters of each earthquake, and by doing a simple comparison of energies. The P_{nl} waves (in velocity) from each station are compared with synthetic P_{nl} waveforms (velocity) as follows:

$$Ratio = \frac{E_{(obs)}}{E_{(syn)}}$$

where

$$E = \frac{\int_{t_{pn}}^{t_{sn}} [V_{(sp)}]^2 dt}{\int_{t_{pn}}^{t_{sn}} [V_{(lp)}]^2 dt}$$

$V_{(sp)}$ is the observed (or synthetic, as the case may be) P_{nl} wave, in velocity, convolved with a short-period Wood–Anderson response, while $V_{(lp)}$ is the observed (or synthetic) P_{nl} wave, in velocity, convolved with an LP3090 instrument response. For the synthetics,

$$V = M_o s(t) * A_i(\theta, \lambda, \delta) * G(t, \mathbf{r})$$

where M_o is the effective moment of the earthquake (average for all stations used), $G(t, \mathbf{r})$ is the propagational Green's function, assuming a point source, and $A_i(\theta, \lambda, \delta)$ contains the radiation pattern of the source. We seek an effective source–time function, $s(t)$, such that

$$Ratio \sim 1$$

by cycling through simple triangles and selecting the appropriate source duration. Comparisons are done broadband, and with data and synthetic convolved with a long–period Press-Ewing (LP3090) instrument response. Vertical and radial P_{nl} waveforms for each station are used, and the results averaged to yield an effective source-duration as observed at that station. Source durations estimated for each station are then averaged to

yield an event duration, which is used, along with the moment estimate for the event, to compute stress–drop (see below).

This procedure gives a conservative estimate of source–time duration and thus stress-drop, and is limited to source triangles no shorter than 0.20 s in duration. This limitation is imposed by the computational technique used, and to a lesser extent, by the frequency content available in the synthetic Green's functions.

Although the exact relationship between earthquake stress-drop and regional tectonic stresses is poorly understood, relative stress drop is a meaningful parameter by which to compare various tectonic provinces. Assuming little or no attenuation, the width of the observed P or S pulse is in general proportional to the source dimension, and thus source duration. The actual pulse-width, as observed, depends on factors as diverse as crustal attenuation, rupture mode, length and velocity, and source complexity. On average, however, it is acceptable to assume a linear relationship between pulse–width and source dimension. Cohn et al. [1982], assuming a circular fault [Brune, 1970], obtained the relation

$$\tau = \frac{2.62a}{\beta}$$

where τ is the source duration in seconds, a is the radius in km, and β is the shear velocity local to the source region. Solving for a in terms of τ, assuming a shear velocity of 3.5 km/s, and substituting the result into the expression for stress–drop on a circular fault [Eshelby, 1957]

$$\triangle\sigma = \frac{7M_o}{16a^3}$$

we obtain

$$\triangle\sigma = \frac{1.84 \times 10^{-22} M_o}{\tau^3}$$

In this study, however, stress drops are usually depicted on plots of moment versus

duration, as will be shown in a later section.

Example events

To illustrate this procedure, we include as examples two earthquakes from the Landers sequence. These events have similar depths and moments, but differ slightly in source mechanism. Both occurred north of the Pinto Mountain fault, within 22 km of each other, at distances of 112 and 90 km from station GSC. Recordings for both events at station GSC are shown, to facilitate comparison by minimizing differences in path and site effects (Figure 2.14). Comparing events of similar moment makes valid the comparison of stress–drops, which are predicated on duration versus moment (i.e., the shorter the event duration for a given seismic moment, the higher the relative stress drop for that particular event).

Event *A* is very high stress–drop, according to the conditions set forth above, with a computed stress–drop of 515 bars; while event *B* is relatively lower, with a stress–drop of 100 bars. Data from events *A* and *B* are shown on Figure 6, where the original broadband records for both events are shown flanked by records convolved with a long–period Press-Ewing instrument (LP3090) response, and a Wood–Anderson short–period (WASP) response, respectively. Event *A* clearly has more high frequency energy in the WASP record than does event *B*. A closer look at the ratio of short–period to long–period energy for both events, easily done by taking the ratio of peak WASP amplitude to peak LP3090 amplitude, shows that event *A* has a short–period to long–period energy

---

Figure 2.14: Modeling for events *A* and *B* (aftershocks 3 and 5, Table 2.5). Broadband data are shown is shown in the middle of each group of time–series, flanked by broadband data convolved with LP3090 (above) and Wood-Anderson short–period (WASP, below) instrument responses. Event *A* is higher stress–drop than event *B*. Note relatively larger high–frequency energy content in event *A*, and higher WASP to LP3090 peak amplitude ratios.

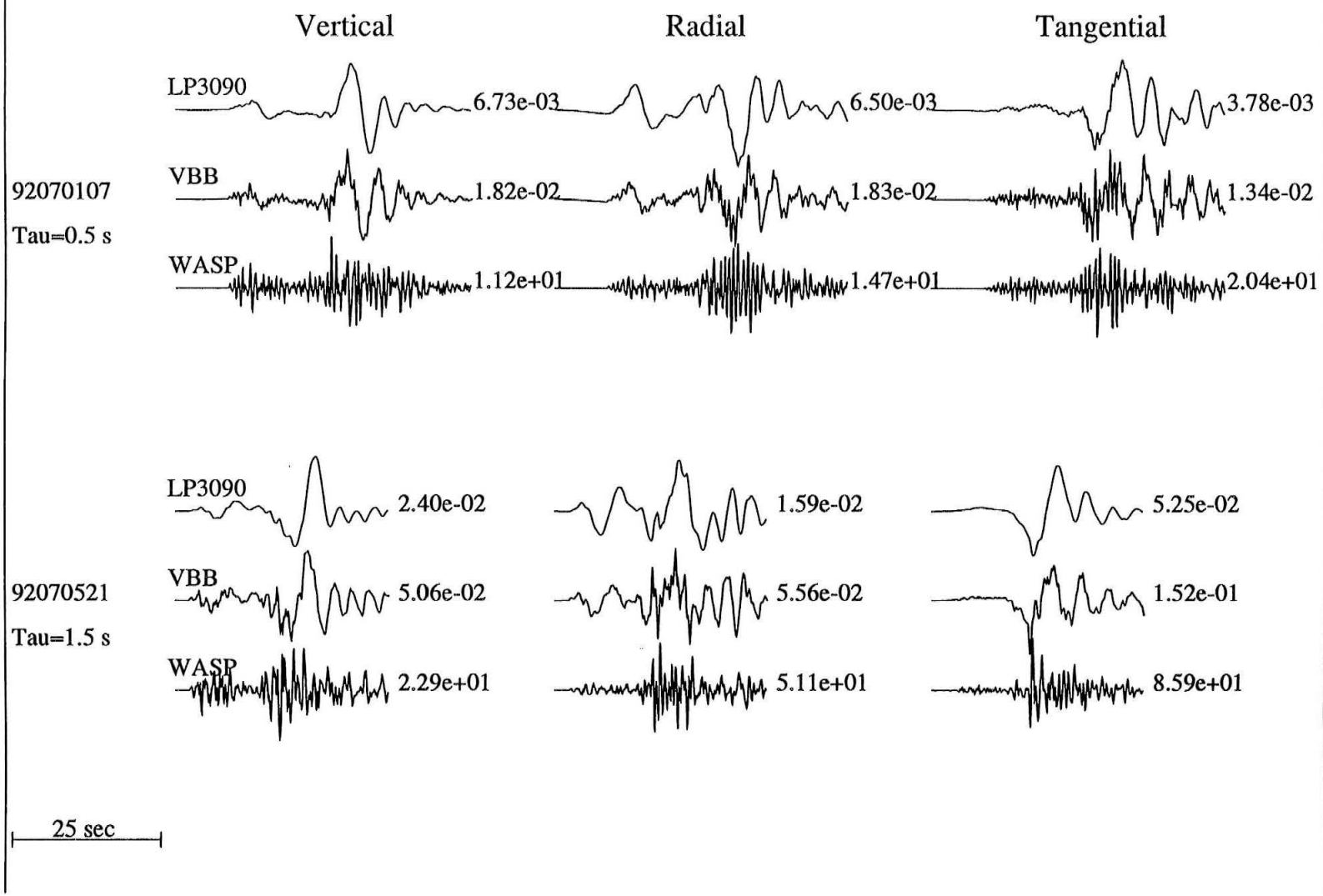
Vertical
Radial
Tangential
LP3090
6.73e-03
6.50e-03
3.78e-03
VBB
1.82e-02
1.83e-02
1.34e-02
92070107
Tau=0.5 s
WASP
1.12e+01
1.47e+01
2.04e+01
LP3090
2.40e-02
1.59e-02
5.25e-02
VBB
5.06e-02
5.56e-02
1.52e-01
92070521
Tau=1.5 s
WASP
2.29e+01
5.11e+01
8.59e+01
25 sec

ratio an average of two times larger than event B (averaged over all three components).

For both events, the modeled duration varies azimuthally, either due to event directivity or to site effects at a given station. After determining an event duration specific to each station, we average these values to find an overall effective duration for the event. Event B has an unusually short duration as recorded at station GSC: 0.85 second, in contrast to the average (over 5 stations) of about 1.5 seconds. Event A has uniformly short durations at every azimuth. The site or directivity effect at station GSC for event B makes this comparison a little less striking than it might otherwise have been.

To further illustrate our method of determining source duration, which is primarily based on correctly modeling the ratios of short–period (i.e., WASP) to long–period (i.e., LP3090) energy, we show modeling results for event A (Figure 2.15). We seek a source–time function for which the ratio of synthetic WASP to LP3090 energies most closely matches the ratio of WASP to LP3090 energies for the data. Given an appropriate choice of source-duration, the "broadband" synthetics should approximate the observed frequency content of the broadband data, keeping in mind the limitations imposed by the available frequency content in the Green's functions. For event A, which had a duration estimated at about 0.50 s, the shorter time function (i.e., $\tau = 0.50$ s) is much more appropriate than the longer time function (i.e., $\tau = 1.0$ s) (Figure 2.15) .

Figure 2.15: Modeling for event A (aftershock 3, Table 2.5). Broadband data are shown in the middle of the plot, flanked by synthetics appropriate to two different choices of source duration. The data are shown broadband, and convolved with both LP3090 and WASP instrument responses, as are the synthetics. Note that the P_{nl} portion of the waveforms only (e.g., see Figure 2.11) are used in the estimation of source–durations.

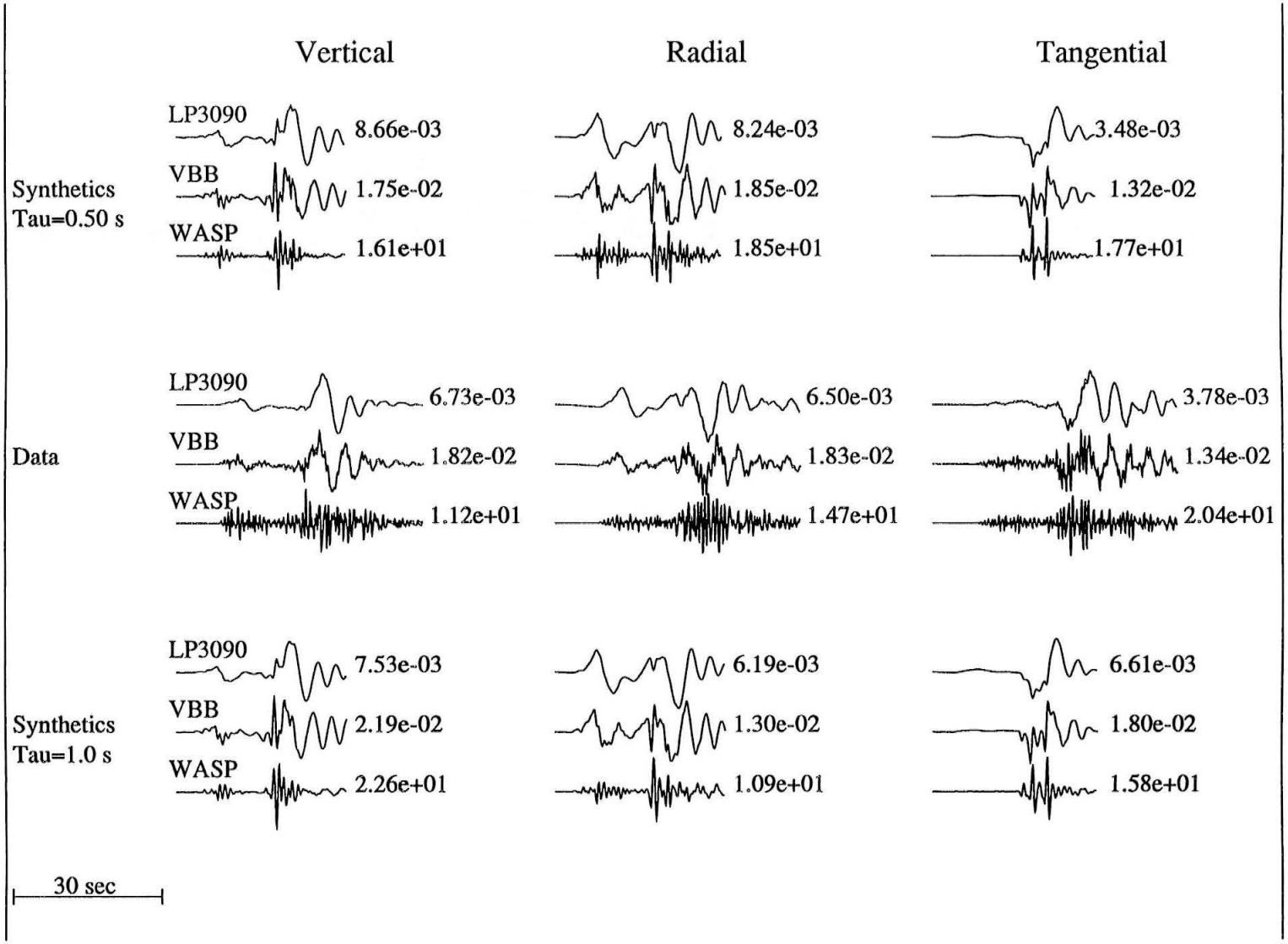
Vertical
Radial
Tangential
Synthetics
Tau=0.50 s
LP3090
VBB
WASP
8.66e-03
1.75e-02
1.61e+01
8.24e-03
1.85e-02
1.85e+01
3.48e-03
1.32e-02
1.77e+01
Data
LP3090
VBB
WASP
6.73e-03
1.82e-02
1.12e+01
6.50e-03
1.83e-02
1.47e+01
3.78e-03
1.34e-02
2.04e+01
Synthetics
Tau=1.0 s
LP3090
VBB
WASP
7.53e-03
2.19e-02
2.26e+01
6.19e-03
1.30e-02
1.09e+01
6.61e-03
1.80e-02
1.58e+01
30 sec

2.5.5 Summary

Source Depths

The procedure we employ to estimate source parameters, including depth, often yields a source–depth substantially deeper than depths obtained by other workers [see Tables 2.3, 2.4, and 2.5]. However, within the error imposed by the depth gridding on our solution space (every 2-3 km), we believe that our depths, obtained from a grid–search routine which is tantamount to direct waveform modeling, are reliable. There is substantial difference in the separation between S_mS and sS_mS phases for events at source–depths of, say, 2 and 5 km. Our estimates suggest that all of the $M > 3.7$ events we studied had depths of 5 km or greater; and average depth is about 8 km.

Site Effects, Moment, and Stress–drop

Station (site) effects for Landers aftershocks recorded at stations GSC, PFO, and SVD seem to be fairly consistent between events, with records from station GSC giving higher than average broadband moment estimations, station PFO giving generally low estimations, and station SVD giving estimates which varied fairly smoothly from relatively high to lower, depending on distance of the source from the station. Estimates of event duration done on a station–by–station basis also suggest that durations at stations GSC and SVD are generally shorter than average. For station SVD, this may be related to the fact that this station produces fairly noisy seismograms which are rich in high–frequency energy content.

However, stress–drops for each event are determined by averaging source-durations obtained from several stations, and using this average duration to estimate moment. From this estimation of moment, stress–drop is estimated. Thus, the anomalous behavior at any one station should be averaged and smoothed somewhat. Furthermore, since the stress drops shown here are obtained using the same set of stations, comparisons of

stress–drops from these events, and the differences and consistencies discovered between events in this population, are meaningful in their own right.

2.6 Source Modeling

2.6.1 Joshua Tree Sequence

The Joshua Tree sequence began on April 23, 1992 at 02:25 GMT with a $M_w = 4.3$ foreshock. This event occurred at a location just south of the Pinto Mountain fault (-116.32 W, 33.94 N), and north of the Coachella Valley segment of the San Andreas fault, within the Little San Bernardino Mountains, in a region which has historically seen frequent earthquake swarms. It was followed by a number of additional smaller foreshocks, then within two-and-a half hours by the nearly co-located $M_w = 6.1$ Joshua Tree mainshock (Mori, 1994). The Joshua Tree mainshock had no observed surface rupture, though a 10-to 12 km south-to-north subsurface fault–plane, striking roughly $N20°W$, was inferred from the distribution of early aftershocks [Wald, personal comm., 1992; Hauksson et al., 1993; Hough and Dreger, 1994].

The Joshua Tree mainshock was followed by an unusually sustained and powerful aftershock series which comprised at least 28 aftershocks of $M > 3.7$, 10 of which were $M4.0 - M4.7$. About 6000 aftershocks, in a sequence which ranged spatially from the mainshock source area northwards to just north of the Pinto Mountain fault, were recorded and located by the Southern California Seismic Network between April and June, 1992 [Hauksson et al., 1993]. Joshua Tree aftershocks partially overlap those from the later Landers earthquake, with a cluster of aftershocks, including one event above $M4$, developing north of the Pinto Mountain fault and slightly east of the Landers mainshock location in early June (e.g., Figure 2.17, aftershock number 9). $M > 3.9$ aftershocks form two separate clusters south of the Pinto Mountain fault which are filled in by and abut later aftershocks from the Landers earthquake (Figure 2.18).

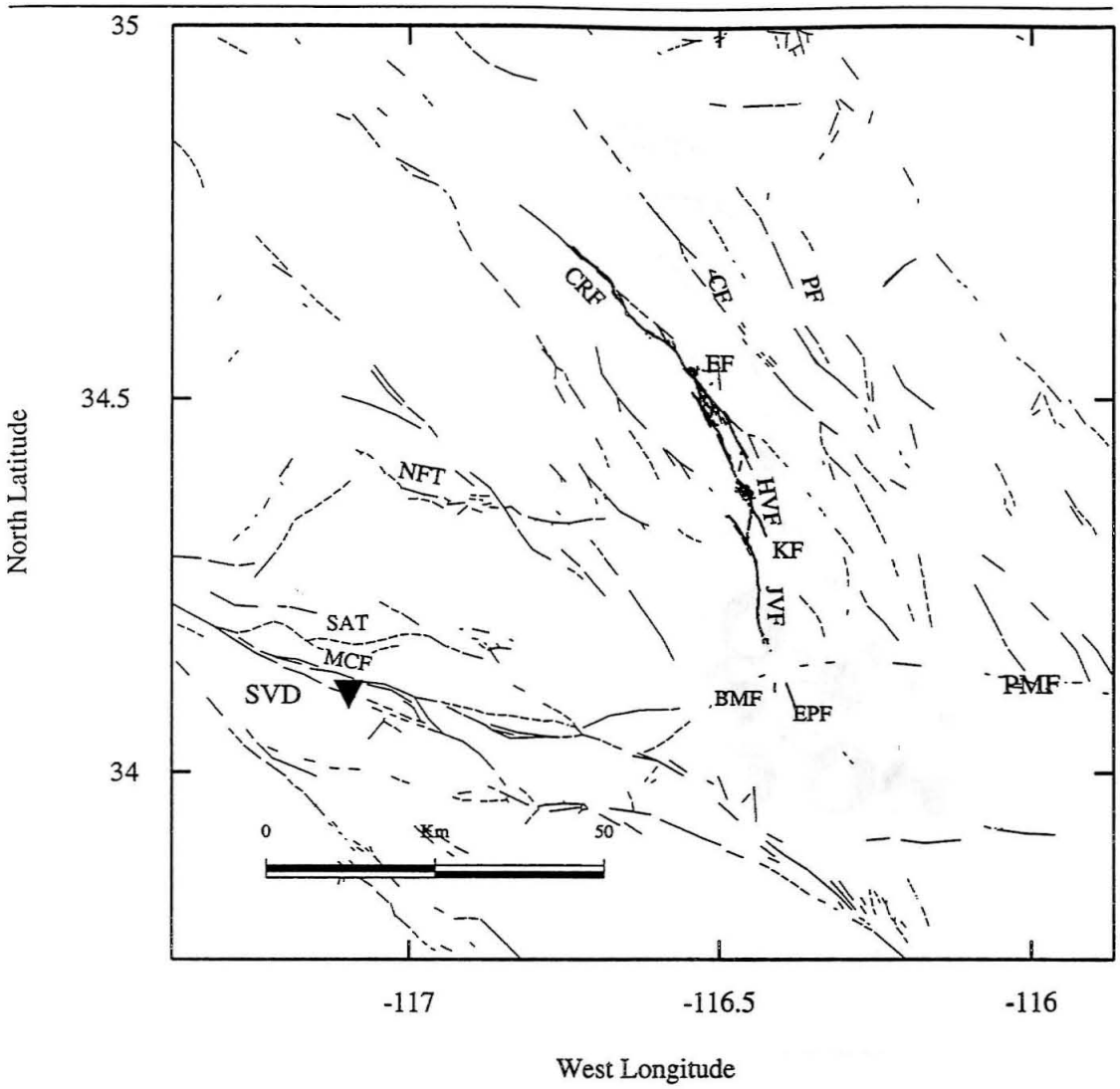

Figure 2.16: Location map showing faults active during the Joshua Tree, Landers and Big Bear sequences. Faults are indicated as follows, clockwise from lower left: MCF, Mill Creek fault; SAT, Santa Ana Thrust; NFT, North Frontal Thrust; CRF, Camp Rock fault; CF, Calico Fault; PF, Pisgah fault; EF, Emerson fault; HVF, Homestead valley fault; KF, Kickapoo (Landers) fault; JVF, Johnson Valley fault; PMF, Pinto Mountain fault; EPF, Eureka Peak fault and BMF, Burnt Mountain fault. The Garlock fault is shown on 2.1.

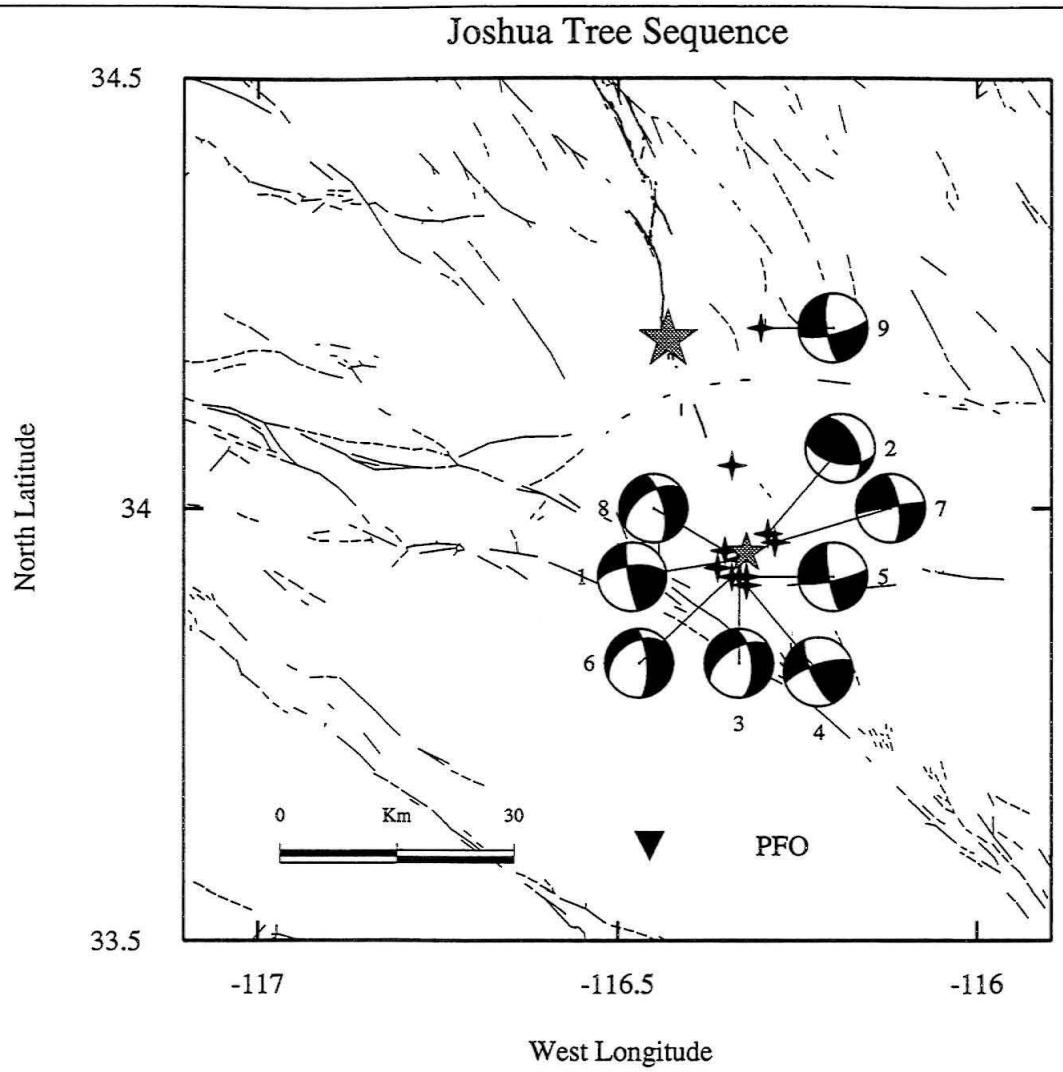

Figure 2.17: Location map showing Joshua Tree aftershocks. Aftershocks are numbered in order of occurrence, and are listed in this order in Table 2.3.

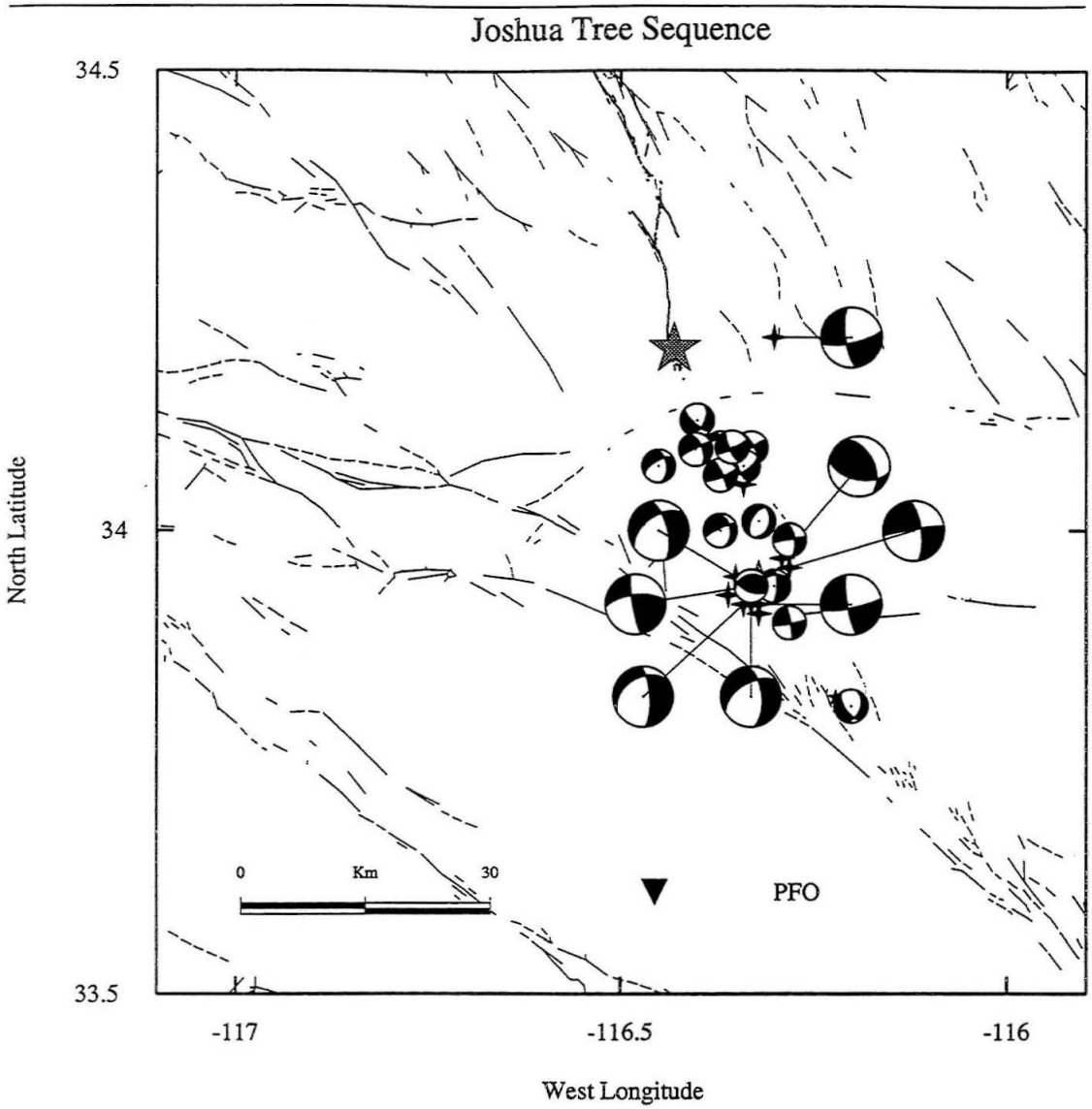

Figure 2.18: Relative locations of Landers and Joshua Tree aftershocks. Joshua Tree aftershocks are indicated with larger spheres; epicentral locations are stars. Landers aftershocks in this area are smaller focal spheres, and epicentral locations are shown as crosses. Size of focal sphere is not related to event magnitude.

Table 2.3: Joshua Tree Aftershocks, $M_w > 4$

						Location		
No.	Date	M_w	strike	dip	rake	Depth	Latitude	Longitude
						km	°N	°W
1.	92042302	4.3	170	82	154	12	33.94	116.33
2.	92042318	4.0	334	50	130	8	33.97	116.29
3.	92042606	4.5	354	60	224	8	33.92	116.33
4.	92042703	4.3	156	74	162	5	33.91	116.34
5.	92050416	4.8	170	80	190	14	33.92	116.32
6.	92050602	4.5	356	72	238	11	33.92	116.32
7.	92051202	4.3	352	70	184	8	33.96	116.28
8.	92051815	4.7	346	66	224	11	33.95	116.35
9.	92061100	4.4	172	74	196	9	34.21	116.30

We present fault–plane solutions, durations, and stress-drops for eight $M > 4$ aftershocks, plus the 02:25 GMT foreshock (Figure 2.17, Table 2.3). This series is dominated by moderate to deep (source–depth 8–14 km) strike–slip and oblique–slip events, including both the foreshock and the mainshock, with epicentral depths of 12 and 10 km, respectively. Events are numbered in the order of occurrence, beginning with the 02:25 GMT foreshock. Source parameters and locations are listed in Table 2.3. Effective stress-drops for these earthquakes are on the order of $10 - 100$ bars. Hough and Dreger [1994] report average stress–drops of 190 bars for Joshua Tree aftershocks of equivalent size ($M3.9$ to $M4.9$) using an empirical Green's function deconvolution method; however, these values include a correction for crustal attenuation.

2.6.2 The Landers Sequence

As mentioned above, clusters of aftershocks from the Joshua Tree event began to form north of the Pinto Mountain fault in early June of 1992. Hours before the Landers mainshock, a third cluster formed at what later became the Landers epicenter [Hauksson et al., 1993]. The Landers earthquake involved rupture on five separate faults north of the Pinto Mountain fault, with a small amount of displacement south of the Pinto Mountain fault on the Eureka Peak fault (Figure 2.16). The latter rupture may not have occurred entirely during the mainshock, but may have been associated with a $M5.7$ aftershock occurring minutes after the mainshock [Hough et al., 1993].

We divide our discussion of the Landers aftershock sequence into three portions: aftershocks south of the Pinto Mountain fault, associated with minimal displacement; aftershocks north of the Pinto Mountain fault, associated with the Landers rupture, and aftershocks north and east of the mapped Landers rupture, in the Barstow and Calico–Pisgah fault clusters, respectively.

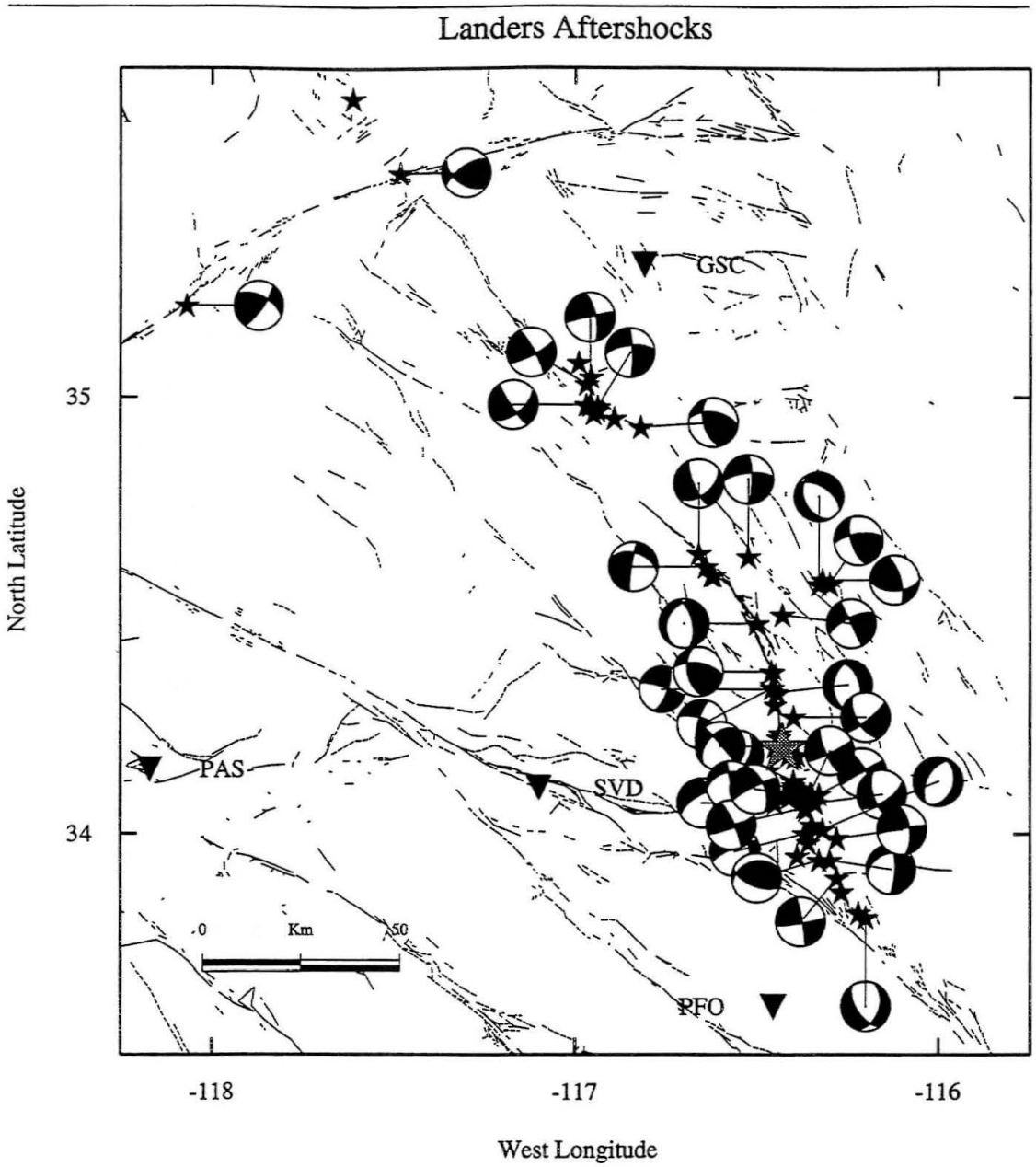

Figure 2.19: Map of locations and focal spheres for the 34 Landers–related Mojave events discussed here, including two earthquakes on the Garlock fault. Epicentral locations are shown as filled (grey) stars. The sequence shown here includes events occurring from June of 1992 through October of 1994. These events will be further broken down and discussed by location and order of occurrence [i.e., 2.20, 2.22].

South of Pinto Mountain Fault

Following the Landers mainshock, large aftershocks were much more common south of the Pinto mountain fault than north of it, along the trace of the fault (Figure 2.19). Less than one minute following initiation of Landers rupture, surface rupture was triggered unilaterally south to north on the Eureka Peak fault (Figure 2.16); this fault re-ruptured three minutes later during a $M5.6$ aftershock on the Eureka Peak fault [Hough, 1994]. Horizontal displacement of about 20 cm was observed along a surface rupture trending about 160°, for about 20 km, along a previously unrecognized fault (now the Eureka Peak fault [Rymer, 1992]). In addition, a small surface rupture (about 7 cm) was observed on the nearby "new" Burnt Mountain fault (Figure 2.16). Almost 76% of the total aftershock energy released post–Landers was released south of the mainshock epicenter, with about 40% of the energy release distributed between the Pinto Mountain fault and the old Joshua Tree epicenter [Ma, 1993].

A tight and dense cluster of early aftershocks formed near the epicentral locations of the triggered events on the Eureka Peak and Burnt Mountain faults, as was observed in the immediate aftermath and epicentral location of the (northern) Landers mainshock (Figure 2.19). Unlike the Landers epicentral area, however, large ($M \geq 4$) aftershocks continued in this southern region for many months. In overall distribution, Landers aftershocks south of the Pinto Mountain fault lie adjacent to and partially overlap those from the earlier Joshua Tree sequence (Figure 2.18), in part filling in the region between the clusters of (larger, i.e., $M > 3.9$) Joshua Tree aftershocks and the Pinto Mountain fault to the north.

Aftershocks extend roughly 40 km south of the mainshock epicenter, forming a NW–SE trending swath 5-15 km in width [Hauksson et al., 1993]. We present source parameters, depths, durations and stress-drops for 14 $M_w \geq 3.7$ aftershocks occurring south of the Pinto Mountain fault, including an $M_w4.5$ event on August 21, 1993 (Fig-

Table 2.4: Landers Events, South of Pinto Mountain Fault

No.	Date	M_w	strike	dip	rake	Location		
						Depth	Latitude	Longitude
						km	°N	°W
1.	92063011	4.2	353	51	215	14	34.07	116.45
2.	92063014	5.1	350	45	200	7	34.00	116.37
3.	92070612	4.2	330	76	182	8	34.09	116.33
4.	92070619	4.3	160	62	208	9	34.07	116.34
5.	92071002	3.9	132	70	218	11	34.12	116.40
6.	92072418	4.9	351	80	173	8	33.90	116.28
7.	92072504	4.7	2	76	238	8	33.94	116.30
8.	92072818	4.7	310	40	100	5	34.09	116.37
9.	92081106	4.1	336	80	170	8	34.06	116.37
10.	92081508	4.5	338	58	190	6	34.088	116.403
11.	92090912	4.2	112	62	110	8	33.94	116.33
12.	92091508	5.2	156	76	188	8	34.09	116.35
13.	93082101	4.5	208	54	278	9	34.010	116.32
14.	94080715	3.7	352	64	184	8	33.99	116.28
15.	94081508	3.8	146	64	240	9	33.81	116.20

ure 2.20, Table 2.4, event number 13) and two events in August of 1994 (Figure 12, Table 2.4, events 14–15). Waveform modeling for these events and others south of the Pinto Mountain fault can be found in Appendix I. For $M > 3.7$ events, the sequence is fairly heterogeneous, including normal and thrust-type faulting, though pure and oblique strike–slip events are most numerous. The strike–slip events are consistent in strike direction; all strike NW, in roughly the same direction as the Joshua Tree mainshock ($N20°W$) and with strike–slip events associated with the Joshua Tree sequence (Figure 2.18).

Like those estimated for Joshua Tree aftershocks, stress-drops for Landers aftershocks south of the Pinto Mountain fault are on the order of 10 – 100 bars; with an average of about 40 bars. Lowest stress–drop events are associated with either the epicentral region of the southern rupture (Figures 3.17, 2.21), or the area active during earlier Joshua Tree seismicity (including the Joshua Tree mainshock) located south of the southern rupture. Events clustered near the Eureka Peak rupture (Figure 2.20, Table 2.4, events 3, 4, 5, 8 and 12) have stress drops from 10 to 30 bars (average is 22 bars). These earthquakes are largely strike–slip to oblique slip, and all are of intermediate depth (8 to 11 km). Two oblique to normal events just south of the Eureka Peak cluster (Figure 2.20, Figure 2.21, Table 2.4, events 2 and 13), are of similar depth but higher stress-drop (89 and 60 bars, respectively). Similarly, an outlying normal–faulting event due west of the Eureka Peak cluster (event 1) is comparatively high stress–drop (126 bars) and is relatively deep (14 km). Just east of event 1 is a shallow, unusually high stress–drop (350 bars) event (Figure 2.20, Figure 2.21, Table 2.4, event 10) with a similar source mechanism. These high stress–drop earthquakes lie west and nearly on the periphery of the low stress–drop Eureka Peak cluster (i.e., events 3, 4, 5, 8, 12) as seen in Figure 2.20. A second low stress-drop cluster occurred near the epicenter of the Joshua Tree mainshock. Events 6, 7, and 11 (Figure 2.20, Figure 2.21, Table 2.4) have stress-drops ranging from about 25 to 50 bars, with an average of about 35 bars. Event

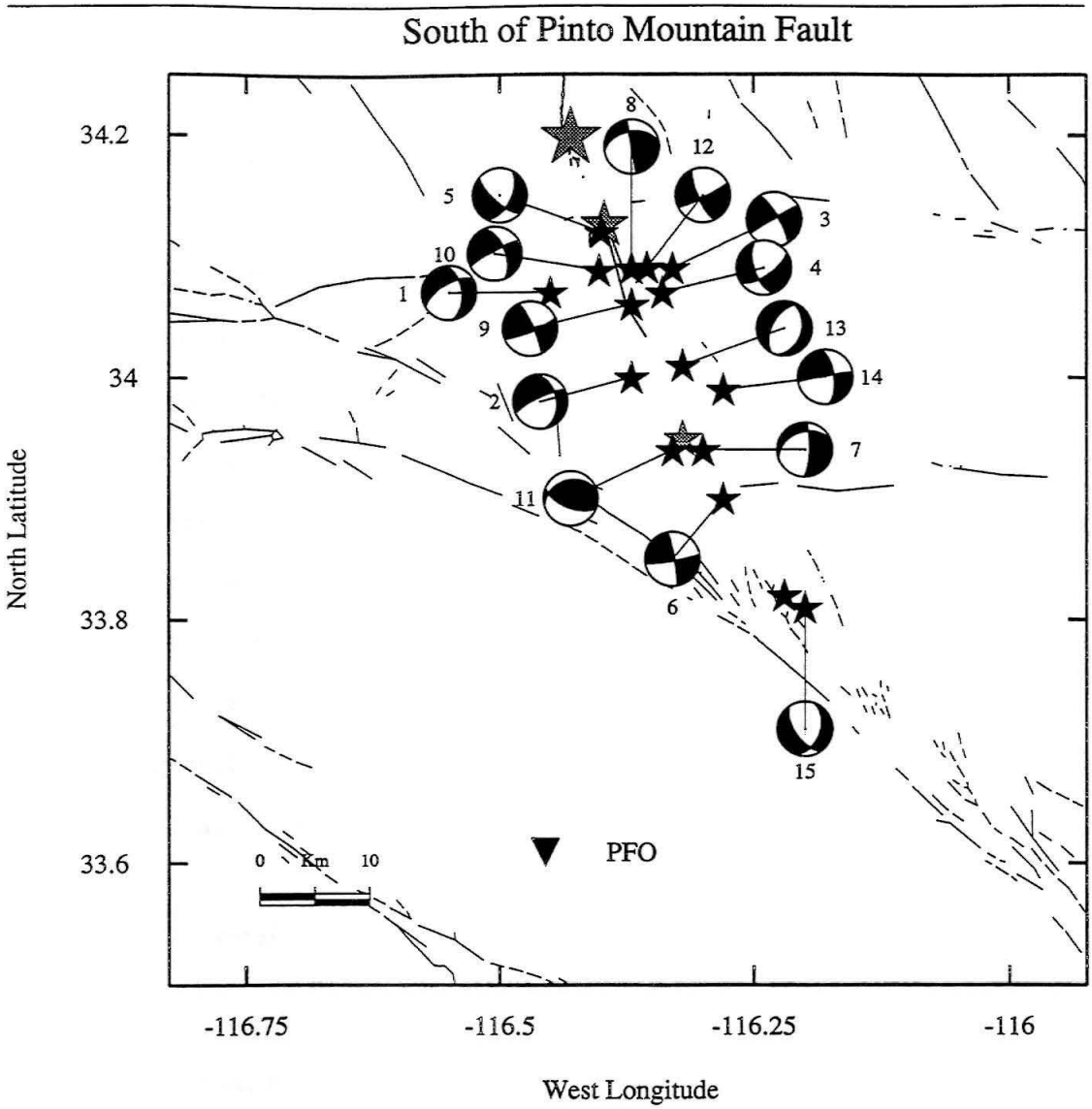

Figure 2.20: Map showing Landers aftershocks south of the Pinto Mountain fault. Locations of these aftershocks were previously shown relative to earlier Joshua Tree aftershocks (Figure 2.18). In this map, the aftershocks are numbered chronologically, and listed in the same order in Table 2.4. The Joshua Tree mainshock is shown as a small filled (grey) star; Landers mainshock and Southern Landers subevent are also shown as filled (grey) stars.

14 is unusually low stress-drop, but occurred after much of the sequence had exhausted itself: this late $M_w 3.7$ event occurred in August of 1994, at a depth of 8 km.

Historically, $M5$ aftershocks in the Mojave region have been shallow, with source depths no greater than 5 km [Hutton et al., 1980]. However, these aftershocks, including two $M5$ events, have moderate (8 to 10 km) to deep (11 to 15 km) source depths; most are roughly 8 km in depth. In map view these events do not define any one fault plane; rather they re-rupture areas associated with the Joshua Tree sequence, and fill in unaffected regions north towards the Pinto Mountain fault. The history of seismic activity in the region, the present heterogeneity of faulting and the lack of any one well-defined fault plane suggest that displacement south of the Pinto mountain fault may be accommodated gradually (i.e., in small increments) across a number of small subsurface faults. The gap in large aftershocks across the Pinto Mountain fault (Figure 2.19) suggests that Landers rupture may not continue across the fault, and that displacement south of the Pinto Mountain fault may be primarily aftershock–related, though disjoint triggered secondary rupture (which lies somewhere in the continuum between subevent and aftershock) is clearly also important.

North of Pinto Mountain Fault

Rupture along the five faults active in the Landers mainshock (from south to north, the Johnson Valley fault, the Kickapoo (Landers) fault, the Homestead Valley fault, the Emerson fault and the Camp Rock fault) extended roughly 60 km N-NW across the Mojave desert north of the Pinto Mountain fault (Figure 2.16). Large ($M > 3.9$) aftershocks along the trend of the Landers rupture are common in three general areas: close to the mainshock epicenter (early aftershocks, within the first 24-48 hours), at fault ends, including the termination of the Johnson Valley fault and the very active Kickapoo (Landers) fault, and the northern extent of rupture, at the northern terminus of the Camp Rock fault (Figure 2.19). Waveform modeling results for these and other

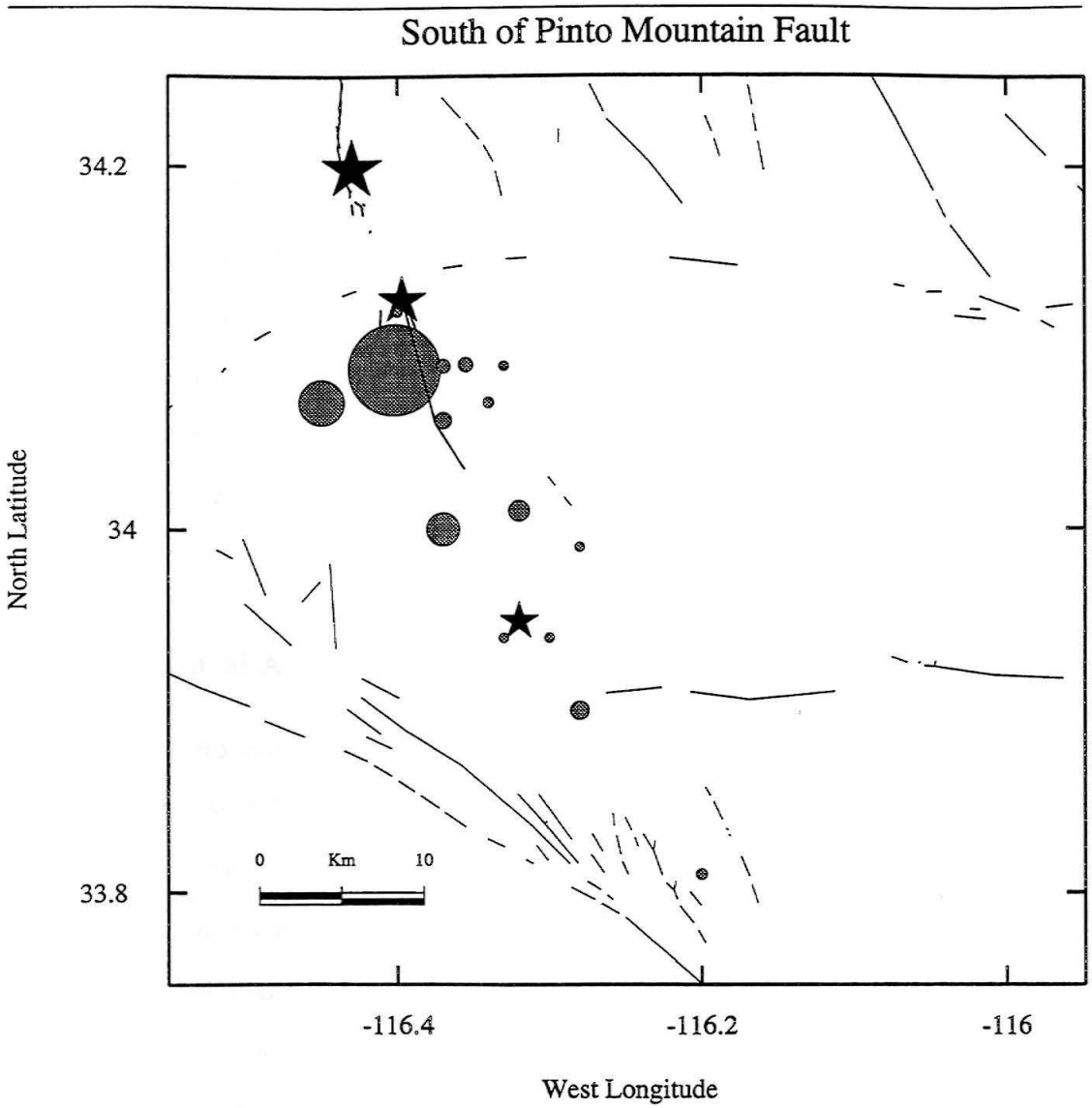

Figure 2.21: Map showing stress–drops for Landers aftershocks south of the Pinto Mountain fault. Filled circles represent relative stress–drops, scaled to a maximum of 350 bars. Circles for the smallest events have been enlarged slightly to make them visible. The Joshua Tree mainshock is shown as a small filled (black) star; Landers mainshock and Southern Landers subevent are also shown as filled (black) stars.

Landers aftershocks north of the Pinto Mountain fault can be found in Appendix II.

We present results for nine $M > 3.9$ aftershocks along or very near the trend of the (northern) Landers rupture. Two of these events are along the Johnson Valley fault, near the mainshock epicenter (Figure 2.22, Table 2.5, events 10 and 19), three are on the Landers or Kickapoo fault (Figure 2.22, Table 2.5, events 1 and 3), one just north of the junction of the Kickapoo with the Homestead Valley fault, one normal-faulting event within the overlapping segments forming the en-echelon stepover between the Homestead Valley and Emerson faults (Figure 2.22, Table 2.5, event 13), and two events near the terminus of surface rupture on the Camp Rock fault (Figure 2.22, events 2 and 16). We consider each of these groups briefly below, proceeding south to north from the mainshock epicentral area (Johnson Valley fault) to the terminus of rupture (Camp Rock Fault).

Mainshock Epicentral Area

The region immediately local to the Landers epicenter, along the previously recognized and active Johnson Valley fault, saw many $M > 4$ aftershocks within the first 24 hours of the mainshock (Figure 2.19), [Hauksson et al., 1993]. However, we were not able to obtain TERRAscope data for these early events. We analyzed two later events, one nearly co–located with the mainshock (Figure 2.22, event 10), and one slightly northeast of the same, a M4.7 event which occurred in June of 1994 (Figure 2.22, event 19). Both events are oblique–slip, and of moderate to shallow source depth. Both are low stress-drop; (9 and 15 bars, respectively, see Figures 2.22, 2.21).

Kickapoo (Landers) Fault

There were an unusual number of $M_w > 3.9$ aftershocks along the short segment of the newly recognized Kickapoo (Landers) fault. This is a previously unmapped, 5 km long N-S trending fault strand running from the southern leg of the Johnson Valley fault and

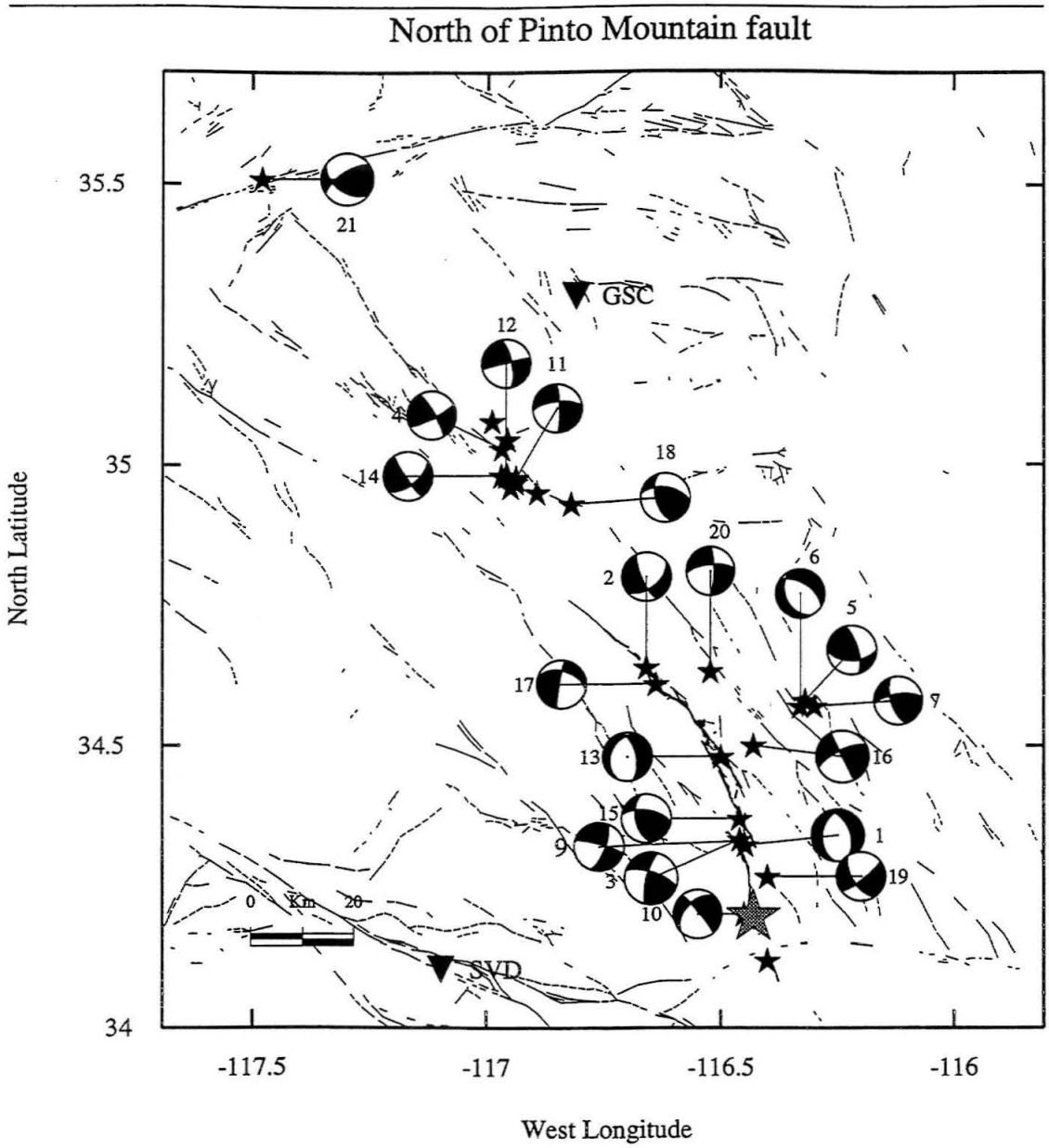

Figure 2.22: Map showing Landers aftershocks north of the Pinto Mountain fault, inluding off-fault clusters at Barstow, and on the Pisgah and Calico faults. Events are numbered in the order of occurrence, and listed in this order in Table 2.5. Event 8 (Garlock) is too far west to be shown on this plot, and is seen on Figure 2.26.

Table 2.5: Landers Events, North of Pinto Mountain Fault

No.	Date	M_w	Strike	Dip	Rake	Location		
						Depth	Latitude	Longitude
						km	°N	°W
1.	92063012	4.0	342	50	254	9	34.32	116.45
	(A.)	4.1	165	60	110	7.4		
2.	92063017	4.1	156	74	222	8	34.64	116.66
	(A.)	4.3	164	51	132	5.6		
	(B.)	4.0	183	53	252	5		
3.	92070107	5.2	194	76	160	7	34.33	116.46
	(A.)	5.2	180	70	156	7.6		
4.	92070510 †	4.5	331	80	169	8	35.03	116.97
	(B.)	4.3	245	80	352	9		
5.	92070521	5.4	344	70	142	8	34.58	116.32
	(B.)	5.3	76	72	34	8		
6.	92070522	4.4	336	64	140	8	34.57	116.33
	(B.)	4.3	323	50	114	9		
7.	92070802	4.6	162	66	156	8	34.57	116.30
	(B.)	4.5	79	77	36	8		
8.	92071118 ‡	5.3	296	58	164	11	35.21	118.07
	(B.)	5.1	213	86	328	24		
9.	92071500	3.9	20	68	186	6	34.33	116.46
	(A.)	3.8	20	85	180	1.1		
10.	920720040	3.9	320	84	224	8	34.20	116.45
	(B.)	3.9	225	60	354	8		

Barstow sequence †; Garlock event ‡

(A.) Hauksson, 1992; (B.) Thio, 1992.

Table 2.5: (cont'd) Landers Events, North of Pinto Mountain Fault

11.	920720044 †	4.4	358	82	204	7	34.96	116.95
	(A.)	4.4	174	70	170	5.9		
	(B.)	4.4	262	83	345	9		
12.	92072013 †	4.5	348	71	183	5	34.98	116.96
	(A.)	4.5	342	80	170	1.8		
13.	92072407	3.8	344	60	260	11	34.48	116.50
	(A.)	3.9	317	51	82	9.7		
	(B.)	3.6	197	65	301	15		
14.	92080522 †	4.6	146	82	210	6	34.98	116.97
	(A.)	4.7	147	80	179	2		
15.	92080815	4.3	168	64	146	8	34.37	116.45
	(A.)	4.1	183	71	160	9.2		
	(B.)	4.2	259	71	345	7		
16.	92083109	4.2	154	90	160	12	34.50	116.43
	(A.)	4.2	271	63	152	12		
	(B.)	4.1	245	62	310	14		
17.	92100207	4.6	189	83	313	5	34.61	116.64
	(A.)	4.3	90	70	159	4		
	(B.)	4.4	262	72	152	5		
18.	92101112 †	4.4	170	64	140	8	34.93	116.82
	(A.)	4.5	248	31	20	6.4		
	(B.)	4.1	244	88	3	12		
19.	94061616	4.7	148	61	193	5	34.267	116.40
20.	94080121	4.4	360	78	202	14	34.633	116.523
21.	94101900 ‡	4.2	126	50	150	8	35.51	117.48

Barstow sequence †; Garlock event ‡

(A.) Hauksson, 1992; (B.) Thio, 1992.

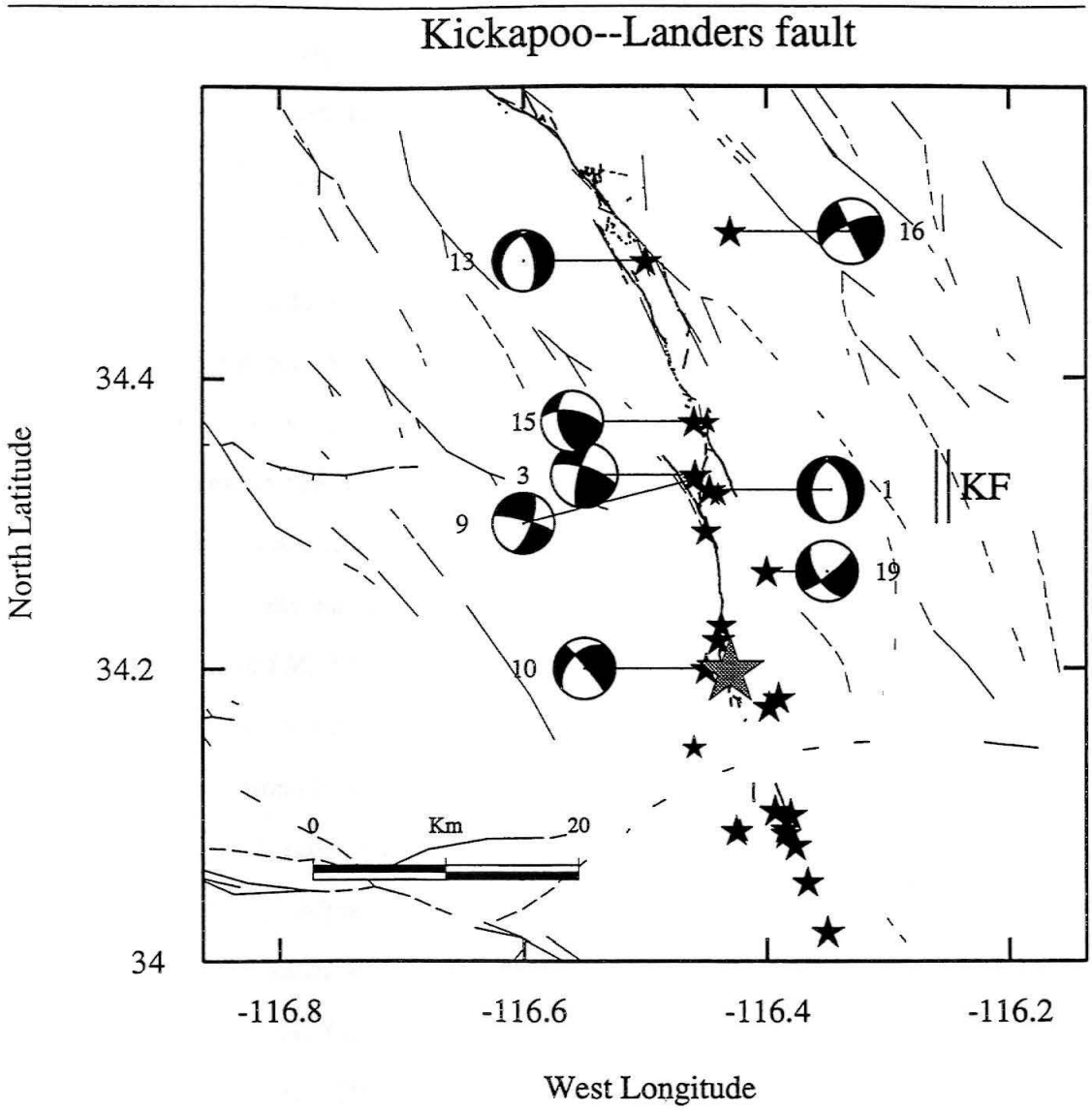

Figure 2.23: Detail of map from Figure 2.22, showing seismicity around the mainshock area (large grey star) and Kickapoo fault (indicated by double line and the letters KF). All events of $M > 4.0$ are shown. Most seismicity south of the Pinto Mountain fault and around mainshock epicenter occurred within the first 24 hours.

northwards to the southernmost end of the Homestead Valley fault. Rupture during the 1992 Landers event propagated from the Johnson Valley fault to the Homestead Valley fault along the Kickapoo fault and secondary fault traces just east of the Kickapoo [Sowers et al., 1994]. We studied four (out of six) $M > 3.9$ aftershocks occurring along or near the Kickapoo fault which were recorded on the TERRAscope array [Figure 2.23].

The earliest event is a normal-faulting event (strike 342, dip 50, rake 254) occurring near the southern end of the zone comprised of the Kickapoo and its secondary faults (Figures 2.22, 2.23, event 1). It is of moderate stress–drop (about 84 bars, Figure 2.24), and average depth (8-9 km) for this region. It was followed by two strike–slip to oblique–slip events just north along the Kickapoo (Figure 2.23, Table 2.5, events 3 and 9). The first of these is the largest aftershock to occur within the Landers rupture region, at $M_w = 5.2$, and also has the highest stress-drop (about 512±176 bars, Figure 2.21). It has a right-lateral mechanism (strike 194, dip 76, rake 160) and a source–depth of about 7 km. A smaller (M_w3.9) colocated right-lateral strike-slip aftershock occurred two weeks later (event 9) at a depth of about 6 km. This event is substantially smaller, and has a lower stress-drop (30 bars), perhaps representing a re-rupturing of a previously ruptured fault-patch. A later M_w4.3 event occurred near the southern end of the Homestead Valley fault approximately near the termination of the Kickapoo fault (Figure 2.23, event 15). This aftershock is of similar depth (7 km), has an oblique–slip source mechanism, and a stress-drop of about 80 bars. It occurred within a region mapped and described by Spotila and Sieh [1995], and exhibiting both strike–slip and thrust faulting.

The presence of the latter three events lends support to the dominantly right-lateral offset "through-going" model suggested by Sowers et al. [1994] for the Kickapoo fault. However, the mechanism of the earliest large Kickapoo aftershock (event 1) suggests extension, which lends credence to the less favored "step-over model" suggested by Sowers et al. [1994]. Clearly the tectonics of the Kickapoo fault is more complicated than either of these simple schemes; perhaps some combination of the two models, or partitioning of

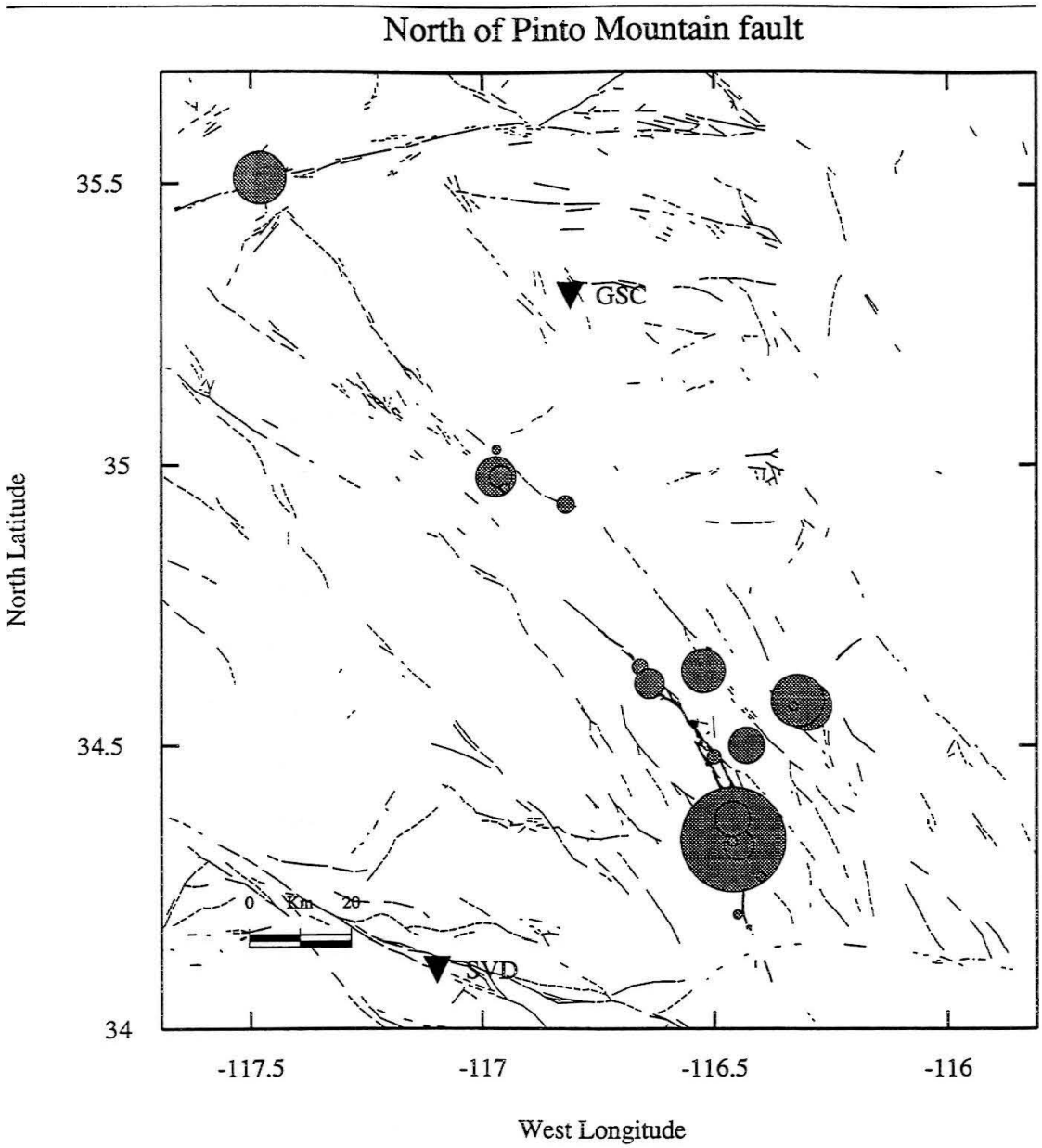

Figure 2.24: Map showing stress–drops for Landers aftershocks Nouth of the Pinto Mountain fault. Filled circles represent relative stress–drops, scaled to a maximum of 500 bars. Circles for the smallest events have been enlarged slightly to make them visible.

strain, might explain the complex seismicity we observe here. The presence of so many heterogeneous and high stress–drop aftershocks along this small segment of fault also lends credence to the suggestion made by Spotila and Sieh [1995], that the connection between the Johnson Valley and Homestead Valley faults is incomplete, and that the Kickapoo fault is still very immature.

2.6.3 Emerson and Camp Rock Faults

Large on–fault aftershocks appear to be much less common north of the Kickapoo Fault. Most $M > 3.9$ aftershock activity appears to be concentrated near the end of rupture on the Camp Rock fault. We present results for two such events (Figure 2.23, events 2 and 17) and one M_w3.8 normal-faulting (strike 344, dip 60, rake 260) aftershock between the overlapping strands of the Homestead Valley and Emerson Faults (Figure 2.23, event 13). The former two events (2 and 17) are both oblique-slip events. Event 2 (M_w4.1) was an early aftershock near the northern end of Landers mainshock rupture. It is of average source depth (8 km) and has a stress–drop of about 46 bars. Event 17 is shallower (source depth 5 km), with a slightly higher stress drop (about 86 bars). Event 13, a purely dip-slip (normal) event between the Homestead Valley and Emerson faults, has a fairly low stress drop (38 bars) and is deeper than average, with a source depth of about 11 km.

Off–Fault Aftershock Activity

In addition, there are clusters of large aftershocks off-fault (i.e., unrelated to any primary rupture during the Landers mainshock). These occurred east of the Landers rupture, near the Pisgah/Calico faults (Figures 2.22, 2.25) and north of the terminus of Landers rupture on the Camp Rock fault, in the Barstow region. We address the off-fault aftershocks below.

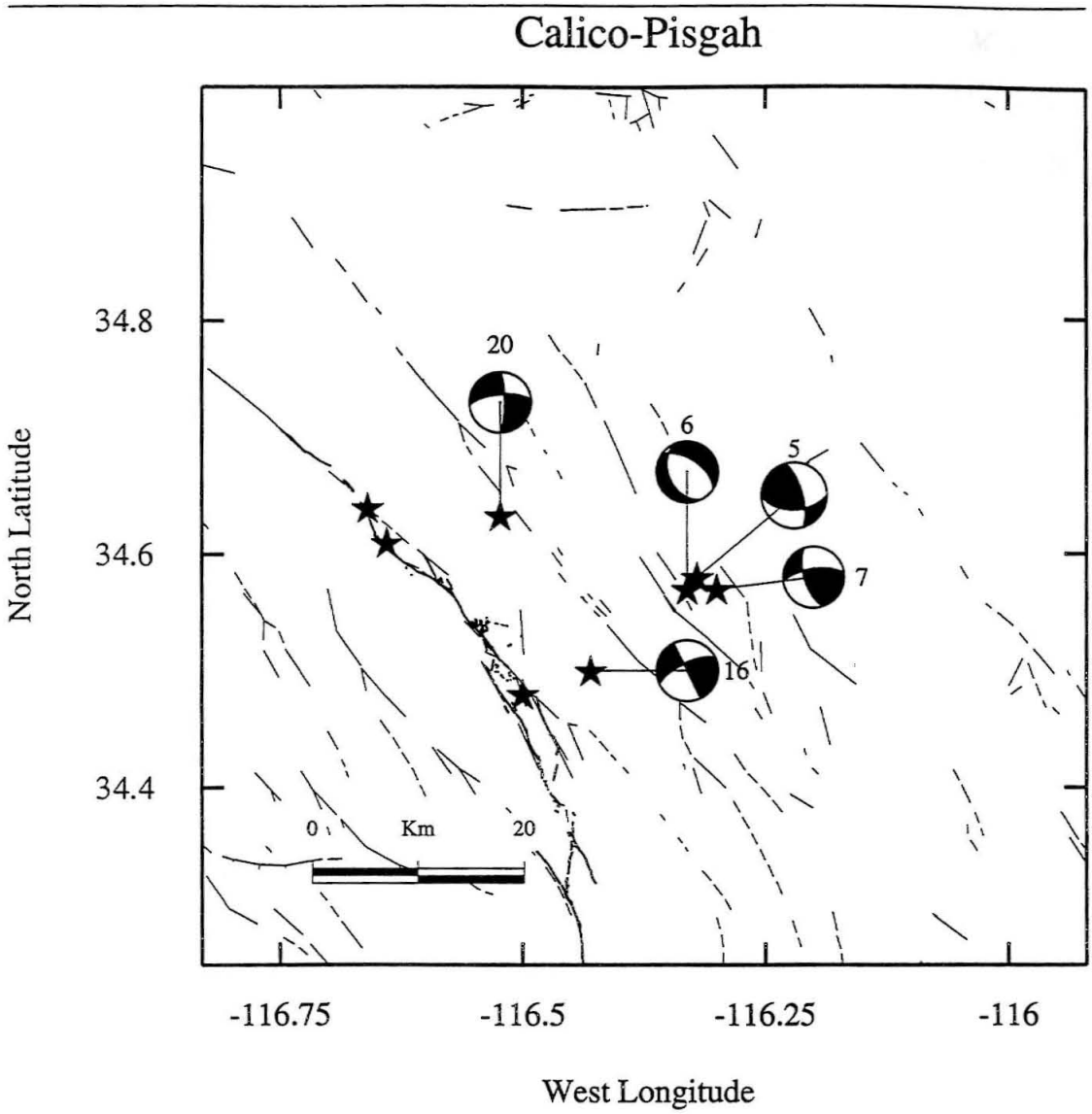

Figure 2.25: Detail of map from Figure 2.19, showing off–fault seismic activity near the Calico and Pisgah area. Events are numbered as in Figure 2.22 and in Table 2.5.

Aftershocks on Pisgah–Calico Faults

Aftershocks near the Calico fault [Figure 2.22] form two east-west alignments perpendicular to the trend of the Landers rupture, roughly at the latitudes of the Emerson and Camp Rock faults [Figure 2.16]. We present results for the two $M > 4$ events near the Calico fault [Figure 2.25, Table 2.5, aftershocks 16 and 20]. The latter event (20) occurred more than two years after the Landers mainshock, but shows similar fault motion and depth as the earlier event in August of 1992. Both are unusually deep (see Table 2.5) for this region. Stress–drops for these two events are high (104 and 126 bars, respectively). In addition, there is a spatially and temporally tight cluster of aftershocks just east of the Pisgah fault, several of which are larger than $M4$. We present results for three of the largest aftershocks for which TERRAscope data were available (Figure 2.25, Table 2.5, events 5, and 6, and 7, at 5, 8 and 8 km, respectively). Two of these occurred within an hour of each other, and were nearly colocated (events 5 and 6). Events 5 and 7 are high stress-drop (100 and 140 bars, respectively). Event 6 is smaller than event 5 and has a substantially lower stress-drop of about 25 bars. It possesses dip-slip rather than strike–slip or oblique motion. Aftershocks on the Pisgah and Calico faults may be related to off–fault strain caused by changes in strike along the Landers rupture [Sieh et al., 1993]. High stress–drops in both regions might suggest high applied shear stresses along north to northwest–striking planes.

The Barstow Sequence

The Barstow cluster was associated with no surface rupture, and occurred approximately 30 to 40 km north of the aftershocks associated with northernmost Landers rupture on the Camp Rock fault. It began approximately 6 hours after the Landers mainshock, and comprised at least 12 aftershocks above $M4$, 4 of which were $M4.5$ or larger. The largest aftershock, at $M_w = 4.8$, occurred on August 5, 1992, at 22:22 GMT, within a tight cluster of larger aftershocks towards the southern end of the trend. The Barstow

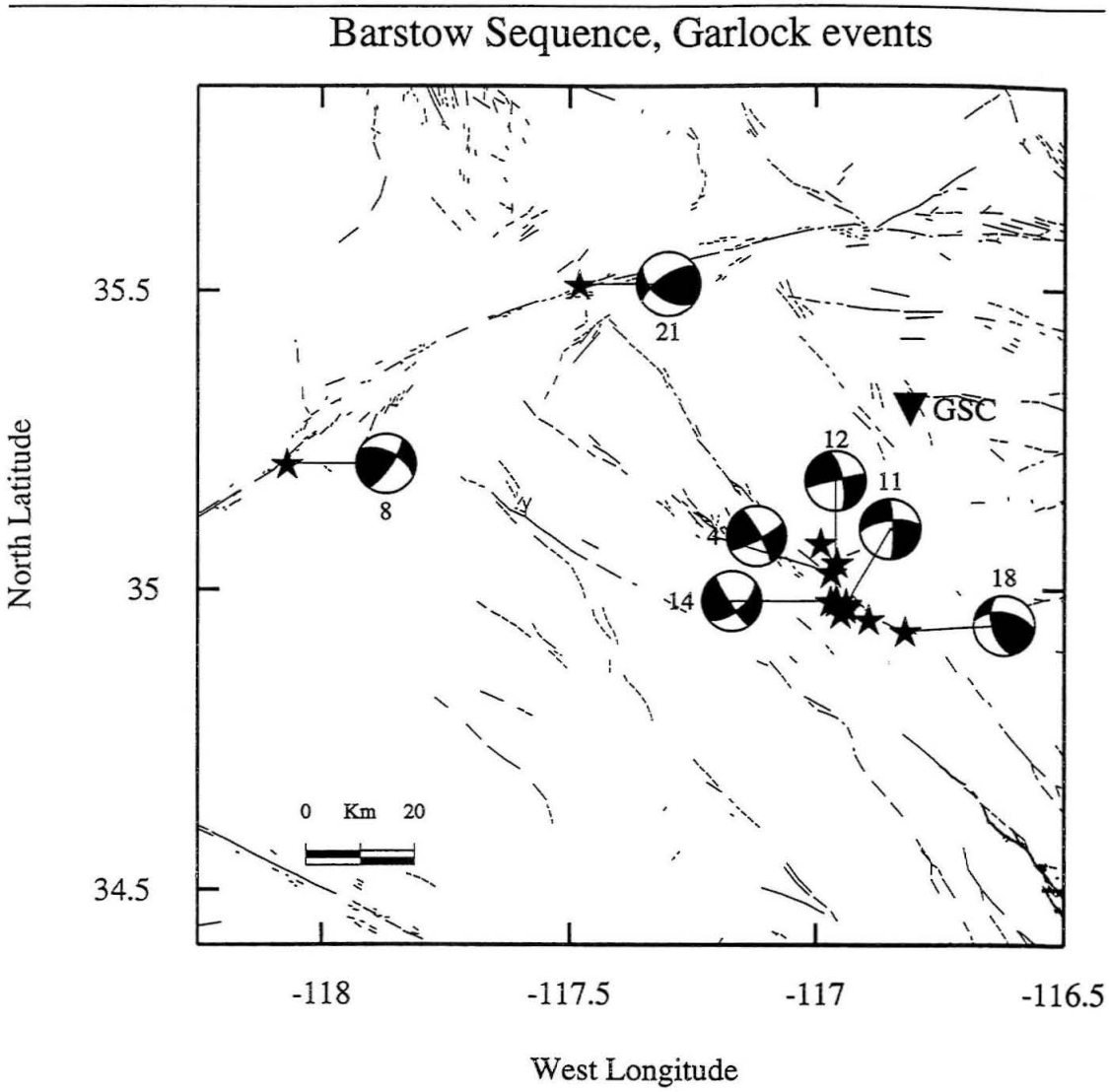

Figure 2.26: Detail of map from Figure 2.19, showing off–fault seismic activity in the Barstow area, and further north along the Garlock fault. Events are numbered as in Figure 2.22 and in Table 2.5.

sequence is fairly narrow in width compared with aftershocks along the Landers rupture; the ratio of length (about 20 km) to width (2–3 km) has been cited as evidence that the Barstow sequence may have occurred on a single fault, unlike the Landers quake [Hauksson et al., 1993]. However, closer examination of the larger aftershocks in the sequence [Figure 2.26] shows a distinct jog in the trend of the aftershocks, with a tight cluster to the southeast (e.g., aftershocks 11, 14, at depths of 8 and 7 km, respectively) which could arguably have occurred on a single fault. There is an abrupt step-over, with events farther to the west (including aftershocks 4, 11, both at 8 km) along a rough trend striking NW–SE. Stress–drops for these earthquakes range from 16 – 90 bars, with an average of about 50 bars. Our depth estimations do not show the shallowing reported by Hauksson et al.,[1993], and shallowest events are at a depth of 5 km.

2.6.4 Aftershocks on the Garlock Fault

The Garlock fault has long been recognized as an important tectonic feature in Southern California [Figure 2.1]. Though it has not produced any large earthquakes within the period of historical record, numerous scarps and left-laterally offset Holocene features suggest that the fault is active and has produced large earthquakes. As recent levels of seismic activity on this fault are low in comparison to those inferred from Holocene displacements, the Garlock fault represents a seismic gap [Astiz and Allen, 1983]. Until the moderately sized earthquakes in July of 1992 [Figure 2.26, event 8] and again in October, 1994, [Figure 2.26, event 21] no such earthquakes were known to have occurred on the Garlock fault, though there were several historical events for which a Garlock fault *source* was possible [McGill and Sieh, 1991].

The July 1992 event was the larger of the two recent events, at $M_w = 5.3$. This was the largest earthquake associated with or local to the Garlock fault since the June 10, 1988, $M_L = 5.4$ earthquake that occurred several km north of the Garlock fault, about 20 km east of its intersection with the San Andreas fault, possibly on the North Branch

of the Garlock [McGill and Sieh, 1991]. Previous to the 1988 event, the most recent moderate earthquakes local to the Garlock fault were two historical events occurring in 1916: a $M5.5$ event 45 km north of the eastern end of fault, in the Quail mountains [Toppozada et al., 1978] and a $M5.2$ quake at the western end of the fault, for which the San Andreas may be responsible. The July 11, 1992, $M_w5.3$ Garlock earthquake was clearly related to and possibly triggered by the sudden changes in the regional stress field caused by Landers. The 1992 event and the October 19, 1994, $M_w4.0$ earthquake lie on either side of the midpoint of the Garlock (near the city of Rand), which marks a change in strike, seismic and aseismic behavior, and geology [Astiz and Allen, 1983]. The two events lie on either side of an en-echelon fault step-over near Rand and Koehn lake, which McGill and Sieh [1991] argue segments the fault into a western and an eastern segment. The eastern segment may itself be segmented further, based on the complexity of its trace.

While the western segment of the Garlock Fault has manifested continuous low level seismicity and demonstrable creep during the last several decades, the eastern segment has had only a few small earthquakes, and no observed creep [Astiz and Allen, 1983]. Holocene slip rates near Koehn Lake/Rand, close to the location of the 1992 event, are between 7 and 8 mm/year [Carter, 1971, 1980; Clark and Lajoie, 1974], while those eastward, near Christmas Canyon and the location of the 1994 event, are at most 4 mm/y during Holocene times [Smith, 1975]. The 1992 event, which took place within two weeks of the Landers mainshock, occurred on a fault striking about 37 degrees east

---

Figure 2.27: Broadband waveform modeling for the $M5.3$ July 11, 1992, Garlock earthquake. Both the standard Southern California model (stations PAS, PFO) and Mojave model (GSC, ISA, SVD) were used in this source estimation. The moment for this solution is $M_b = 7.64 \pm 2.85 \times 10^{23}$; the time function is (0.25, 0, 0.25) s.

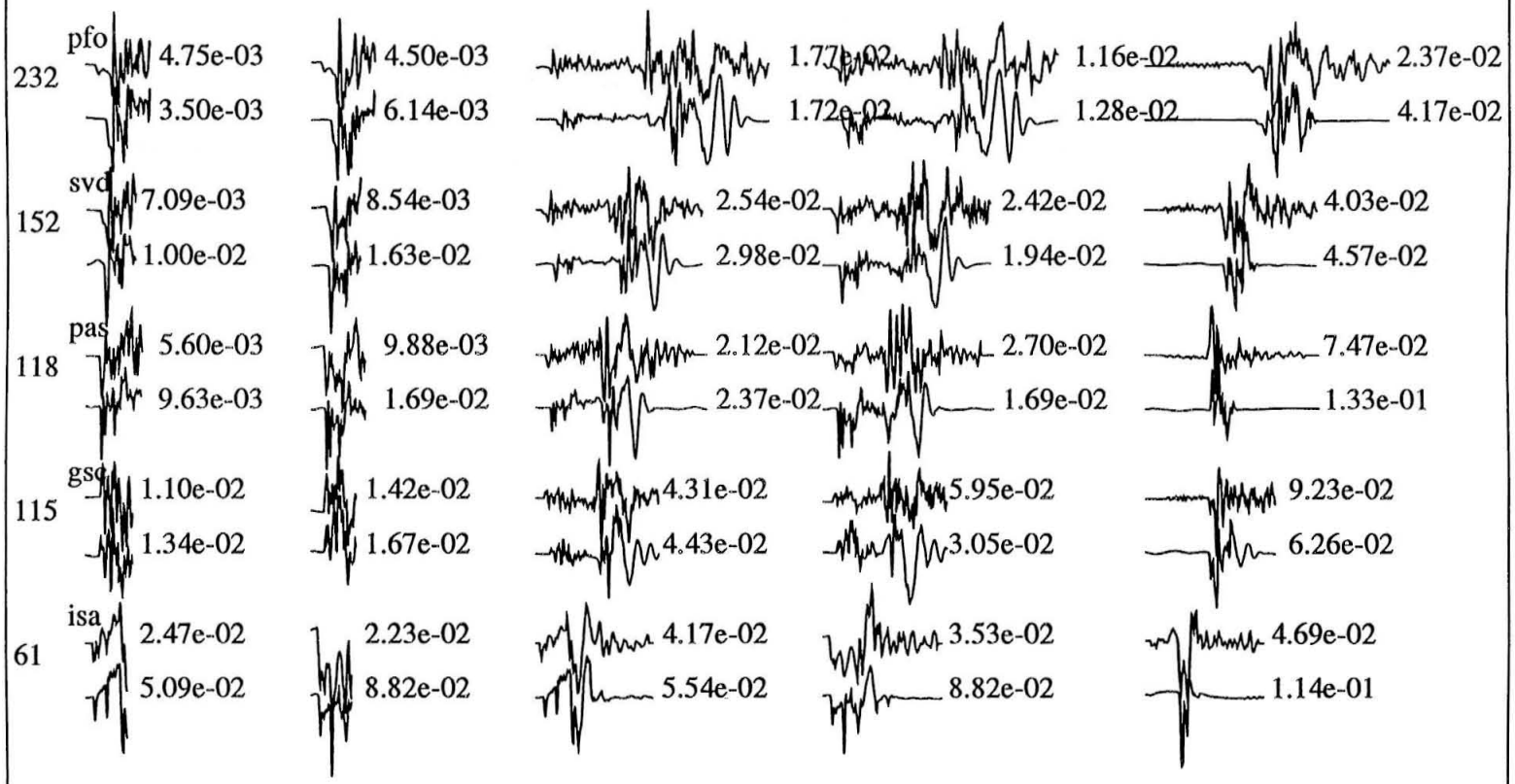

Broadband

Event 8, Table 2.4, Garlock Fault

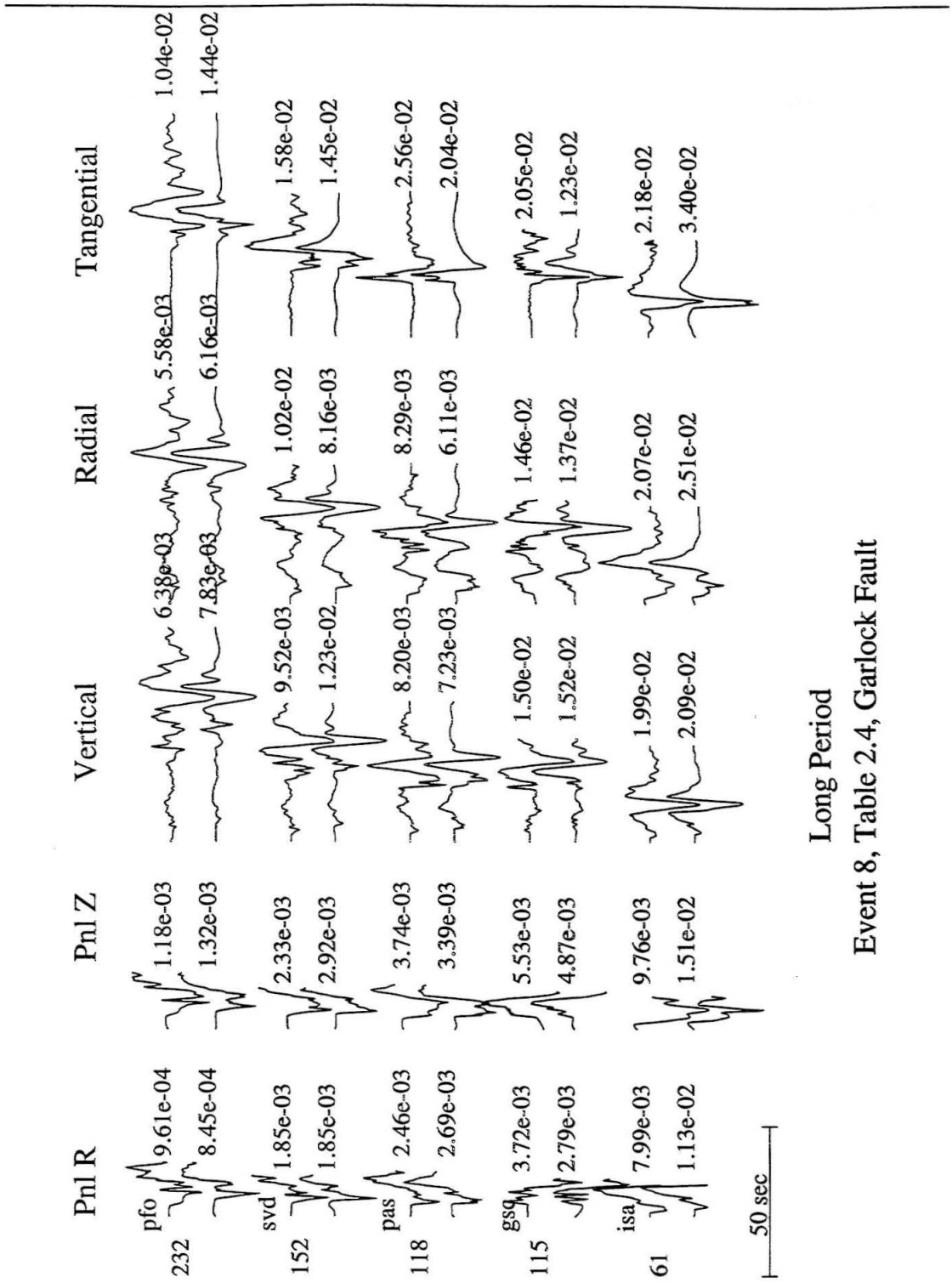

Figure 2.28: Long–period waveform modeling for the July 11, 1992, Garlock earthquake. Moment is $M_o = 9.44 \pm 2.29 \times 10^{23}$ for the long–period solution.

of north, dipping about 74 degrees (assuming left-lateral motion), and at a depth of 12-13 km. This event was moderate in size, with a moment of $M_o = 9.44 \pm 2.29 \times 10^{23}$ (from our long–period solution), but extremely short in source duration, which yields an unusually high stress-drop of about 1044 ± 253 bars. Broadband and long–period waveform fits for the June 11, 1992, Garlock event are shown on Figures 2.6.4 and 2.28, respectively.

The broadband modeling yields a slightly lower stress-drop of 840 ± 316 bars. Error associated with moment determination is greater for the broadband records, which translates into higher error in the stress-drop estimation. The second, smaller 1994 event ($M_w 4.0$) has more thrust component to its motion [Figure 2.26, event 21], striking 56^o, with a dip of 67^o, a rake of 136^o, and a depth of about 8 km. The stress–drop is lower than that obtained for the earlier event, but nonetheless high: 192 ± 90 bars for the long–period solution.

2.6.5 The Big Bear Sequence

The Big Bear earthquake is considered an aftershock of the Landers earthquake because it occurred within one fault length of the mainshock [Sieh et al., 1993], yet it occurred on a separate and previously unmapped fault or faults. The lack of observed surface rupture makes the rupture process of this event enigmatic [Jones and Hough, 1994]. The Big Bear earthquake is associated with its own fore– and aftershock sequences, including several earthquakes in the $M4-5$ range. This sequence, or at least the larger ($M > 3.8$) aftershocks we studied, appears to have occurred entirely within the San Bernardino Mountains block, which is bounded on the north by the North Frontal fault zone [Meisling and Weldon, 1989], and on the south by the Mill Creek fault and the San Bernardino segment of the San Andreas fault [Matti et al., 1992][Figure 2.16]. There are several arguably related earthquakes which occurred in the San Gorgonio Pass and Lake Arrowhead areas, as recently as April 1994. Seismicity appears to shallow overall

to the north and to the south, suggesting that these bounding faults may define a spatial boundary for the deformation associated with the Big Bear sequence [Hauksson, 1993].

Mainshock

The Big Bear sequence began at 14:43 GMT on June 28, 1992, with a M_w5.2 foreshock located at 34.16° N, 116.85° W [Figure 2.29, Table 2.6, event 1]. Given its source-depth of about 14 km, this event was both deep and high stress-drop (about 200 bars). Rupture directivity studies comparing foreshock to "master event" amplitude ratios at stations GSC, ISA, PAS, and PFO indicate that this event had strong northward directivity [Jones et al., 1993]. This foreshock was followed by a second, smaller foreshock at 15:04 GMT in a location due east. The Big Bear mainshock occurred only 40 s later, at 15:05 GMT, in a location north of the 14:43 foreshock. There is some confusion about the location of the mainshock, since it was preceded by a M4.0 foreshock only a few tens of seconds earlier. Hauksson et al. [1993] assign both the location and focal mechanism of the 15:04 foreshock to the mainshock. However, the foreshock is too small to have appreciable amplitudes on strong–motion records. Furthermore, the mainshock location obtained from the SCSN strong motion array agrees with that obtained by the TERRAscope array, and is significantly distinct from that of the immediate foreshock location (34.16, -116.82) [Jones et al., 1993]. Observations of aftershock activity within the first 24 hours of the mainshock reveals a T-shaped pattern of seismicity, which, along with evidence of initial Big Bear rupture to the northwest rather than the northeast, suggests rupture on conjugate fault-planes (Figure 3.4). Evidence of complex rupture has also been observed by Hauksson et al. [1993], who note a minor northeast–striking band of aftershocks northwest of the Big Bear aftershock trend, and suggest on this basis that "subparallel" faults were activated during or after the mainshock. Seeber and Armbruster [1995] show evidence of such complexity in aftershock patterns from the Big Bear earthquake: both NW–striking faults and NE–striking faults were active

Table 2.6: Big Bear Events

No.	Date	M_w	Strike	Dip	Rake	Location		
						Depth km	Latitude °N	Longitude °W
1.	9206281443	5.2	210	86	330	14	34.16	116.85
2.	Mainshock	6.5	320	86	200	11–14	34.21	116.83
3.	9206281701	4.8	118	83	145	14	34.18	116.92
4.	9206281748	4.3	324	90	200	8	34.22	116.75
5.	9206291441 †	4.4	113	85	150	7	34.12	116.99
6.	9207012053	4.0	343	90	214	6	34.29	116.72
7.	9207030415	3.9	230	80	150	16	34.18	116.78
8.	9207090143	5.3	246	46	102	2	34.24	116.84
9.	9208172041	4.8	285	65	150	15	34.18	116.87
10.	9208180946	4.0	268	52	118	11	34.18	116.88
11.	9208241351	4.0	330	75	178	8	34.28	116.78
12.	9211271600	5.2	118	70	176	5	34.34	116.88
13.	9212040208	5.1	126	43	117	7	34.35	116.90
14.	9212040525	4.3	106	72	140	5	34.37	116.92
15.	9212041259	4.2	100	40	102	8	34.35	116.90
16.	9305310855 †	4.2	118	78	152	11	34.12	116.99
17.	9404061904 ‡	4.6	104	86	150	14	34.19	117.10

Banning Pass †

Arrowhead event ‡

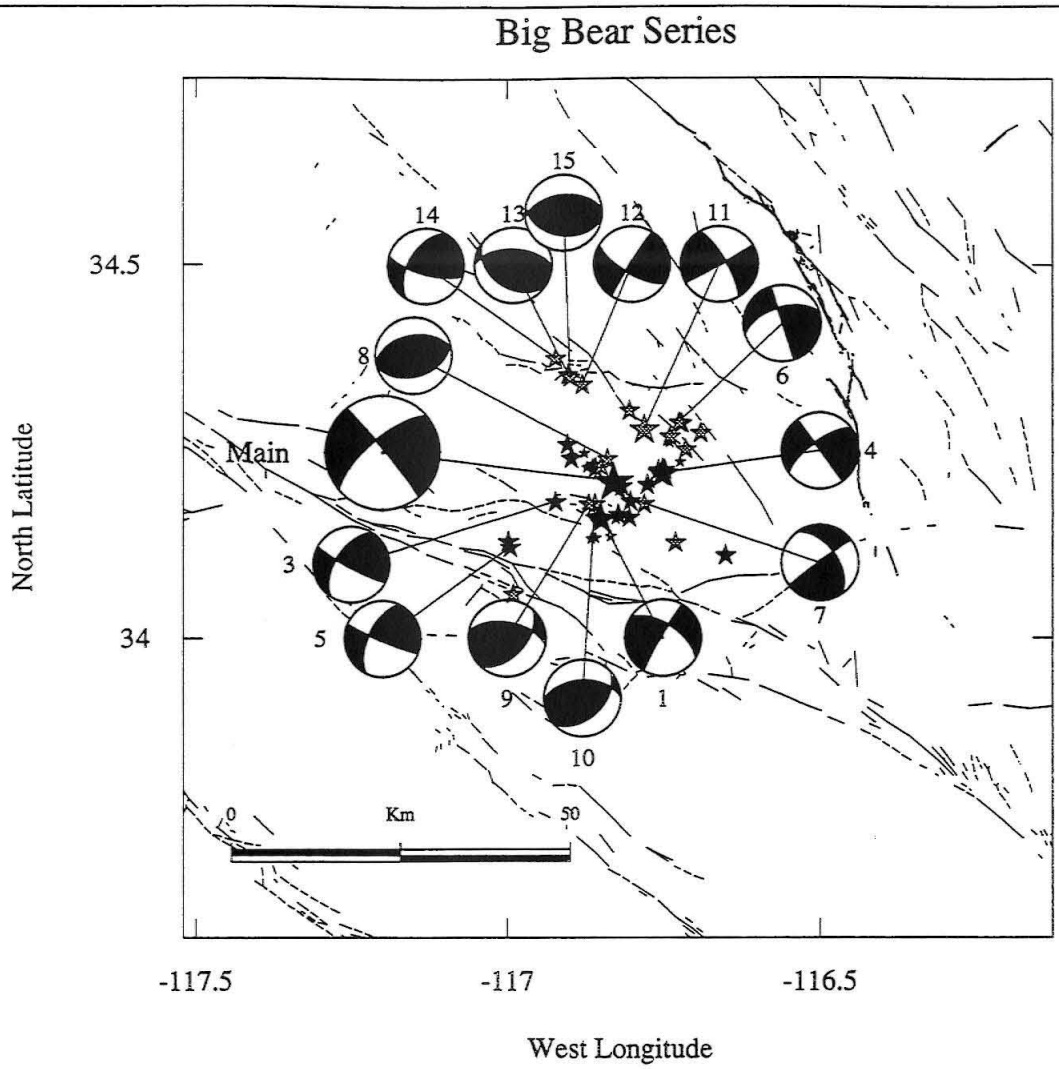

Figure 2.29: Map showing locations and focal spheres for Big Bear mainshock and aftershocks. Events are numbered and listed chronologically [Table 2.5]. The Mojave model was used for stations GSC and SVD, and the Standard Southern California model used for stations ISA, PAS, PFO. Events 16 and 17 are shown on Figure 2.31.

after the mainshock. We discuss source complexity of the Big Bear mainshock in detail and show further evidence for activity on conjugate fault–planes during the mainshock in Chapter 3.

Big Bear Aftershocks

Comprising hundreds of $M > 1.9$ aftershocks, of which we present 17 ($M > 4$), the Big Bear sequence is dominated by relatively deep (12–17 km) to intermediate (7–11 km) depth northwest–striking right–lateral and north–east striking–left lateral strike–slip events on trends parallel to both planes of the mainshock source mechanism. Primarily strike–slip earthquakes (presumably left–lateral, from their alignment) lie along or form trends parallel to the broad northeast trending swath of seismicity seen in Figure 2.29, while right–lateral (again from alignment) and thrust events tend to lie along northwest trends, and along the northern and southwestern ends of the aftershock trends. Deep events yield the highest stress-drops, even for smaller earthquakes [Figure 2.35].

Aftershocks along the North Frontal fault (Figure 2.16, Figure 2.29, Table 2.6, events 6, 11, 12, 13, 14, 15) tend to have low to moderate stress–drops, with values ranging from 20 to 112 bars, and an average value of about 55 bars. Event 12 is the largest of these events, with a magnitude of $M_w = 5.2$, and a stress–drop of 112 bars, unusually high for a shallow event in this region. North–frontal fault aftershocks also tend to be moderate to shallow in depth, while those just south of the mainshock are deep. Furthermore, events south of the mainshock, including the 14:43 GMT foreshock (Figures 2.29, 2.30, 2.31, Table 2.6, event 1, 280 bars) and near the Santa Ana thrust (Figures 2.29, 2.31, Table 2.6, events 3, 9, 10 and 17) are on average much higher stress–drop, with an average of about 200 bars. Thus there is an apparent shallowing of *larger* aftershocks from south to north within the San Bernardino mountains block, with the deep, high stress–drop earthquakes south of the Big Bear Mainshock, and shallower, moderate to low stress–drop events north of the mainshock [Figure 2.30].

Arrowhead and Banning Pass events

Following the Landers and Big Bear earthquakes, the San Gorgonio–Banning Pass region saw increased seismic activity, with clusters of earthquakes forming on or near the Mill

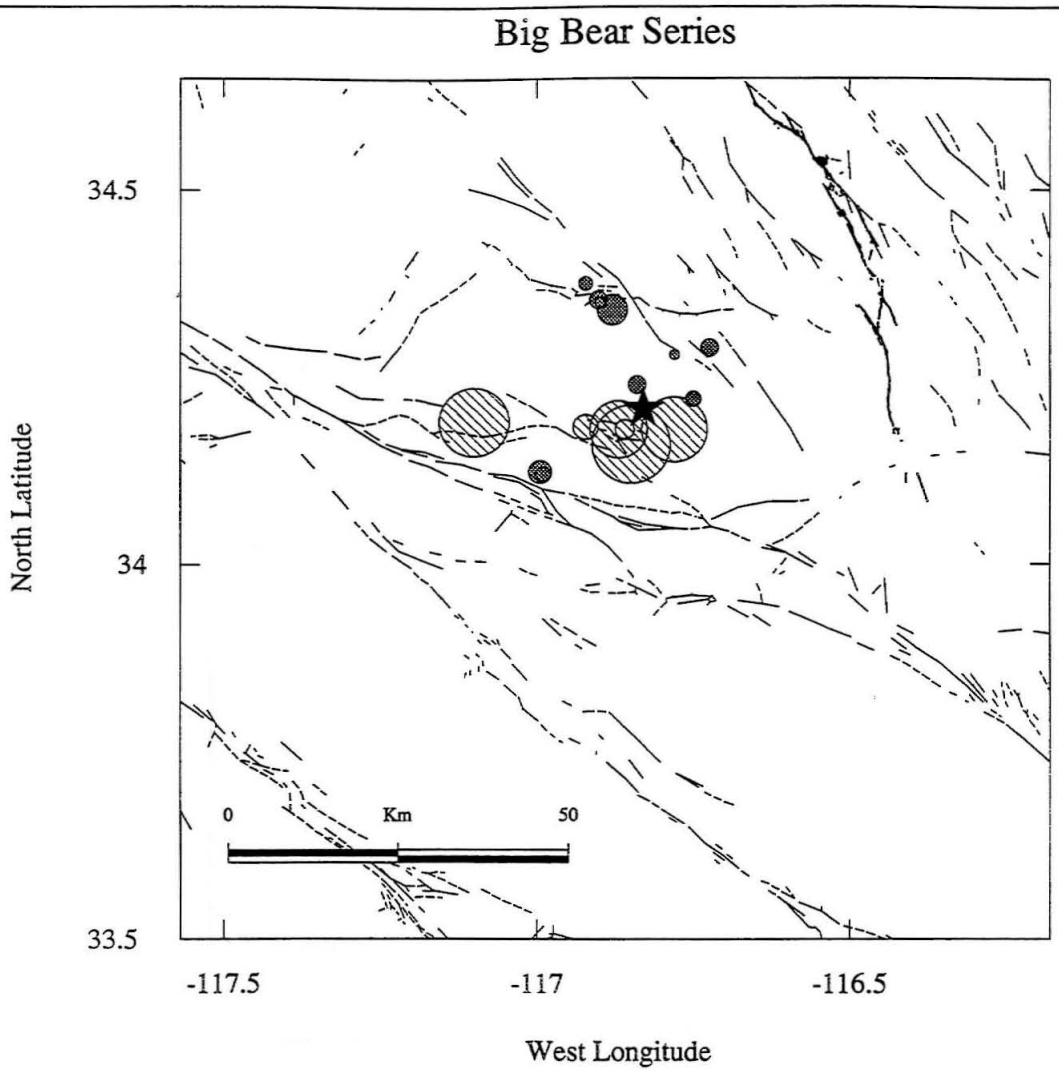

Figure 2.30: Map showing locations and stress–drops for Big Bear, Yucaipa and Arrowhead events. Stress–drops of deep events are hatched; shallow events and events of moderate depth are shown filled (grey). Stress-drop circles are scaled to a maximum of 280 bars. The Big Bear mainshock is indicated by a filled (black) star. Note the correspondence between deeper epicenters (hatched) and high stress–drop.

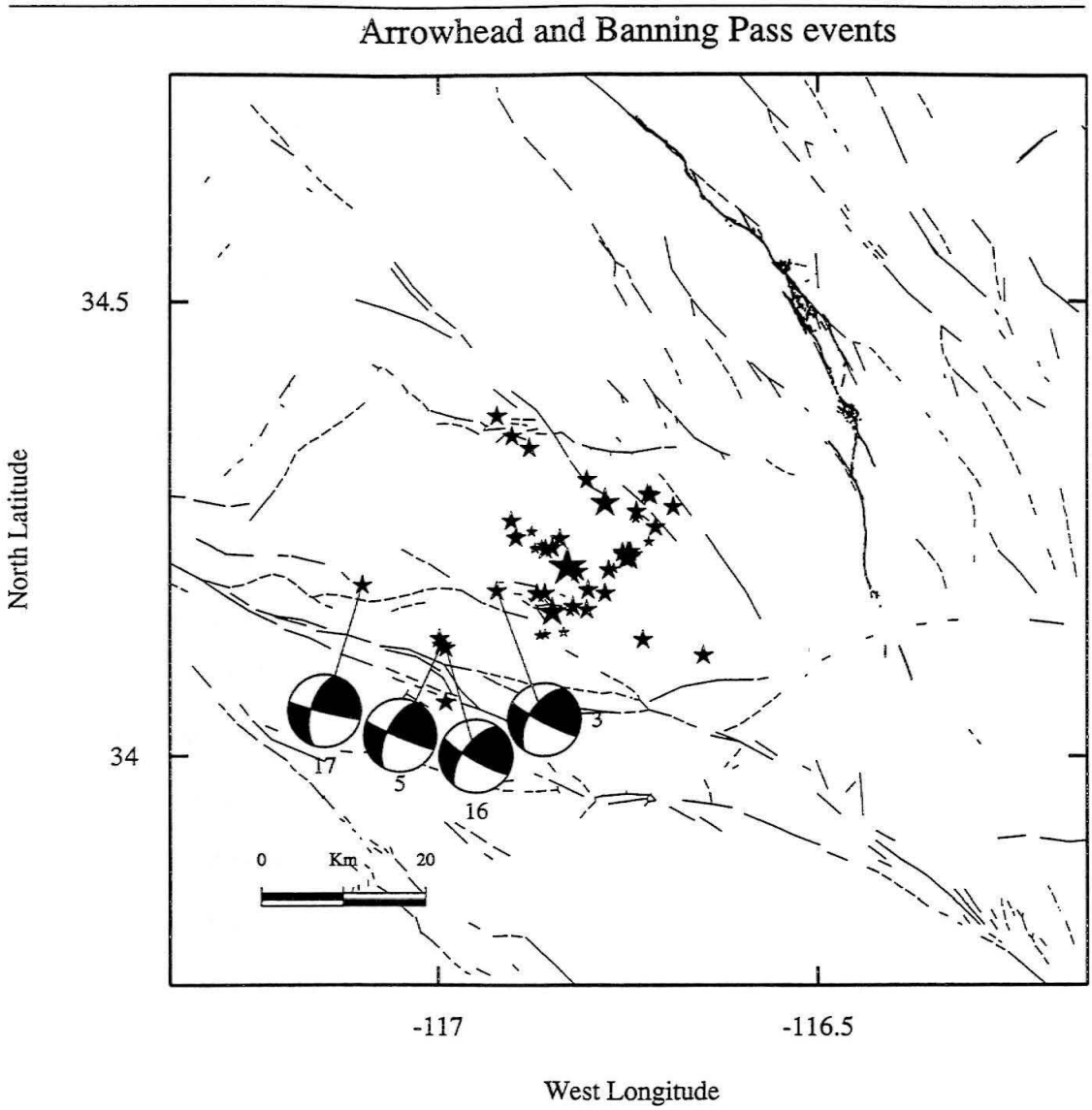

Figure 2.31: Events from the Yucaipa/Mill Creek and Arrowhead regions, listed chronologically. Source parameters appear on Table 2.6.

Creek fault [Figure 2.16]. Prior to the Big Bear mainshock, seismicity in this region occurred almost exclusively on the Mill Creek Fault; thereafter, seismicity shifted to other faults, perhaps due to static stress– changes caused by the nearby ($\sim 10km$) Big Bear mainshock [Seeber and Armbruster, 1994]. We present results for two events on the Mill Creek fault (Figure 2.31, Table 2.6, events 5 and 16) and a more recent event which occurred near the Santa Ana Thrust near Lake Arrowhead (event 17). The prior two events lie within a tight cluster (Yucaipa cluster) which began to form shortly after the Big Bear mainshock. One of the events presented (event 5) occurred within 24 hours of the mainshock, at a depth of about 7 km. It has a strike-slip source mechanism, presumably right–lateral (and parallel to the trend of the Mill Creek fault in that area), and is fairly low stress-drop, about 56 bars. The second event occurred about a year later with a deeper epicenter (h=11), but with a similar mechanism, and a stress-drop of about 32 bars. In contrast, the "Arrowhead" event (event 17) was high stress-drop (about 250 bars), and deeper, with an estimated source–depth of 14 km, though its source mechanism is similar to those of the earlier events located on the Mill-Creek fault. Broadband waveform modeling for this event (Figure 2.6.5) documents its high stress–drop nature: with a magnitude of 1.04×10^{23}, it has an average source duration of only about 0.38 s. It is of similar depth (and mechanism), however, to an event near the Santa Ana Thrust located due west of it (Figure 2.31, Table 2.6, event 3) which occurred within an hour of the mainshock and was classified as a Big Bear aftershock due to mainshock proximity. The stress drop of the latter, while high at 140 bars, is

---

Figure 2.32: Broadband waveform modeling for the $M4.6$ April 6, 1994, Arrowhead earthquake. Both the standard Southern California model (stations BAR, PAS) and Mojave model (GSC, ISA) were used in this source estimation. The moment for this solution is $M_b = 1.04 \times 10^{23}$; the time function is (0.19, 0, 0.19) s.

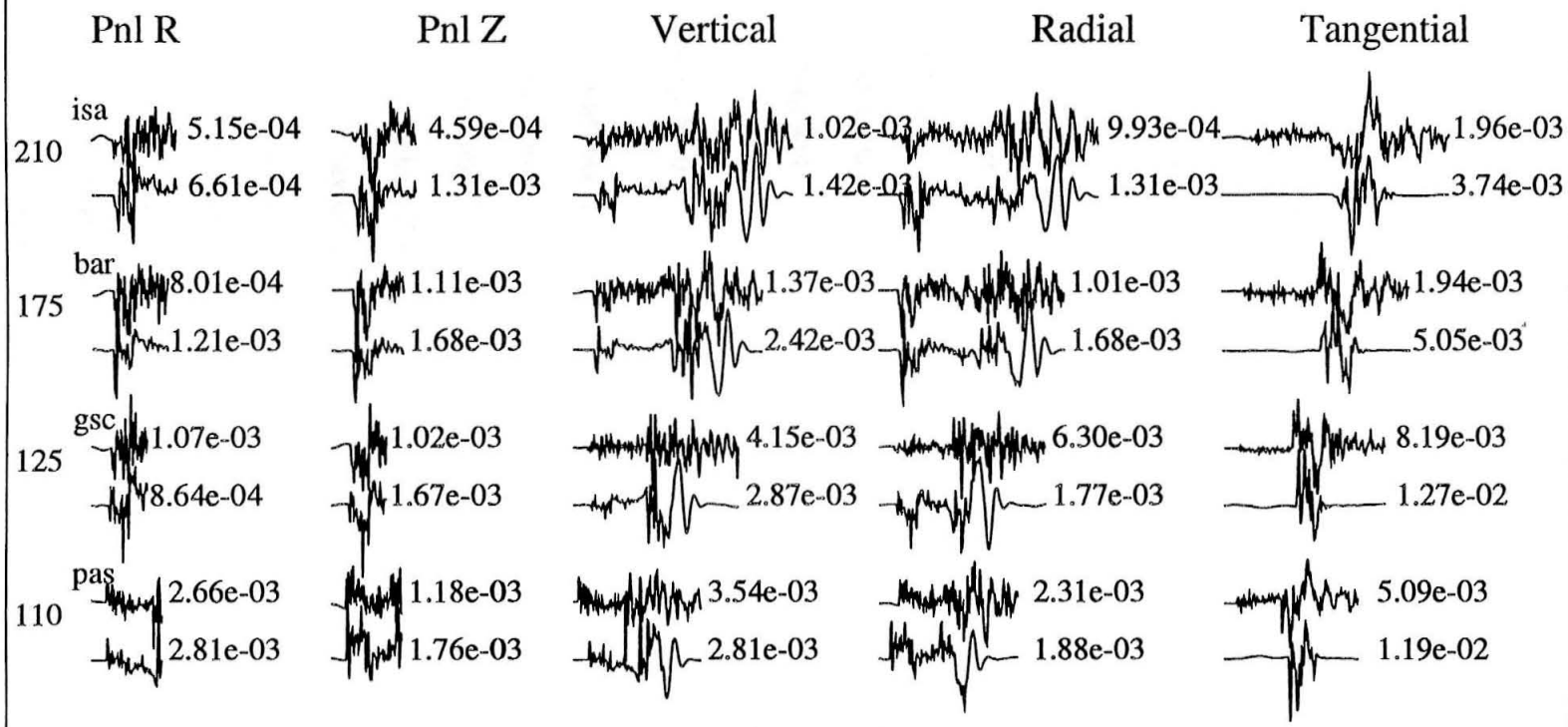

Broad Band

Event 17, Table 2.6, Arrowhead

lower than the "Arrowhead" event (event 17).

2.7 Discussion

Large aftershocks occurring up to two-and-a-half years after the onset of the Joshua Tree–Landers–Big Bear series are the most recent events to populate a long and incompletely understood episode of seismicity. Coulomb stress changes caused by four $M > 5$ earthquakes preceding the Landers mainshock (i.e., the 1975 M_L5.2 Galway Lake, 1979 M_L5.2 Homestead Valley, M_L6 North Palm Springs and M_L6.1 Joshua Tree earthquakes) progressively increased stresses at the site of the future Landers epicenter [King et al., 1994]. In turn, changes in static stresses caused by the Landers event triggered the Big Bear event within hours of the Landers mainshock, and earthquakes as far away as the western Garlock fault and Yucca Mountain in the ensuing months [Hill et al., 1993, Gomberg and Bodin, 1994].

2.7.1 Seismicity South of the Pinto Mountain Fault

The Joshua Tree mainshock and subsequent aftershocks are now viewed as preshocks to the later Landers mainshock. While the Landers mainshock apparently either recharged or "reactivated" aftershock activity in the Joshua Tree region [Hauksson, 1994], $M > 3.8$ aftershocks from the Joshua Tree and later Landers events can be viewed as distinct populations. Spatially, they occupy distinct but ajoining volumes rather than overlapping completely (Figures 2.17, 2.18, 2.20). Their mechanisms are similar, essentially strike–slip on north to northwest–striking planes, though Joshua Tree aftershocks are on average deeper [Tables 2.3, 2.4]. Stress–drops of Landers aftershocks (south of the Pinto Mountain fault) are slightly higher in general (Figure 2.33), which might suggest a "re-charging" of stress in the region south of the Pinto mountain fault. However, Landers aftershocks in the area local to the Joshua Tree epicenter (Figure 2.20, events 6, 7,

and 11) comprise a low stress–drop cluster for the region post–Landers. The presence of several $M > 4$ aftershocks in the Joshua Tree epicentral region suggests post–Landers reactivation of stresses local to the Joshua Tree epicentral area [Hauksson, 1994]; however, these $M > 4$ events are not numerous, are low in stress–drop relative to other aftershocks south of the Pinto Mountain fault, and are generally not vertical strike–slip.

Unusually high stress–drop Landers aftershocks south of the Pinto Mountain fault are located west and just south of the Burnt Mountain and Eureka Peak ruptures (Figure 2.20, events 1 and 2) and may be related to the termination of rupture there.

2.7.2 Seismicity North of the Pinto Mountain Fault

Over twenty $M > 3.8$ aftershocks occurring between June 1992 and October 1994 north of the Pinto Mountain fault were studied. These include events both along the Landers rupture and aftershocks which occurred at some distance from the fault. We here attempt to compare the spatial distribution of these moderate to large aftershocks with slip models for the Landers rupture [i.e., Wald and Heaton, 1994; Cohee and Beroza, 1994]. Serious prior attempts at this comparison have not been published, as the only source–depths commonly available are those from the SCSN catalog, and these depths are often of questionable accuracy [Ma, 1993]. In the next several sections, we

---

Figure 2.33: Moments versus durations for Joshua Tree aftershocks and Landers events both north and south of the Pinto Mountain fault. Event depths are indicated by different symbols: filled triangles indicate comparatively "deep" events (12 to 17 km); filled crosses indicate "intermediate" depth events (8 to 11 km); and filled hexagons indicate "shallow" events (2 to 7 km). Lines of constant stress drop are plotted diagonally across the figure; from top to bottom: 100, 10, and 1 bar(s). The first panel shows Landers events north the of Pinto Mountain fault, the second shows events south of the Pinto Mountain fault and the third shows Joshua Tree events.

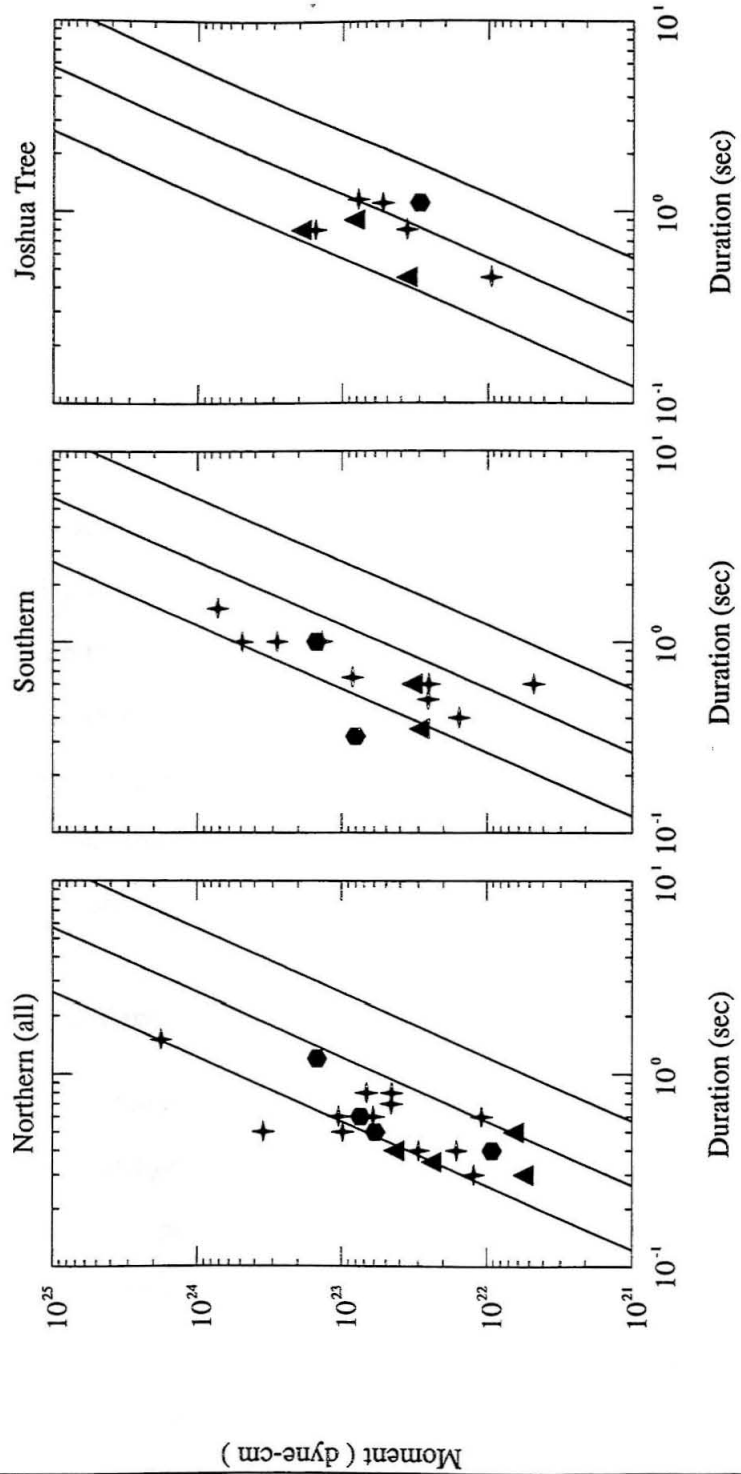
Northern (all)
Southern
Joshua Tree
Moment (dyne-cm)
Duration (sec)
Duration (sec)
Duration (sec)
10^{25}
10^{24}
10^{23}
10^{22}
10^{21}
10^{-1}
10^{0}
10^{1}

compare aftershock activity with mainshock rupture characteristics on each segment of the Landers mainshock rupture.

Johnson Valley Fault

According to Wald and Heaton [1994], the Landers mainshock initiated on the Johnson Valley fault at depth, and the first seconds of rupture involved deep slip. Rupture then continued shallowly on the Johnson Valley fault for the subsequent 4 seconds. In the first 24 hours following the Landers mainshock, the area local to the mainshock epicenter was very active; unfortunately, we were not able to obtain any records for these early events. However, the later events we studied, including a recent large $M4.7$ aftershock [Table 2.5, event 19] were both shallow and low stress–drop, suggesting that later seismicity continued shallowly, even up to two years after the mainshock, and that stresses around the mainshock area were fairly low in the hours and months following the Landers earthquake. Indeed, according to Abercrombie and Mori [1994], the mainshock itself began with a shallow, slow, low stress-drop preshock composed of two $M \sim 4-5$ subevents (stress–drops for both $\sim$ 12 bars), which triggered or grew into the $M7.3$ Landers mainshock.

Kickapoo (Landers) Fault

On reaching the junction of the Johnson Valley and Kickapoo (Landers) faults, rupture slowed and delayed [Wald and Heaton, 1994], and rupture patterns appear to be complex. The Kickapoo fault has some of the lowest surface slip distribution values of any fault (north of the Pinto Mountain fault) involved in the Landers rupture [Sieh et al., 1993]. This 5-km fault segment has a complex aftershock history as well, with an unusually large number of $M > 4$ aftershocks. Among these is an $M5.2$ aftershock (Table 2.5, Figure 2.23, event 3) which is the largest on–fault aftershock and also yields the highest stress–drop (512 bars) of all events we studied from the Landers se-

quence (omitting Garlock events). Event 3 occurred at a depth of 7-8 km, which is just below the region of maximum slip for the Kickapoo fault [Wald and Heaton, 1994; Cohee and Beroza, 1994]. This slip may have been accommodated along secondary traces as well [Sowers et al., 1994], but Wald and Heaton [1994] and Cohee [1994] resolve it onto a single plane representing the Kickapoo. Event 3 was followed by a nearly colocated event (event 9), which is much lower stress–drop (30 bars).

Focal planes for aftershocks on the Kickapoo fault are fairly heterogeneous, and distributed over an area nearly as wide as the fault segment is long. Immediately southeast of the fault a normal–faulting event (Table 2.5, Figure 2.23, event 1), occurred at a depth of about 8-9 km. A later oblique event, of moderate stress–drop (80 bars), occurred near the junction of the Kickapoo and the Homestead Valley faults (Table 2.5, Figure 2.23, event 15), suggesting compression within the restraining bend formed at the fault junction. It appears to have occurred within or on the margins of a slip minimum [Wald and Heaton, 1994] at depth ($\sim 6 - 11$ km) near the junction of the southern Homestead Valley and Kickapoo faults. The slowing in rupture across the Kickapoo fault [Wald and Heaton, 1994], the low surface slip values there, the unusual numbers of larger aftershocks on this fault segment, as well as the observed heterogeneity of aftershock mechanisms all suggest that rupture on this segment was not smooth, and that slip may have occurred across more than one fault strand, or on a discontinuous fault, possibly involving extension as well as strike–slip motion. Observations of unusually numerous and high stress–drop aftershocks along this small segment of fault support the suggestion of Sieh and Spotila [1995] that the Kickapoo (Landers) fault is a nascent and incomplete connection between the Johnson Valley and Homestead Valley fault systems.

Homestead Valley Fault

Just north of the southern Homestead Valley fault, rupture either slowed or stopped [Wald and Heaton, 1994], then resumed, and accelerated erratically across the Home-

stead Valley fault, pausing again before it jumped to the Emerson fault. Aftershocks were plentiful on the central and northern Homestead Valley fault [Cohee and Beroza, 1994], but none were large (i.e., $M > 3.9$). Between the overlapping strands of the northern Homestead Valley and southern Emerson faults, we observe one $M3.8-3.9$ normal–faulting event, whose anomalous focal mechanism may be explained by its position between two fault–strands. The northern Homestead Valley fault experienced maximum slip at depth, while maximum shallow slip occurred further north on the Emerson fault [Wald and Heaton, 1994; Cohee and Beroza, 1994]. Large aftershocks are not present at any depth, however, between the northern Homestead Valley fault and Emerson faults. They appear again in the central–northern Camp Rock fault (Figure 2.19), for which primarily shallow rupture has been inferred [Wald and Heaton, 1994]. Aftershocks 2 and 17 (Table 2.5, Figure 2.22) occurring on the northern Camp Rock fault are shallow oblique–slip events, of moderate stress–drop (46 and 80 bars, respectively).

Off–fault Activity

Areas off–fault (i.e., not associated with primary rupture during the mainshock) also saw increased seismic activity after the Landers mainshock. The Barstow aftershock cluster began within hours of Landers, and comprised a number of $M > 4$ aftershocks.

Figure 2.34: Moments versus durations for Landers events north of the Pinto Mountain fault. Event depths are indicated by different symbols: filled triangles indicate comparatively "deep" events (12 to 17 km); filled crosses indicate "intermediate" depth events (8 to 11 km); and filled hexagons indicate "shallow" events (2 to 7 km). Lines of constant stress drop are plotted diagonally across the figure; from top to bottom: 100, 10, and 1 bar(s). The first Panel shows all Landers events north of Pinto Mountain fault, the second and third show events on and off the trace of the Landers rupture, respectively.

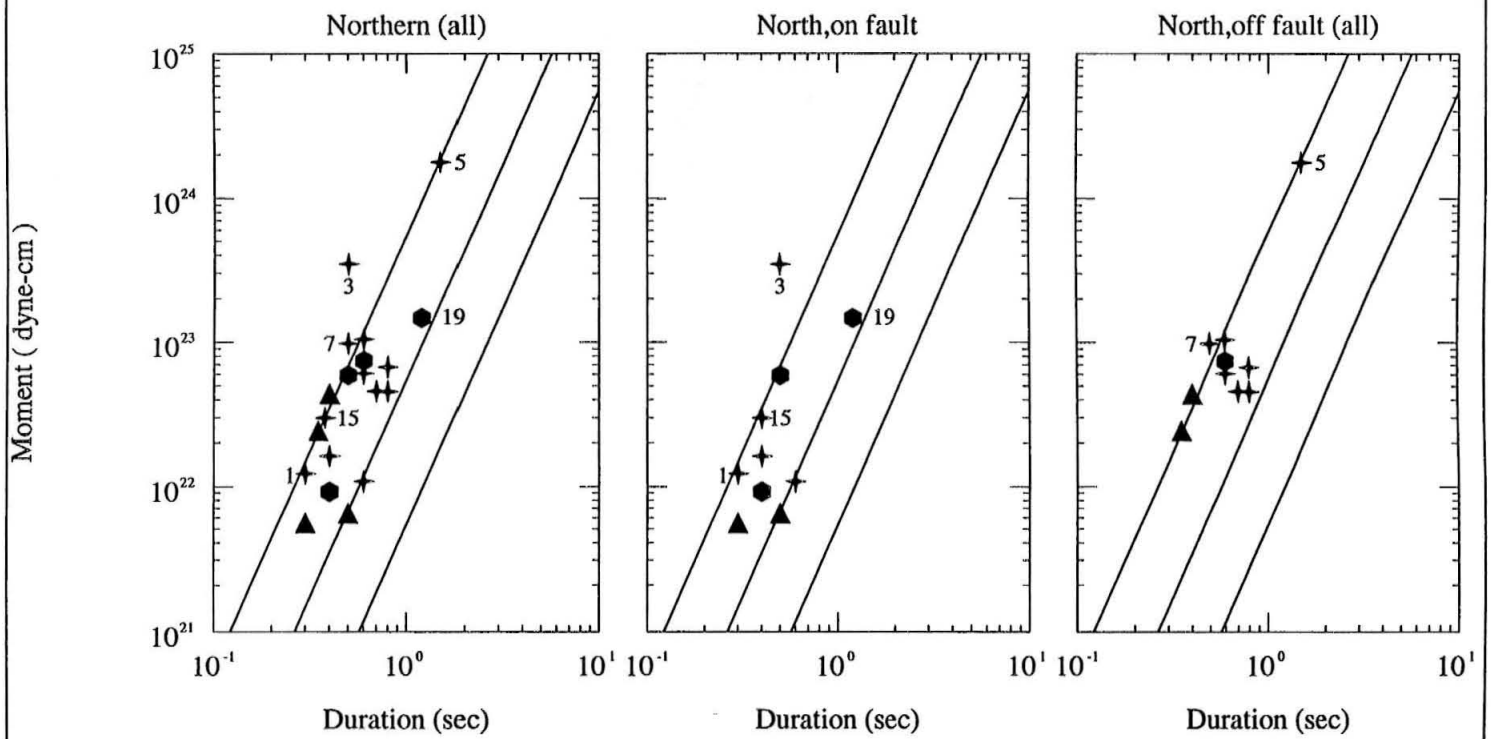
Northern (all)
North,on fault
North,off fault (all)
Moment (dyne-cm)
Duration (sec)
Duration (sec)
Duration (sec)
10^{25}
10^{24}
10^{23}
10^{22}
10^{21}
10^{-1}
10^{0}
10^{1}
1
3
5
7
15
19

Stress–drops for these events averaged about 50 bars, ranging from 16 to 89 bars. The Barstow region exhibited unusually high rates of post–seismic deformation, associated with no primary surface rupture during the mainshock [Shen et al., 1993].

Stress–drops for off–fault events on the Pisgah and Calico faults were slightly higher, with average stress–drops hovering around 125 bars. On average, aftershocks occurring off–fault generally have higher stress–drops than those occurring along the trace of the Landers rupture (Figure 2.34). The primary exception to this is event 3, described earlier as a very high stress–drop event on the Kickapoo fault.

Some Landers–related events such as the Garlock events were completely unrelated to and distant from primary Landers rupture, and given their depths, probably did not break the surface. Both of these events yield unusually high stress–drops (Figure 2.35), suggesting fairly high confining pressures at depth on the fault, as well as the potential for a large and energetic earthquake there.

2.7.3 The Big Bear Sequence

The Big Bear sequence, including the Arrowhead and Yucaipa events, appears to have occurred almost entirely within the San Bernardino Mountains block, bounded to the north by the North Frontal fault zone [Meisling and Weldon, 1989], and on the south by the Mill Creek fault zone and San Bernardino segment of the San Andreas fault zone. The Big Bear sequence was fairly heterogeneous, comprising strike–slip, oblique–slip and thrust–type events. Unlike the Landers sequence, Big Bear aftershocks are

---

Figure 2.35: Moments versus durations for Landers and Big Bear aftershocks. Symbol conventions as in Figure 2.34. Lines of constant stress drop are plotted diagonally across the figure; from top to bottom: 100, 10, and 1 bar(s). Garlock events (high stress–drop) are indicated by stars.

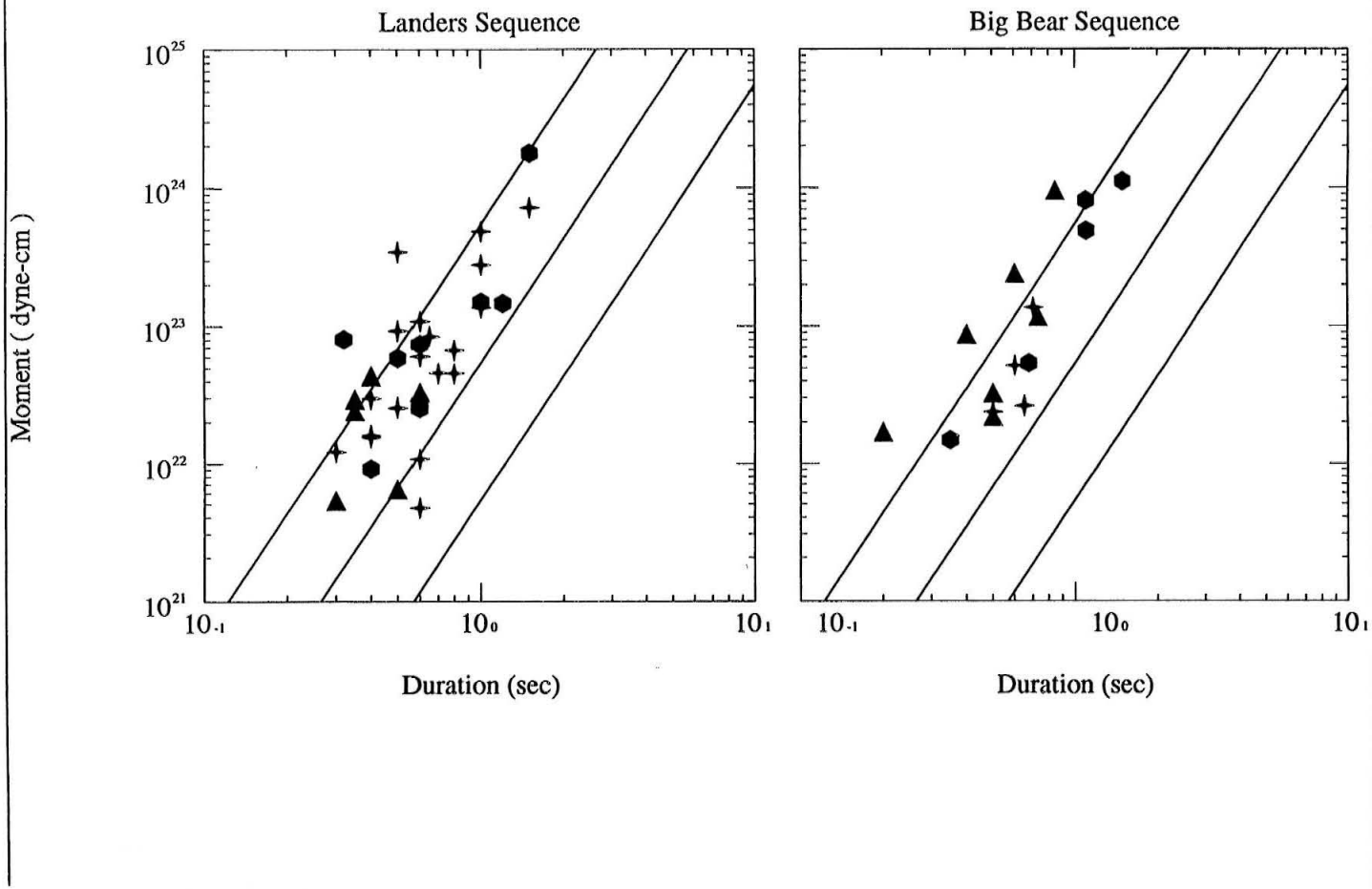
Landers Sequence
Big Bear Sequence
Moment (dyne-cm)
10^{25}
10^{24}
10^{23}
10^{22}
10^{21}
10_{-1}
10_{0}
10_{1}
Duration (sec)
Duration (sec)

primarily deep to moderate in depth. Only 4 of the 17 events studied are shallower than 7 km; 8 are 11 km or deeper. In contrast, out of the 36 Landers events studied, 6 are 11 km or deeper, and 6 are 6 km or shallower. Stress–drop distributions for both sequences also show marked differences. For Big Bear, stress–drop generally increases with depth (Figures 2.35, 2.30); while for Landers events elevated stress–drops seem to correlate with position off the Landers rupture, with the exception of aftershocks along the Kickapoo fault.

2.8 Conclusions

The Landers mainshock and related events altered the tectonic landscape and stress budget of Southern California in ways not yet fully assessed. The Landers earthquake itself involved surface rupture and displacement on six separate faults, including rupture south of the Pinto Mountain fault on the Eureka Peak fault. Aftershocks and triggered events occurred as far away as Mammoth Lakes and Yucca Flat [Hill et al., 1993], and included the complex $M6.5$ Big Bear mainshock, and several unusual earthquakes on the Garlock fault.

In this paper, we discuss modeling results for more than sixty moderately–sized ($M_w > 3.8$) earthquakes from the Joshua Tree, Landers and Big Bear sequences. These events occurred between April 1992 and October 1994, spanning the period of greatest energy release related to these sequences. This data set includes every event over $M3.8$ for which we could obtain clean, high signal–to–noise broadband TERRAscope records and reliable timing and location information. For each of these events, we estimate source parameters, including depth, moment, and source duration. As error in the estimation of moment is directly related to misfit between velocity model and observed, we develop and present a new velocity model for the Mojave region. The Mojave model is slower and has a thinner crust than the standard Southern California model

(Tables 2.1, 2.2).

For a given event, moment is computed for each station, and the results examined for systematic variations of moment with distance. Stations GSC and SVD are shown to yield higher than average moments, while stations PFO and ISA yield lower than average estimations of moment. This behavior is found to vary with increasing source–receiver distance for stations SVD and PFO: for station SVD, elevated moments drop as epicentral diatance increases, while for PFO lower than average moments increase with distance, drawing closer to the average.

Since duration and moment are routinely computed for each event we study, we infer stress-drops for these events, assuming a circular fault. Stress–drops appear to vary systematically with location, with respect to previous seismicity or rupture, and with respect to depth. Our event sample size is arguably small in number for any given region, but the events we consider are of moderate size (on average $M \sim 4.2$) thus associated with more energy release than smaller (and more numerous) events.

For the Landers sequence, stress–drops of events located at some distance from the Landers rupture are higher than those located on the faults involved in the mainshock, with the exception of aftershocks on the Kickapoo (Landers) fault. Rupture on this fault segment was complicated, and displacement may have been accommodated across a number of subsidiary or discontinuous fault traces. The fact that the Kickapoo fault had some of the lowest measured surface displacements during the Landers mainshock lends credence to this idea. Aftershocks South of the Pinto Mountain fault occurred in a region associated with high rates of post–seismic deformation, like those in the Barstow region [Shen et al., 1993]. Lower stress–drop aftershocks seem to occur in regions which previously experienced the most local moment release; i.e., near the Eureka Peak fault, and near the Joshua Tree mainshock epicenter. The Big Bear region exhibits a strong correlation between high stress–drop and deep sources, suggesting high confining stresses at depth, or local depression of the brittle–ductile transition zone.

Bibliography

Abercrombie, R. and J. Mori, Local observations of the onset of a large earthquake: 28 June 1992 Landers, California, *Bull. Seism. Soc. Am.*, **84**, No. 3, 725-234, 1994.

Astiz, L. and C. R. Allen, Seismicity of the Garlock fault, California, *Bull. Seism. Soc. Am.,73*, 1721-1734, 1983.

Cohee, B. P. and G. C. Beroza, Slip Distribution of the 1992 Landers Earthquake and Its Implications for Earthquake Source Mechanics, *Bull. Seism. Soc. Am.*, **84**, No. 3, 692–712, 1994.

Cohn, S. N., T. L. Hong and D. V. Helmberger, The Oroville earthquakes: a study of source characteristics and site effects, *J. Geophys. Res., 87*, 4585–4594, 1982.

Dreger, D. S. and D. V. Helmberger, Source parameters of the Sierra Madre earthquake from regional and local body waves, *Geophys. Res. Lett.,18*, 2015–2018, 1991.

Eshelby, J. D., The determination of the elastic field of an ellipsoidal inclusion and related problems, *Proc. Roy. Soc. London,* Series A, **241**, 376–396, 1957.

Gomberg, J. and P. Bodin, Triggering of the $M_s = 5.4$ Little Skull Mountain, Nevada, Earthquake with Dynamic Strains, *Bull. Seism. Soc. Am.*, **84**, No. 3, 844–853, 1994.

Hadley, D. and H. Kanamori, Seismic structure of the Transverse Ranges, California, *Geol. Soc. Am. Bull., 88*, 1469–1478, 1977.

Harris, R. A. and Simpson, R. W., Changes in static stress on Southern California faults after the 1992 Landers earthquake, *Nature, 360*, 251–254, 1992.

Hauksson, E., State of Stress from Focal Mechanisms Before and After the 1992 Landers Earthquake Sequence, *Bull. Seism. Soc. Am.*, **84**, No. 3, 917–934, 1994.

Hauksson, E., L. M. Jones, K. Hutton and D. Eberhart-Phillips, The 1992 Landers Earthquake Sequence: Seismological Observations, *J. Geophys. Res., 98*, 19,835–19,858, 1993.

Hill, D. P. et al., Seismicity in the eastern United States remotely triggered by the $M7.4$ Landers, California earthquake of June 28, 1992, *Science, 260*,1617-1623, 1993.

Hough, S. E., Southern Surface Rupture Associated with the $M7.3$ Landers, California, Earthquake, *Bull. Seism. Soc. Am.*, **84**, No. 3, 817-825, 1994.

Hough, S. E. and Dreger, D. S., Source Parameters of the 4/23/92 M6.1 Joshua Tree Earthquake and its Aftershocks: Empirical Green's Function Analysis of GEOS and TERRAscope Data, submitted to *Bull. Seism. Soc. Am.*, 1994.

Hough, S. E., J. Mori, E. Sembera, G. Glassmoyer, C. Mueller, and S. Lydeen, Southern surface rupture associated with the 1992 M7.4 Landers earthquake: Did it all happen during the mainshock? *Geophys. Res. Lett., 20*, 2615–2618, 1993.

Jaume, S. C. and Sykes, L. R., Changes in State of Stress on Southern San Andreas Fault Resulting from the California Earthquake Sequence of April to June, 1992, *Science, 258*, 1325–1329, 1992.

Jones, L. E. and D. V. Helmberger, Broadband modeling of aftershocks from the Landers, Big Bear and Joshua Tree events, *(abstract), Eos, Transactions, 73*, 383, 1992.

Jones, L. E., D. V. Helmberger and S. H. Hough, Rupture Process of the June 28, 1992, Big Bear Earthquake, *Geophys. Res. Lett., 20*, 1907–1910, 1993.

King, G. C. P., R. S. Stein and J. Lin, Static Stress Changes and the Triggering of Earthquakes, *Bull. Seism. Soc. Am.*, **84**, No. 3, 935–953, 1994.

Ma, Kuo-Fong, Broadband waveform observations of local earthquakes, *Ph.D. Thesis*, California Institute of Technology, Pasadena, 1993.

McGill, S. F. and K. Sieh, Surficial Offsets on the Central and Eastern Garlock Fault Associated With Prehistoric Earthquakes, *J. Geophys. Res., 96*, 21,597–21,621, 1991.

Mori, J., Rupture directivity and slip distribution of the M4.3 foreshock to the 1992 Joshua Tree earthquake, in press, *Bull. Seism. Soc. Am.*, 1994.

Rymer, M., The 1992 Joshua Tree, California, Earthquake: tectonic setting and triggered slip, (abstract) *EOS: Trans. Am. Geophys. U.*, 73, 363, 1992.

Seeber, L. and J. G. Armbruster, The San Andreas Fault system throught the Transverse Ranges as illuminated by earthquakes, *J. Geophys. Res.*, in press, 1995.

Shen, Z–K, D. D. Jackson, Y–J Feng, M. Cline, and M. Kim, Postseismic Deformation following the Landers Earthquake, California, June 28, 1992, *Bull. Seism. Soc. Am.*, **84**, No. 3, 780–791, 1994.

Sieh, K. and 19 others, Near–field investigations of the Landers earthquake sequence, April to July, 1992, *Science*, 260, 171-176, 1993.

Song, X., L. E. Jones and D. V. Helmberger, Source characteristics of the January 17, 1994, Northridge, California, earthquake from regional broadband modeling, submitted to *Bull. Seism. Soc. Am.*, 1994.

Sowers, J. M., J. R. Unruh, W. R. Lettis, and T. D. Rubin, Relationship of the Kickapoo fault to the Johnson Valley and Homestead Valley faults, San Bernardino County, California, *Bull. Seism. Soc. Am.*, **84**, No. 3, 528–536, 1994.

Spotila, J. A., and K. Sieh, Geologic investigations of a "slip gap" in the surficial ruptures of the 1992 Landers earthquake, southern California, *J. Geophys. Res., 100*, 543–559, 1995.

Stead, R., Finite Differences and a Coupled Analytic Technique with Applications to Explosions and Earthquakes, *Ph.D. Thesis*, California Institute of Technology, Pasadena, California, 1990.

Stein, R. S., G. C. P. King, and J. Lin, Change in failure stress on the Southern San Andreas fault system caused by the 1992 Magnitude=7.4 Landers earthquake, *Science, 258*, 1328–1332, 1992.

Toppozada, T., D. L. Parke, C. T. Higgins, Seismicity of California, 1900–1931, *Calif. Div. of Mines and Geol. Special Report 135,* 1978.

Wald, D. J., and T. H. Heaton, Spatial and Temporal Distribtion of Slip for the 1992 Landers, California, Earthquake, *Bull. Seism. Soc. Am.*, **84**, No. 3, 668–691, 1994.

Zhao L-S. and D. V. Helmberger, Source Estimation from Broadband Regional Seismograms, *Bull. Seism. Soc. Am.*, **84**, No. 3, 91-104, 1994.

Chapter 3

Analysis of Broadband Records From the Big Bear Mainshock

> It is now that the temptation is strongest to leave these regions. We have seen enough; let's go. Why burn our hands any more than we have to? But two years have passed; the price of gold has risen. I return to the same buried alluvial beds and pick through the strata again.
>
> Annie Dillard, *Teaching a Stone to Talk*

3.1 Abstract

The June 28, 1992 Big Bear earthquake occurred at 15:05:21 GMT and is considered to be an aftershock of the earlier $M_w = 7.3$ Landers earthquake. From overall aftershock locations and long–period focal studies, rupture is generally assumed to have propagated northeast. No surface rupture was found, however, and the mainshock locations determined from both strong motion and TERRAscope data are mutually consistent and do not lie on the assumed fault plane. Further, directivity analysis of records from the TERRAscope array suggests significant short– and long–period energy propagating northwest along the presumed antithetic fault–plane. This observation is supported by

significant early aftershocks distributed along both the presumed rupture plane and the antithetic plane to the northwest. An empirical Green's function (eGf) approach using both the M_w = 5.2, June 28, 1992, 14:43 GMT foreshock and the M_w = 5.0 August 17, 1992, aftershock produces consistent results and suggests that the Big Bear event comprised at least two substantial subevents. From the eGf results, we infer that the second, and possibly a third subevent occurred on the presumed (northeast striking) mainshock rupture surface, but that significant moment release occurred on the antithetic northwest striking surface. We present results from line–source fault modeling of broadband displacement recordings of the Big Bear mainshock which indicate that a two fault event is necessary to produce the waveforms observed during the Big Bear mainshock. The limitations imposed by the mainshock location and directivity analysis require that the initial rupture be towards the northwest, striking 320°. This was followed approximately 4 seconds later by unilateral or perhaps bilateral rupture along a northeast–southwest fault striking 50° east of north.

3.2 Introduction

The M_w = 7.3 Landers earthquake of 11:58 GMT, June 28, 1992, was followed by tens of thousands of aftershocks [Kanamori et al., 1992; Hauksson et al., 1993; Sieh et al., 1993]. The largest of these was the Big Bear earthquake that occurred three hours later and was associated with significant damage in Big Bear City. This event was assigned a M_w of 6.2 based on preliminary surface wave modeling (H. K. Thio, personal comm., 1992). In this paper we obtain a total M_w of 6.4–6.5 distributed over two distinct fault ruptures.

The Big Bear earthquake was considered an aftershock of the Landers earthquake because it occurred within one fault length of the mainshock [Sieh et al., 1993], yet it occurred on a separate and previously unmapped fault. Although eclipsed by the larger

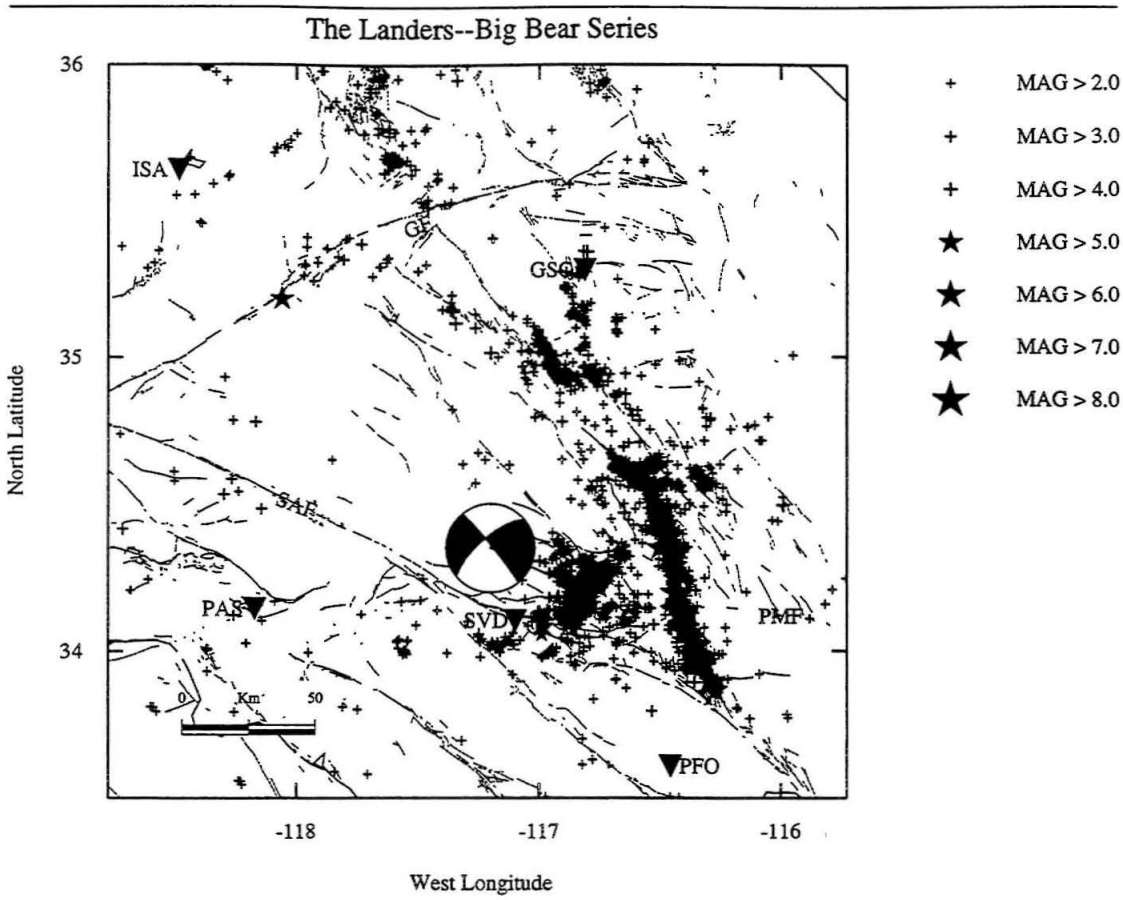

Figure 3.1: Map showing overall Landers and Big Bear seismicity. Broadband TERRAscope stations are indicated by triangles. Faults are indicated as follows: SAF (San Andreas Fault), GF (Garlock fault) and PMF (Pinto Mountain Fault).

Landers mainshock, the Big Bear earthquake was a significant event in its own right. In addition to the considerable damage caused by the event, the lack of observed surface rupture makes the rupture process of this event more enigmatic. The Big Bear earthquake is associated with its own fore– and aftershock sequences, including several earthquakes in the $M4-5$ range. Hereafter we refer to the Big Bear event as a 'mainshock'. The Big Bear event was recorded on–scale by the low–gain channels at 5 stations of the TERRAscope array (Figure 3.1).

We obtain a focal mechanism for the Big Bear mainshock using the grid–search

method of Zhao and Helmberger [1993] and broadband data convolved with a long–period Press-Ewing (LP3090) instrument response; it is shown on the location map (Figure 3.1), which also shows the patterns of seismicity that developed during the Landers–Big Bear sequence. The mainshock focal mechanism and depth (Table 3.1) agree with those obtained using long-period regional and teleseismic surface waves [Thio, personal comm., 1992]. No surface rupture was observed for this event, but aftershocks generally delineate the extent of an earthquake rupture, and in this case they appear to line up primarily along the NE-striking nodal plane.

The Southern California Seismic Network (SCSN) location of the Big Bear event was presumed to be unreliable because of a $M_b = 4$ foreshock that occurred 40 seconds before the mainshock [Hauksson et al., 1993]; however, the foreshock was too small to yield appreciable amplitudes on the strong–motion recordings. The network location estimated from strong motion data of 34^o $12.36'N$, 116^o $50.11'W$ yields a low RMS residual of 0.15 sec and appears to be well resolved [L. Wald, personal comm., 1992]. This location is consistent with the location obtained from TERRAscope data: 34^o $12.6'N$, 116^o $50.4'W$. Both locations are significantly distinct from the immediate foreshock location, 34^o $9.94'N$, 116^o $49.38'W$, which lies roughly 5.5 km to the southeast of the mainshock. The Big Bear earthquake was recorded by strong motion stations operated by the SCSN, and by six broadband TERRAscope stations. In this paper, we analyze data from five TERRAscope stations (GSC, ISA, PAS, PFO, SVD, see Figure 3.1) to investigate the Big Bear fore-, main, and aftershock sequence, and to place limits on the rupture characteristics of the Big Bear mainshock.

3.3 The Big Bear Mainshock

To guide our subsequent more detailed investigations, we first obtain average source parameters, including source depth, for the Big Bear mainshock using a grid–search source

Table 3.1: Big Bear Events

No.	Date	M_w	strike	dip	rake	Location		
						Depth	Latitude	Longitude
						km	°N	°W
1.	9206281443	5.2	210	86	330	14	34.16	116.85
2.	Mainshock	6.5	320	86	200	11–14	34.21	116.83
3.	9206281701	4.8	118	83	145	14	34.18	116.92
4.	9206281748	4.3	324	90	200	8	34.22	116.75
5.	9206291441 †	4.4	113	85	150	7	34.12	116.99
6.	9207012053	4.0	343	90	214	6	34.29	116.72
7.	9207030415	3.9	230	80	150	16	34.18	116.78
8.	9207090143	5.3	246	46	102	2	34.24	116.84
9.	9208172041	4.8	285	65	150	15	34.18	116.87
10.	9208180946	4.0	268	52	118	11	34.18	116.88
11.	9208241351	4.0	330	75	178	8	34.28	116.78
12.	9211271600	5.2	118	70	176	5	34.34	116.88
13.	9212040208	5.1	126	43	117	7	34.35	116.90
14.	9212040525	4.3	106	72	140	5	34.37	116.92
15.	9212041259	4.2	100	40	102	8	34.35	116.90
16.	9305310855 †	4.2	118	78	152	11	34.12	116.99
17.	9404061904 ‡	4.6	104	86	150	14	34.19	117.10

Banning Pass †

Arrowhead event ‡

estimation algorithm developed by Zhao and Helmberger [1994]. This algorithm selects the source mechanism which minimizes the L1 and L2 norms between the data and synthetics, using P_{nl} waveforms plus whole waveforms (ideally) for all three components to reduce the effects of data–model misfit and produce a stable solution from a relatively sparse data set. In this case, however, the broadband P_{nl} waveforms were too complex to be usable; attempts to estimate the depth of rupture initiation using depth phases in the P_{nl} waveforms were not successful. An "average" depth was therefore obtained, based primarily on surface wave to P_{nl} amplitude ratios, using whole waveforms from TERRAscope stations Goldstone (GSC), Isabella (ISA), Pasadena (PAS) and Pinon Flats (PFO). (Seven Oaks Dam (SVD) was too proximate to the source to use in this source estimation scheme.)

We cycled through source depths (5, 8, 11, 14, and 17 km) to obtain an average depth for the event (Figure 3.3). Source parameters for the five depths are consistent within ten degrees (Table 3.2), and depths of 11 and 17 km provide minimum error solutions for the broadband waveforms, followed closely by a depth of 14 km. Note that for every station, the modeled duration of the tangential component underpredicts that of the data, and that several peaks observed on the mainshock data for this component are not (and could not be) matched at stations GSC and PAS. Similar mismatches are observed for the radial and vertical components. Ratios of P_{nl} to surface wave amplitude clearly require a source depth of at least 11 km. For broadband data convolved with a LP3090 instrument, a depth of 17 km produces the lowest error solution.

Figure 3.2: Point–source modeling results for the Big Bear mainshock for source–depths of 8, 11, 14, and 17 km. The source orientations (listed by depth in Table 3.2) are determined using a grid-search algorithm developed by Zhao and Helmberger [1994]. The best–fit source–time function (assuming one source) is a 1.0 second triangle, though records at PFO clearly require a longer time function. Synthetics for the source estimation are computed using the reflectivity method and the Standard Southern California model [Hadley and Kanamori, 1978].

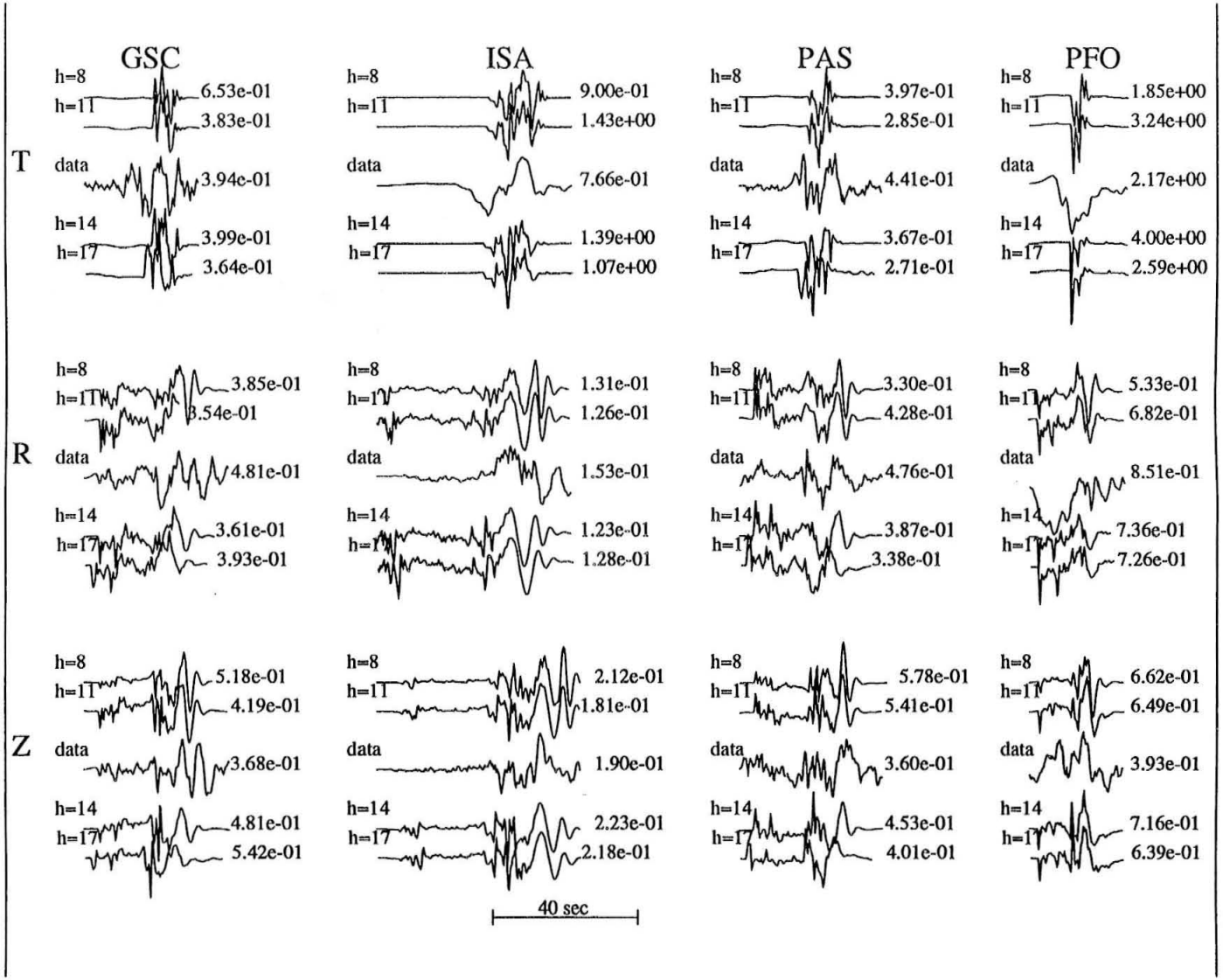
GSC
ISA
PAS
PFO
T
R
Z
h=8
h=11
data
h=14
h=17
6.53e-01
3.83e-01
3.94e-01
3.99e-01
3.64e-01
9.00e-01
1.43e+00
7.66e-01
1.39e+00
1.07e+00
3.97e-01
2.85e-01
4.41e-01
3.67e-01
2.71e-01
1.85e+00
3.24e+00
2.17e+00
4.00e+00
2.59e+00
3.85e-01
3.54e-01
4.81e-01
3.61e-01
3.93e-01
1.31e-01
1.26e-01
1.53e-01
1.23e-01
1.28e-01
3.30e-01
4.28e-01
4.76e-01
3.87e-01
3.38e-01
5.33e-01
6.82e-01
8.51e-01
7.36e-01
7.26e-01
5.18e-01
4.19e-01
3.68e-01
4.81e-01
5.42e-01
2.12e-01
1.81e-01
1.90e-01
2.23e-01
2.18e-01
5.78e-01
5.41e-01
3.60e-01
4.53e-01
4.01e-01
6.62e-01
6.49e-01
3.93e-01
7.16e-01
6.39e-01
40 sec

Table 3.2: Point Source Results

Source	depth km	Moment dyne-cm	strike	dip	rake
This study	5	7.5×10^{24}	223	62	353
This study	8	1.4×10^{25}	216	71	347
This study	11	2.1×10^{25}	220	85	348
This study	14	1.9×10^{25}	216	82	344
This study	17	2.1×10^{25}	217	88	337
Thio, 1992	13	2.8×10^{25}	217	86	343

The source–time function was fixed by cycling through simple triangles (0.4 to 4 seconds duration) and selecting the one which minimized error, in this case, a 1.0 second triangle, though records at PFO clearly require a longer time-function. A solution using records from PFO alone produced a source–mechanism consistent with the four–station solution (Table 3.2) but required a 3.5 second triangle, suggesting rupture directivity away from station PFO. Given the modeled source-duration of about one second, and a moment (averaged for depths of 11 and 14 km, see Table 3.2) of 2.0×10^{25} dyne-cm, we estimate a stress–drop of about 3.62 Kbars assuming a circular fault model. Not only is the moment obtained assuming a single source too low, but the stress-drop under this assumption is unreasonably high. This result, and the complexity of the recorded waveforms, suggest that the mainshock may be composed of separate smaller subevents, initiating several seconds after each other.

3.4 The Big Bear Sequence

Three significant ($M > 4$) foreshocks to the Big Bear mainshock and more than 550 aftershocks ($M > 1.9$) were recorded between June 28, 1992, and December 31, 1992. The Big Bear sequence appears to have occurred entirely within the San Bernardino Mountains block, which is bounded on the north by the North Frontal fault zone [Meisling and Weldon, 1989], and on the south by the Mill Creek fault and the San Bernardino segment of the San Andreas fault [Matti et al., 1992]. Seismicity appears to shallow to the north and to the south, suggesting that these bounding faults may define a spatial boundary for the deformation associated with the Big Bear sequence [Hauksson, 1993].

We determine fault–plane solutions for twelve significant ($M_w > 4$) aftershocks, plus the 14:43 GMT $M_w = 5.3$ foreshock and the mainshock using a grid–search algorithm developed by Zhao and Helmberger [1994]. The selection of earthquakes examined includes every event above magnitude 3.9 for which coherent, high signal–to–noise TERRAscope data are available (Figure 3.3, Table 3.1). The sequence is dominated by relatively deep (12–17 km) to intermediate (7–11 km) depth northwest–striking right–lateral and northeast striking left–lateral strike–slip events on trends parallel to both planes of the mainshock source mechanism. We infer that the left–lateral earthquakes lie along or form trends parallel to the broad northeast–trending swath of seismicity seen in Figure 3.1, while right–lateral and thrust events tend to lie along northwest trends, and along the northern and southwestern ends of the aftershock trends. Two shallow thrust events occurred (December 4, 1992) along the frontal fault which bounds the northern extent of the aftershock sequence, and two oblique–slip to thrust events (August 17 and 18, 1992) were recorded at the southwestern ends of the aftershock trends. Focussing on aftershocks which occurred within the first 24 hours of the Big Bear mainshock (Figure 3.4), an upside–down "T"-shaped pattern is evident, with events both along the presumed NE–striking rupture plane and the NW–striking antithetic plane.

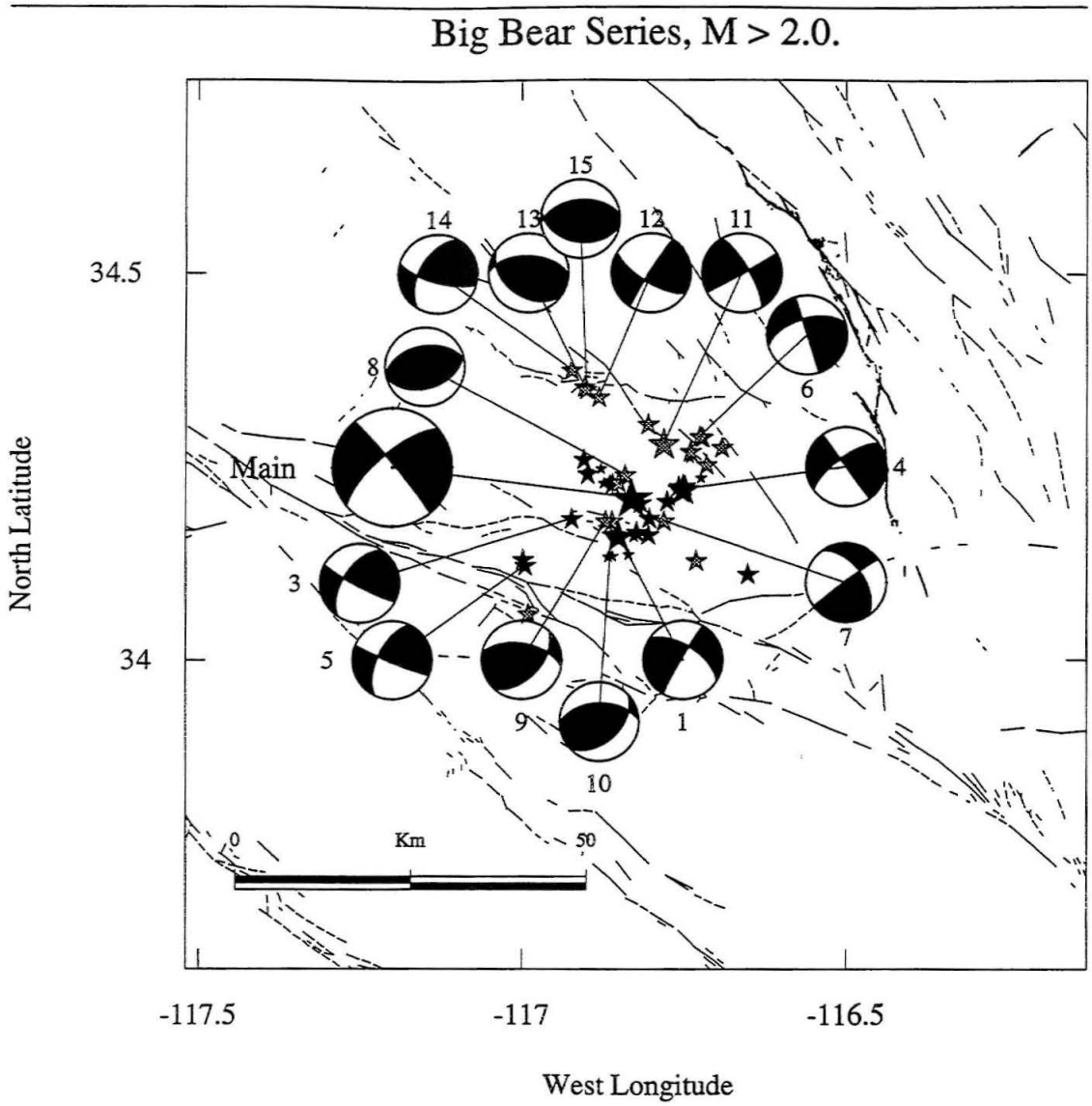

Figure 3.3: Map showing the location of the Big Bear earthquake (large star) and the location of other $M > 1.9$ aftershocks in the sequence, through December 31, 1992 (smaller stars). Filled symbols indicate fore– and aftershocks occurring within the first day of the mainshock; open symbols indicate later events. Events with focal spheres are numbered in the order of occurrence, and listed in the same order on Table 3.1. The focal mechanisms are determined by a grid-search method [Zhao and Helmberger, 1994]. Landers rupture is shown with heavy line.

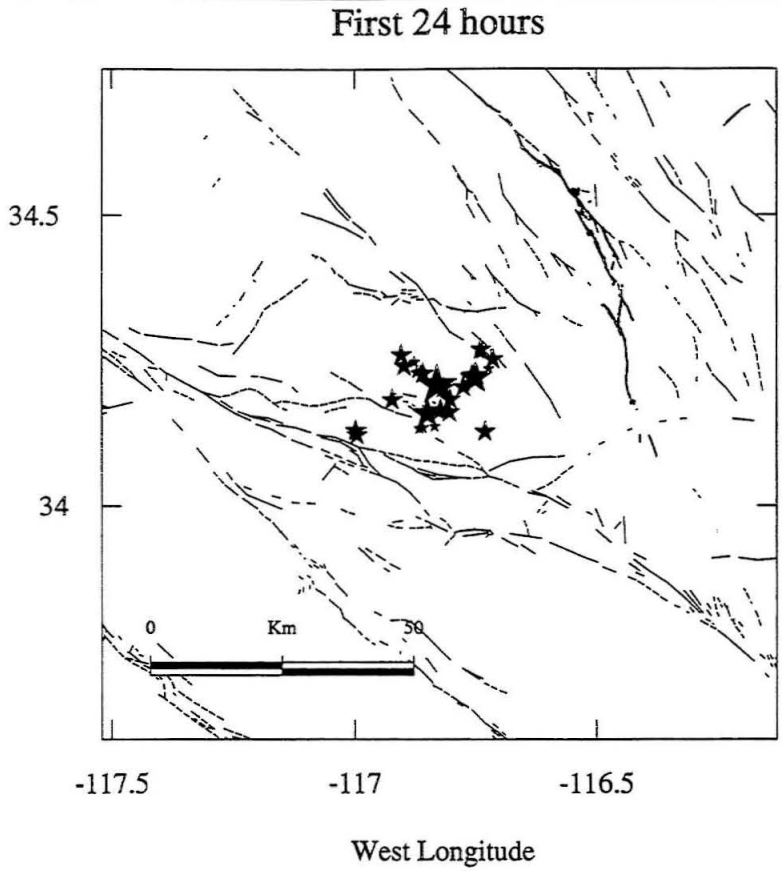

Figure 3.4: First 24 hours of post-Big Bear mainshock seismicity in the Big Bear region. Mainshock is shown as large star.

3.5 Analysis

3.5.1 Directivity Analysis

The location of the Big Bear mainshock hypocenter north and west of the observed long-term NE–trending aftershock trend, yet parallel to northwest-trending short-term aftershock activity [Figures 3.3, 3.4], suggests initial rupture to the northwest. To investigate rupture directivity, we compare the short– and long–period amplitudes of the Big Bear event with amplitudes of smaller events in the sequence. As discussed by Helmberger et al., [1992], this type of comparison can be used to indicate the rupture direction.

Analogous to the empirical Green's function method, this amplitude analysis isolates source properties of the mainshock by assuming path effects and (in this case) radiation pattern are similar between the mainshock and the nearby smaller event.

Method

For this study we have used the June 28, 1992, 14:43 GMT foreshock, the June 28, 1992, 17:48 GMT aftershock, the August 17, 1992, $M4.8$ aftershock, and the August 24, 1992, aftershock as 'master' or reference events. Again, because ISA and PFO are nodal or near nodal for P energy and are at SH maxima, we examine the tangential components of displacement for these stations. Similarly, since PAS and GSC are at or near SH minima, we examine their vertical components of motion. The broadband displacement records (integrated from acceleration in the case of the mainshock, and

---

Figure 3.5: a, Short–period Wood–Anderson amplitude ratios for the tangential component of displacement, Big Bear mainshock. *b*, Short–period Wood–Anderson amplitude ratios for the vertical, components of displacement, Big Bear mainshock. *c*, Short–period Wood–Anderson amplitude ratios for the tangential component of displacement, 14:43 GMT foreshock.

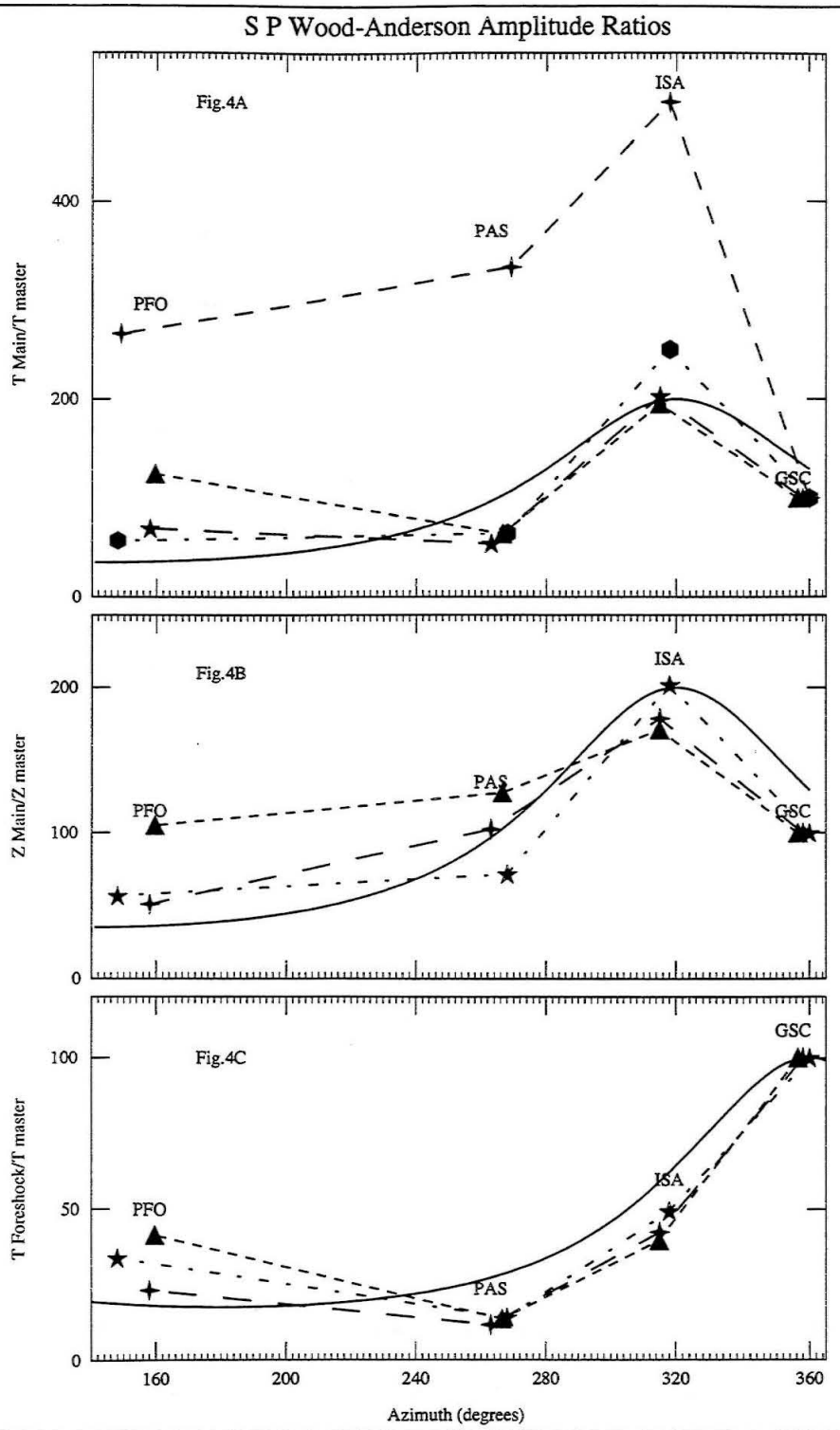
S P Wood-Anderson Amplitude Ratios
Fig.4A
ISA
PAS
PFO
GSC
T Main/T master
400
200
0
Fig.4B
ISA
PAS
PFO
GSC
Z Main/Z master
200
100
0
Fig.4C
GSC
ISA
PFO
PAS
T Foreshock/T master
100
50
0
160
200
240
280
320
360
Azimuth (degrees)

from velocity in the case of the 'master' events) have been convolved with a short–period Wood–Anderson instrument response, which has a peak response at a dominant frequency of about 1 Hz. Amplitudes of the mainshock tangential components for the stations PFO, PAS, ISA and GSC are then divided by the peak short–period amplitudes of the "master" events, and normalized so that station GSC has an amplitude ratio of 100. The ratios of the peak short–period amplitudes for the tangential component (all four stations) are shown plotted against station–event azimuth in Figure 3.5.1, Panel *a*. The average station–event azimuth is indicated above the top curve (see station names).

It is immediately evident that short–period amplitudes are highest in the direction of ISA, and taper off to minima about 180 degrees azimuth from ISA, i.e., in the approximate direction of PFO. The solid thick curve represents a simple theoretical computation for the doppler–shift effects on amplitude, assuming rupture toward station ISA and a rupture velocity of 0.7 times the assumed crustal shear wave velocity (3.0 km/s)[Aki and Richards, 1980]. The same comparison for the vertical components is shown in Figure 3.5.1, Panel *b*. Again, the amplitude ratios at ISA are consistently higher, and the ratios at stations PAS and GSC behave more as we might expect them to from the theoretical computation (unbroken line). Similar short–period analysis was performed for the June 28, 1992, 14:43 foreshock, using the June 28, 1992, 17:48 aftershock, the August 17, 1992, aftershock and the August 24, 1992, aftershock as 'master events' (Figure 3.5.1, Panel *c*). Here, the solid curve respresents a theoretical doppler–shift computation assuming propagation towards station GSC. In this case, it is evident that energy release was primarily to the north, in the direction of station GSC.

Long–period directivity studies were also performed, in which the broadband records were convolved with an LP3090 instrument response, which has a peak response at about 30 seconds, and the amplitude ratios examined as described above. In this case, the curves flattened out at the lower frequencies, retaining only amplitude affects from small

radiation pattern differences (between mainshock and master event) at nodal stations.

3.5.2 Empirical Green's Function Analysis

To investigate the apparent complexity of the mainshock, particularly the possibility that it is composed of distinct subevents, we first apply an empirical Green's function (eGf) method. Numerous studies have demonstrated that the eGf method, whereby complex path effects are deconvolved from an earthquake recording using a nearby smaller earthquake, can provide accurate estimates of source parameters under certain circumstances [Bakun and Bufe, 1975; Mori and Hartzell, 1990; Ammon et al., 1992]. Empirical Green's functions can be used either with inverse methods to deconvolve source properties (e.g., Mueller, 1985; Mori and Hartzell, 1990), or in forward modeling efforts to 'construct' a large earthquake from one or more smaller events [e.g., Wennerberg, 1993]. Ideally, an eGf should be at the same location and have the same source mechanism as the event that is being investigated to insure that both events have similar source and propagation characteristics. However, with longer period data, the method has been applied successfully using eGf–mainshock pairs that are separated by as much as a few km [Ammon et al., 1992].

Choice of an Appropriate eGf

Applying an eGf method to the Big Bear earthquake is complicated by the fact that no well–recorded Big Bear aftershock is an ideal empirical Green's function. Furthermore, if the mainshock consisted of two separate subevents at different depths, no single ideal eGf could exist. The foreshock is approximately 7 km southwest of the mainshock, but has a similar depth of 14 km (from grid-search solution), a similar mechanism and waveforms (Figure 3.3 and Table 3.1). Likewise, two aftershocks have similar mechanisms, and locations within 6 to 9 km of the mainshock (roughly 8.8 km east and 6 km southwest of the mainshock and at depths of 8 and 15 km, respectively). For the Big Bear event,

we select as eGfs the $M4.8$ aftershock which occurred at 20:41 GMT on August 17, 1992, and the $M5.2$ foreshock which occurred at 14:43 GMT on June 28, 1992.

Method

Empirical Green's function deconvolutions for source–time functions are unstable for myriad reasons [Mori and Hartzell, 1990]. The deconvolution procedure involves computation of a spectral ratio and then an inverse Fourier transform to the time domain. The computational uncertainties associated with these procedures are well–documented in other studies. In this study, we adopt a forward modeling approach whereby recordings of the eGf are convolved with source time functions that contain one or more pulses. We prefer this approach for the Big Bear earthquake because it allows a direct investigation of the number of subevents *required* to fit the data (deconvolutions are often plagued by side–lobes that can be difficult to interpret). Fundamentally, however, the two methods are conceptually consistent; they differ only in the choice of how to deal with computational uncertainty. The pulses used for convolution with the empirical Green's functions are computed using a simple exponential function designed to scale the frequency content of the source and insure that the low frequency energy of the eGf is scaled up to higher magnitudes. This is conceptually analogous to the frequency-domain method presented by Wennerberg, [1990].

The mainshock observations used in this study are accelerograms from four stations (GSC, ISA, PAS, PFO) in the TERRAscope array. Instrument gain was removed from these records; they were doubly integrated to obtain displacement, bandpass filtered from 0.02 to 7 Hz using a zero–phase, second–order Butterworth filter to preserve the broadband nature of the record, and then rotated. The aftershock records used as empirical Green's functions were very broadband (VBB) velocity records from the TERRAscope array. They were processed similarly: instrument gain removed, integrated once to obtain displacement, bandpass filtered from 0.02 to 7 Hz, and rotated.

Results

Although numerous aftershocks and a foreshock to the Big Bear earthquake were satisfactorily modeled with a point source and a standard earth structure [Jones and Helmberger, 1993], we have shown that the observed mainshock waveform complexity cannot be fit with a simple, single–pulse source–time function (Figure 3.3). Using the August 17, 1992, aftershock as an eGf, we test a single–pulse source–time function of duration appropriate to an $M = 6 - 6.5$ earthquake (5 seconds) using the eGf approach discussed above (Figure 3.6), but the results fail to approximate either the frequency content or waveform shape of mainshock records. As the previous fixed–pulse models clearly fail, we test a simple, variable width single–pulse time history using the eGf approach (Figure 3.7).

Source-time function durations are assumed to be one second for stations ISA and GSC, 1.2 seconds at PAS, and 3.5 seconds at PFO, based on earlier point-source modeling (Figure 3.3) and from single–station point–source solutions using data from PAS and PFO, respectively. In each case, even allowing for variation in pulse width between stations, the single–pulse model fails to match significant arrivals on the mainshock waveforms (Figure 3.7).

Substantially better results are obtained with the addition of a second pulse (Figures 3.8, 3.9). Records at stations PAS and GSC require source–time functions composed of two pulses (Figure 3.9). For TERRAscope stations PFO and ISA, a third subevent is also suggested (Figure 3.9). We apply the same method to the 14:43 GMT foreshock as eGf, and obtain consistent results (Figures 3.10, 3.11).

Although the modeling results are not perfect, they are successful in matching many

---

Figure 3.6: The four Panels show results for the August 17, 1992, aftershock as eGf, assuming a simple, single–pulse model. The pulse duration is 5 seconds, roughly what might be expected for an earthquake the size of the Big Bear mainshock.

920817

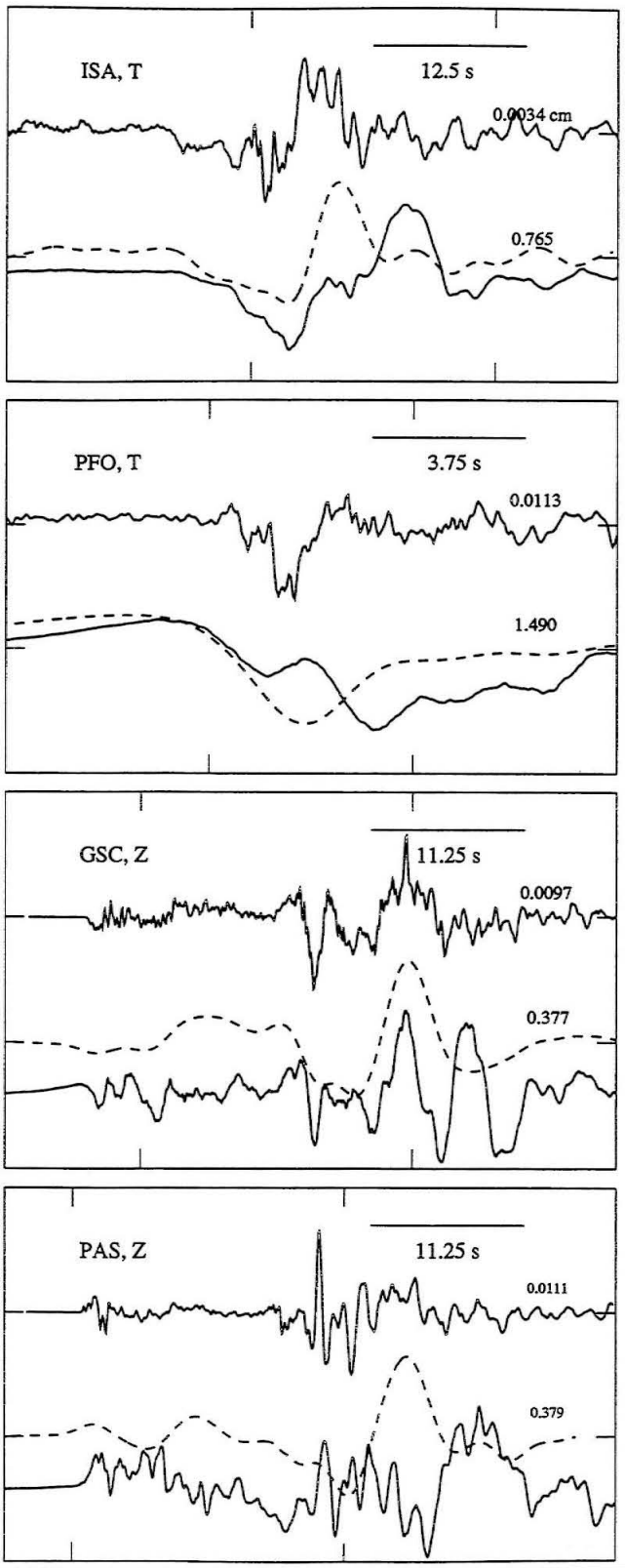
ISA, T
12.5 s
0.0034 cm
0.765
PFO, T
3.75 s
0.0113
1.490
GSC, Z
11.25 s
0.0097
0.377
PAS, Z
11.25 s
0.0111
0.379

of the more salient features of the observations, and represent a clear improvement over the single–pulse model results shown in Figures 3.3, 3.6 and 3.7.

Interpretation

The pulse widths in the inferred source–time functions (Figures 3.9, 3.11) cannot be interpreted in terms of source–time function durations because they indicate the pulse width relative to that of the empirical Green's function (note that amplitudes are relative to the amplitude ratios of the mainshock and empirical Green's function at each station). For the August 17, 1992, aftershock (Figures 3.8– 3.9) with a moment of 2.93×10^{23}, we obtain a moment of 5.34×10^{25}, equivalent to a moment magnitude of $M_w = 6.42$. Given the effective source–time functions we derived from the foreshock [Jones et al., 1993] and the moment of the foreshock, a moment of 5.3×10^{25} is obtained for the Big Bear mainshock. This is equivalent to a moment magnitude of $M_w = 6.48$.

Assuming that the two pulses at stations GSC and PAS correspond to the first two pulses at stations ISA and PFO, we can use the inferred subevent spacings to solve for a relative location of the second subevent. Assuming further that the first subevent occurs at the SCSN–determined epicenter and that the subevent spacing is small compared to the event–station spacings, a parameter–search method is used to infer the subevent temporal and spatial spacing. An optimal solution yields a second subevent occurring 3.7 seconds after the first, roughly 3.2 km and 15° east of south from the first subevent. Thus, the inferred subevent spacing toward PFO is 3.7 seconds minus the travel time projected on the azimuth towards PFO, while the inferred spacing

Figure 3.7: The four Panels show results assuming a simple variable-width single pulse model. In each Panel, the top trace is the raw eGf data, the dashed trace is the convolution of the eGf with the source-time function, and the bottom solid trace is mainshock data. Prior to convolution, the source-time functions are scaled to unit area.

920817

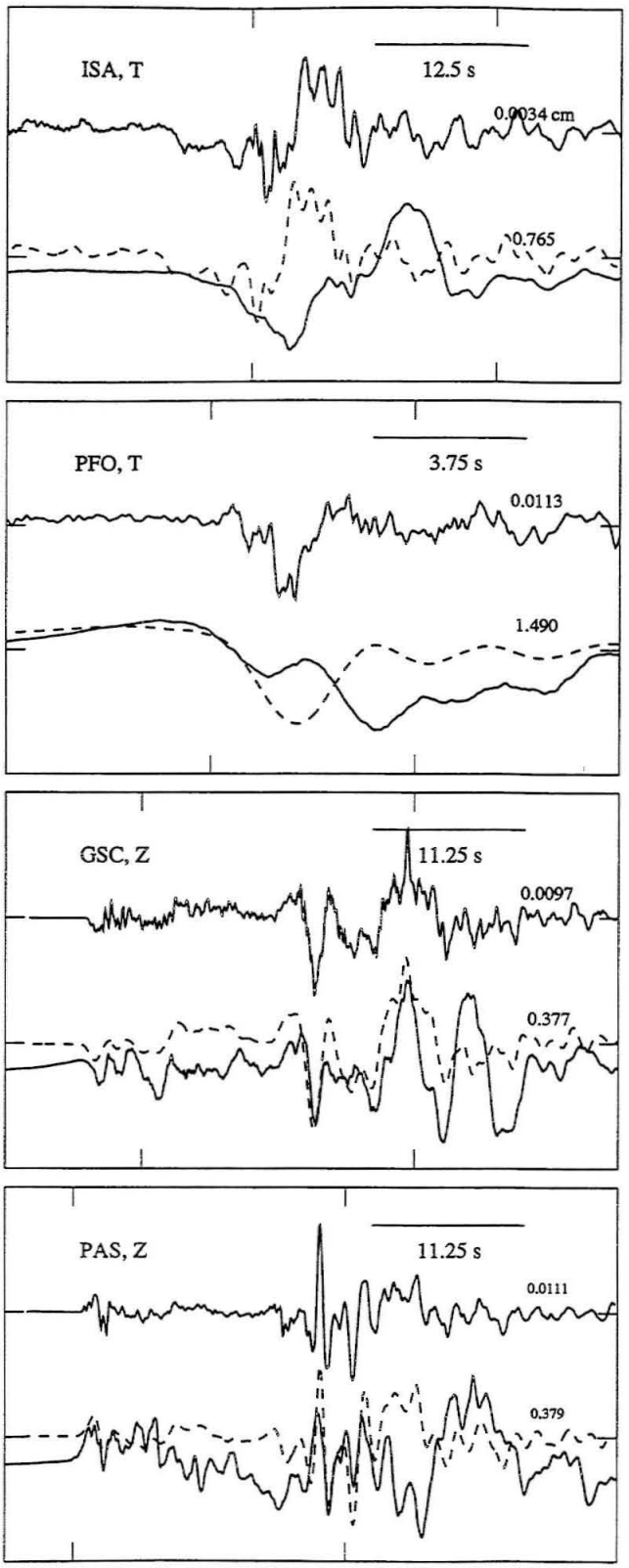
ISA, T
12.5 s
0.0034 cm
0.765
PFO, T
3.75 s
0.0113
1.490
GSC, Z
11.25 s
0.0097
0.377
PAS, Z
11.25 s
0.0111
0.379

towards ISA is roughly 3.7 seconds plus the same amount. The location of the third postulated subevent cannot be determined from our results.

3.6 Line–Source Fault Models

Motivated by results from our empirical Green's function study, which suggest a Big Bear mainshock composed of at least two subevents, coupled with directivity results suggesting substantial rupture to the northwest, we attempt to place further limits on the Big Bear rupture characteristics by performing a line-source fault inversion study.

A damped, non–negative, least squares inversion procedure [Lawson and Hanson, 1974] is used to obtain the subfault weighting values that give the best fit to the mainshock velocity and displacement waveforms. Additional limits are imposed by the choice of empirical Green's function used in the summation and inversion. As with the earlier point-source study, the eGf must be chosen carefully so that source depth, source mechanism, and source–station distance are appropriate for each source–station pair used in the inversion. To solve for the weighting amplitudes on each subfault, given the selected eGf seismograms and the mainshock observations, we solve the following overdetermined system of linear equations:

$$\mathbf{Ax} = \mathbf{b}$$

where $\mathbf{A}$ is the matrix of subfault synthetics (in this case, eGf's), $\mathbf{x}$ is the solution vector, consisting of subfault weights, and $\mathbf{b}$ is the data (observed) vector. We invert explicitly

Figure 3.8: The four Panels show results for the choice of the August 17, 1992, aftershock as *eGf*. For stations ISA and PFO, on or near *SH* maxima, results for the tangential component of motion are shown. For stations GSC and PAS, on or near *P*–wave maxima, results for the vertical component of motion are shown. The top trace is the raw *eGf* data, the dashed trace is the convolution of the *eGf* with the source-time function, and the bottom solid trace is mainshock data.

920817

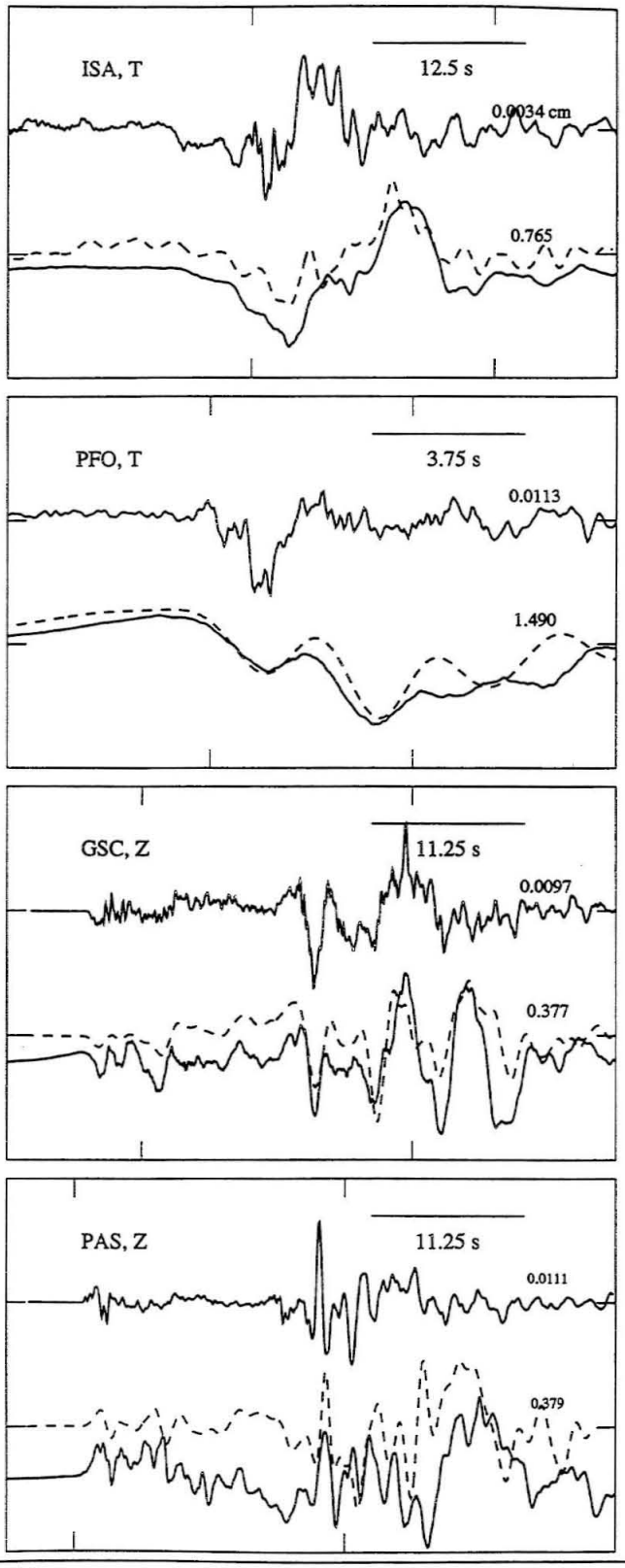
ISA, T
12.5 s
0.0034 cm
0.765
PFO, T
3.75 s
0.0113
1.490
GSC, Z
11.25 s
0.0097
0.377
PAS, Z
11.25 s
0.0111
0.379

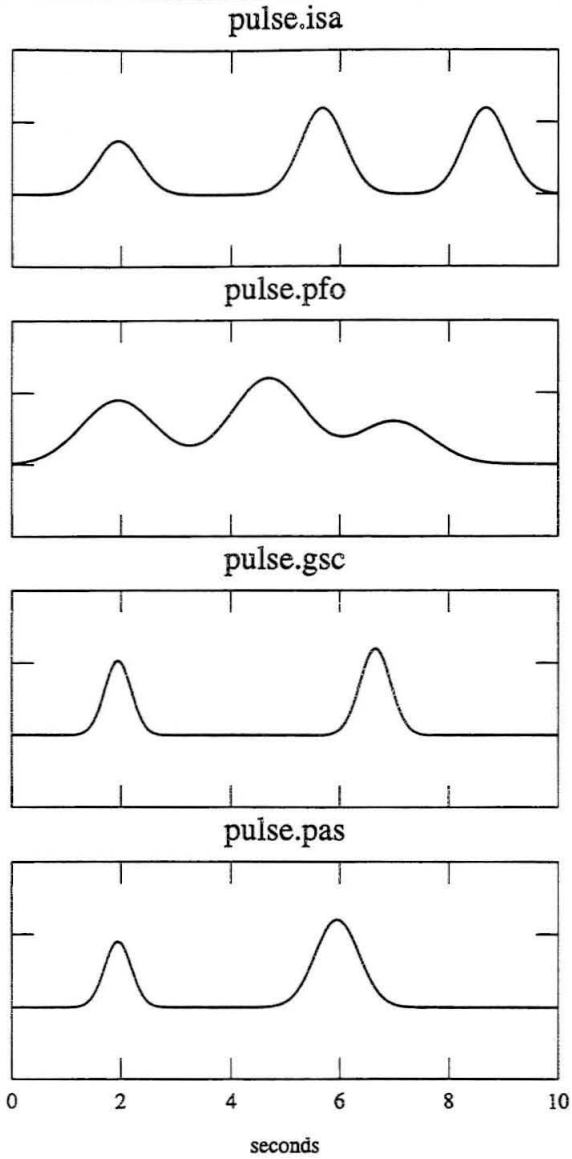

Figure 3.9: Preferred source–time functions for the choice of the August 17, 1992, aftershock as *eGf*. The source-time functions are scaled to unit area prior to convolution.

for subfault weightings. Other parameters must be specified, i.e., the smoothing weights for each inversion, rupture velocities, weighting for each trace, lag time between fault ruptures (for rupture geometries including more than one fault), and fault geometry. Numerous inversions were performed in this study and the results presented below represent our best solutions for each given choice of eGf, and contain features consistent across all eGfs. Inversions were also run using theoretical Green's functions similar to those used in the point–source modeling shown in Figure 3.3, producing results consistent with those obtained from the two eGfs, but with a substantially higher least–squares misfit.

3.6.1 Error Analysis

A quantitative measure of error was obtained for each inversion by taking the euclidian norm between the data and synthetic for each pair of traces, then summing these, and normalizing for the number of traces in the inversion, as follows:

$$E = \frac{\sum_{i=1}^{m}[\sum_{j=1}^{n}(X_{d_j} - X_{m_j})^2]_i}{m}$$

where **m** is number of observations, X_d is a data vector, X_m is the appropriate synthetic and **n** represents the number of time–points in the **i**th pair of time-series. The error is normalized to facilitate comparisons between inversions using fewer waveforms (one less station) and those using waveforms from all five stations. Trace–by–trace least–squares analysis was also performed, so that individual improvements in waveform fit could be checked.

Figure 3.10: The four Panels show results for the choice of the June 28, 1992, 14:43 GMT foreshock as *eGf*. The top trace is the raw *eGf* data, the dashed trace is the convolution of the *eGf* with the source-time function, and the bottom solid trace is mainshock data.

92062814

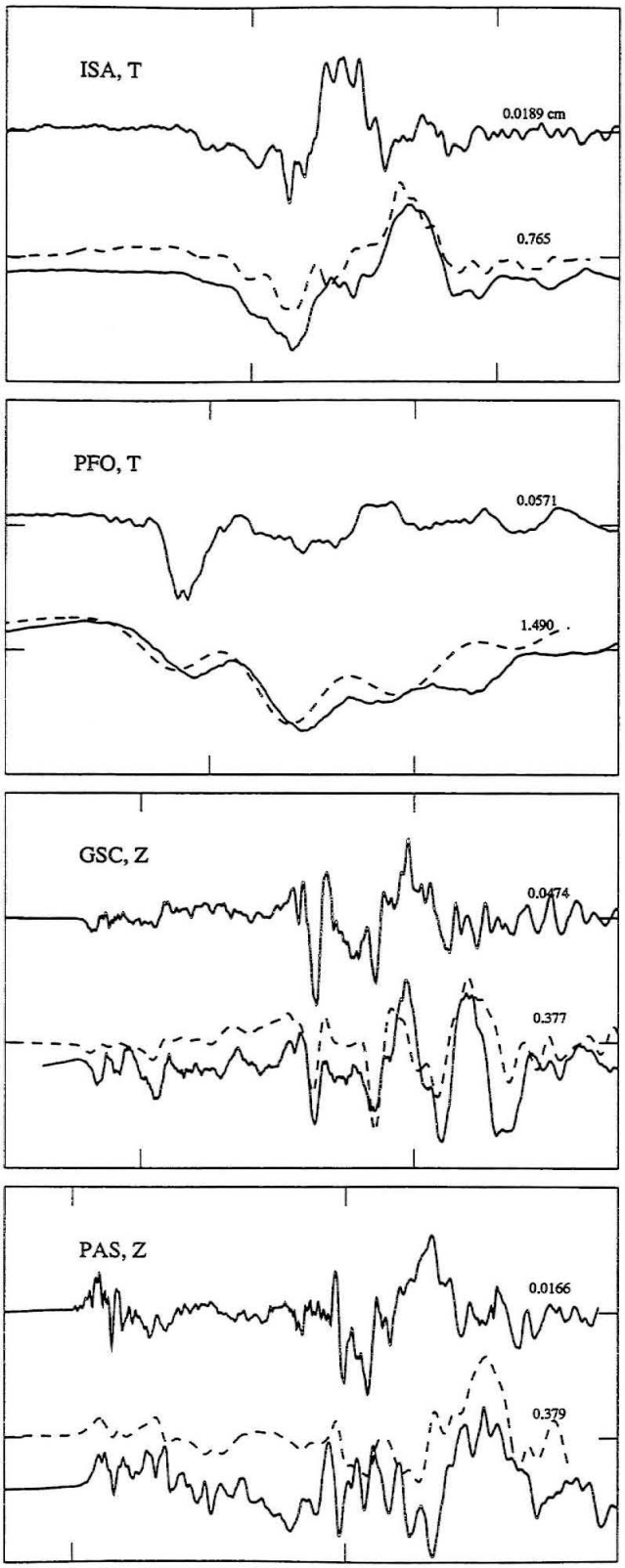
ISA, T
0.0189 cm
0.765
PFO, T
0.0571
1.490
GSC, Z
0.0474
0.377
PAS, Z
0.0166
0.379

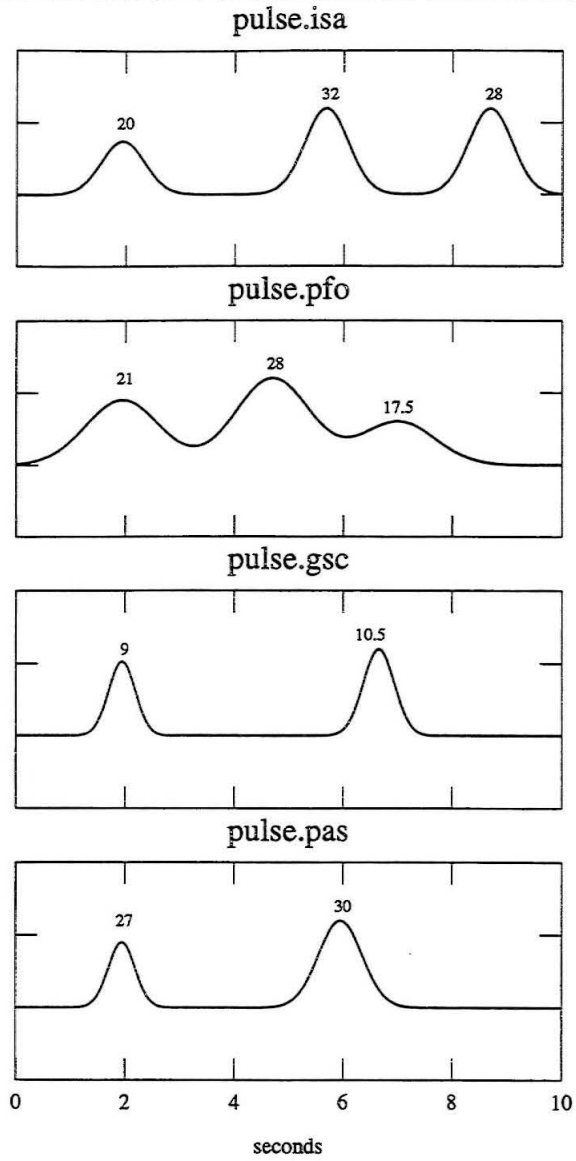

Figure 3.11: Preferred source–time functions for the choice of the June 28, 1992, 14:43 GMT foreshock as *eGf*. The source-time functions are scaled to unit area prior to convolution.

Table 3.3: Summary of Line Source Results

eGf Date yymmddhhmm	eGf M_w (dyne-cm)	Mainshock M_w (dyne-cm)	NW fault (dyne-cm)	NE fault (dyne-cm)	T_lag (s)
9206281748	5.17×10^{22}	5.86×10^{25}	2.61×10^{25}	3.25×10^{25}	3.75–4.00
9208172041	2.35×10^{23}	5.83×10^{25}	2.64×10^{25}	3.19×10^{25}	4.00–4.25

3.6.2 Empirical Green's Functions

Two aftershocks (June 28, 1992, 17:48 GMT, August 17, 1992, 20:41 GMT) were selected as empirical Green's functions for this procedure. Mainshock data and the data used as empirical Green's functions were processed as described earlier in the section on eGf summation. Both the mainshock and eGf data were subsequently low–pass filtered with a corner at 0.5 Hz. Again, we use the vertical records at PAS and GSC, and add the radial as well. For ISA and PFO we use all three components. Nodal or near nodal components of motion at each station were given lower weightings in the inversion. Waveforms from station SVD (at an epicentral distance of 27.4 km) were included when available as we felt it was important that the solution provide good fits for a station so close to the source. Moment was obtained, in this case and those that follow, by summing the weighting functions at each subfault and multiplying this sum by the moment of the appropriate eGf (Table 3.6.2).

3.6.3 Models

Single Fault Models

We use four initial single–fault models for the Big Bear earthquake, each consisting of a 16 km long, linear fault composed of 16 1-km long blocks, with a point–source in the middle of each block. Fault lengths were chosen upon examination of the spatial

distribution of aftershocks toward the northwest and toward the northeast. Based on directivity results, two of the models consisted of faults with northwestern strikes of 320°. In one case, rupture was specified to proceed unilaterally from the southeastern end of the fault to the northwestern end, at a rupture velocity of V_r = 2.7 km/s. Rupture velocities of 1.7, 2.3, 3.0, 3.3 and 3.7 were also tested, but the best results were obtained assuming V_r = 2.7 km/s. The other case featured bilateral (NW–SE) rupture at the same rupture velocity on a northwest–striking fault. To force the inversion to simulate the effect of separate, discrete subevents, we apply minimal smoothing between subfaults.

We also test two models which feature single linear 16–km faults with a 50° northeasterly strike. In these cases rupture proceeds unilaterally from the southwestern end of the fault to the northeastern in one case, and bilaterally from the epicenter in the other. Other rupture scenarios (that is, rupture beginning at the northwest end of the northwest–striking fault or at the northeast end of the northeast–striking fault) are inconsistent with mainshock location and aftershock distribution.

Both unilaterally and bilaterally rupturing single–fault parameterizations failed to produce reasonable solutions even after the fault lengths were increased so subevents could distribute themselves spatially and thus temporally as far apart as possible. Of the models run, quantified least–squares misfit analysis indicates that overall, weighted waveform fits provided by the NE–striking unilaterally rupturing fault are about 9% better than those provided both by the NW–striking unilaterally rupturing fault and the NE–striking, bilaterally rupturing fault. However, visual waveform comparisons indicate that significant phases are not matched by the results from any of these models. Figure 3.12 shows results from one such single–fault model; a single bilaterally rupturing fault striking to the northeast (N50°E), assuming a rupture velocity of V_r = 2.7 km/s. This fault model is suggested by the mainshock source location with respect to aftershock distribution along a NE–SW trend (Figure 3.4). For this inversion, the June 28,

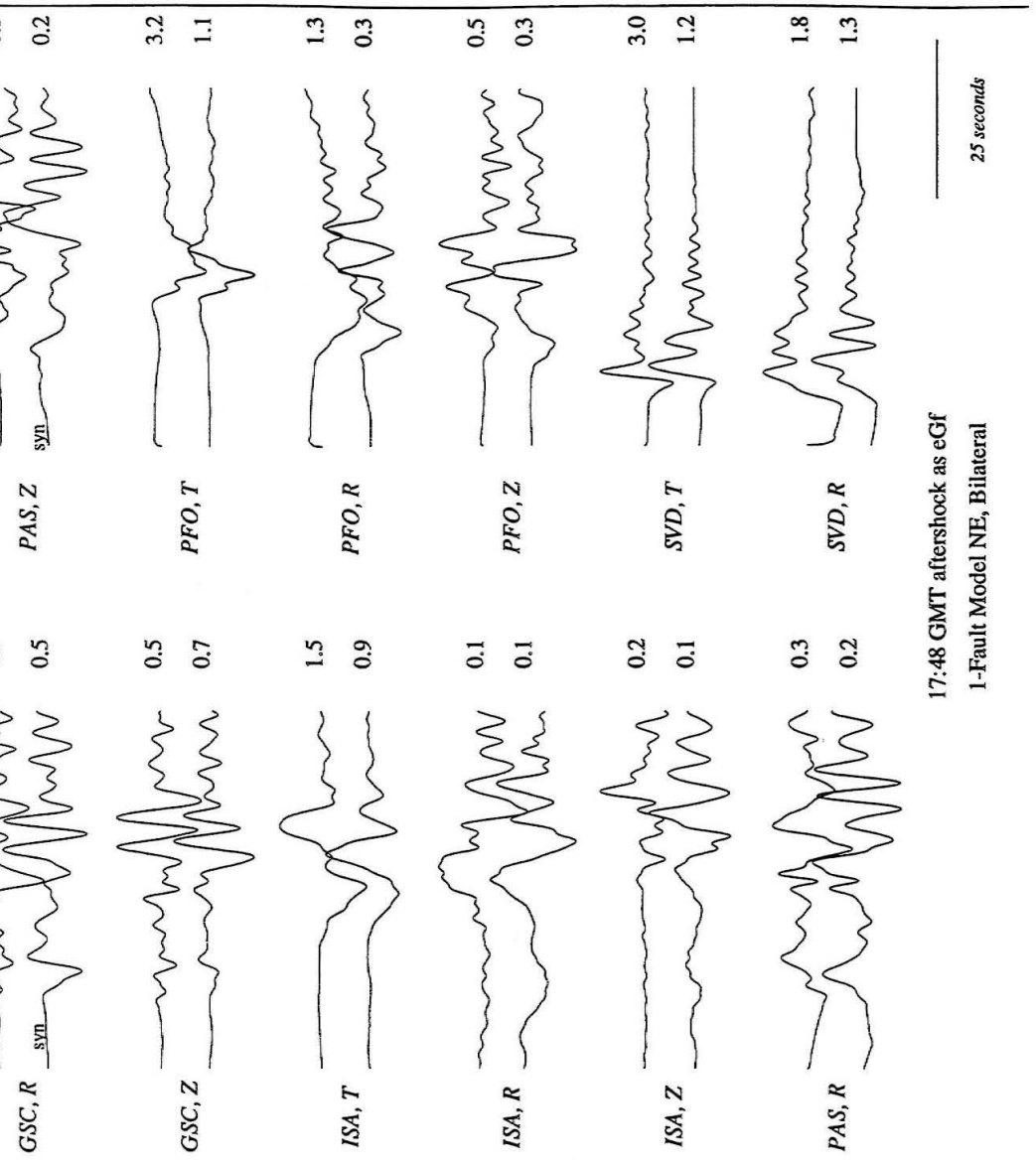

Figure 3.12: Line–source fault inversion results, in displacement, for a single–fault model striking 50° (northeast). The June 28, 1992, 17:48 GMT aftershock was selected as eGf. Synthetics are shown plotted below the data for each station, and relative amplitudes are indicated to the right of each pair of traces.

1992, 17:48 GMT aftershock was used as an eGf. Important characteristics of several waveforms are not well modeled, including the prolonged duration of ISA (tangential component).

Double Fault Models

As we could not obtain required temporal subevent spacings from one fault without increasing its length beyond that suggested by extent of seismicity, we experimented with a number of two–fault models, using both NW and NE–striking faults. The geometry and orientation of the two faults is again based on aftershock distribution, as well as on the results from the empirical Green's function summation study. Due to directivity results and mainshock location (Figure 3.4), initial unilateral rupture was specified to occur on the NW–striking fault. Parameterization of the second fault is similar to that of the first: 16 1-km blocks, with a point–source in the middle of each. Given the relative amplitudes at stations GSC, ISA and PAS, (i.e., GSC not substantially larger than PAS, and smaller than ISA), and given the results for NE–trending faults in the single–fault study, unilateral and bilateral ruptures at a rupture velocity of $V_r = 2.7$ km/s were initially assumed. Rupture velocities of 1.7, 2.3, 3.0, 3.3 and 3.7 km/s were again tested, but the best results were obtained assuming $V_r = 2.7$.

We also test several other double–fault models (Figure 3.13). In Figure 3.13, a triangle indicates misfit value from a single NW–trending, unilaterally rupturing fault; an octagon shows misfit from a single NE–striking, unilaterally rupturing fault; and a star indicates that from a single bilaterally–rupturing NE–striking fault. For the two–fault models, triangles indicate misfit results from a two–fault model composed of two unilaterally rupturing NW–striking faults; hexagons show results from two unilaterally rupturing NE–striking faults. Crosses show results from a NW–striking unilaterally rupturing fault followed by a NE–striking unilaterally rupturing fault. Stars indicate misfit results from a NW–striking, unilaterally rupturing fault followed by a NE–striking

bilaterally rupturing fault.

Lowest misfit is obtained from the NW–striking fault paired either with the unilaterally or bilaterally rupturing NE–striking fault, depending on the choice of eGf. A two–fault model composed of two NE–trending faults also provided low misfit values for both eGfs, though the synthetics failed to fit several key waveforms, including all three components of displacement recorded at station ISA. Since no choice of empirical Green's function is perfect, we present results from two eGfs and illustrate the consistencies between them.

3.6.4 Results

June 28, 1992, 17:48 GMT Event as eGf

We obtain a good fit to the data using the June 28, 1992, 17:48 aftershock as an eGf and assuming an initial northwest–trending rupture, with the two–fault geometry described above (Figure 3.14). Although depth mismatch between eGf and observed has contributed to overlarge synthetic surface wave to *Pnl* wave amplitude ratios at some stations, we have matched the more unusual and salient characteristics of these waveforms. A comparison of least–squares misfit for the chosen single–fault model (NE–striking, bilateral rupture) and the two–fault model indicate an 11% improvement in overall weighted misfit for the two–fault model over the one–fault model. Comparing the quantitative misfit values for each trace, we find some cases in which results for a two–fault model are actually higher than those provided by the lowest error one–fault model, although the overall weighted misfit to the collective data set is decreased. Variance is decreased by approximately 11%–49% for traces weighted most heavily in the inversion (ISA tangential 49%; SVD radial 30%, tangential 23%; PFO tangential 11%).

The distribution of subfault weights resulting from this inversion are shown in Fig-

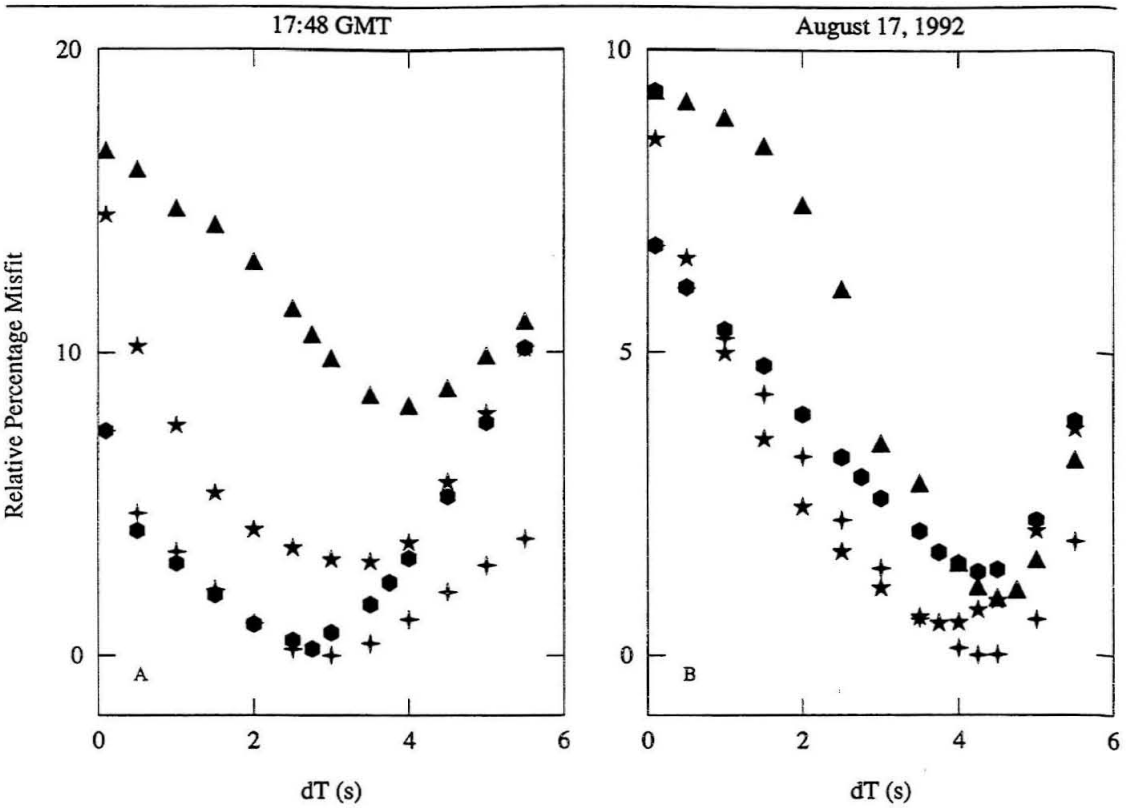

Figure 3.13: *a*, Percentage misfit relative to the lowest misfit value for each eGf, plotted against delay time (in seconds) between ruptures for four two–fault models, from line–source modeling using the June 28, 1992, 17:48 GMT aftershock as eGf. Values shown are percentage increase in misfit relative to the minimum misfit for all models. Each misfit value is normalized with respect to number of traces used in the inversion (in this case, 12). Associated one–fault models are shown at delay time (**dT**) equals zero. *b*, Norm of misfit plotted against delay time between the two ruptures for four two–fault models, from line–source modeling using the August 17, 1992, aftershock as eGf. Values shown are percentage increase in misfit relative to the minimum misfit for all models, and misfits are normalized with respect to the number of mainshock waveforms used in the inversion, in this case, 10.

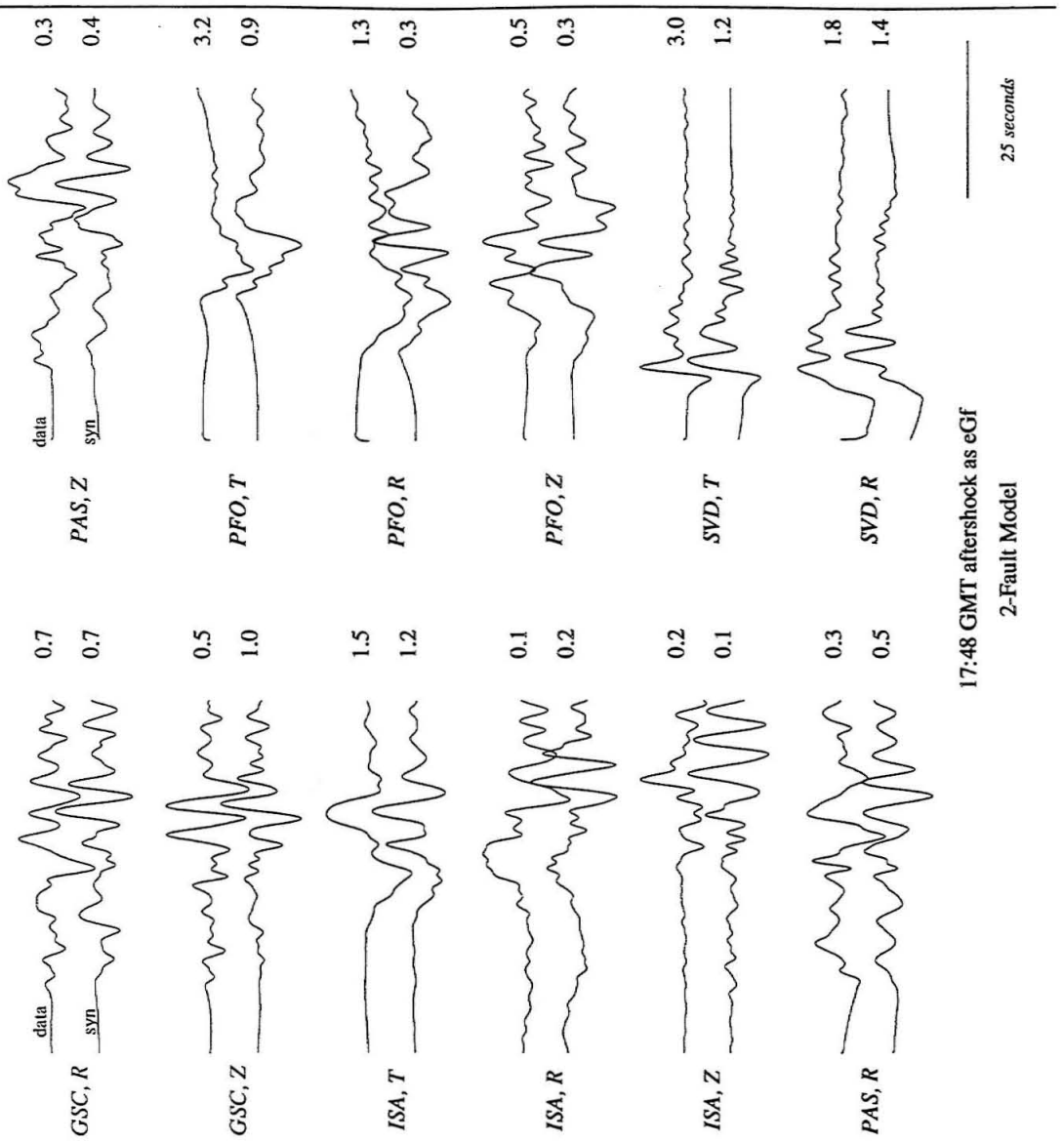

Figure 3.14: Line–source fault results, in displacement, for the choice of the June 28, 1992, 17:48 GMT aftershock as eGf and assuming the fault orientation shown in Figure 3.15. Synthetics are shown plotted below the data for each station, and relative amplitudes are indicated to the right of each pair of traces. The rupture velocity was $V_r = 2.7$ km/s for both faults, and best–fit time lag between rupture on the first (NW) and second (NE) faults is (Figure 3.13a) $T_{lag} = 3.75 - 4.0$ s.

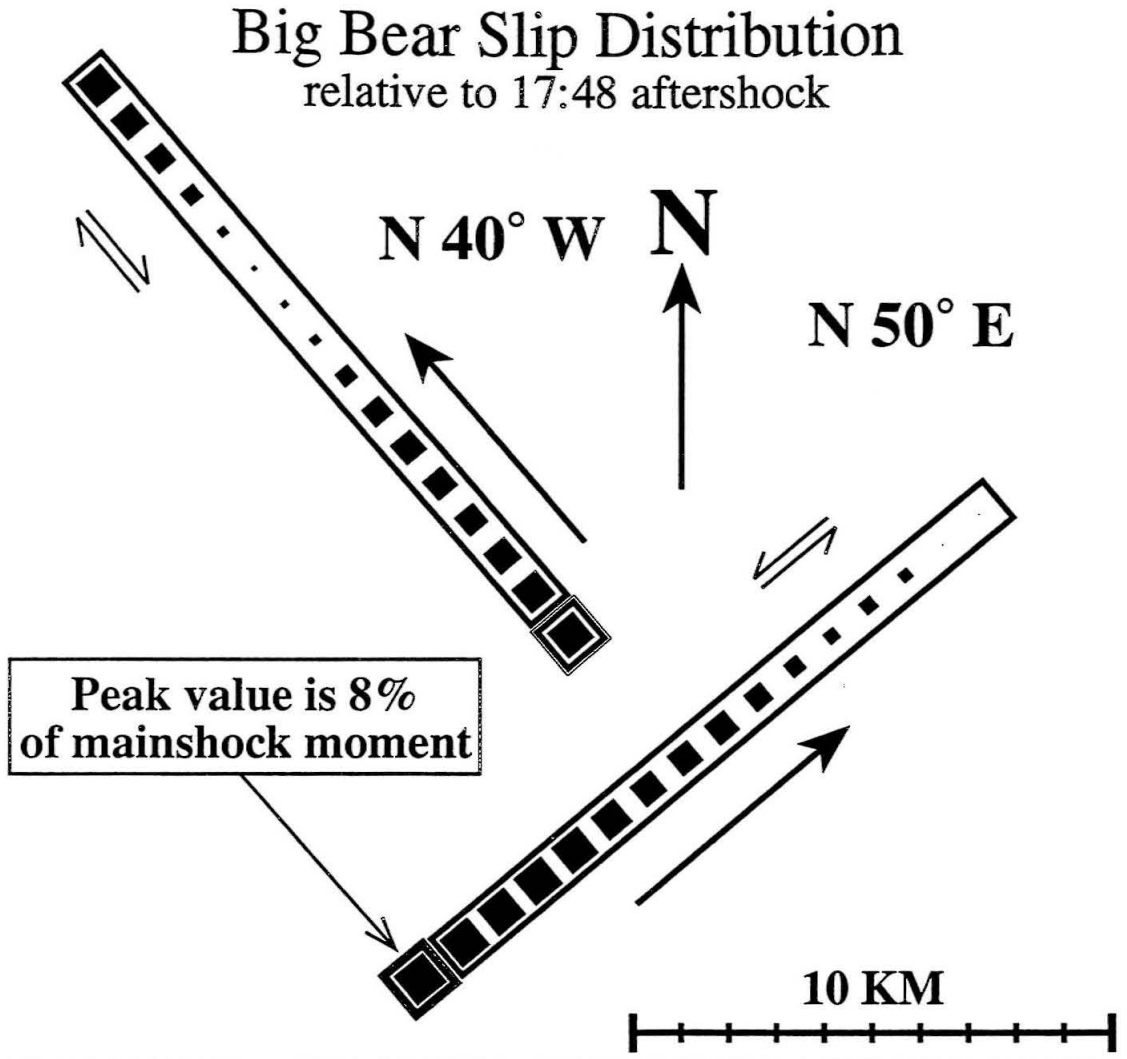

Figure 3.15: Cartoon showing the assumed two–fault geometry for the June 28, 1992, 17:48 GMT aftershock inversion and final distribution of subfault weightings obtained from this inversion. Note the two subevents on the NW–trending fault plane. Each subfault is a 1 km by 1 km square. Subfault weightings are indicated by square area, and are scaled to the peak subfault weighting value.

ure 3.15. Here we see the suggestion of two subevents on the NW–striking fault, and moment release distributed in both directions on the NE–striking fault. The total moment for this inversion is 5.86×10^{25} dyne-cm, which is equivalent to a moment–magnitude of 6.44, with 2.61×10^{25} dyne-cm (44.6% of moment release) distributed on the NW striking fault and 3.25×10^{25} dyne-cm (55.4% of moment release) distributed on the NE striking fault. The best–fit time–lag between rupture on the first and second faults is (Figure 3.13a) $T_{lag} = 3.75 - 4.0$ s.

August 17, 1992, Event as eGf

We also perform a line–source inversion for subfault weightings using the August 17, 1992, aftershock as eGf. This event has a source–depth of about 15 km, and produced high–quality records at stations GSC, ISA, PAS, and PFO. In this case station SVD is not included in the inversion, as records were not available for this event. Results for the inversion using this eGf are shown in Figure 3.16, and distribution of subfault weights for this inversion is shown in Figure 3.17. The inversion featuring bilateral rupture on the second, NE–striking fault had lowest error, so we show these results here. Again, the inversion suggests two subevents on the NW–trending fault, with moment release in both directions on the NE–SW trending fault. Total moment for this inversion is 5.83×10^{25} dyne-cm, which is equivalent to a moment–magnitude of 6.44, with 2.64×10^{25} dyne-cm (45% of moment release) distributed on the NW–trending fault and 3.19×10^{25} dyne-cm (55% of moment release) distributed on the NE–trending fault. The best–fit time–lag between rupture on the first and second faults is (Figure 3.13b) $T_{lag} = 4.0 - 4.25$ s.

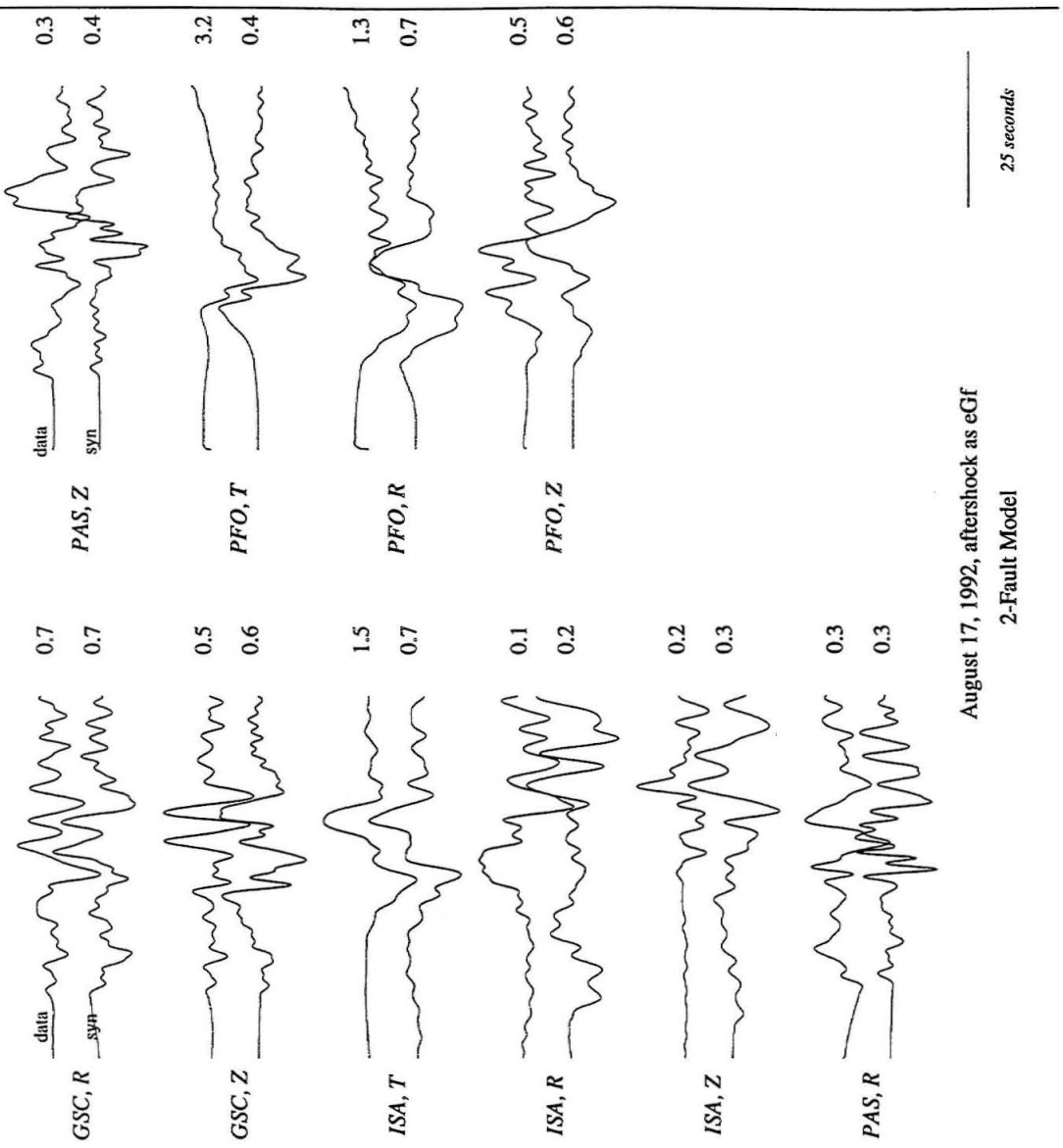

Figure 3.16: Line–source fault results, in displacement, for the choice of the August 17, 1992, aftershock as eGf and assuming the fault orientation shown in Figure 3.17. The rupture velocity was $V_r = 2.7$ km/s for both faults, and best–fit time lag between rupture on the first (NW) and second (NE) faults is (Figure 3.13b) $T_{lag} = 4.0 - 4.25$ s.

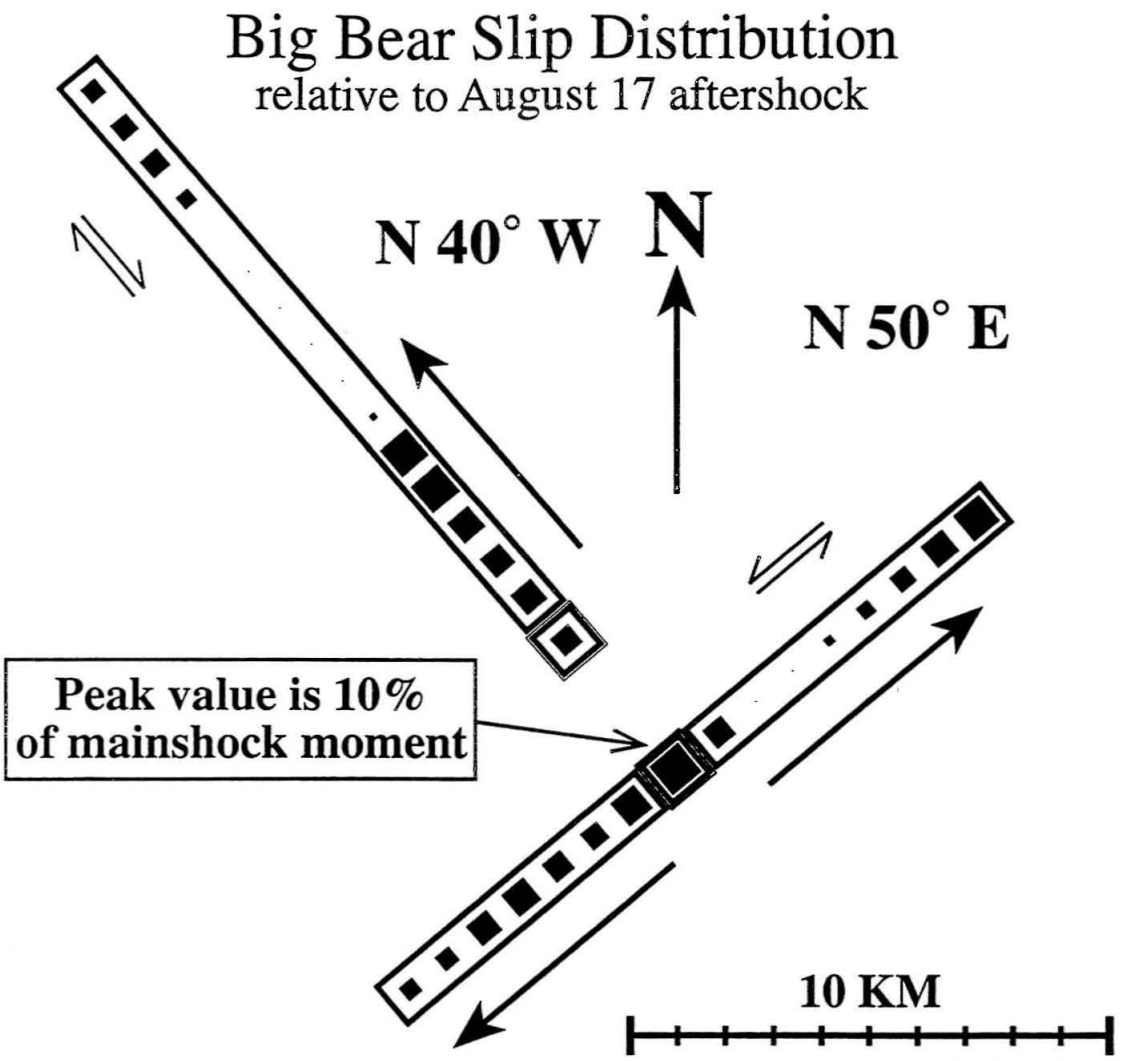

Figure 3.17: Cartoon showing the assumed two–fault geometry for the inversion using the August 17, 1992, aftershock as eGf, and distribution of subfault weightings obtained from the inversion. Note the two subevents on the NW–trending fault plane. Each subfault is a 1 km by 1 km square. Subfault weightings are indicated by square area, and are scaled to the peak subfault weighting value.

Summary

The two line–source inversions thus yield consistent results, with a time–lag of roughly 4 seconds between the onset of initial unilateral rupture on the NW plane and a second unilateral or bilateral subevent on the NE plane. The inferred moment partitioning between the NW– and NE– striking faults is roughly equal. These results are generally consistent with the eGf point–source results, which yielded a second subevent initiating a few km S–SE of the first. The inferred time–lag between subevents is consistent with our optimal results from the (3.7 s versus 3.75–4.25 s). The line–source results are also consistent with results from the directivity analysis; the overall event directivity is controlled by the unilateral NW rupture rather than the NE–SW rupture, which may have been bilateral.

3.7 Discussion

The Big Bear mainshock was a significant, if enigmatic, earthquake in its own right. A M_b4.1 foreshock which preceded the mainshock by only 40 seconds, the lack of surface rupture, and the demonstrated source complexity together obscure the rupture history of this event. It is possible that the two mainshock subevents occurred at different depths, and thus possible that the mainshock "hypocentral depth" may never be accurately determined. These uncertainties inevitably complicate any analysis, including the eGf procedure presented in this paper.

Notwithstanding these limitations, we have presented a combination of point–source eGf, line–source eGf, and directivity analysis that reaches a consistent rupture scenario for the Big Bear earthquake. Our interpretation derives some support from general geologic evidence that the NW–trending lineaments in the region are better developed than the NE–trending features (P. M. Sadler, personal comm., 1993), and from an independent engineering assessment that the damage pattern from the earthquake is

suggestive of NW–directivity (S. Mendes, personal comm., 1994).

We suggest the following scenario for the sequence: The 14:43 $M5.2$ foreshock occurred near $34^{\circ}\ 10'N$, $116^{\circ}\ 49'W$ and ruptured north–northeastward. A smaller, $M4.0$ foreshock occurred in a similar location at 15:04 GMT. Rupture during the Big Bear earthquake began at 15:05 GMT at $34^{\circ}\ 12.4'N$, $116^{\circ}\ 50.1'W$, to the north of the foreshocks, and ruptured primarily to the northwest, with possibly a few kilometers of rupture to the southeast as well. Approximately 4 seconds later, rupture initiated along a NE-striking surface close to the location of the foreshocks. Rupture along the NE–striking plane may have been bilateral.

Rupture on conjugate nodal planes, while considered unusual, has been suggested or inferred in other sequences, including the 1947 Manix earthquake [Doser, 1990], the 1984 Round Valley sequence [Priestly et al., 1988], the 1986 Chalfant sequence [Smith and Priestly, 1988], and the 1987 Superstition Hills sequence [Hudnut et al., 1989]. In the 1984 Round Valley sequence, initial rupture on a NE–striking fault was followed within a few hours by activity on a NW–striking conjugate fault. The 1986 Chalfant sequence featured a $M_l5.7$ foreshock which ruptured downward and to the southwest along a NE–striking fault, followed by a $M_l6.4$ mainshock which initiated deeper and ruptured upward along the NW–striking conjugate fault. In the Superstition Hills sequence, Hudnut et al. [1989] conclude that cross–fault triggering occurred after a delay of about 11 hours. Coseismic rupture on conjugate normal faults was observed in the 1980 Irpinia, Southern Italy, sequence [Crosson et al., 1986; Bernard and Zollo, 1989], and conjugate normal faulting was observed in the 1984 Devil Canyon, Idaho, sequence [Jackson, 1994].

Classic cross–fault triggering features an 'L'–shaped rupture on conjugate planes, consistent with predicted coulomb stress change triggering (e.g., Hudnut et al., 1989). In our case, simple static stress considerations predict that unilateral NW rupture would trigger SW but not NE rupture on the conjugate surface. However, earthquake trigger-

ing processes are likely to be more complex than simple coloumb stress changes would dictate. Dynamic forces on the SW–NE nodal plane may have been sufficient to overcome the coulomb stress increase due to the NW rupture. It is moreover likely that, overall, the sequence of Big Bear subevents occurred in response to considerable static changes caused by the $M_w = 7.3$ Landers event just three hours earlier.

In addition to static stress changes caused by the Landers earthquake, it is possible that the Big Bear sequence accommodated rotational forces. The primary manifestation of clockwise rotation caused by the right–lateral Landers rupture should be left–lateral motion on NE–striking faults. However, the predominance of NW–striking lineaments within the San Bernardino mountains block suggests that the region may be subdivided into smaller blocks that do not each span the full width of the mountains. If this is the case, right–lateral motion may occur on NW–striking faults within the San Bernardino mountains (i.e., right–lateral shear is accommodated across a system of faults, rather than only on the bounding faults). The paucity of well–developed NE–trending faults and lineaments through the Big Bear region (P. M. Sadler, personal comm., 1993) supports this hypothesis.

The high relative amplitudes at station ISA northwest of the mainshock, and on azimuth with the northwest-striking nodal plane, provide *prima facie* evidence for substantial moment release along this surface. We note that these amplitudes cannot be explained as an artifact of bilateral rupture along the NE–striking plane because PFO would then be expected to have similar high amplitudes, which is not observed. However, it is possible that bilateral rupture of the second subevent results in minimal northeast directivity.

We conclude that the previous presumption of a NE–striking mainshock rupture plane is attributed to an overall (long term) aftershock distribution that is misleading. It is not necessarily true that regions of high mainshock slip will correspond to regions of the most intense aftershock activity; in fact, areas of high slip and/or total stress release

may correlate instead with sparse aftershock activity [Beroza, 1991]. We also note that a dense concentration of aftershocks occurred south of the Pinto Mountain fault (Figure 3.1) within the Landers sequence, associated with only 20–40 cm of aftershock–related slip [Hough et al., 1993].

In the aftermath of the Landers mainshock, the Barstow region has also been characterized by high aftershock activity, in this case with no primary rupture. It is interesting to note that Barstow, the Pinto Mountain fault, and the proposed NE–trending Big Bear 'fault' are all areas of high post–seismic deformation [Shen et al., 1993]. Moreover, several lines of evidence suggest that the Big Bear event was, overall, a high stress drop earthquake [Jones and Helmberger, 1993], and the NW–striking rupture could be shorter than the NE–striking rupture if the former were particularly high stress drop.

Although surface rupture was not identified in the immediate aftermath of the Big Bear mainshock, evidence of surface rupture was later found, with a maximum of 3-4 cm of right–lateral displacement over several hundred meters [Rasmussen, personal comm., 1993]. The strike of this trace, which was roughly $N48°W$, agrees with our inferred rupture direction, displaced approximately 4 km to the southwest. This feature might be aftershock-related or co-seismic, and was first observed within a few days of the Big Bear mainshock.

Our results have several implications for the tectonic structure of the Big Bear region. The NW–trending rupture plane coincides with a topographic lineament which extends from the Sugarloaf epicenter past Moon Ridge (and the nearby subdivision of Moonridge), suggesting that this lineament is fault–controlled [L. Seeber, personal comm., 1993]. Both the surface rupture and the NW–striking 'Moon Ridge lineament' or fault are parallel to both the Helendale fault to the NE and to the distributed faults in the Mojave shear zone [Dokka et al., 1992], suggesting that the fabric of the Mojave shear zone may persist under the San Bernardino mountains.

Geological investigations in the San Bernardino mountains also provide evidence

for both NE and NW faulting, with a better–developed NW–trending fabric [Sadler, 1993; Sadler, personal comm., 1993]. The complex nature of the Big Bear rupture, the observed complications of aftershock mechanisms, and the distributed locations of the aftershocks further suggest that the San Bernardino mountains may be characterized by pervasive conjugate (NE/NW) fault sets. Thus, it is possible that numerous faults within the region are capable of producing earthquakes of moderate size.

The second implication of our results concerns the effect of the Landers/Big Bear sequence on the nearby San Andreas fault. Several studies (e.g., Stein et al., 1993; Harris and Simpson, 1993; Jaume and Sykes, 1992) have concluded that the stress changes caused by the Landers earthquake and the presumed (i.e., northeast–trending) Big Bear rupture would tend to move the San Andreas fault closer to failure both along a southern segment (Indio to the Salton Sea) and along the San Bernardino segment, while reducing normal stress on the San Andreas in between the two segments. However, the NW–striking 'Big Bear' fault is roughly parallel to the San Bernardino segment of the San Andreas and would thus tend to reduce its shear stress. Although a definitive partitioning of moment release on the two faults is beyond the scope of our investigations (and may be beyond the resolving capacity of the data), our results suggest that substantial moment release did occur on the presumed antithetic fault plane and that the effects of this event on the nearby San Andreas fault should be re–examined.

Bibliography

Aki, K. and Richards, P., Quantitative Seismology, Theory and Methods, *W. H. Freeman and Company, New York*, Vol. 2, 807-812, 1980.

Ammon, C. J., A. A. Velasco, and T. Lay, Rapid estimation of rupture directivity: Application to the 1992 Landers (M_s = 7.4) and Cape Mendocino (M_s = 7.2), California, earthquakes, *Geophys. Res. Lett., 20*, 97-100, 1993.

Bakun, W. H. and C. G. Bufe, Shear wave attenuation along the San Andreas fault zone in central California, *Bull. Seism. Soc. Am., 65*, 439-459, 1975.

Bernard, P. and A. Zollo, The Irpinia (Italy) 1980 Earthquake: Detailed analysis of a complex normal faulting, *J. Geophys. Res., 94*, 1631-1647, 1994.

Beroza, G. C. and P. Spudich, Linearized inversion for fault rupture behavior: application to the 1984 Morgan Hill, California, earthquake, *J. Geophys. Res., 93*, 6275–6296, 1988.

Crosson, R. S., M. Martini, R. Scarpa, and S. C. Key, The Southern Italy earthquake of November 23, 1980: An unusual pattern of faulting, *Bull. Seism. Soc. Am., 76*, 381–394, 1986.

Dokka, R. K., D. F. MacConnell and J. P. Ford, Active and inactive faults of the northern Mojave Desert Block: Implications for strain partitioning in the Eastern California Shear Zone, *(abstracts), Eos, Transactions, 73*, 363, 1992.

Doser, D. I., A re-examination of the 1947 Manix, California, earthquake sequence and comparison to other sequences within the Mojave Block, *Bull. Seism. Soc. Am., 80*, 267–277, 1990.

Hadley, D. and H. Kanamori, Seismic Structure of the Transverse Ranges, California, *Geol. Soc. Am. Bull., 88*, 1469–1478, 1977.

Harris, R. A. and R. W. Simpson, Changes in static stress on Southern California faults after the 1992 Landers earthquake, *Nature, 360*, 251–254, 1992.

Hauksson, E., L. M. Jones, K. Hutton and D. Eberhart-Phillips, The 1992 Landers Earthquake Sequence: Seismological Observations, *J. Geophys. Res., 98*, 19,835–19,858, 1993.

Helmberger, D. V., R. Stead, P. Ho-Liu, and D. Dreger, Broadband modeling of regional seismograms, Imperial Valley to Pasadena, *Geophys. J. Int., 110*, 42-54, 1992.

Hough, S. E., J. Mori, E. Sembera, G. Glassmoyer, C. Mueller, and S. Lydeen, Southern surface rupture associated with the 1992 M7.4 Landers earthquake: Did it all happen during the mainshock? *Geophys. Res. Lett., 20*, 2615–2618, 1993.

Hudnut, K., L. Seeber, T. Rockwell, J. Gormacher, R. Klinger, S. Lindvall, and R. McElwain, Surface ruptures on cross–faults in the November 24, 1987, Superstition Hills, California, earthquake sequence, *Bull. Seism. Soc. Am., 79*, 282–296, 1989.

Jackson, S. M., Seismic evidence of conjugate normal faulting: the 1984 Devil Canyon earthquake sequence near Challis, Idaho, Masters Thesis, 150 pp., Boise State Univ., Boise, Idaho, 1994.

Jaume, S. C. and L. R. Sykes, Changes in State of Stress on Southern San Andreas Fault Resulting from the California Earthquake Sequence of April to June, 1992, *Science, 258*, 1325–1329, 1992.

Jones, L. E. and D. V. Helmberger, Broadband modeling of aftershocks from the Landers, Big Bear and Joshua Tree events, *(abstract), Eos, Transactions, 73*, 383, 1992.

Jones, L. E., D. V. Helmberger and S. H. Hough, Rupture process of the June 28, 1992, Big Bear earthquake, *Geophys. Res. Lett., 20*, 1907–1910, 1993.

Kanamori, H., H–K. Thio, D. Dreger, E. Hauksson, and T. Heaton, Initial Investigation of the Landers, California, earthquake of June 28, 1992 using TERRAscope, *Geophys. Res. Lett., 19*, 2267-2270, 1992.

Lawson, C. L. and R. J. Hanson, Solving Least Squares Problems, *Prentice–Hall, Inc., Englewood Cliffs, N. J.*, 340 pp., 1974.

Matti, J. C., D. M. Morton, and B. F. Cox, The San Andreas Fault System in the vicinity of the central Transverse Ranges Province, Southern California, in *Earthquake Geology: San Andreas Fault System Palm Springs to Palmdale, 35th Annual Meeting, Oct. 2–9, 1992*, 13-62, Southern California Section, Assn. of Engineering Geologists, Los Angeles, California, 1992.

Meisling, K. E. and R. J. Weldon, Late Cenozoic tectonics of the northwestern San Bernardino Mountains, Southern California, *Bull. Geol. Soc. Amer., 101*, 106-128, 1989.

Mori, J. and S. Hartzell, Source inversion of the 1988 Upland, California, earthquake: determination of fault plane for a small event, *Bull. Seism. Soc. Am., 80*, 507–518, 1990.

Mueller, C. S., Source pulse enhancement by deconvolution of an empirical Green's function, *Geophys. Res. Lett., 12*, 33-36, 1985.

Priestly, K. F., K. D. Smith, and R. S. Cockerham, The 1984 Round Valley, California, earthquake sequence, *Geophys. J.*, 95, 215–225, 1988.

Sadler, P. M., The Santa Ana basin of the central San Bernardino Mountains: Evidence of the timing of uplift and strike slip relative to the San Gabriel Mountains, *G.S.A. Memoir 178*, 307–321, 1993.

Shen, Z–K, D. D. Jackson, Y–J Feng, M. Cline, and M. Kim, Postseismic Deformation following the Landers Earthquake, California, June 28, 1992, Submitted to *Bull. Seism. Soc. Am.*, 1993.

Sieh, K. and 19 others, Near–field investigations of the Landers earthquake sequence, April to July, 1992, *Science*, 260, 171-176, 1993.

Smith, K. D. and K. F. Priestly, The foreshock sequence of the 1986 Chalfant, California, earthquake, *Bull. Seism. Soc. Am., 78*, 172-187, 1988.

Stein, R. S., G. C. P. King, and J. Lin, Change in failure stress on the southern San Andreas fault system caused by the 1992 Magnitude=7.4 Landers earthquake, *Science, 258*, 1328–1332, 1992.

Wennerberg, L., Stochastic summation of empirical Green's functions, *Bull. Seism. Soc. Am., 80*, 1418–1432, 1990.

Zhao L-S. and D. V. Helmberger, Source Estimation from Broadband Regional Seismograms, *Bull. Seism. Soc. Am., 84*, 91-104, 1994.

Chapter 4

Appendix I

4.1 Modeling 1: South of the Pinto Mountain Fault

This Appendix comprises a catalog of much of the modeling results for Landers events south of the Pinto Mountain fault. The modeling was done using theoretical Green's functions from the Mojave model [Table 2.1], and between three and five stations. The stations most commonly used are stations GSC, PFO, and SVD. When the solutions seemed unstable, or records from one of the above stations were not available, records from stations ISA or PAS were included. The waveform fits shown on the next few pages and in Appendix II result from source modeling using the grid–search algorithm briefly discussed in section 2.5.

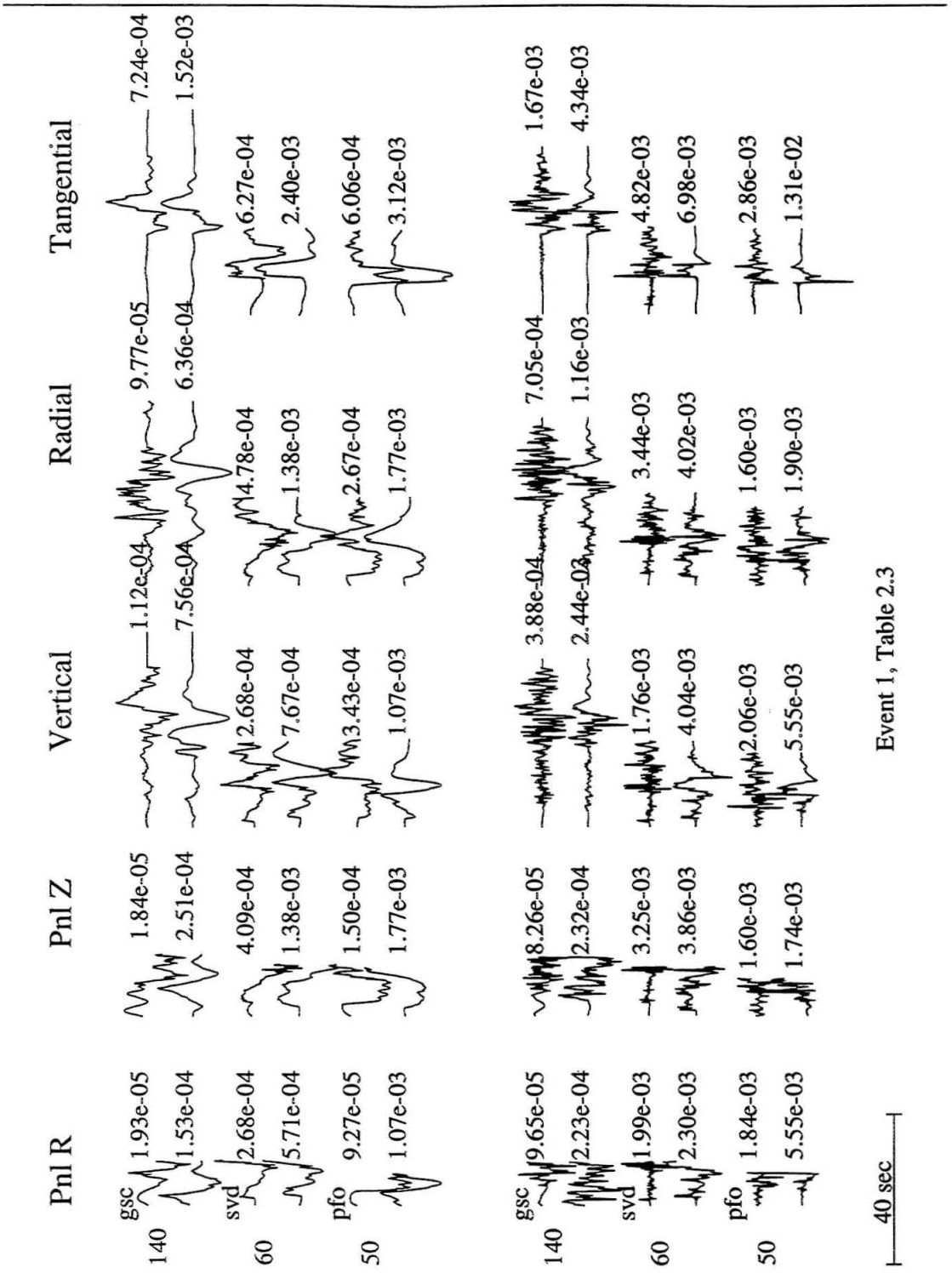

Figure 4.1: Broadband and long–period modeling for event 1, Table 2.4 (June 30, 1992, 11: GMT). Average time function is a 0.35 s triangle. Source depth is estimated at 14 km.

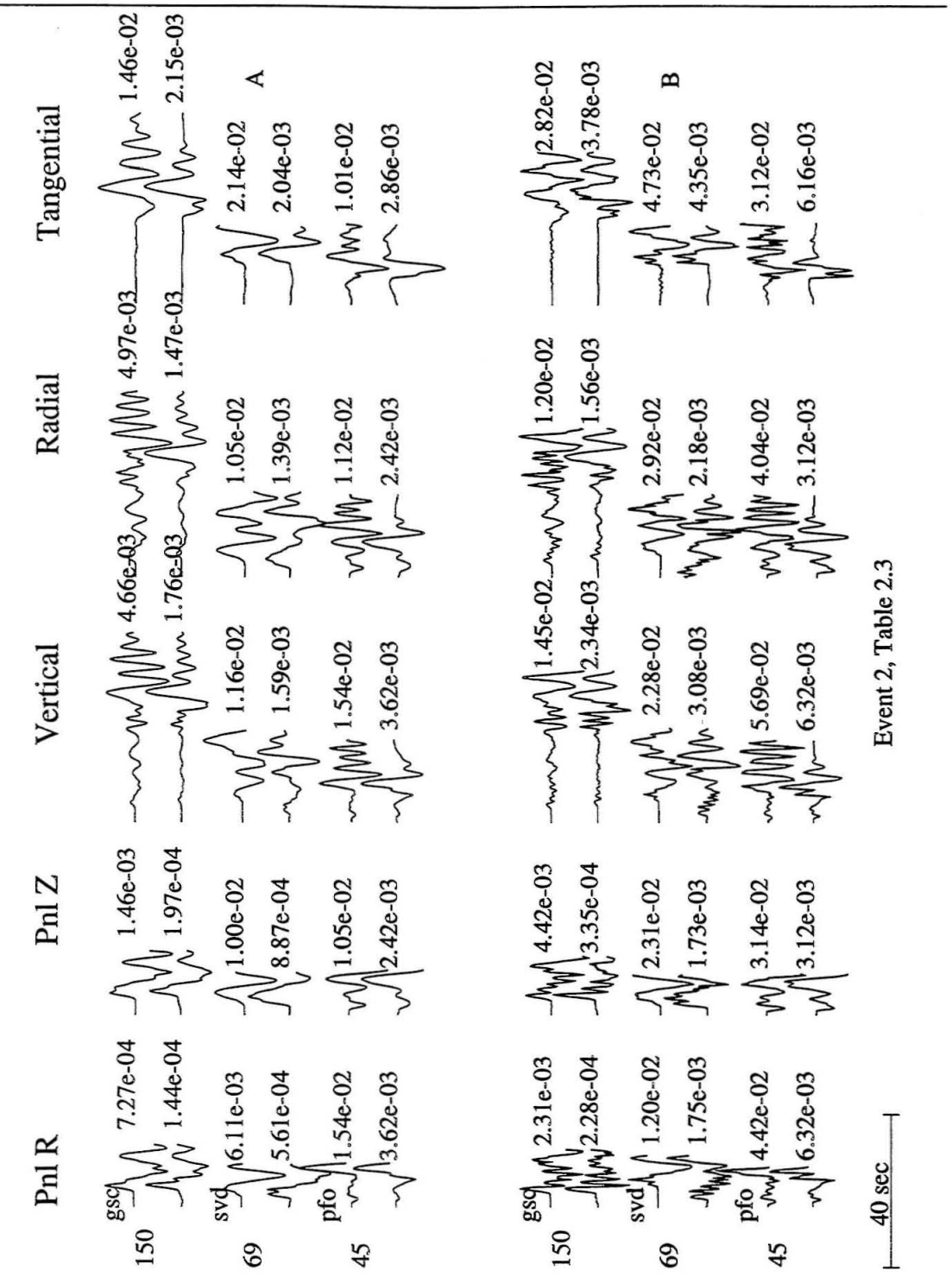

Figure 4.2: Broadband and long–period modeling for event 2, Table 2.4 (June 30, 1992, 14: GMT). Average time function is a 1.0 s triangle. Source depth is estimated at 7 km.

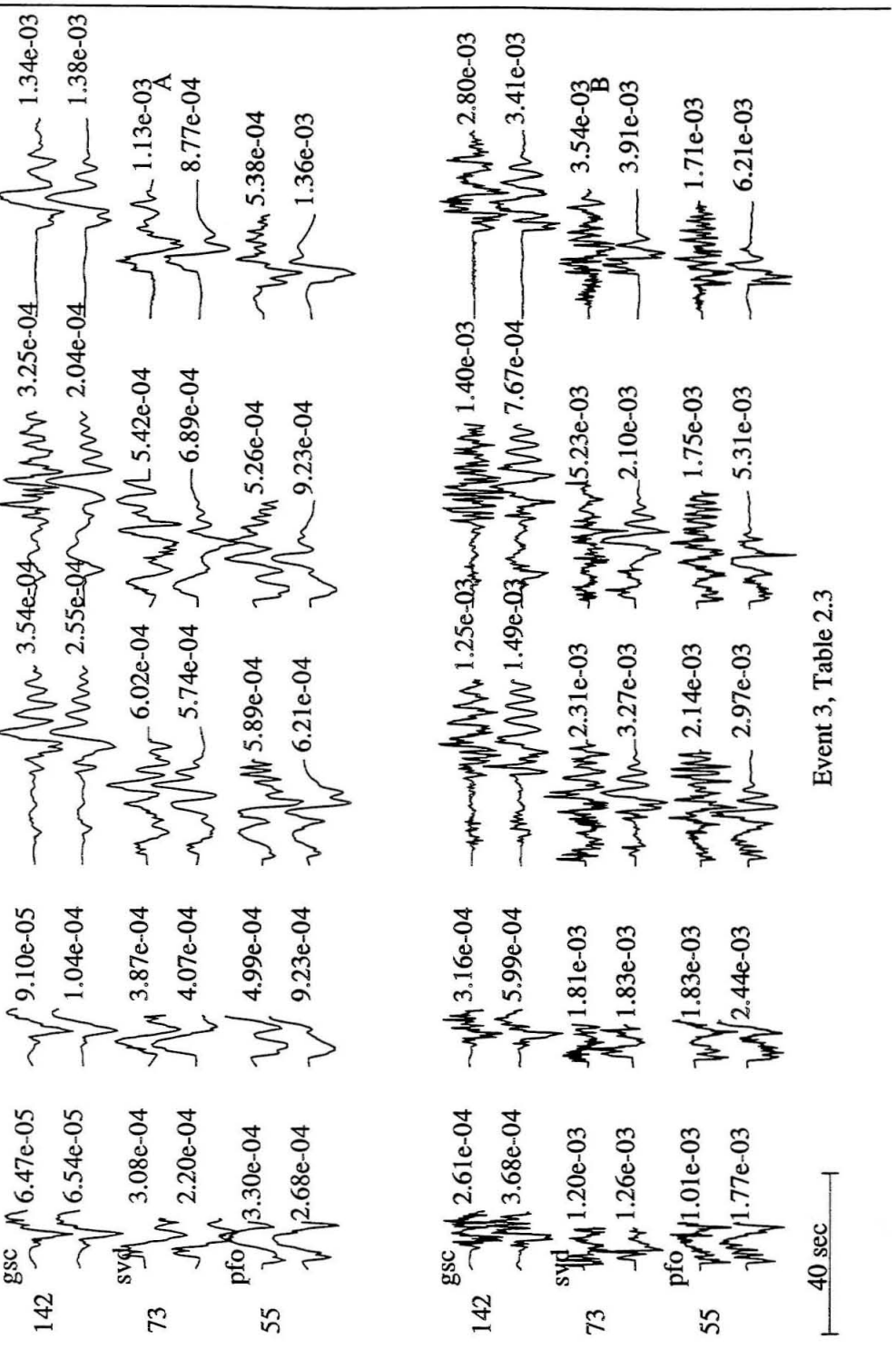

Figure 4.3: Broadband and long–period modeling for event 3, Table 2.4 (July 6, 1992, 12: GMT). Average time function is a 0.6 s triangle. Source depth is estimated at 8 km.

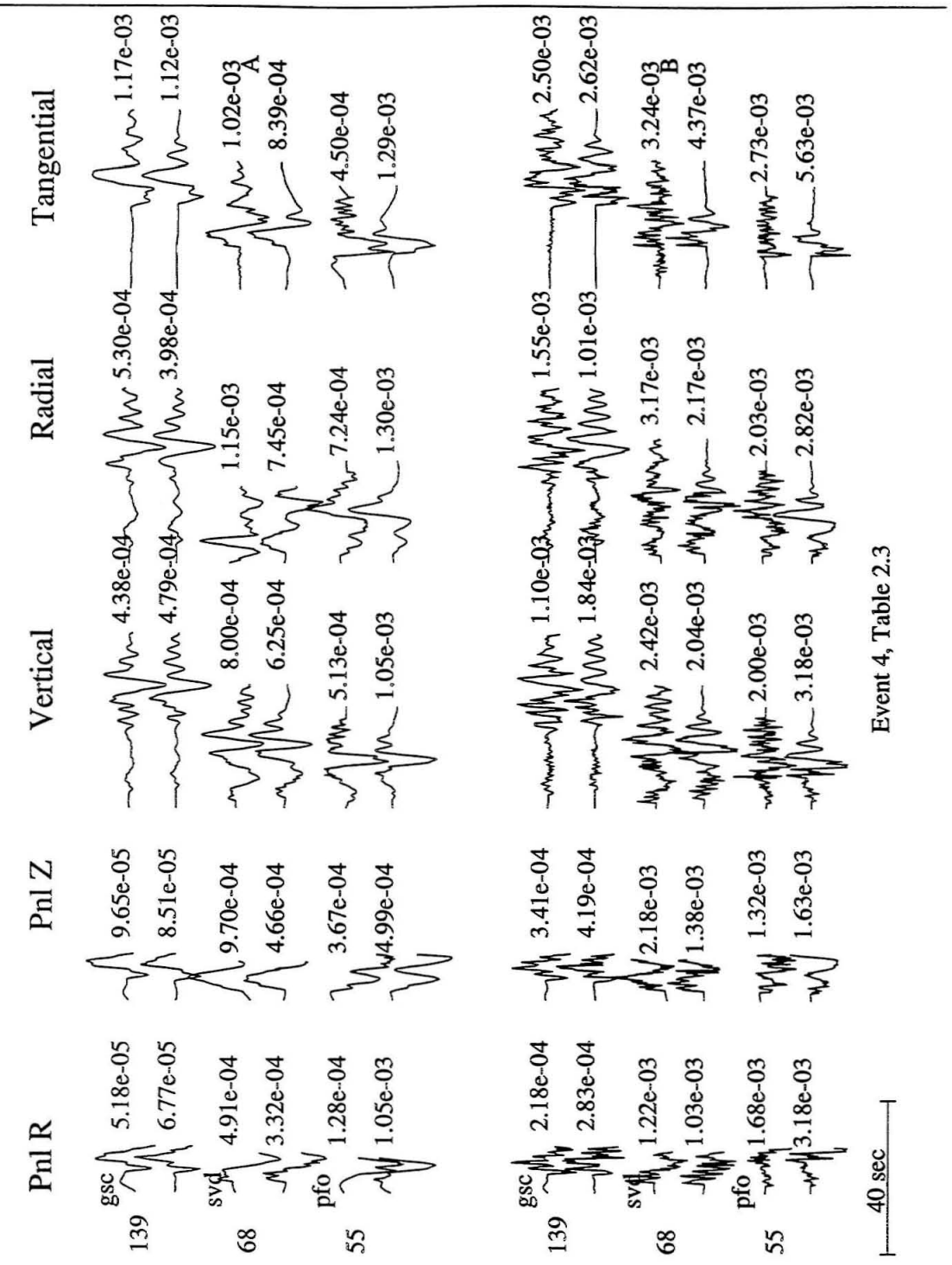

Figure 4.4: Broadband and long–period modeling for event 4, Table 2.4 (July 6, 1992, 19: GMT). Average time function is an 0.4 s triangle. Source depth is estimated at 9 km.

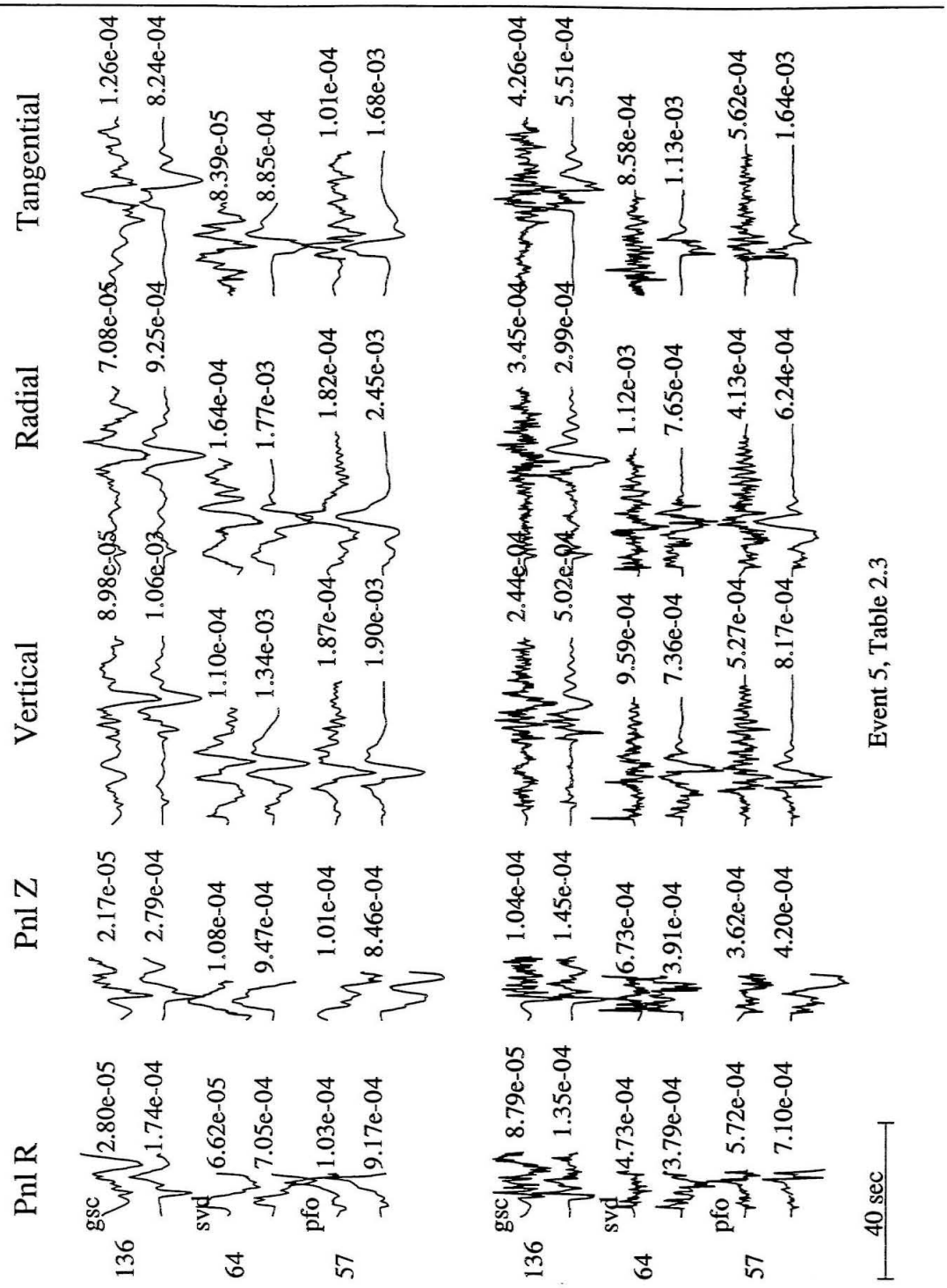

Figure 4.5: Broadband and long–period modeling for event 5, Table 2.4 (July 10, 1992). Average time function is a 0.35 s triangle. Source depth is estimated at 11 km.

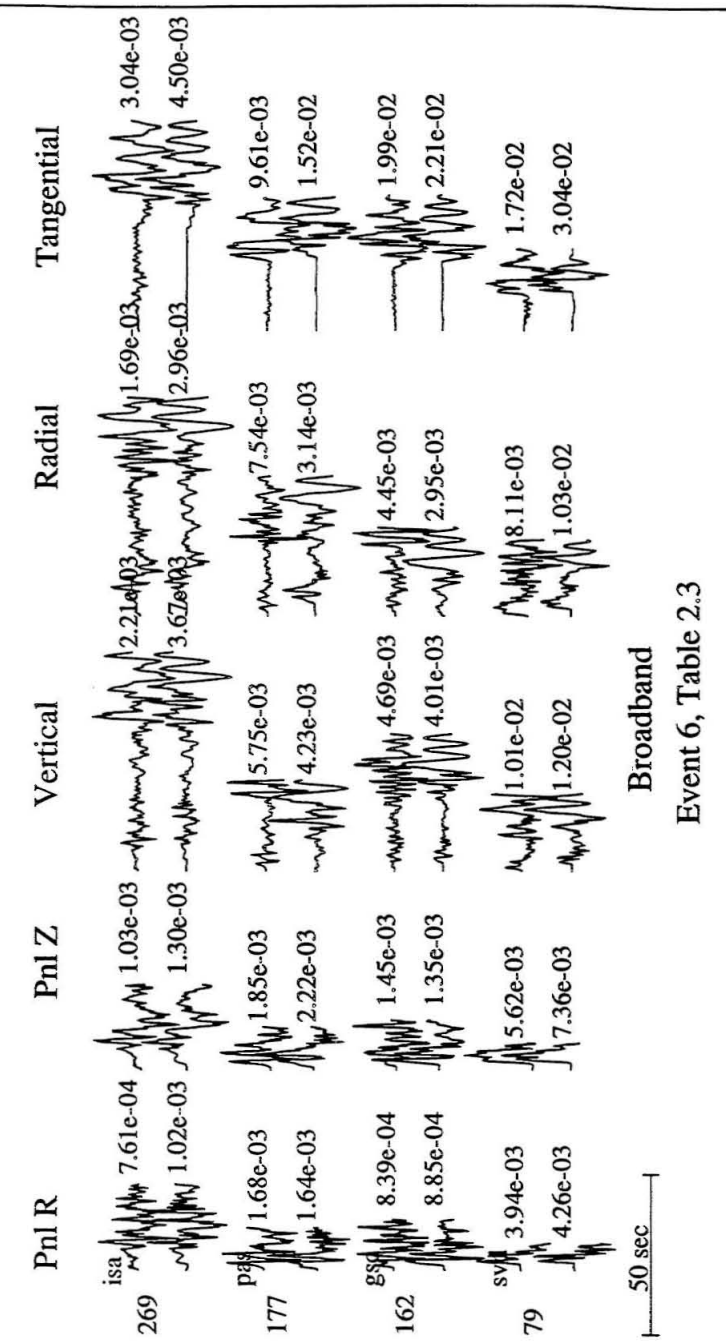

Figure 4.6: Broadband modeling for event 6, Table 2.4 (July 24, 1992). Average time function is a 0.9 s trapezoid (0.3,0.3,0.3). Source depth is estimated at 8 km.

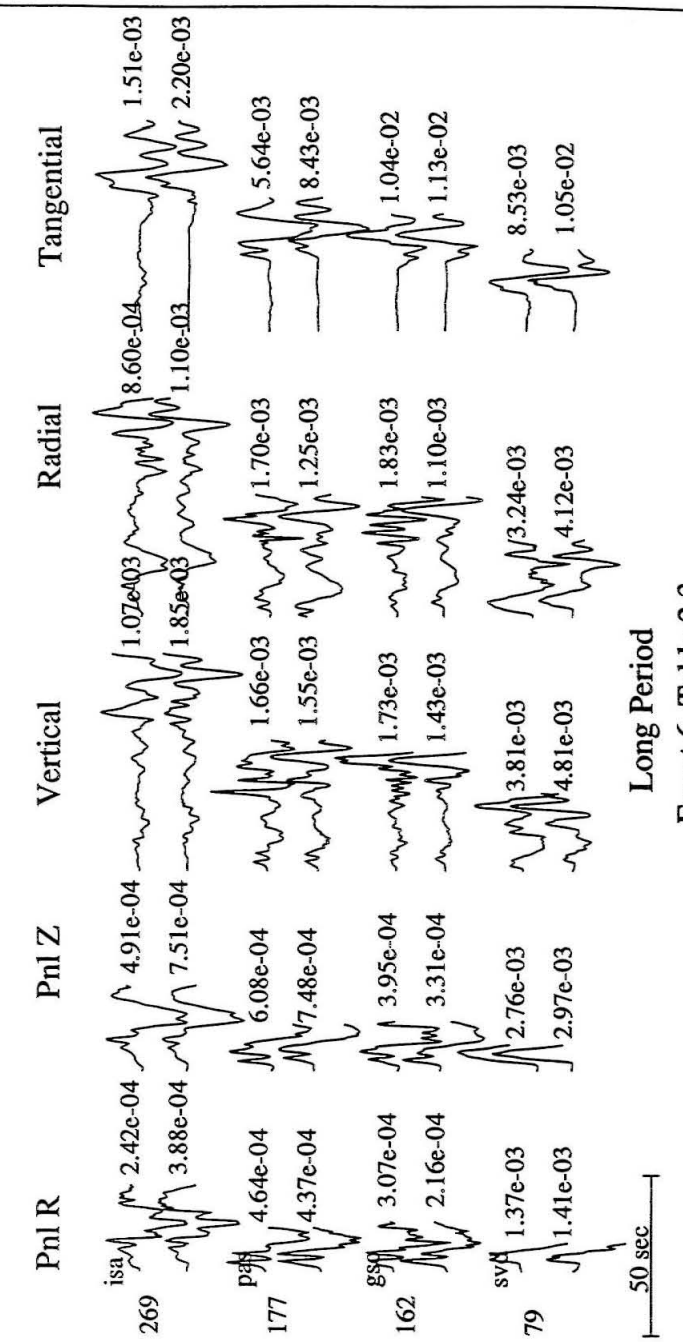

Figure 4.7: Long–period modeling for event 6, Table 2.4 (July 24, 1992). Average time function is a 0.9 s trapezoid (0.3,0.3,0.3). Source depth is estimated at 8 km.

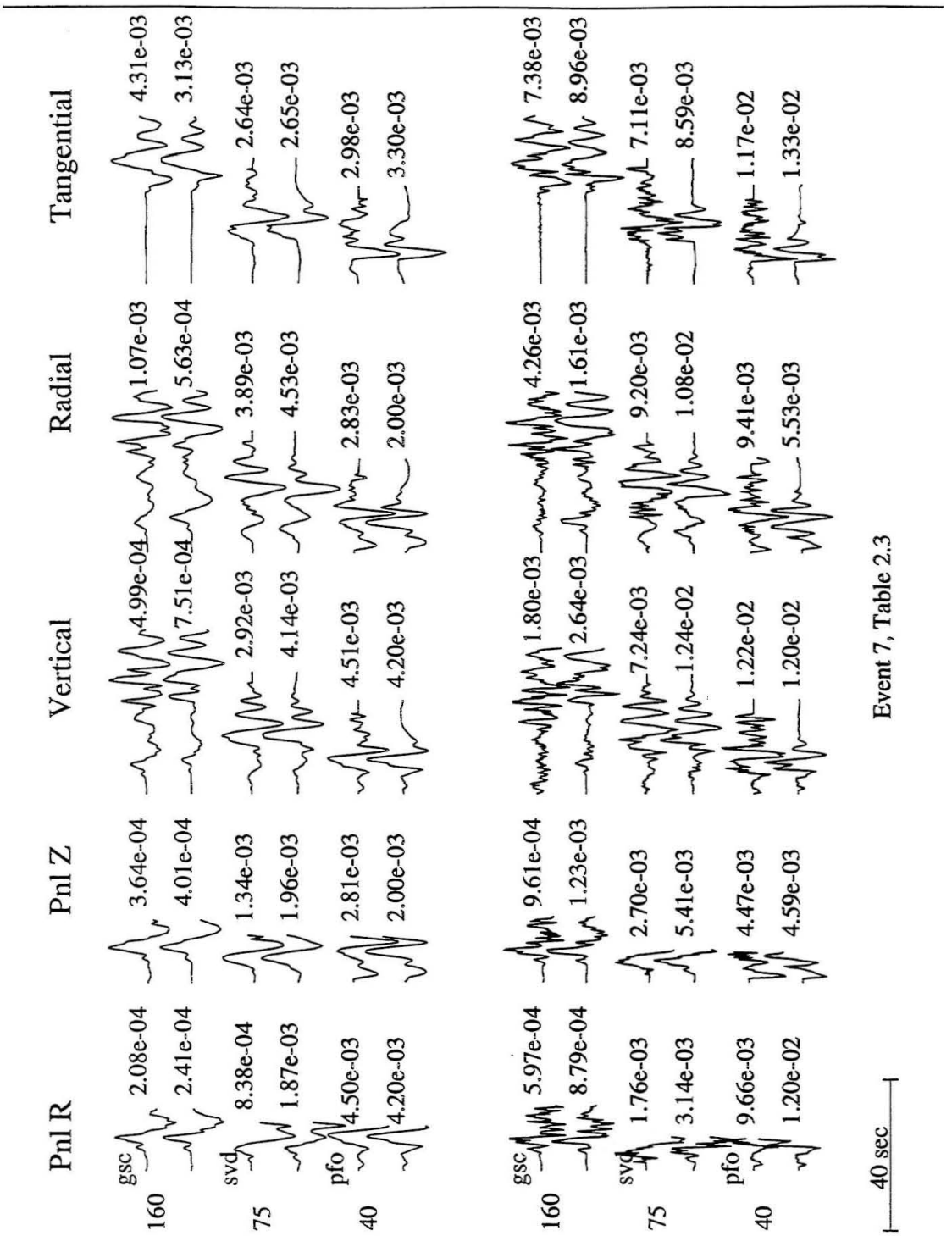

Figure 4.8: Broadband and long-period modeling for event 7, Table 2.4 (July 25, 1992). Average time function is a 1.0 s triangle. Source depth is estimated at 8 km.

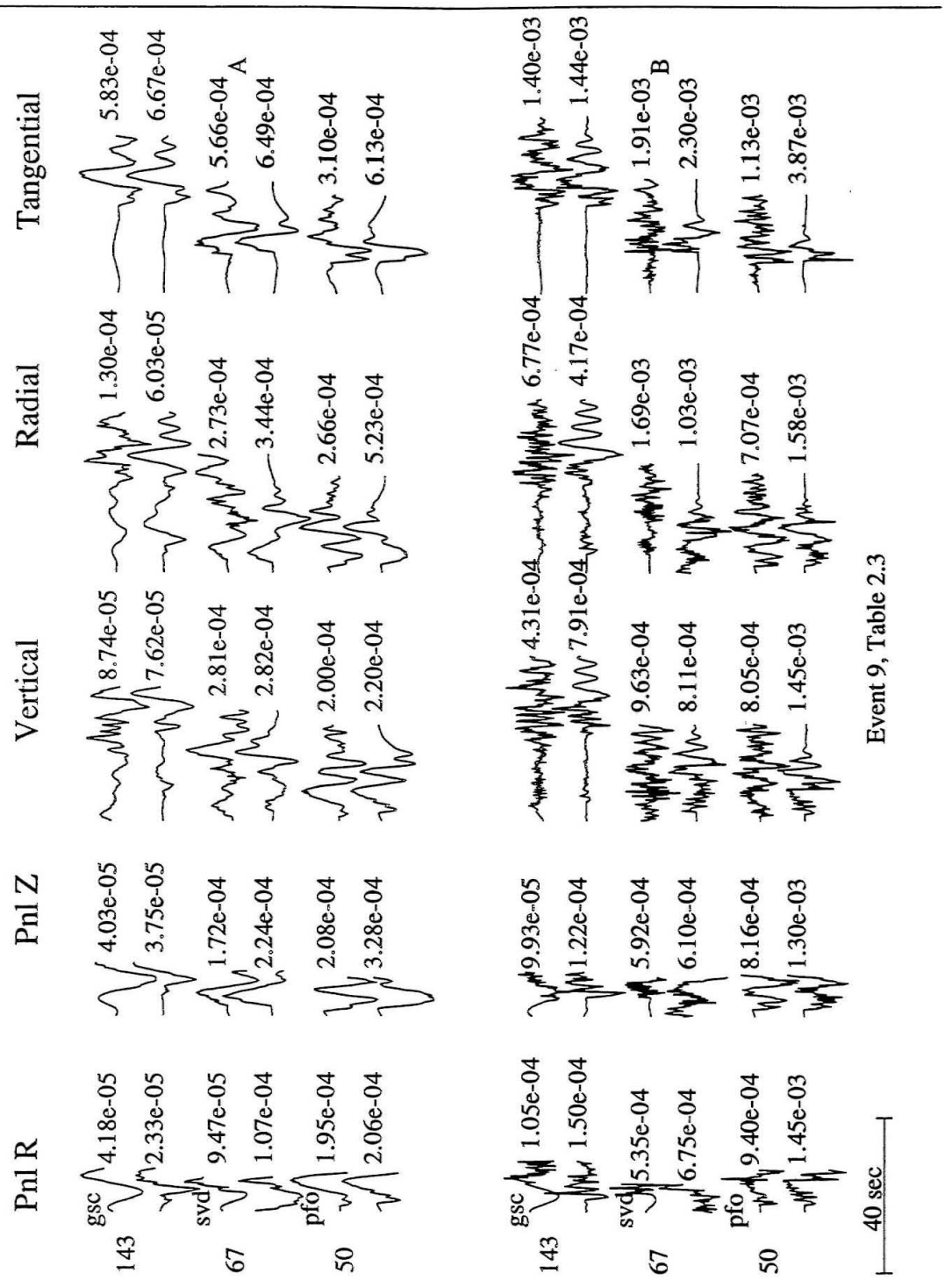

Figure 4.9: Broadband and long–period modeling for event 9, Table 2.4 (August 11, 1992). Average time function is a 0.30 s triangle. Source depth is estimated at 8 km.

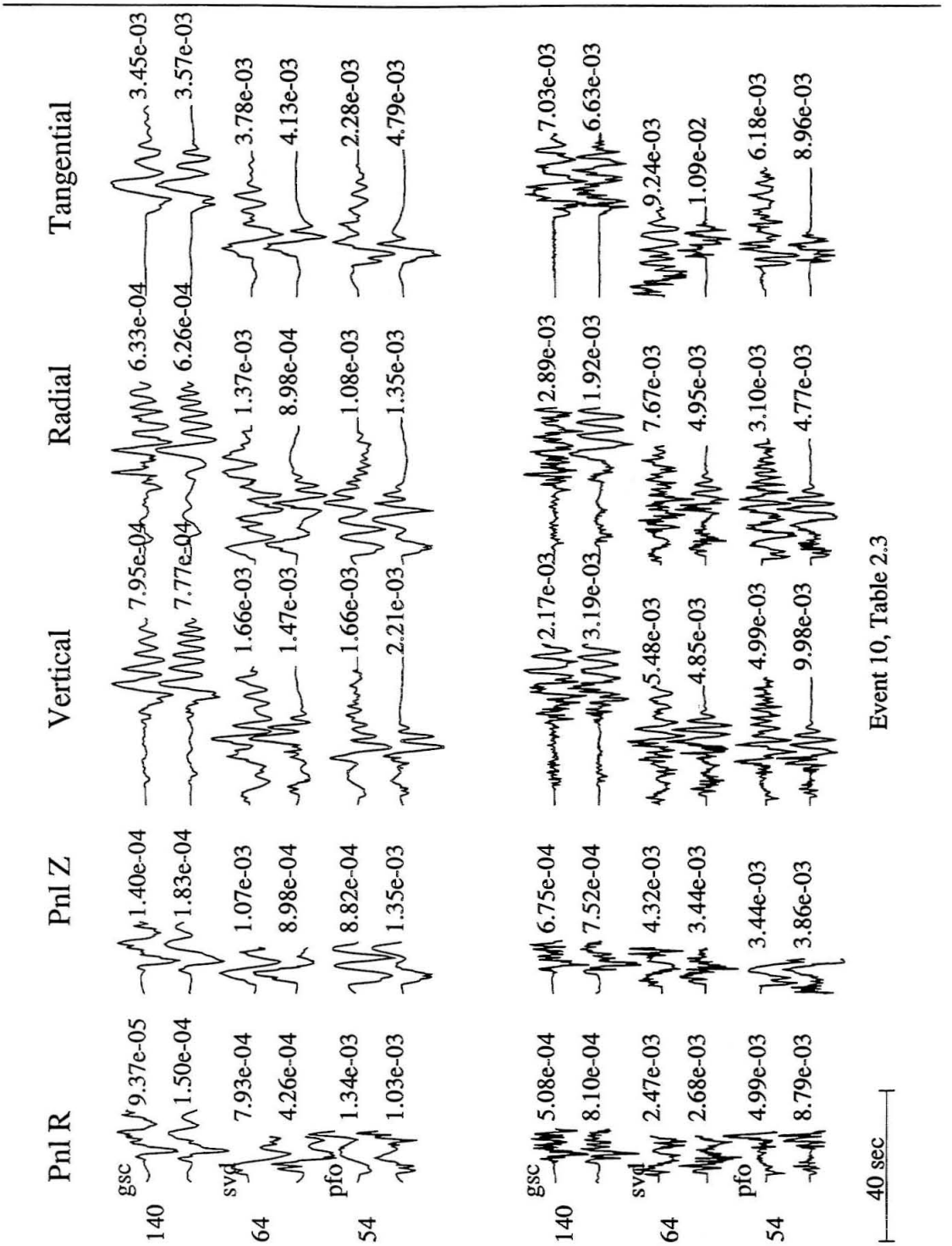

Figure 4.10: Broadband and long–period modeling for event 10, Table 2.4 (August 15, 1992). Average time function is a 0.30 s triangle. Source depth is estimated at 6 km.

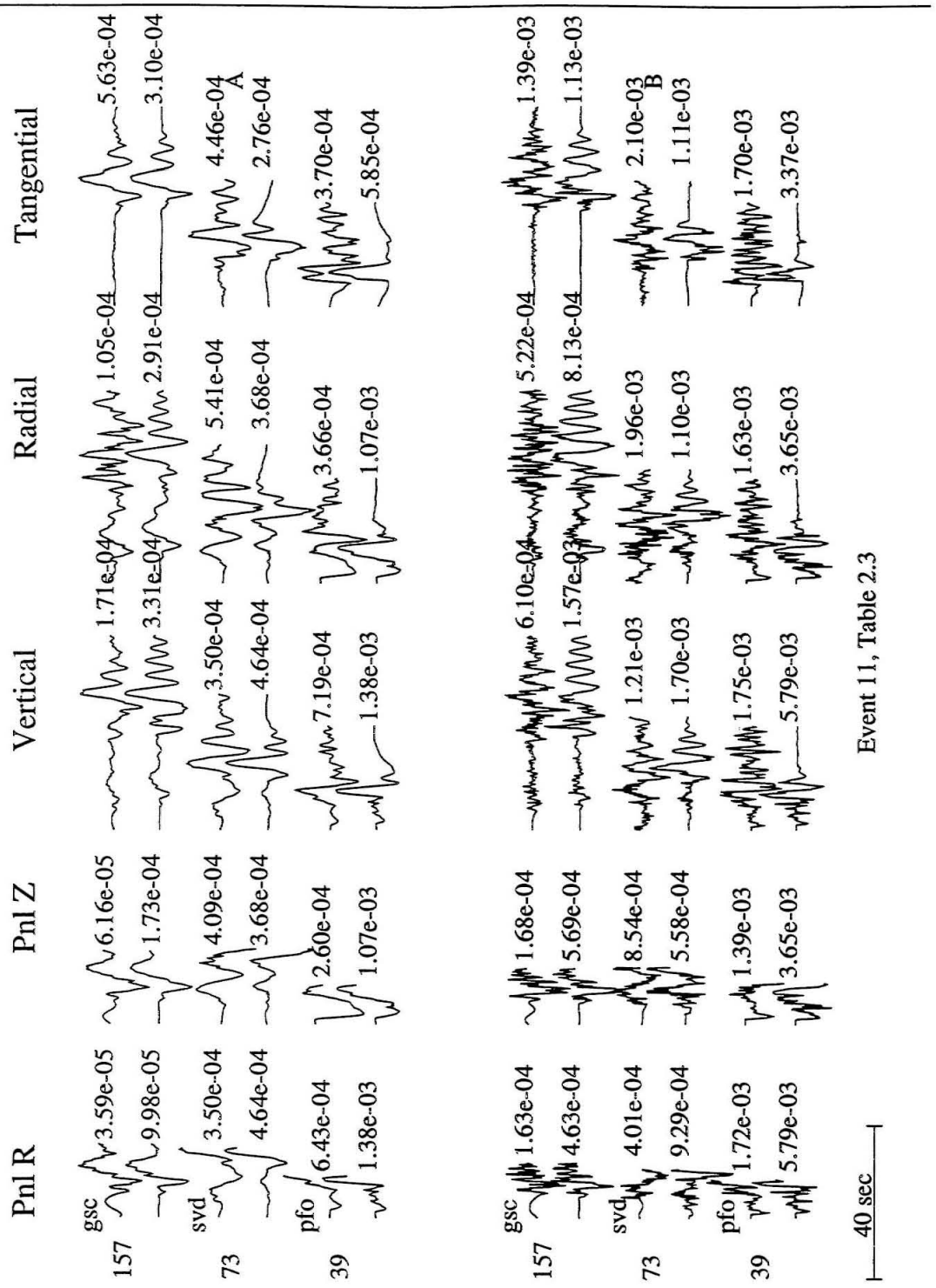

Figure 4.11: Broadband and long–period modeling for event 11, Table 2.4 (September 9, 1992). Average time function is a 0.50 s triangle. Source depth is estimated at 8 km.

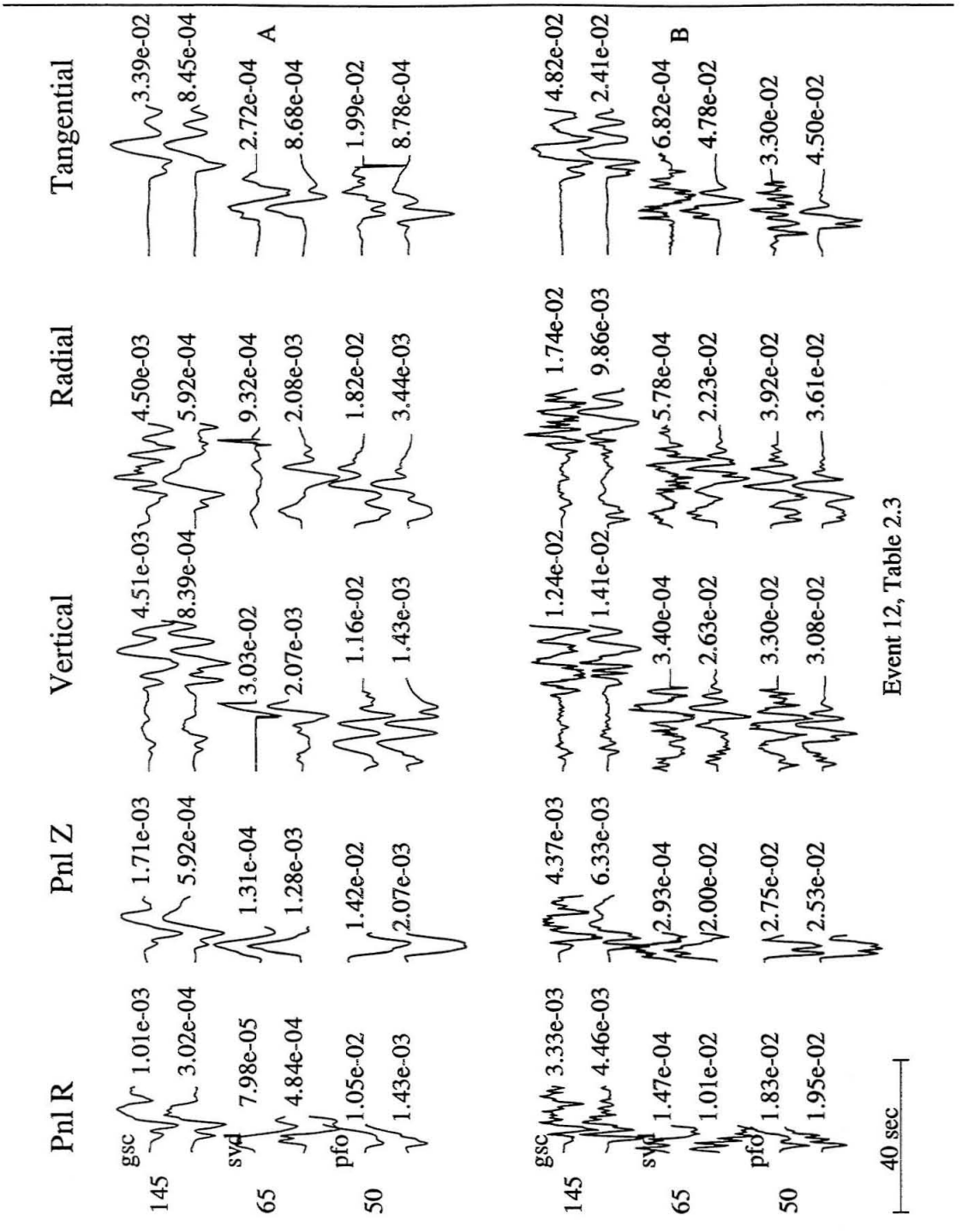

Figure 4.12: Broadband and long–period modeling for event 12, Table 2.4 (September 15, 1992). Average time function is a 1.1 s triangle. Source depth is estimated at 8 km.

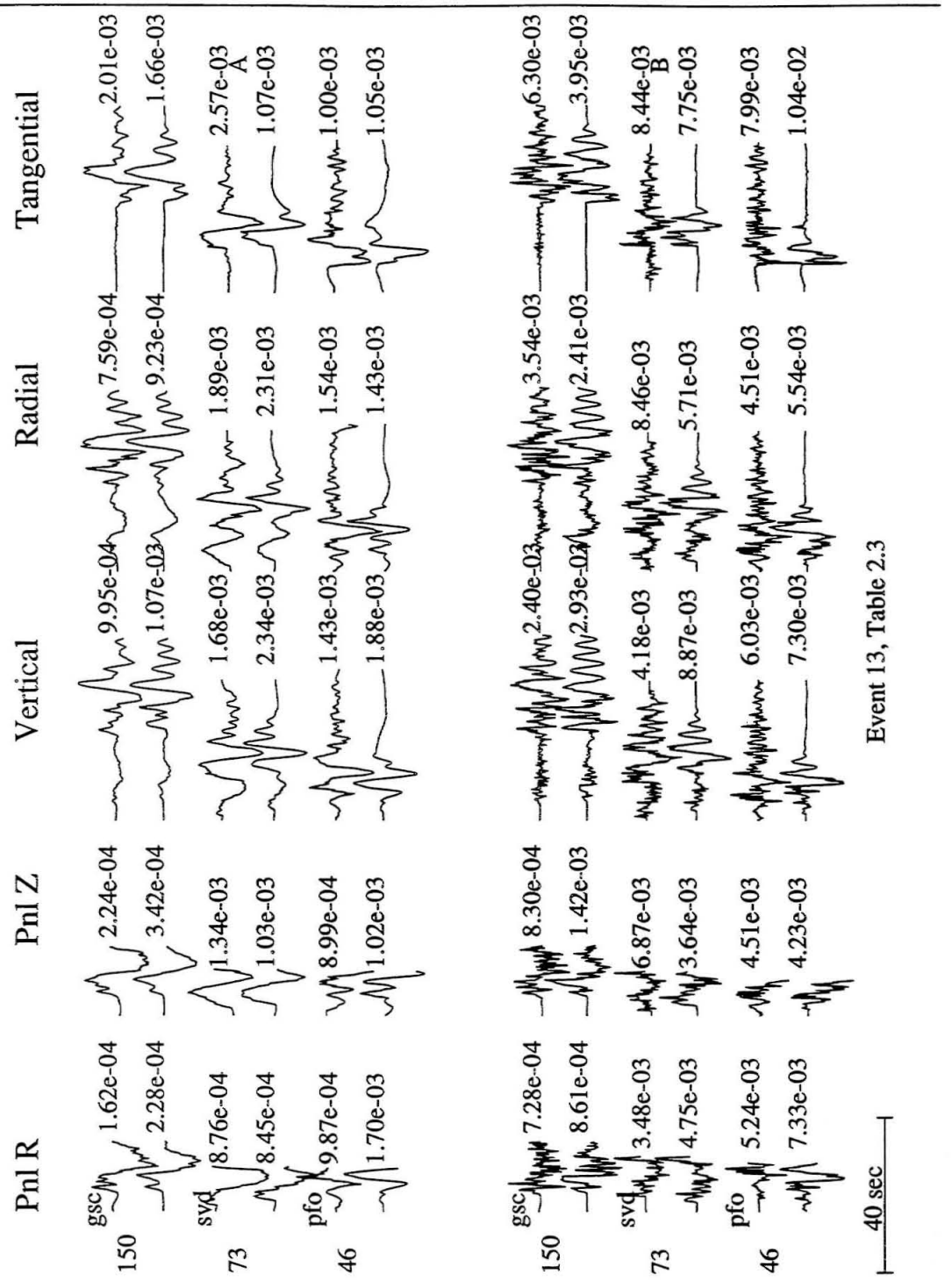

Figure 4.13: Broadband and long–period modeling for event 13, Table 2.4 (August 21, 1993). Average time function is a 0.6 s triangle. Source depth is estimated at 9 km.

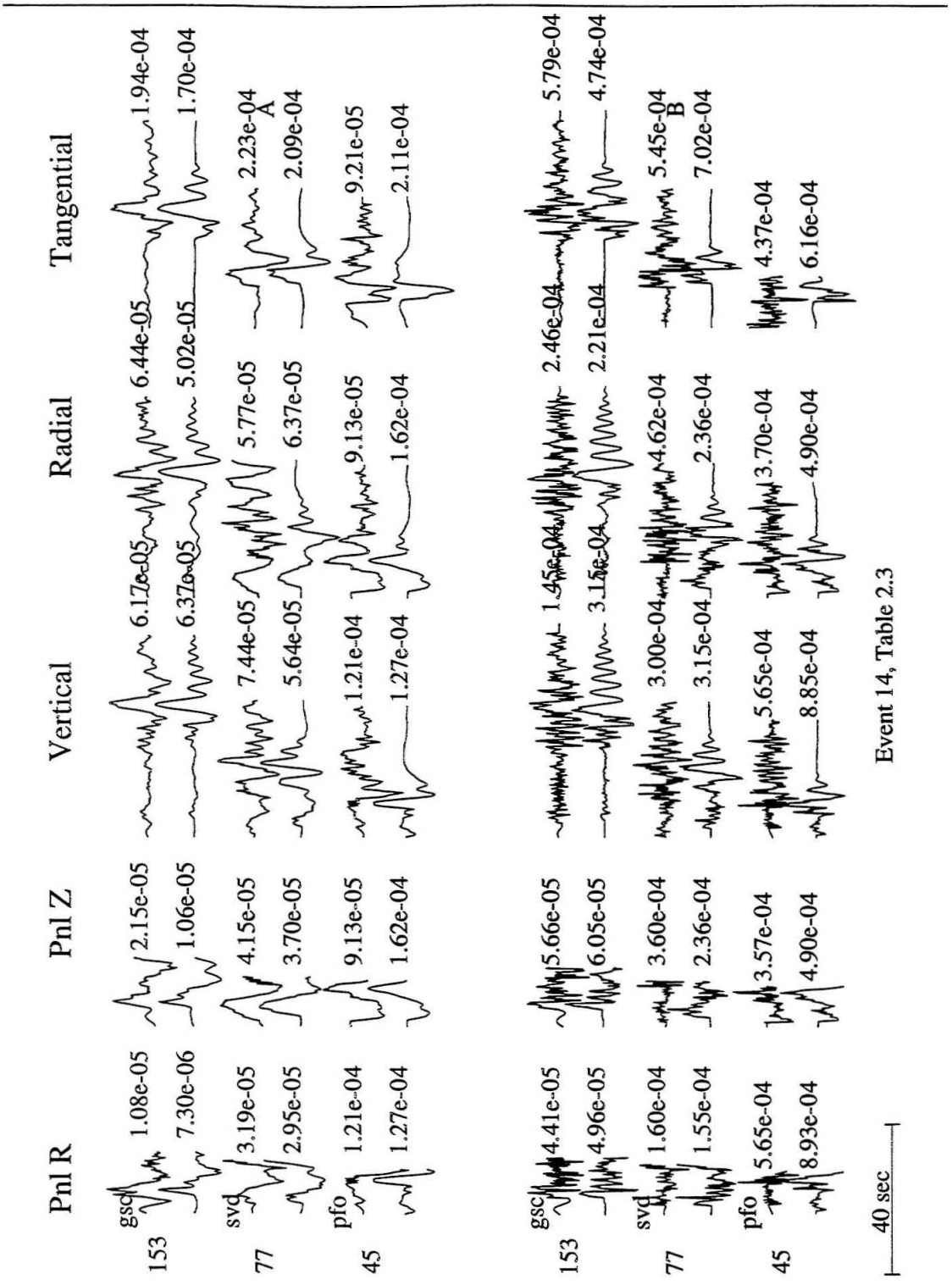

Figure 4.14: Broadband and long-period modeling for event 14, Table 2.4 (August 8, 1994). Average time function is a 0.55 s triangle. Source depth is estimated at 8 km.

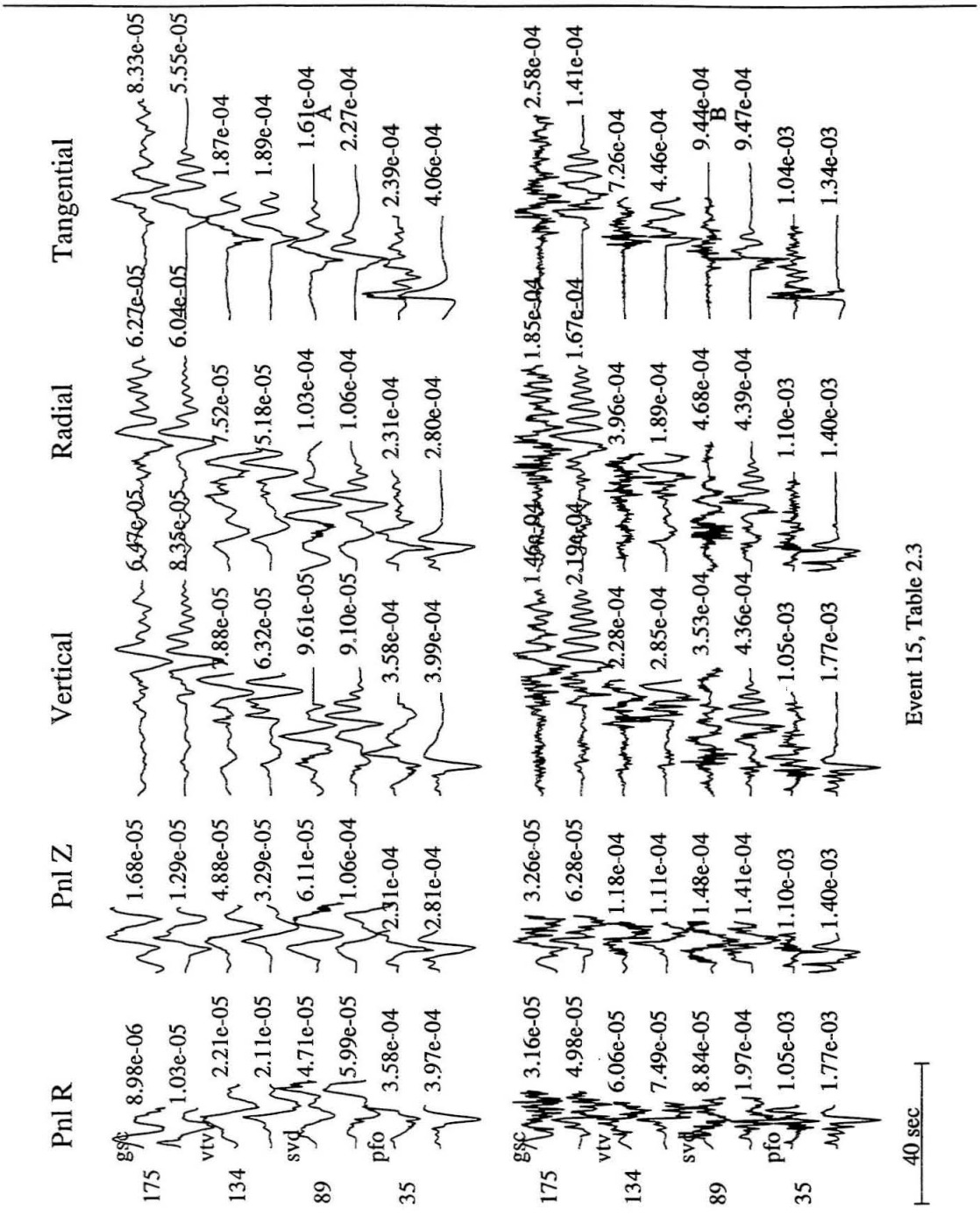

Figure 4.15: Broadband and long-period modeling for event 15, Table 2.4 (August 15, 1994). Average time function is a 0.55 s triangle. Source depth is estimated at 9 km.

Chapter 5

Appendix II

5.1 Modeling 2: North of the Pinto Mountain Fault

This Appendix comprises a catalog of much of the modeling results for Landers events North of the Pinto Mountain fault [Table 2.5]. The modeling was done using theoretical Green's functions from the Mojave model [Table 2.1], and between three and five stations. The stations most commonly used are stations GSC, PFO, and SVD. When the solutions seemed unstable, or records from one of the above stations were not available, records from stations ISA or PAS were included. The waveform fits shown on the next few pages and in Appendix I result from source modeling using the grid–search algorithm briefly discussed in section 2.5.

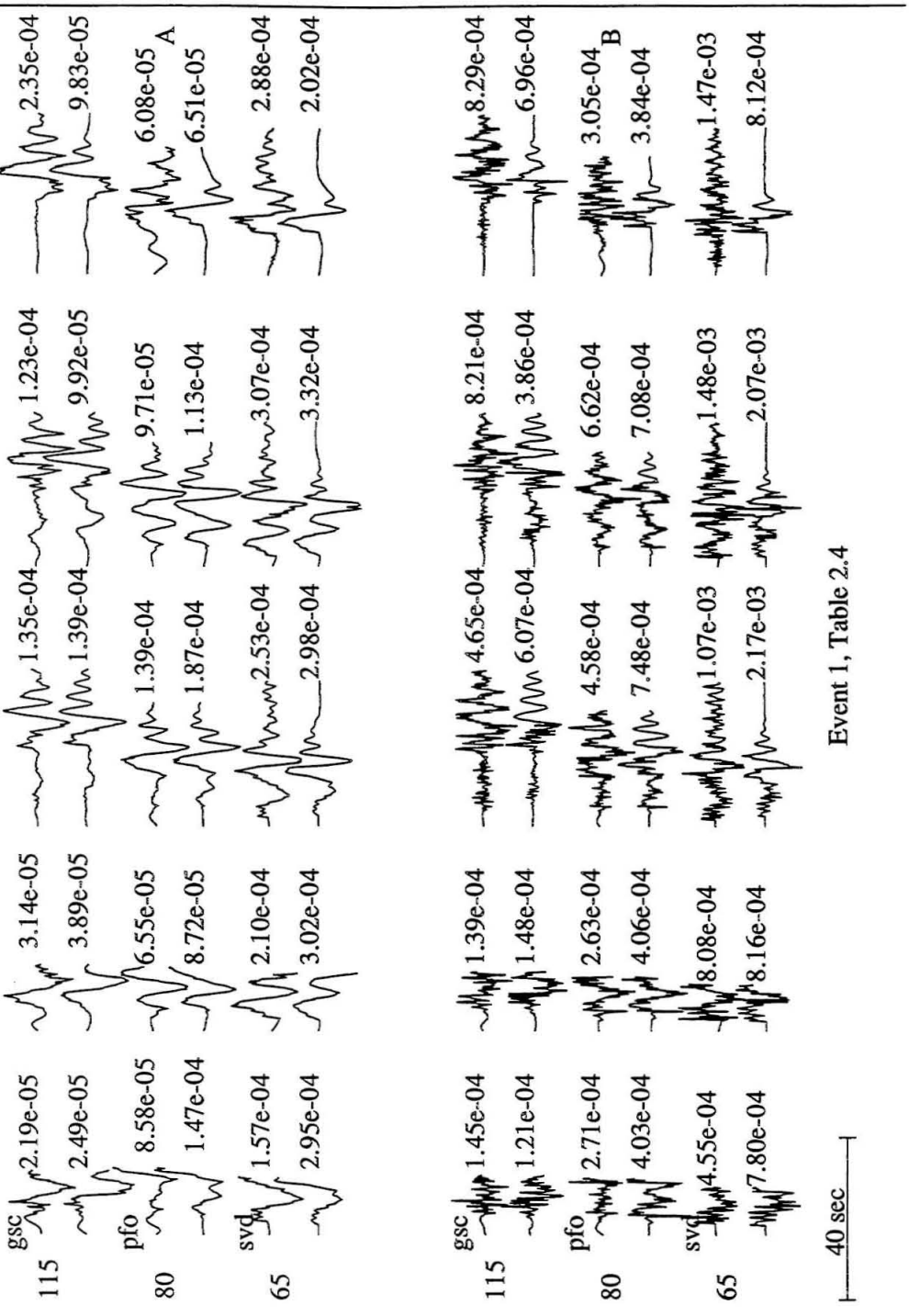

Figure 5.1: Broadband and long–period modeling for event 1, Table 2.5 (June 30, 1992, 12: GMT). Average time function is a 0.30 s triangle. Source depth is estimated at 9 km.

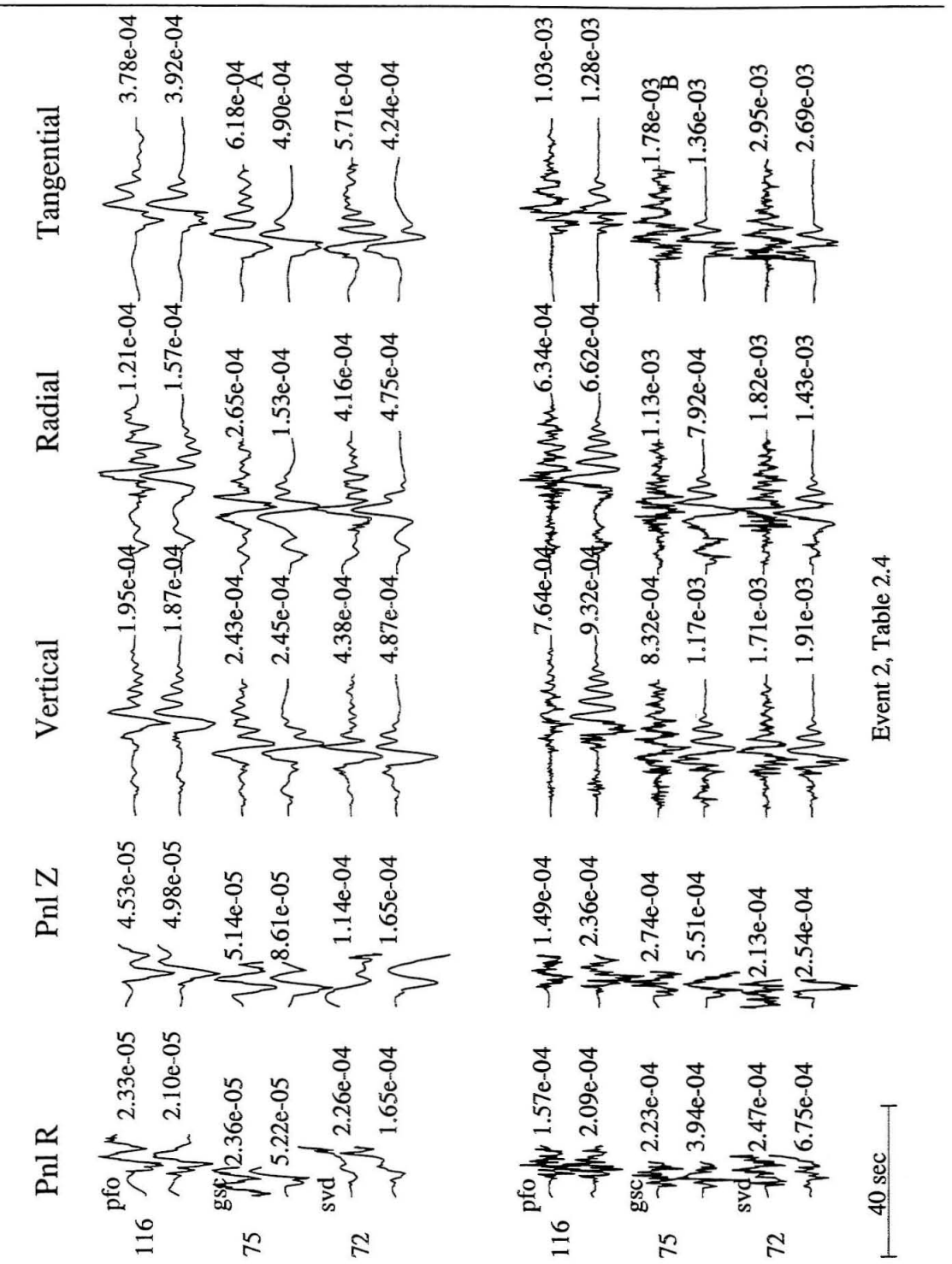

Figure 5.2: Broadband and long–period modeling for event 2, Table 2.5 (June 30, 1992, 17: GMT). Average time function is a 0.5 s triangle. Source depth is estimated at 8 km.

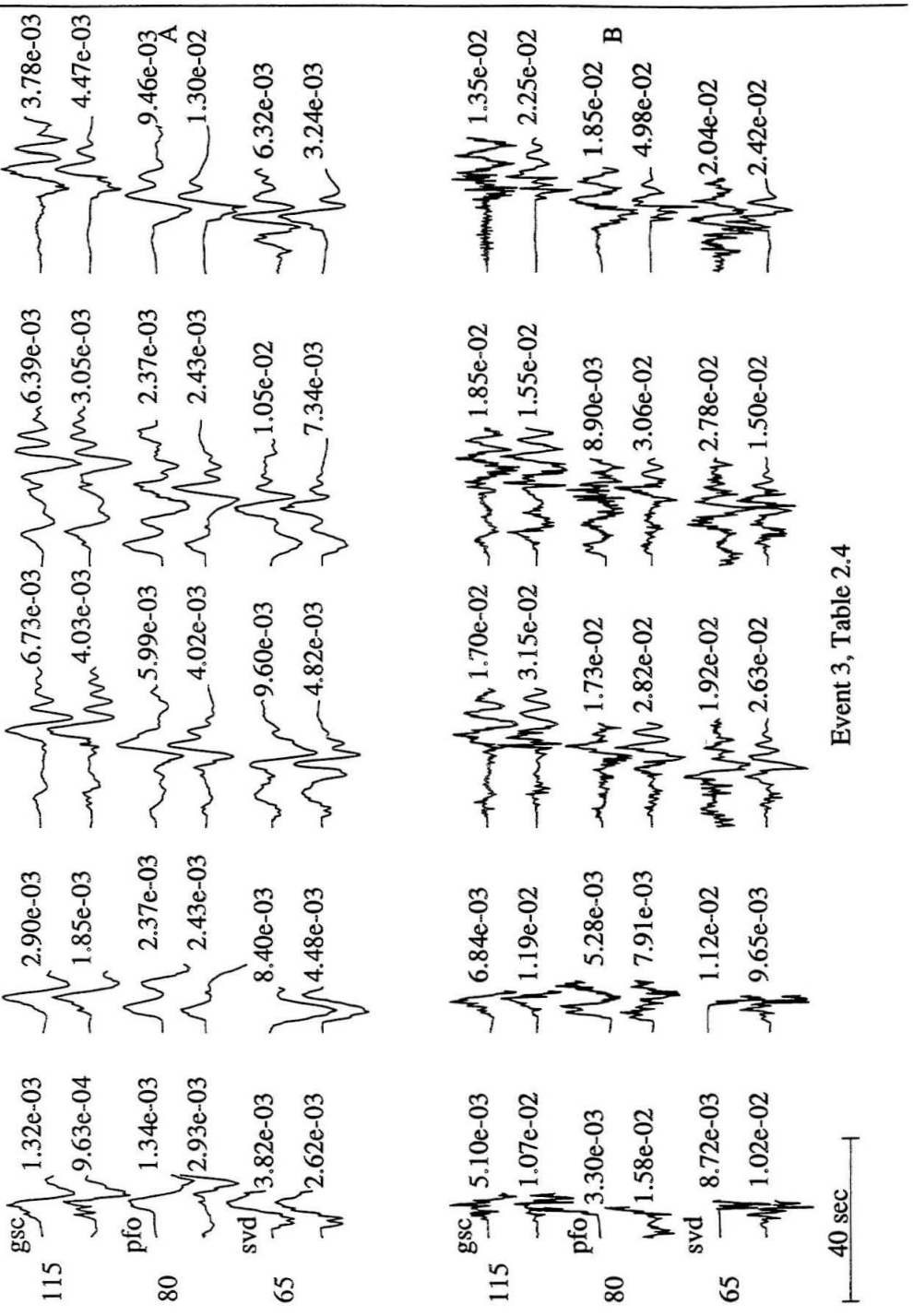

Figure 5.3: Broadband and long-period modeling for event 3, Table 2.5 (July 1, 1992). Average time function is a 0.6 s triangle. Source depth is estimated at 7 km.

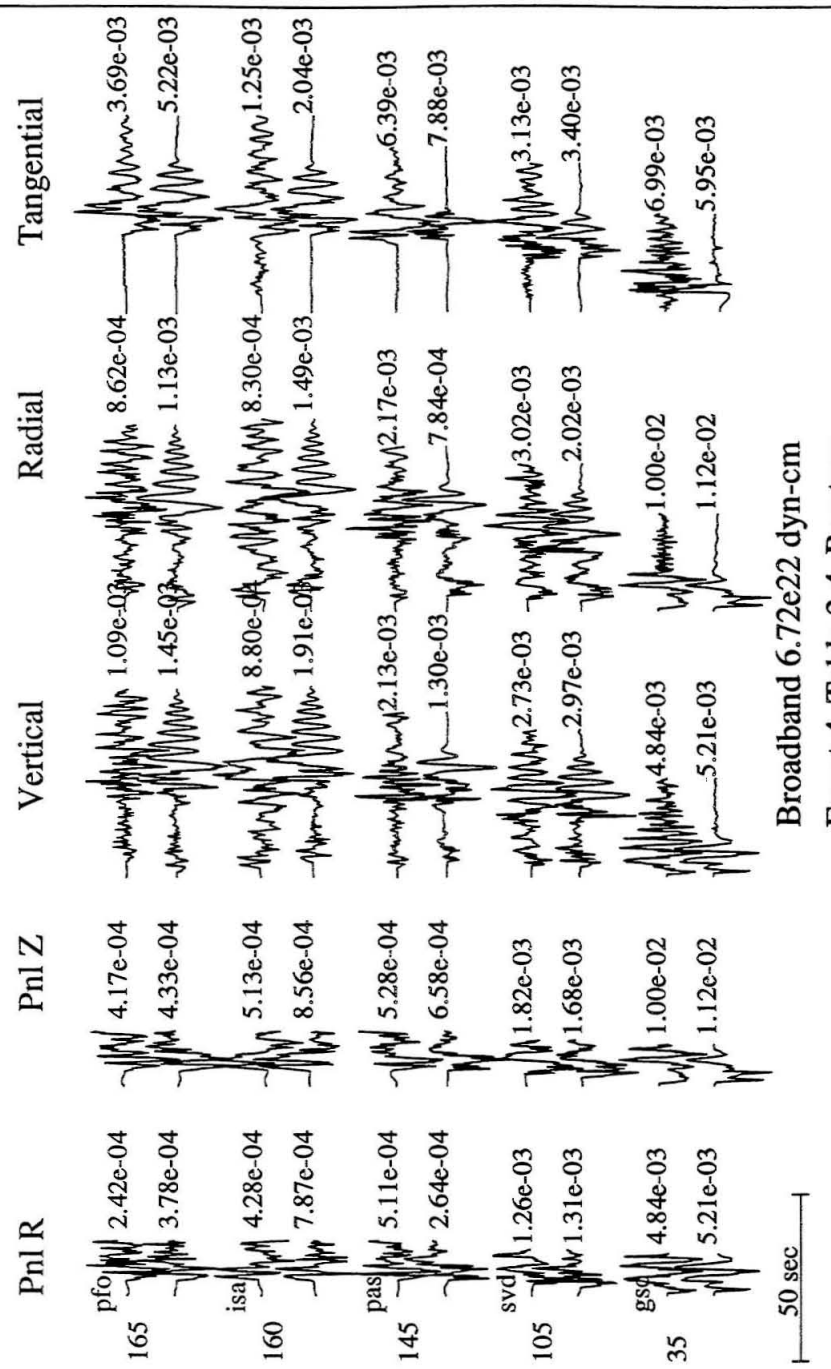

Figure 5.4: Broadband modeling for event 4, Table 2.5 (July 5, 1992, 10:55 GMT). Average time function is a 0.6 s triangle. Source depth is estimated at 8 km.

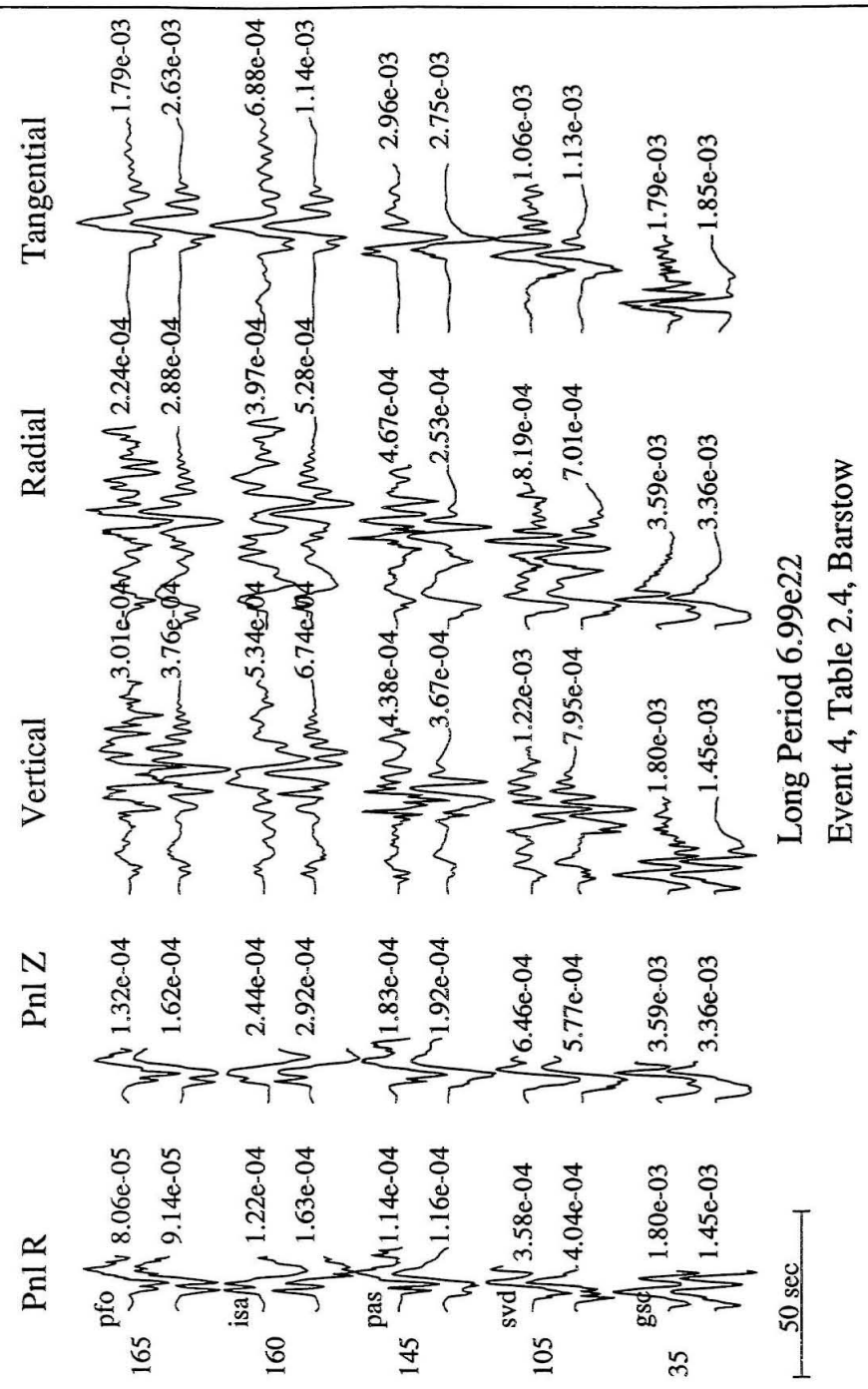

Figure 5.5: Long–period modeling for event 4, Table 2.5 (July 5, 1992, 10:55 GMT). Average time function is a 0.6 s triangle. Source depth is estimated at 8 km.

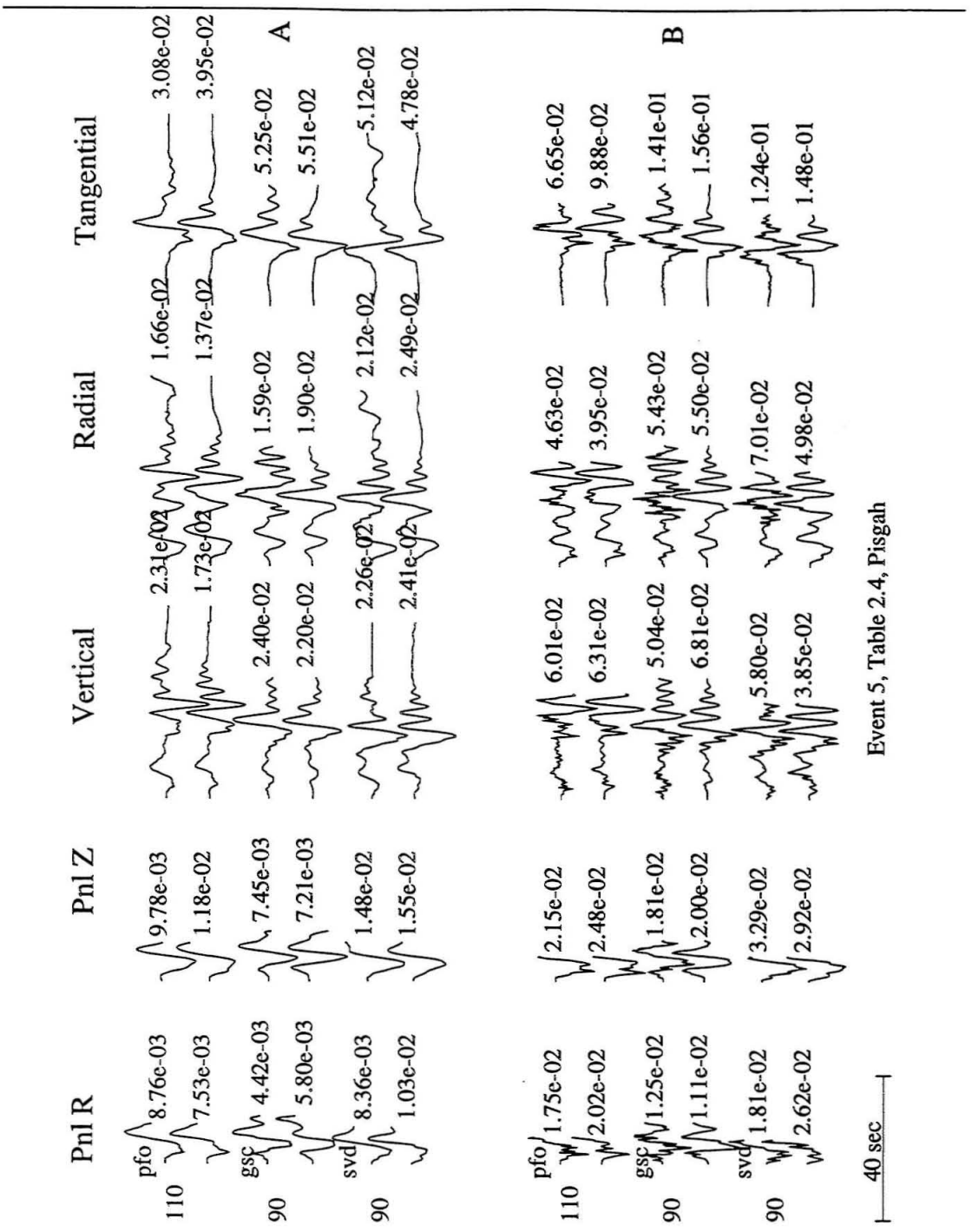

Figure 5.6: Broadband and long–period modeling for event 5, Table 2.5 (July 5, 1992, 21:18 GMT). Average time function is a 1.5 s triangle. Source depth is estimated at 8 km.

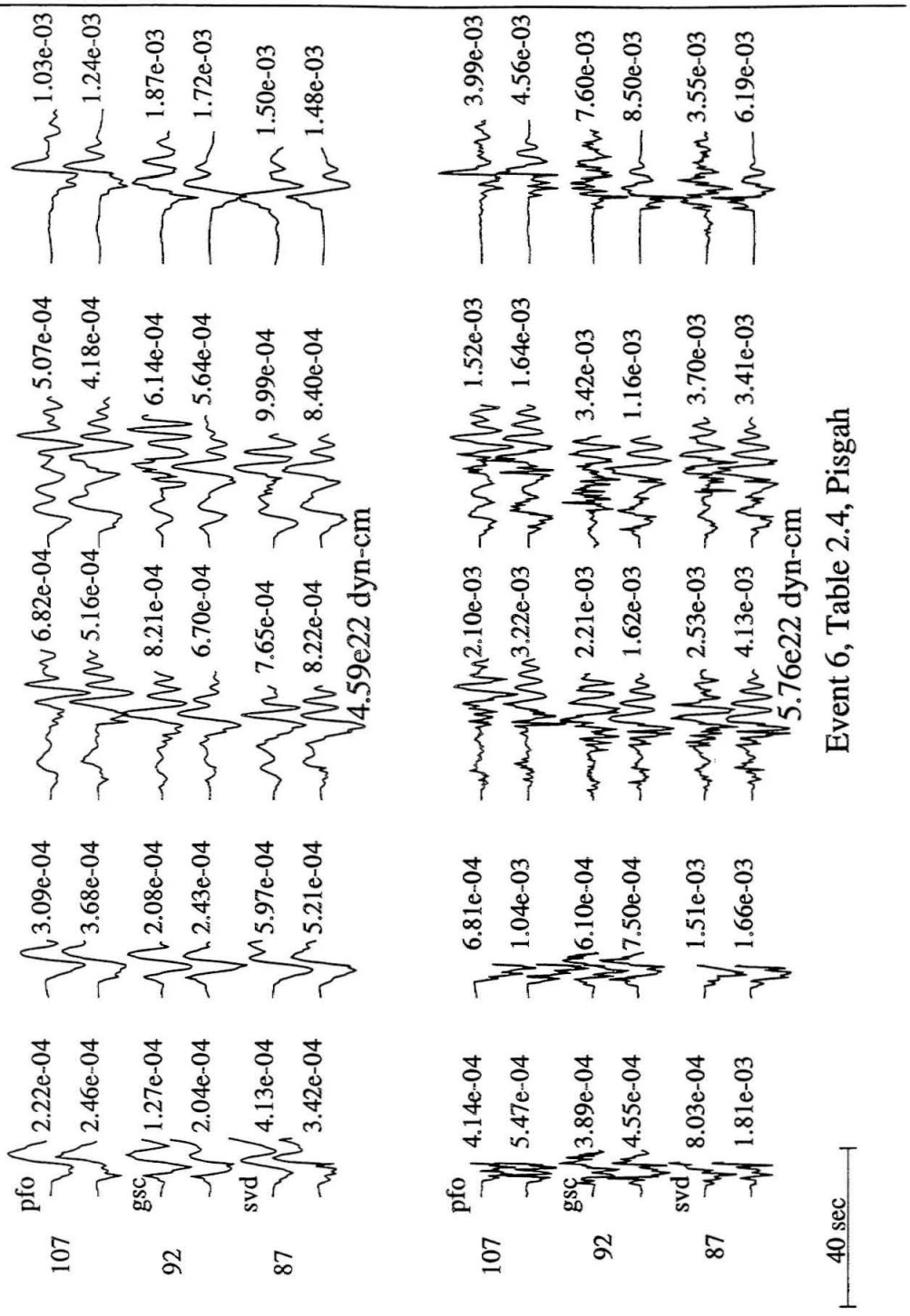

Figure 5.7: Broadband and long-period modeling for event 6, Table 2.5 (July 5, 1992, 22:33 GMT). Average time function is a 0.7 s triangle. Source depth is estimated at 9 km.

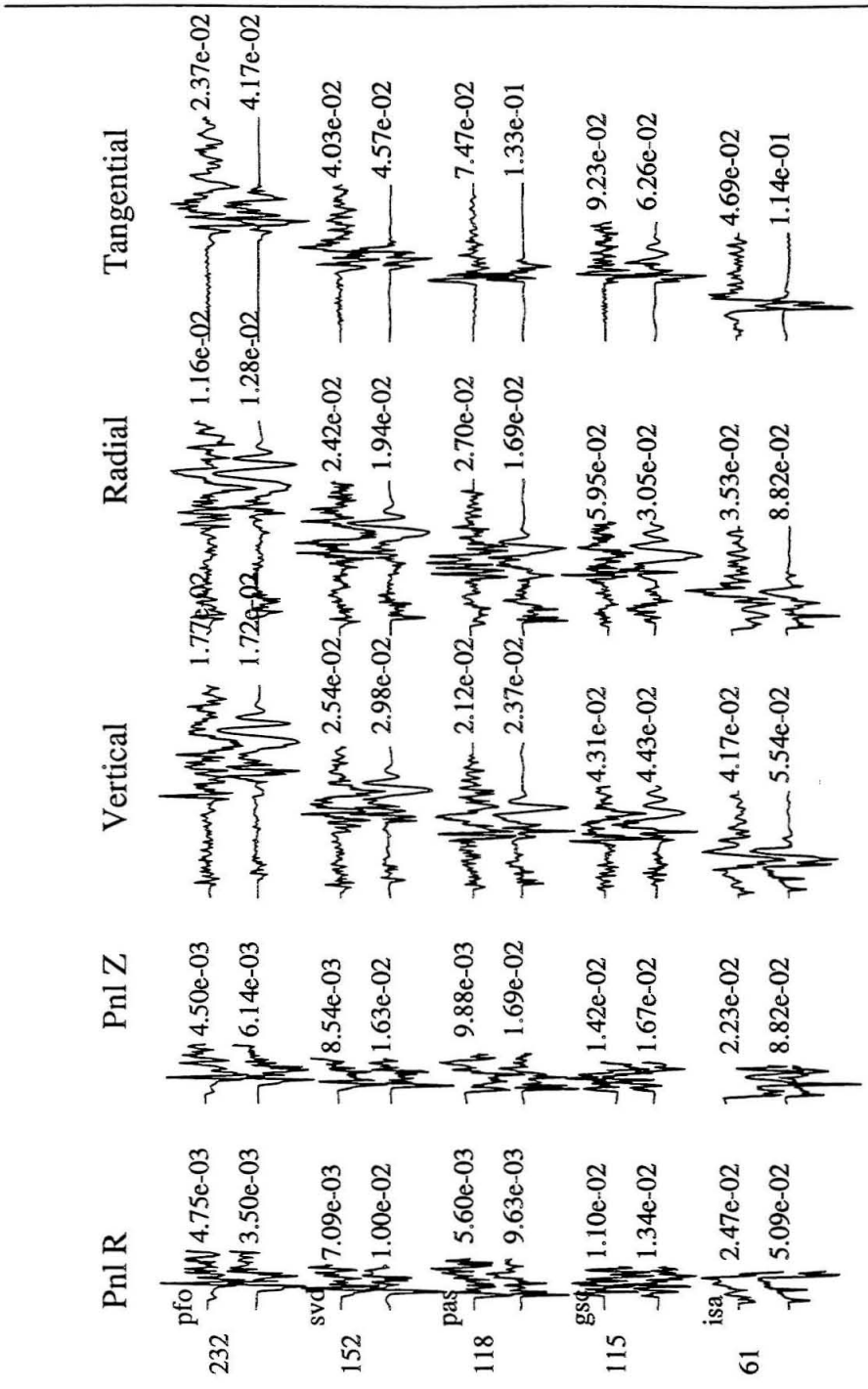

Figure 5.8: Broadband modeling for event 8, Table 2.5 (July 11, 1992, Garlock). Average time function is a 0.5 s triangle. Source depth is estimated at 11 km.

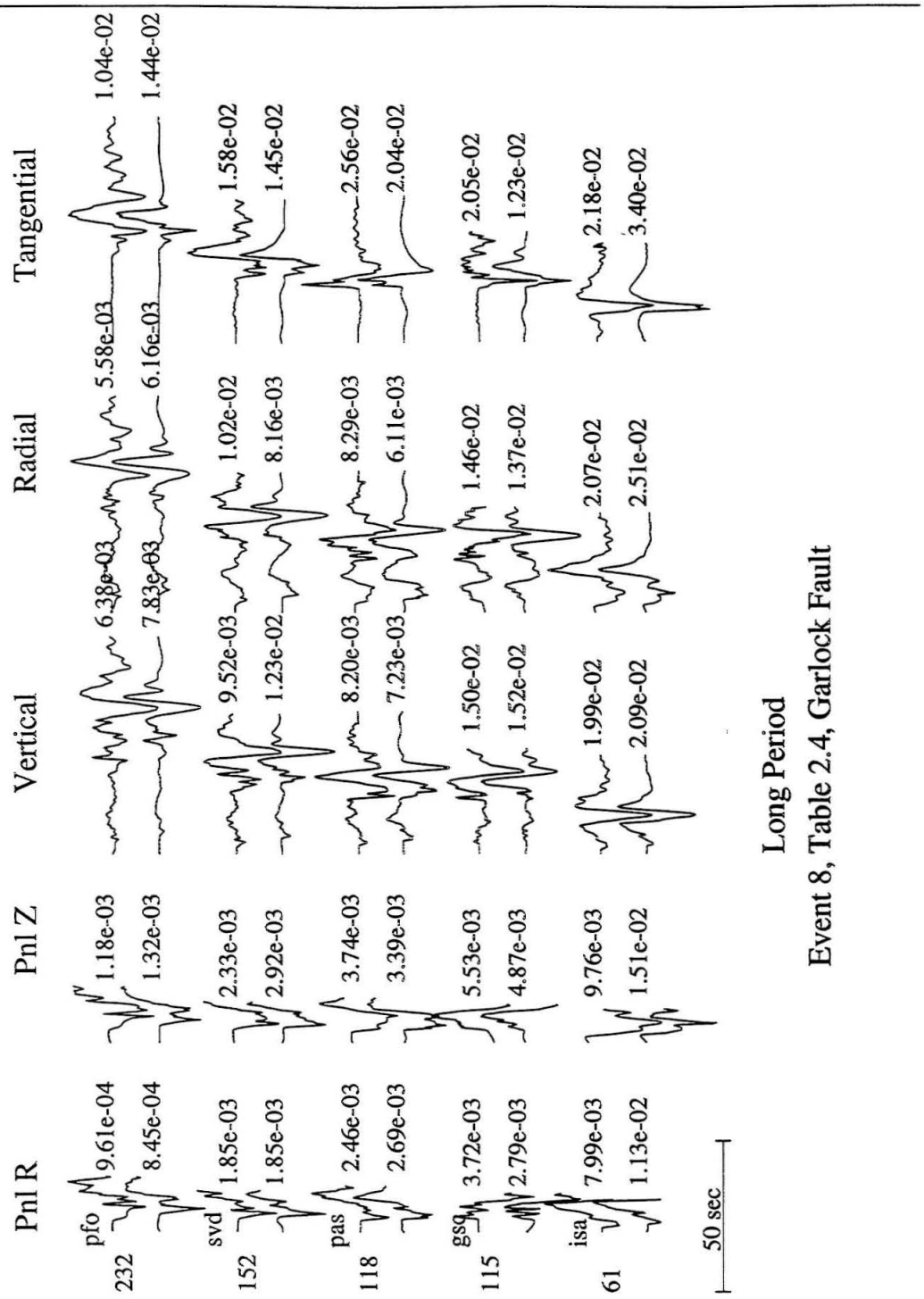

Figure 5.9: Long–period modeling for event 8, Table 2.5 (July 11, 1992, Garlock). Average time function is a 0.5 s triangle. Source depth is estimated at 11 km.

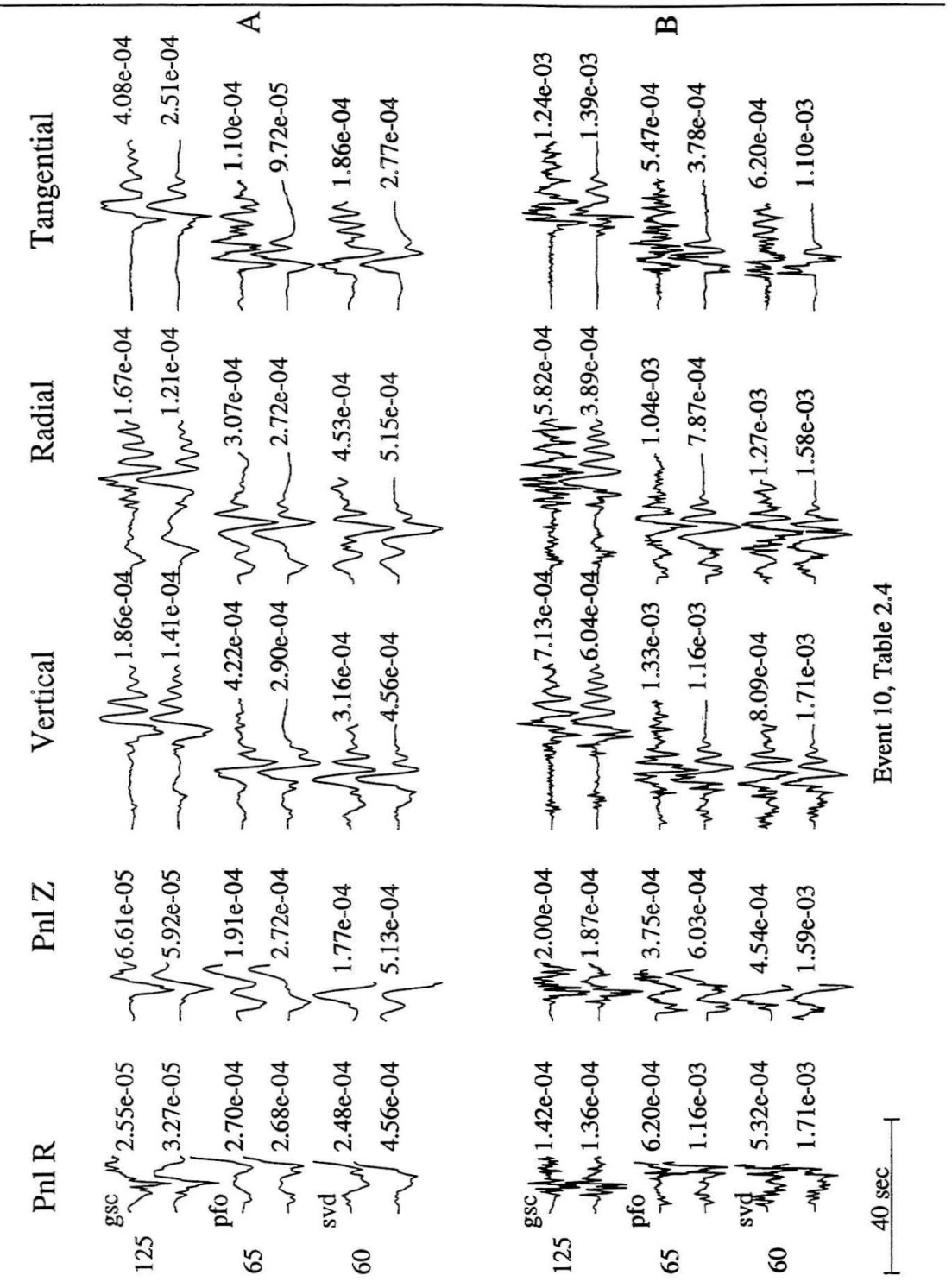

Figure 5.10: Broadband and long–period modeling for event 10, Table 2.5 (July 20, 1992, 04:0 GMT). Average time function is a 0.6 s triangle. Source depth is estimated at 9 km.

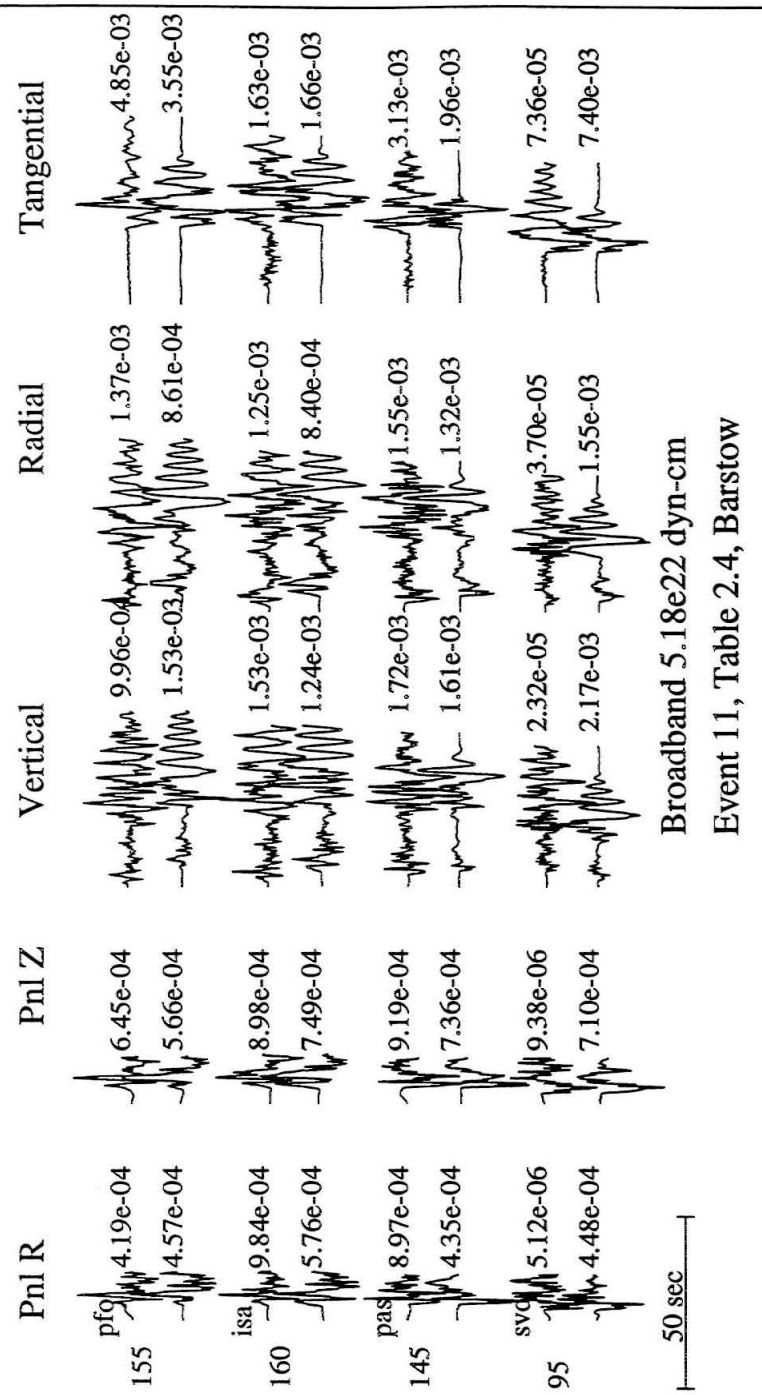

Figure 5.11: Broadband modeling for event 11, Table 2.5 (July 20, 1992, 04:4 GMT, Barstow). Average time function is a 0.8 s triangle. Source depth is estimated at 7 km.

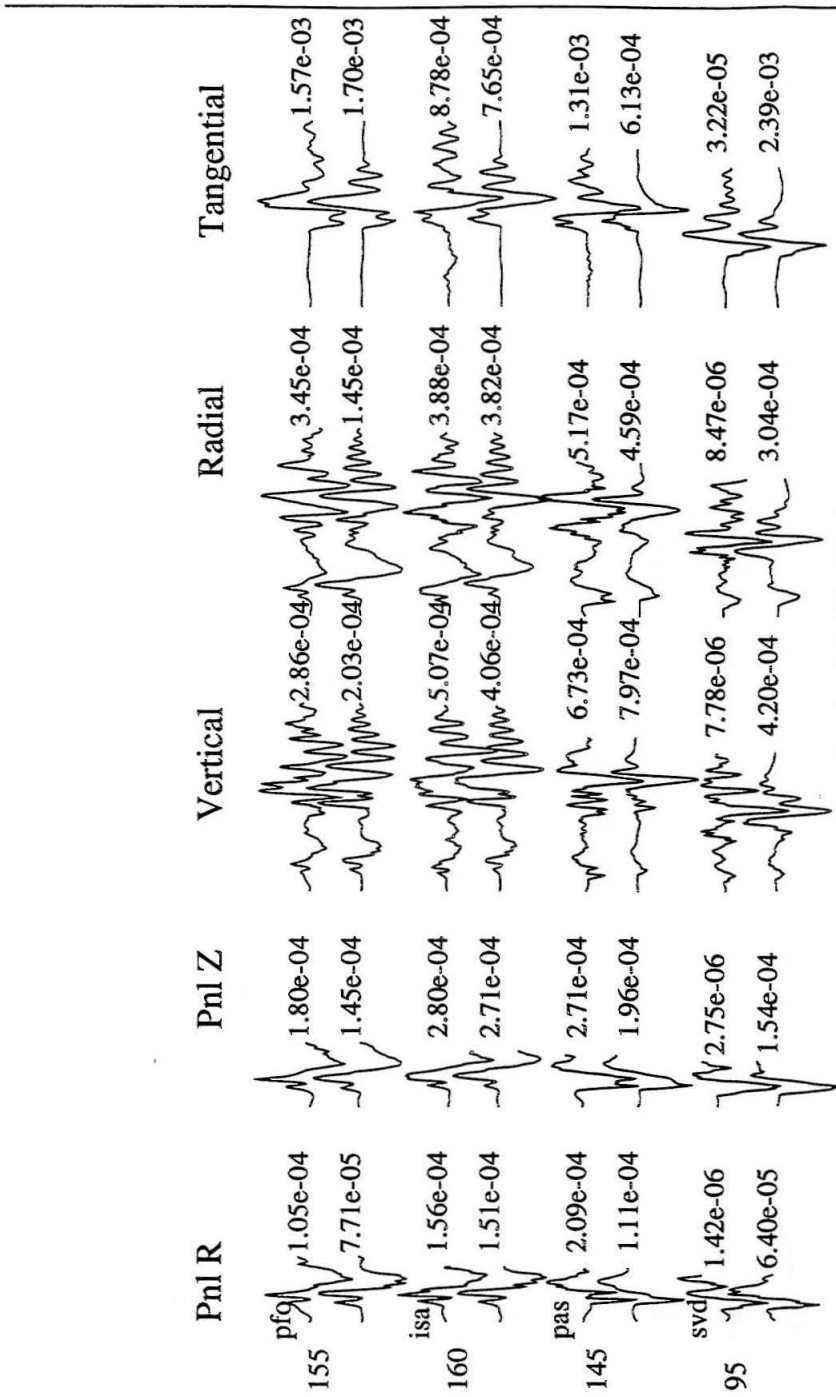

Figure 5.12: Long–period modeling for event 11, Table 2.5 (July 20, 1992, 04:4 GMT, Barstow). Average time function is a 0.8 s triangle. Source depth is estimated at 7 km.

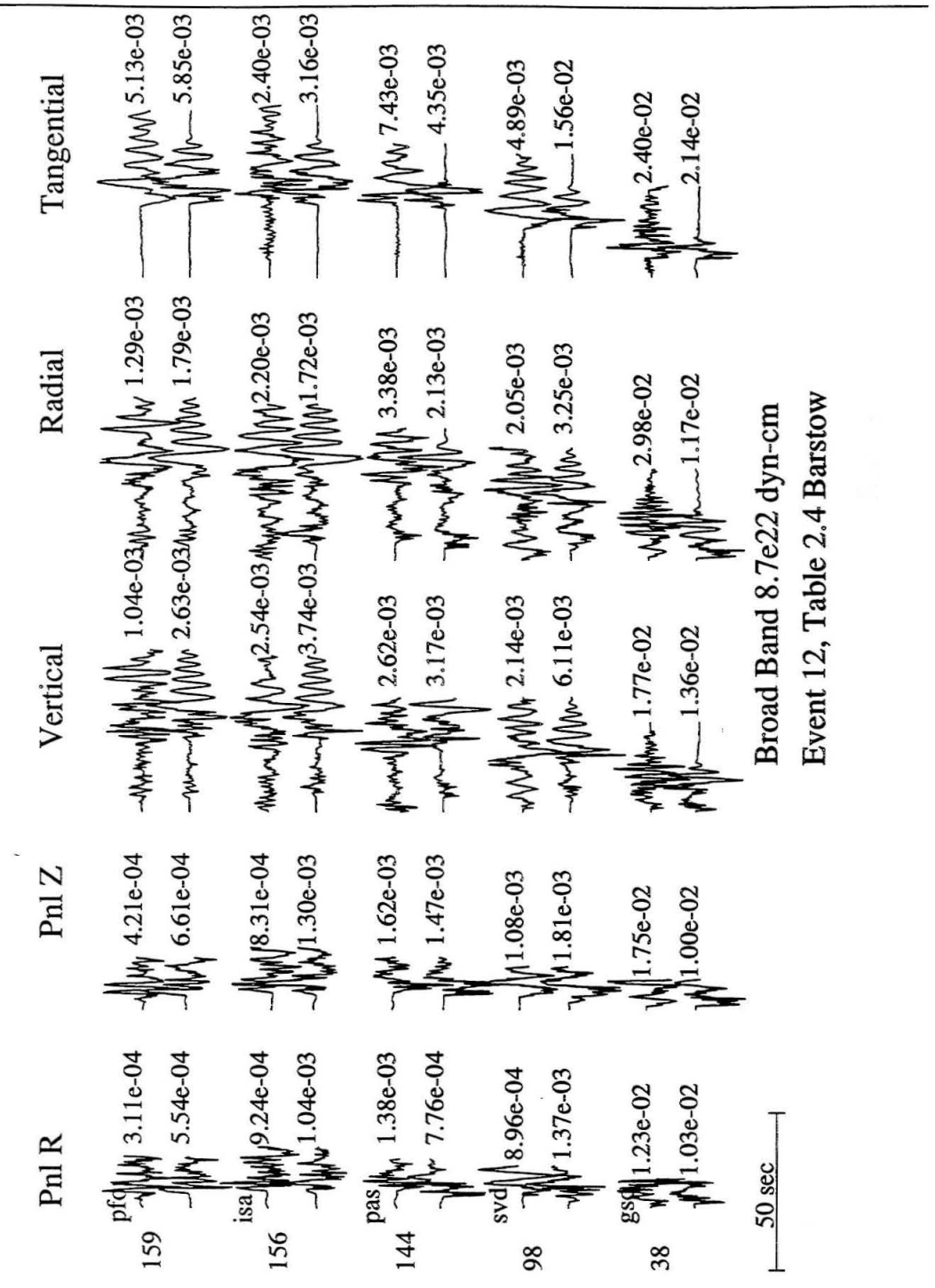

Figure 5.13: Broadband modeling for event 12, Table 2.5 (July 20, 1992, 13: GMT, Barstow). Average time function is a 0.6 s triangle. Source depth is estimated at 5 km.

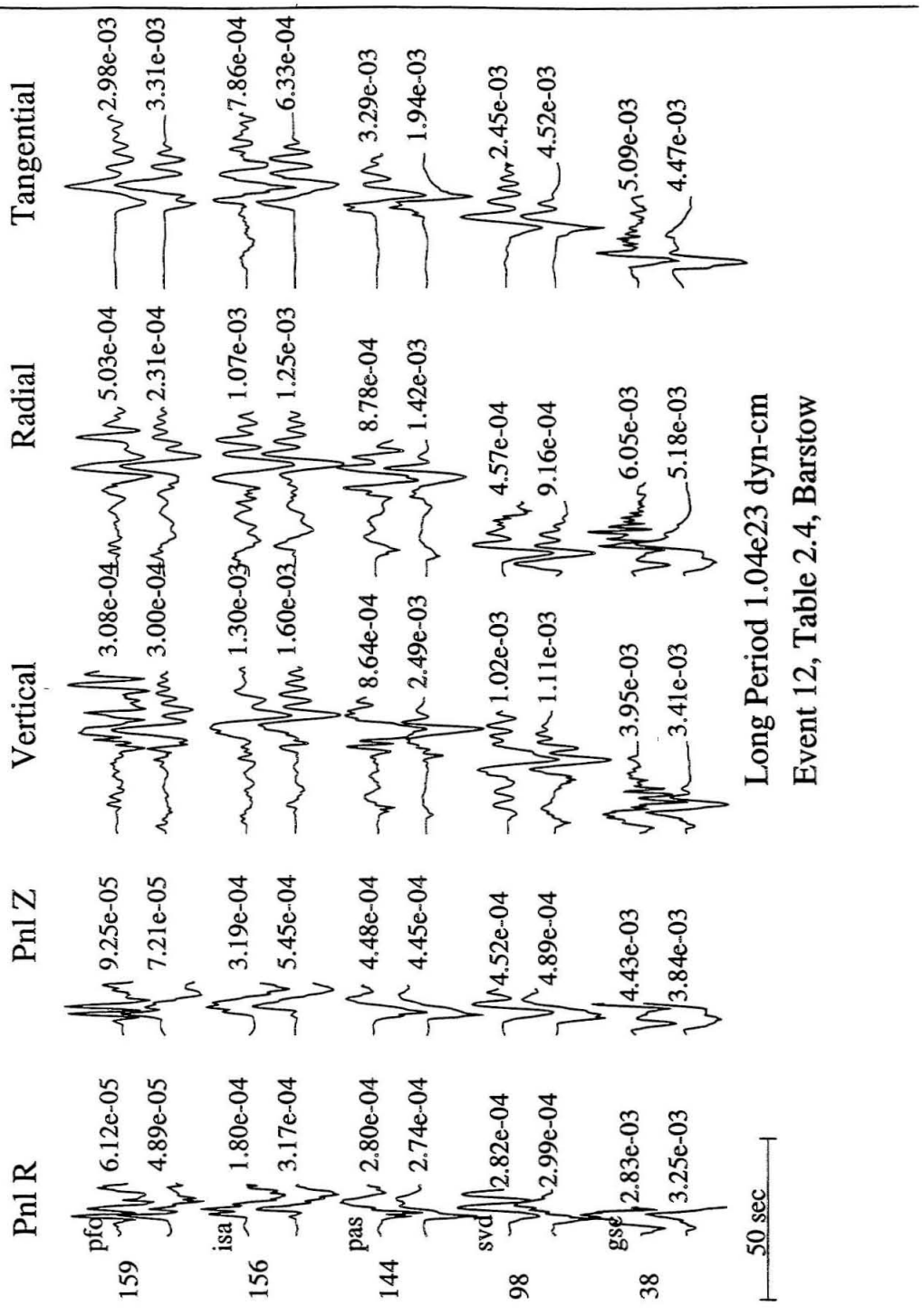

Figure 5.14: Long–period modeling for event 12, Table 2.5 (July 20, 1992, 13: GMT, Barstow). Average time function is a 0.6 s triangle. Source depth is estimated at 5 km.

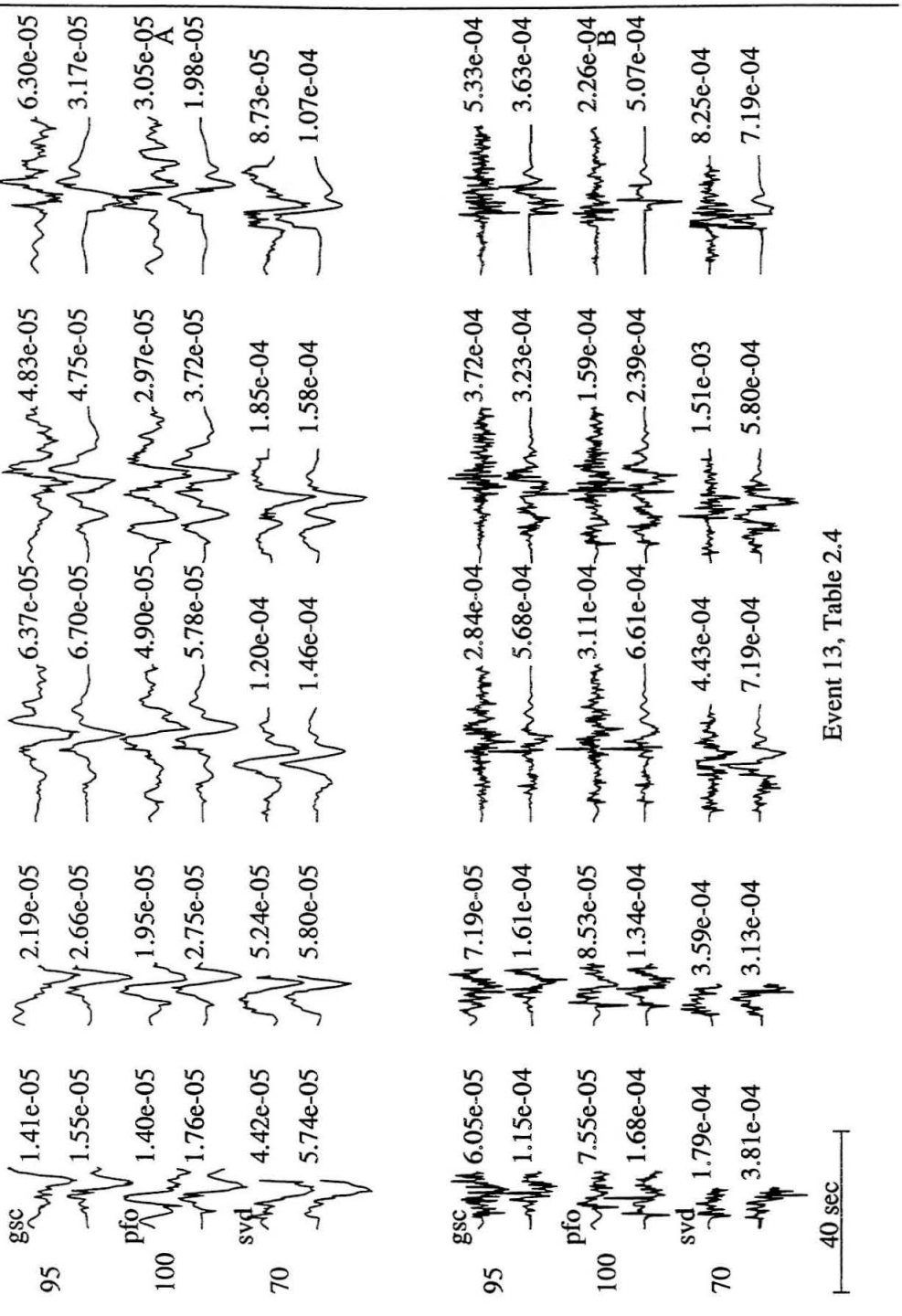

Figure 5.15: Broadband and long–period modeling for event 13, Table 2.5 (July 24, 1992). Average time function is a 0.3 s triangle. Source depth is estimated at 11 km.

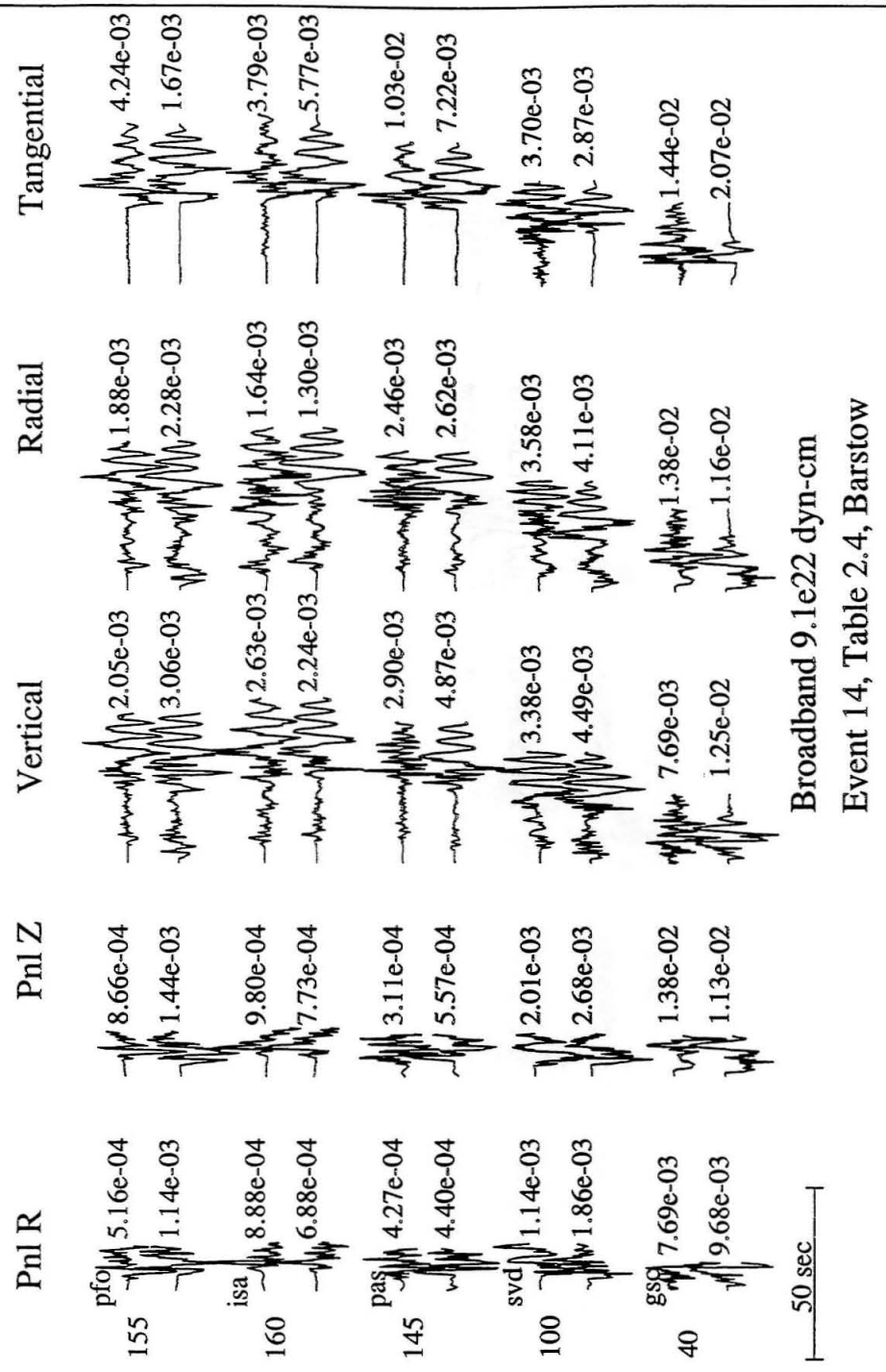

Figure 5.16: Broadband modeling for event 14, Table 2.5 (August 5, 1992). Average time function is a 0.6 s triangle. Source depth is estimated at 6 km.

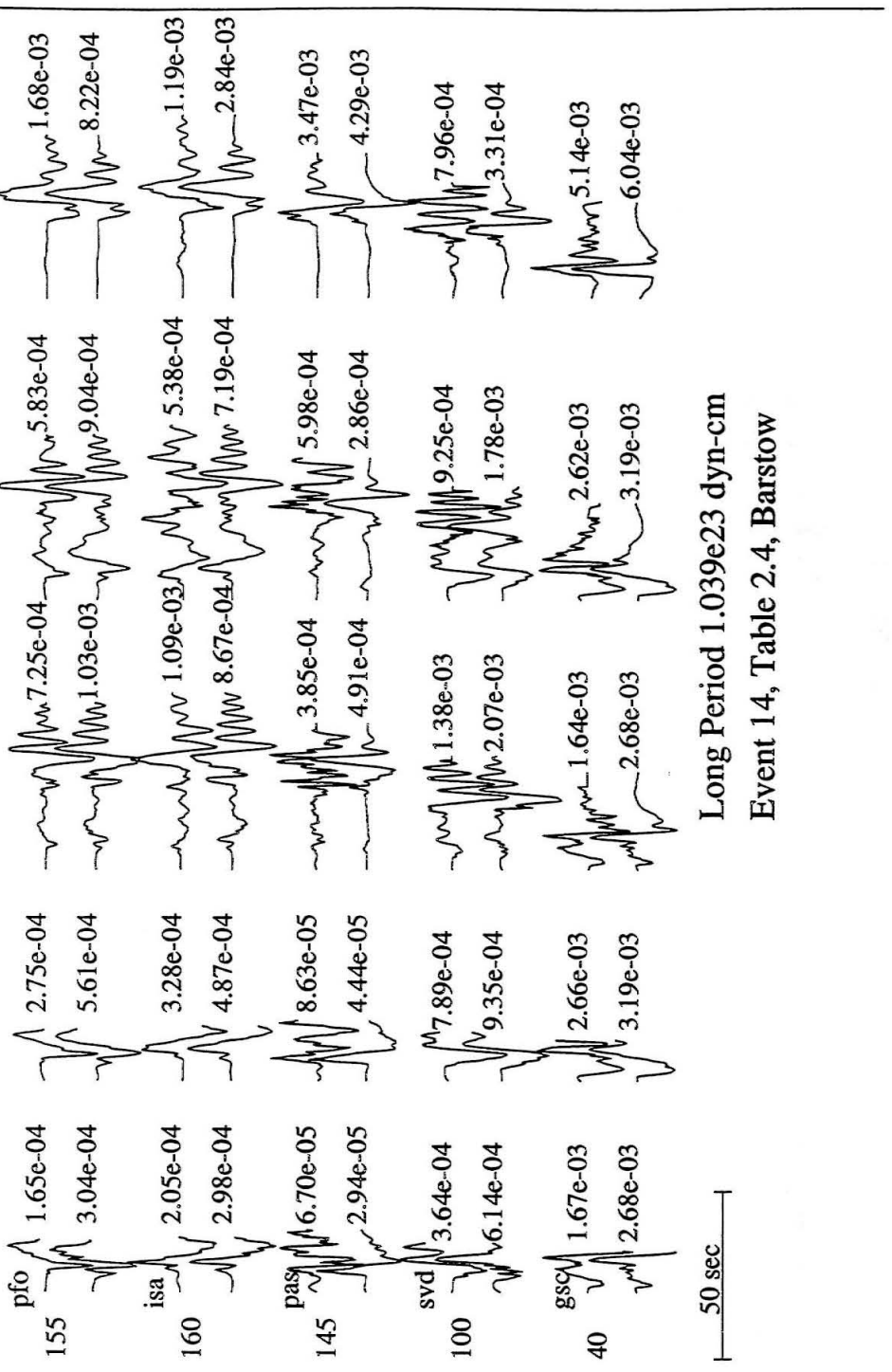

Figure 5.17: Long-period modeling for event 14, Table 2.5 (August 5, 1992). Average time function is a 0.6 s triangle. Source depth is estimated at 6 km.

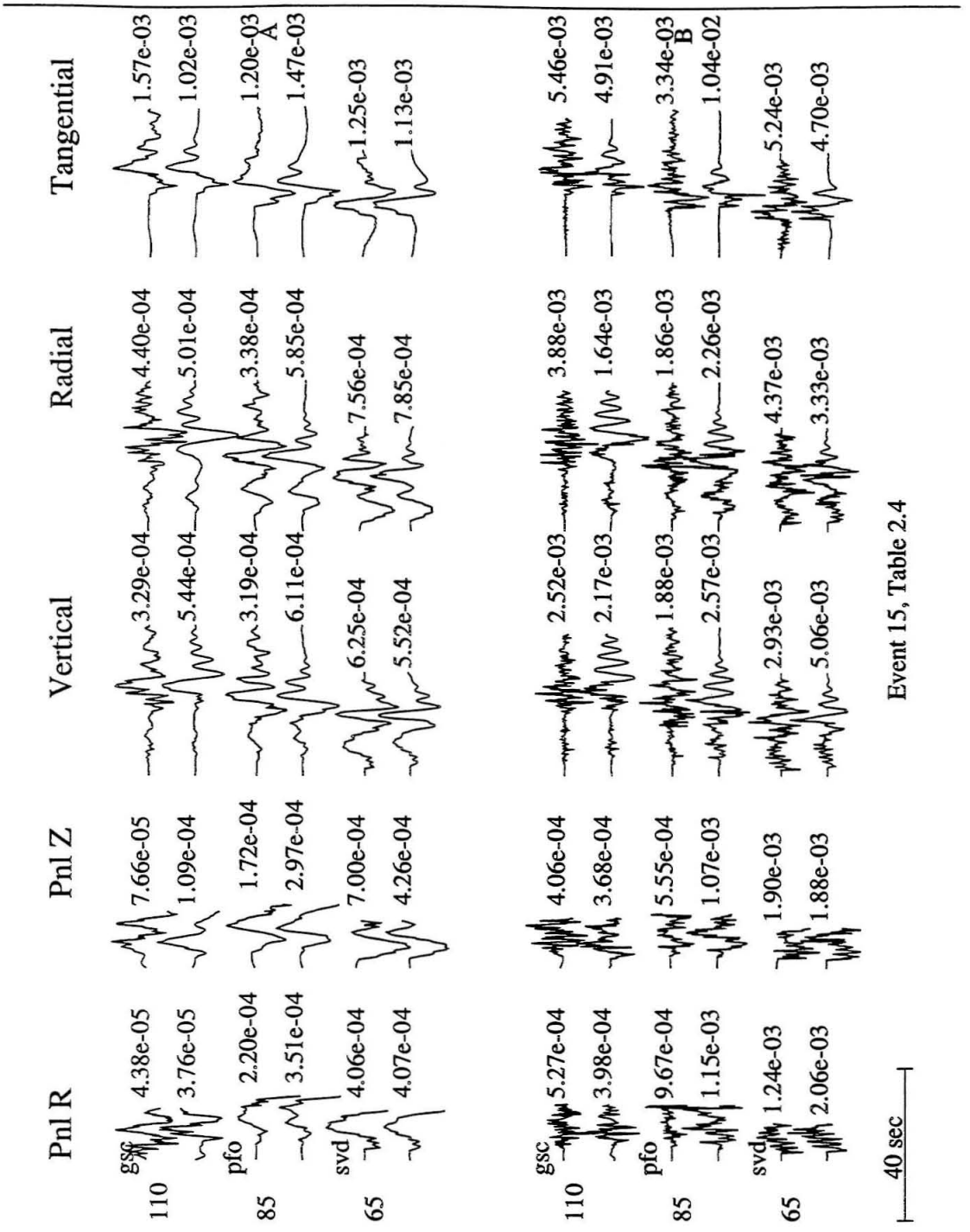

Figure 5.18: Broadband and long–period modeling for event 15, Table 2.5 (August 8, 1992). Average time function is a 0.4 s triangle. Source depth is estimated at 8 km.

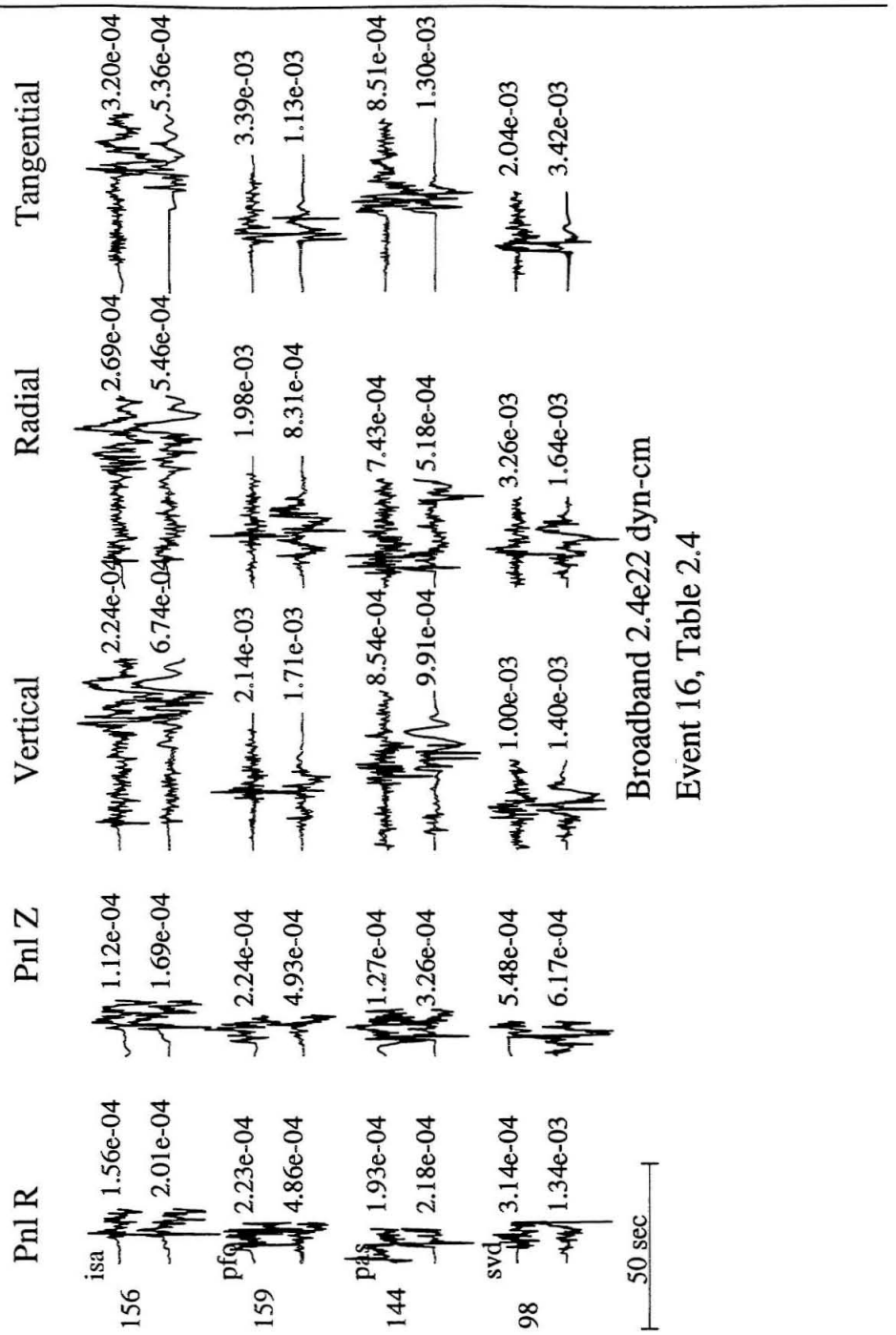

Figure 5.19: Broadband modeling for event 16, Table 2.5 (August 31, 1992). Average time function is a 0.3 s triangle. Source depth is estimated at 12 km.

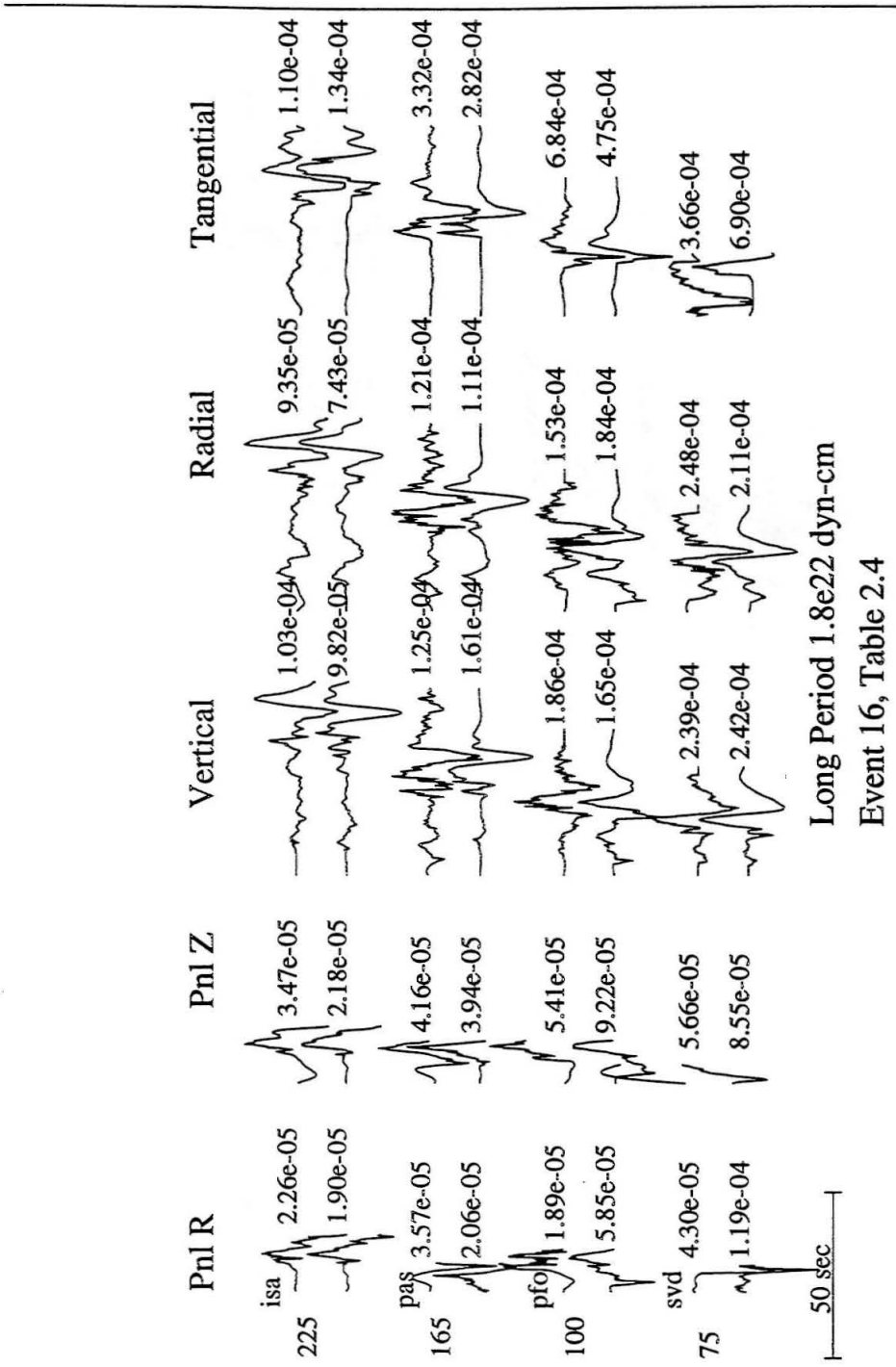

Figure 5.20: Long–period modeling for event 16, Table 2.5 (August 31, 1992). Average time function is a 0.3 s triangle. Source depth is estimated at 12 km.

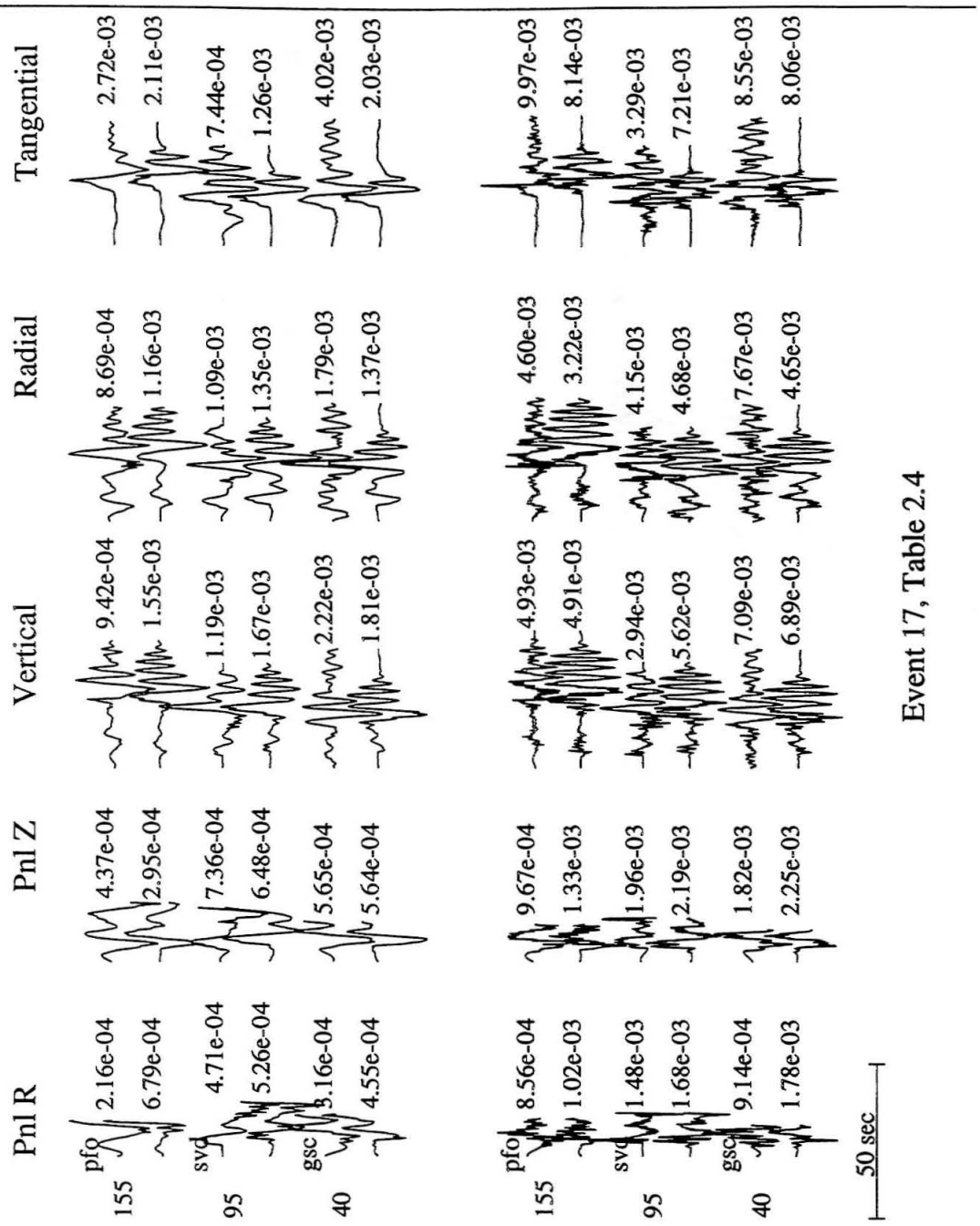

Figure 5.21: Broadband and long–period modeling for event 17, Table 2.5 (October 2, 1992). Average time function is a 0.5 s triangle. Source depth is estimated at 5 km.

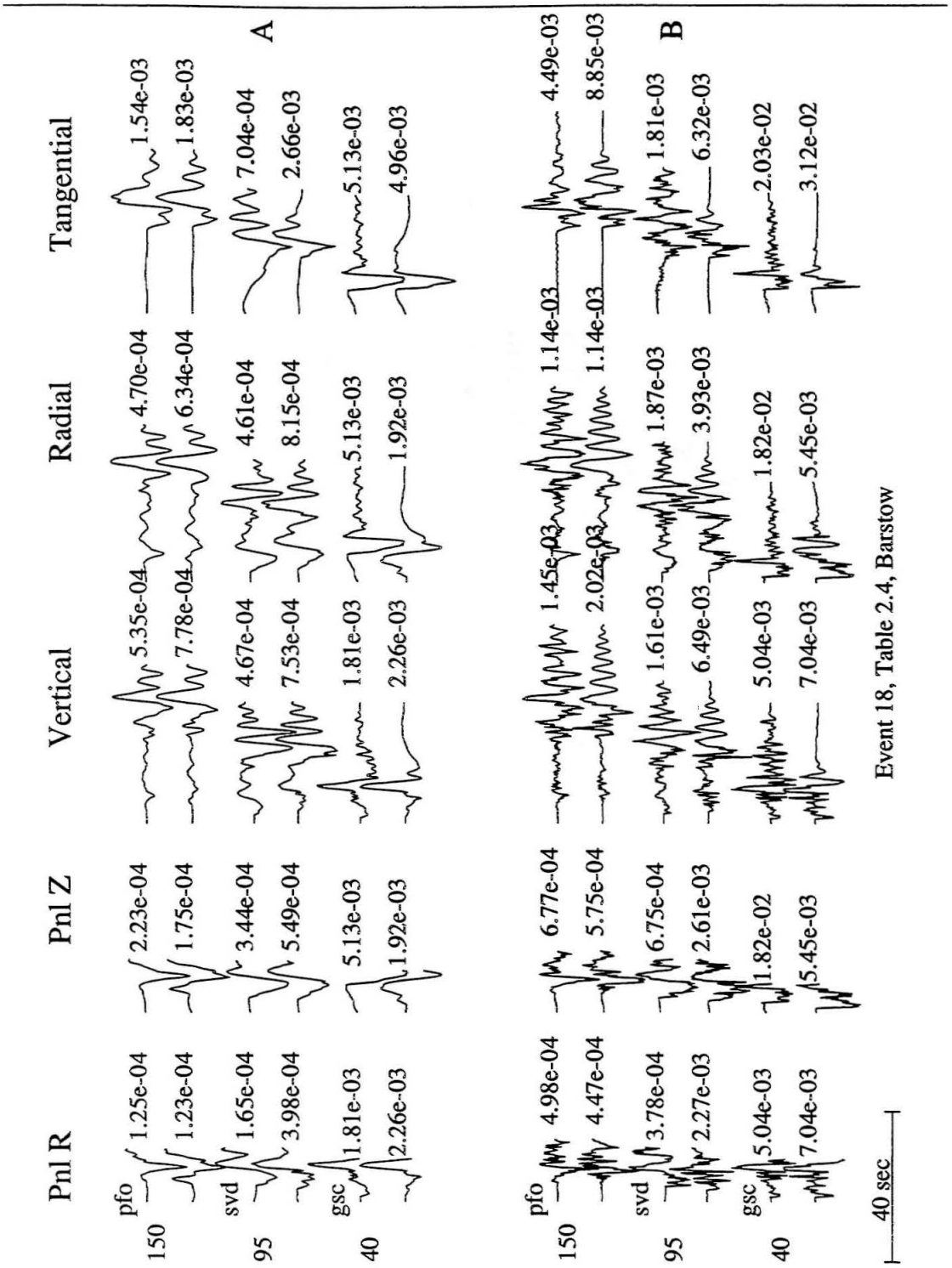

Figure 5.22: Broadband and long–period modeling for event 18, Table 2.5 (October 10, 1992). Average time function is a 0.6 s triangle. Source depth is estimated at 8 km.

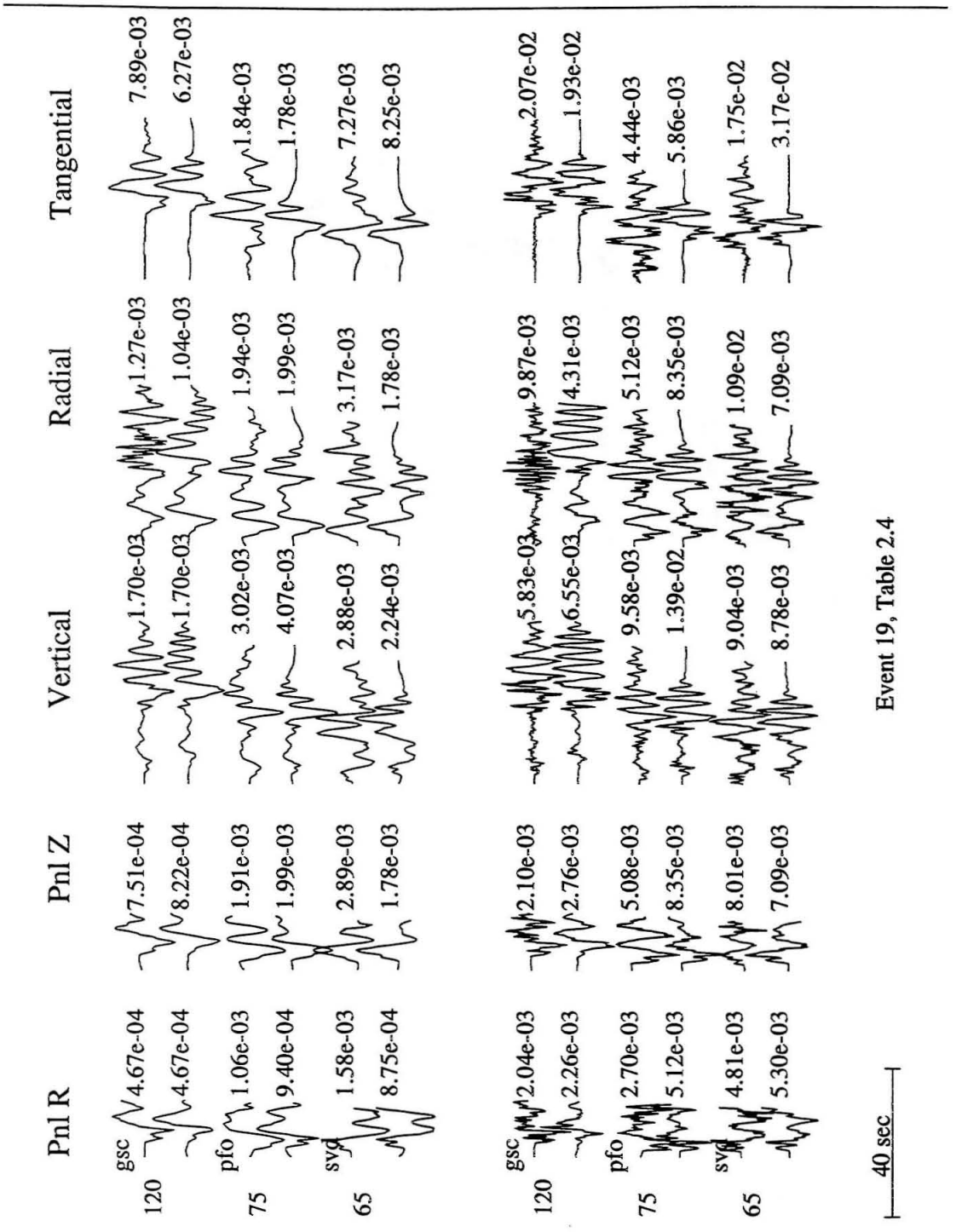

Figure 5.23: Broadband and long–period modeling for event 19, Table 2.5 (June 16, 1994). Average time function is a 1.0 s triangle. Source depth is estimated at 5 km.

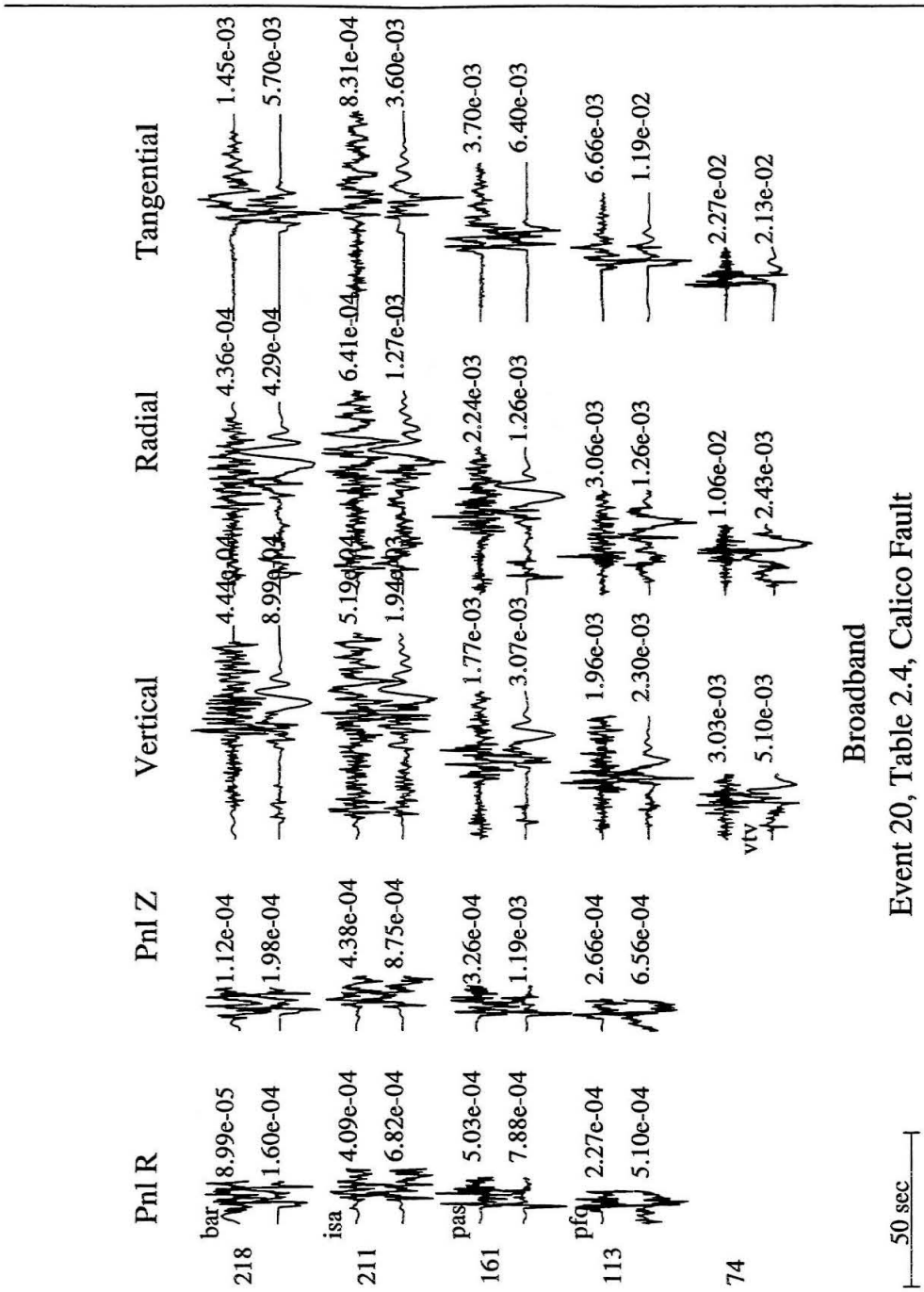

Figure 5.24: Broadband modeling for event 20, Table 2.5 (August 1, 1994). Average time function is a 0.4 s triangle. Source depth is estimated at 14 km.

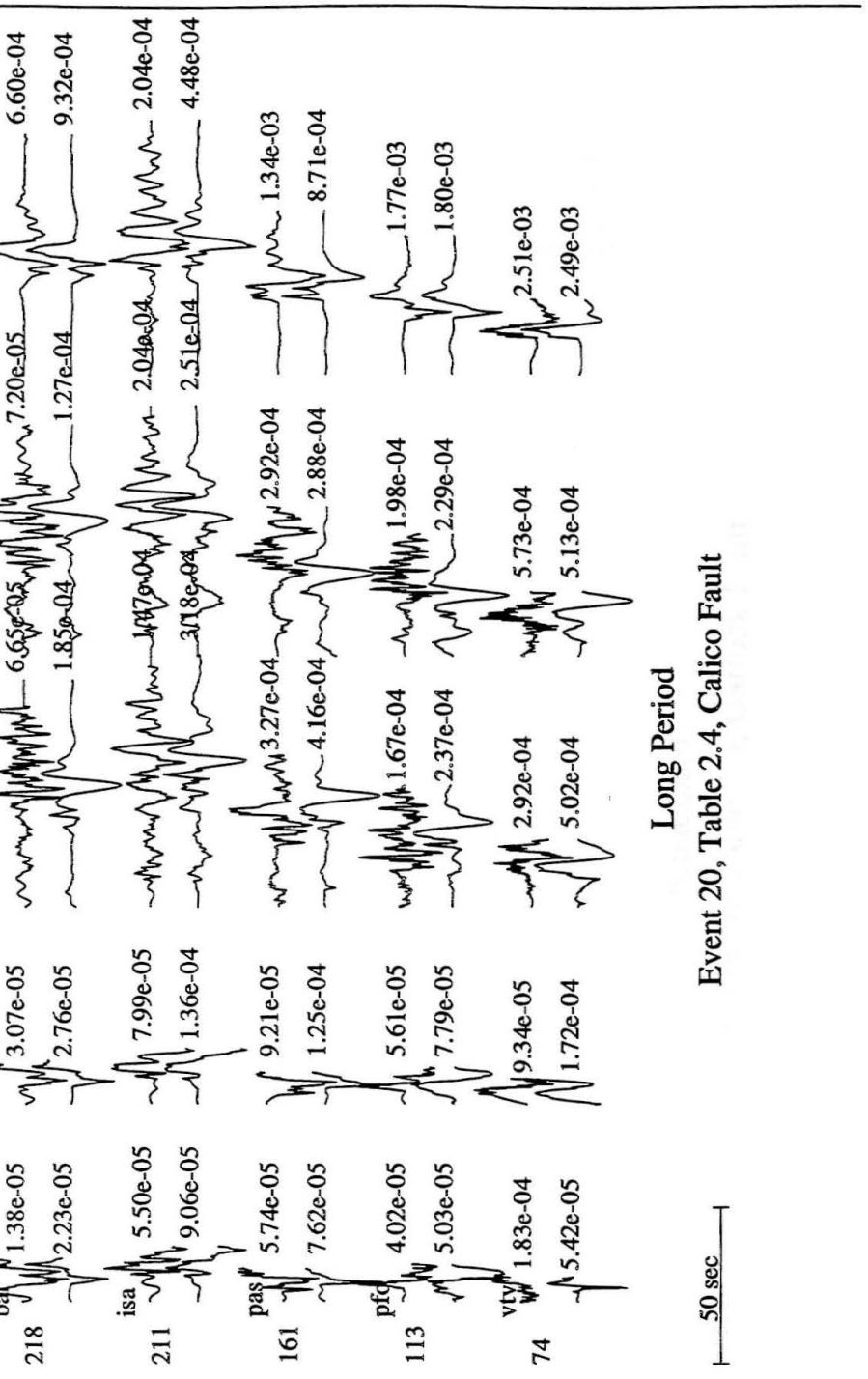

Figure 5.25: Long–period modeling for event 20, Table 2.5 (August 1, 1994). Average time function is a 0.4 s triangle. Source depth is estimated at 14 km.

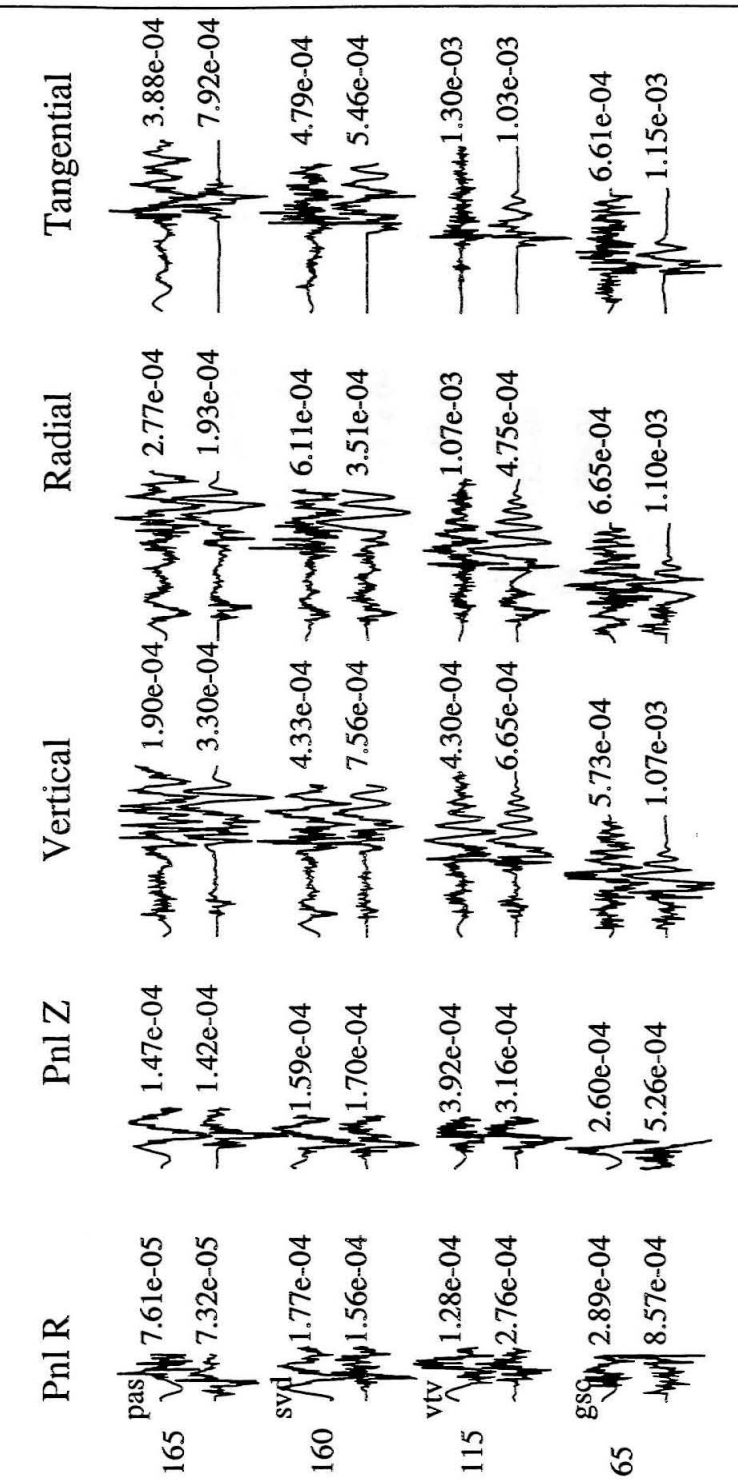

Figure 5.26: Broadband modeling for event 21, Table 2.5 (October 19, 1994, Garlock). Average time function is a 0.25 s triangle. Source depth is estimated at 8 km.

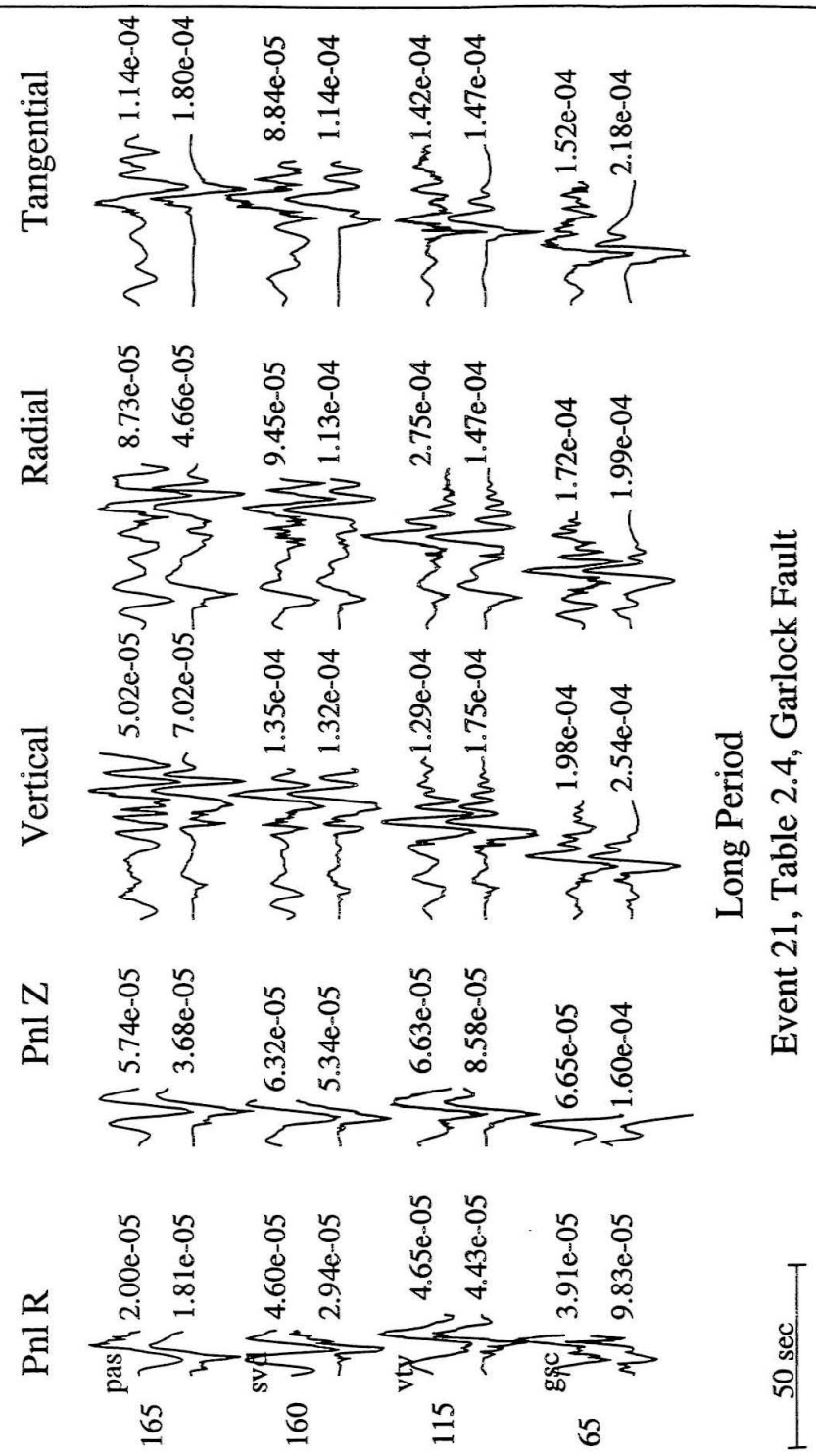

Figure 5.27: Long–period modeling for event 21, Table 2.5 (October 19, 1994, Garlock). Average time function is a 0.25 s triangle. Source depth is estimated at 8 km.